Université de Lille 1 SCIENCES ET TECHNOLOGIES

THESE

Présentée à l'Université de Lille

Ecole Doctorale Sciences Pour l'Ingénieur

Pour obtenir le grade de :

DOCTEUR DE L'UNIVERSITE

Spécialité : Micro et Nano technologies

Par

Ezgi DOGMUS

Characterization and Fabrication of InGaN Solar Cells

Soutenue le 26 novembre 2015 devant la Commission d'examen :

Rapporteurs :	M. Joël EYMERY	Chercheur senior (CEA)
	M. Zakaria DJEBBOUR	Enseignant Chercheur (Laboratoire de Génie Electrique de Paris)
Directeur de thèse :	Mme. Nathalie ROLLAND	Professeur (Lille)
Encadrant :	M. Farid MEDJDOUB	Chercheur CNRS (IEMN)
Examinateurs :	M. Didier DECOSTER	Professeur (Lille)
	M. Abdallah OUGAZZADEN	Professeur (Georgia Tech)
Invité :	M. Elhadj DOGHECHE	Professeur(Valenciennes)

Université de Lille 1 SCIENCES ET TECHNOLOGIES

THESE

Présentée à l'Université de Lille

Ecole Doctorale Sciences Pour l'Ingénieur

Pour obtenir le grade de :

DOCTEUR DE L'UNIVERSITE

Spécialité : Micro et Nano technologies

Par

Ezgi DOGMUS

Characterization and Fabrication of InGaN Solar Cells

Soutenue le 26 novembre 2015 devant la Commission d'examen :

Rapporteurs :	M. Joël EYMERY	Chercheur senior (CEA)
	M. Zakaria DJEBBOUR	Enseignant Chercheur (Laboratoire de Génie Electrique de Paris)
Directeur de thèse :	Mme. Nathalie ROLLAND	Professeur (Lille)
Encadrant :	M. Farid MEDJDOUB	Chercheur CNRS (IEMN)
Examinateurs :	M. Didier DECOSTER	Professeur (Lille)
	M. Abdallah OUGAZZADEN	Professeur (Georgia Tech)
Invité :	M. Elhadj DOGHECHE	Professeur(Valenciennes)

To my aunt Idil,

who believed in a world without terror…

Acknowledgements

It is my pleasure to express my sincere gratitude to all people, who helped me on the journey to complete my PhD research at Institute of Microelectronics and Nanotechnology (IEMN). This thesis would not be possible without their support.

First of all, I want to thank my supervisor Dr. Farid MEDJDOUB, for his valuable guidance and contribution of time, ideas and funding for numerous projects and conferences. His persistent curiosity and enthusiasm for the research have been definitely contagious and motivational for me to pursue my PhD work. I am grateful for his encouragement to establish numerous national and international collaborations, which provided added value to this work.

I am thankful to Prof. Nathalie ROLLAND for accepting me as a PhD student. I would like to extend my gratitude to Dr. Joël EYMERY and Dr. Zakaria DJEBBOUR, members of the jury, for agreeing to be the reporters of this work. My special thanks go to Prof. Abdallah OUGAZZADEN, Prof. Didier DECOSTER, and Prof. Elhadj DOGHECHE for accepting to be members of the jury.

I would like to acknowledge the all the IEMN staff in Clean Room and Characterization Platforms, for their technical support throughout my work and their kind and welcoming attitudes.

I would to like to express my gratitude to Dr. Malek ZEGAOUI for precious advices and discussions in development of the technological process in the Clean Room. I am impressed by his immense knowledge and experience in microelectronics and technology, he has taught me many things both consciously and unconsciously. I'm sincerely grateful to Astrid LINGE for creating very productive and friendly environment in the Clean Room, as well as for her patience when I speak French. I greatly enjoyed working with her and improving my French vocabulary.

I would like to acknowledge the valuable contribution from Dr. Ludovic LARGEAU for the material analyses at Laboratoire de Photonique et de Nanostructures. I want to thank him for his patience, time and fruitful discussions, which provided me with valuable and high quality material characterization of my samples. I would like to acknowledge the ANR program of future investment Equipex TEMPOS (No. ANR-10-EQPX-50) for having funded the acquisition of the STEM microscope.

I convey my thanks to Dr. Brigitte SIEBER and Dr. Ahmed ADDAD for material analyses in University of Lille 1 at Unité Matériaux et Transformations (UMET). I am grateful for their interest towards my research and the time they devoted to material characterization.

I would like to express my gratitude to Prof. Martin STUTZMANN in Walter Schottky Institute (WSI) for accepting me as a visiting PhD student in his group. My special thanks go to his group, especially Saskia and Fabien, for teaching me to conduct optical measurements and for the valuable discussions.

I would like to acknowledge the valuable contribution from Dr. Maria Tchernycheva at Institut d'Electronique Fondamentale for very interesting EBIC analyses and fruitful discussions. My special thanks go to Vladimir for the analyses of my samples and friendly lunch hours. I convey my gratitude to Dr. Martin Foldyna in Laboratoire de Physique des Interfaces et Couches Minces (LPCIM) for his time and interest for EQE analyses of my solar cells.

Last but not least, I want to thank my officemates and friends Etienne (je ne m'appelle pas Guy) and Nicolas for all the funny times that we had during both the working and non-working hours, even though the 1st was very rare. Honestly I learned a lot from you guys, French culture and language, all the songs from 90's and much more (from Etienne) and perfect advices about techno, sports and holiday destinations (from Nico). I want to sincerely thank Manon, who has always been on my side against these two, and with Jeremy, who made the "tea" and "let's get fat'" sessions enjoyable. I would like to thank Paul, who was seriously a great help during the boring PhD writing period. Without forgetting Mohamed, Moez, Colin, Philippe, Wei and many other PhD students for their friendship and all the nice soirées in Lille. I sincerely thank Sezin and Aycan for the valuable time we spent together and the Turkish nights we had. Besides, thanks to my new lunch mates Farid, Malek and Astrid for all the ultra-funny lunch hours and for their friendship and personal advices. I also thank Maria, whom I met while teaching, for her humor, friendship and perfect Lebanese food.

Finally, I would like to thank my family back in Turkey for their encouragement, my father for teaching me to think critically, my mother to listen to my heart and my sweet brother for showing me how to do both. My special thanks go to my loving, supportive and patient Efflam and his lovely family.

Abbreviations

InGaN	Indium Gallium Nitride
MQW	Multiple quantum well
PV	Photovolatic
SC	Solar cell
LCOE	Levelized cost of electricity
MOCVD	Metal-organic chemical vapor deposition
HRXRD	High Resolution X-Ray Diffraction
EDX	Energy Dispersive X-Ray
SAED	Selected Area diffraction
HAADF	High Angle Annular Dark Field
BF	Bright field
STEM	Scanning Transmission Electron Microscopy
SEM	Scanning Electron Microscopy
AFM	Atomic Force Microscopy
PL	Photoluminescence
FWHM	Full-width at half maximum
QCSE	Quantum Confined Stark effect
RT	Room temperature
EQE	External quantum efficiency
EBIC	Electron beam induced currrent
AM	Air mass
RSM	Reciprocal space mapping
FF	Fill factor
ICP	Inductive Coupling plasma
RIE	Reactive Ion Etching
RTA	Rapid thermal annealing
CSL	Current spreading layer
TLM	Transmission length method
PECVD	Plasma-enhanced chemical vapor deposition
BOE	Buffered oxide etch

Symbols

V_{OC}	Open circuit voltage
J_{SC}	Short circuit current density
J_0	Dark saturation current
η	Conversion efficiency
E_G	Band gap
P_{PZ}	Piezoelectric polarization
P_{SP}	Spontaneous polarization
x	Indium fraction
R_{Series}	Series resistance
R_{Shunt}	Shunt resistance
t_W	InGaN well thickness
t_B	GaN barrier thickness
h_C	Critical thickness
n	Number of InGaN/GaN MQW pairs
ω	Angle of rotation of the sample in XRD analysis
θ	Angle of rotation of the detector in XRD analysis

Table of Contents

Table of Contents

Table of Contents

Introduction

The III-Nitride semiconductor material systems, which include GaN, InN, AlN and their alloys, are currently used in many applications from brilliant light-emitting diodes (LEDs) and lasers to high frequency, high power transistors capable of operating at high temperatures. Over the last decade, InGaN alloy has been spotlighted for another possible application: photovoltaics. The candidacy of InGaN for photovoltaics was possible after long years of efforts and remarkable breakthroughs in growth of high structural quality InGaN/GaN heterostructures for blue LEDs [1-10] in addition to re-evaluation of the band gap of InN as 0.7 eV [11]. InGaN material system possesses the desired characteristics, such as wide and direct band gap (0.7-3.4 eV), high absorption coefficient, high thermal resistance and radiation tolerance, for achieving high efficiency PV.

The main motivation for development of InGaN based solar cells is the need for a material system, which can provide band gaps (E_g) higher than 2.4 eV. Current efficiency record of 46% is held by GaAs based 4-junction tandem solar cell in a concentrated system [12]. However, this structure is very close to its achievable theoretical limit and requires materials of E_g>2.4 eV to go beyond the 50% efficiency barrier [13]. Therefore, the development and possible integration of InGaN solar cells with the current high efficiency PV technologies would play an important role for more efficient sun-harvesting. Furthermore, the remarkable capability of III-nitrides to withstand irradiation damage and relatively high temperature makes InGaN alloys a promising candidate for harsh PV applications, i.e. space or concentrated sunlight applications.

However, the journey of InGaN solar cells has been challenging and they have still not demonstrated the expected performances. This is due to some significant difficulties related to material quality and device fabrication. The growth of high quality InGaN layers with more than 20% of indium, which can achieve the attractive band gaps unreachable by current high efficiency PV technologies, is challenging mainly due to formation of extended crystalline defects and phase separation within the alloy. As a result, the choice of the active region design is crucial for enhanced material quality of the solar cells. Besides, difficulties in p-type doping and strong polarization in InGaN material system can limit significantly the device performances. Furthermore, a well optimized device processing sequence is required for fabrication of fully functional InGaN based solar cells.

In this frame, this thesis work focuses on the material characterization of solar cell structures with various active region designs and different substrates as well as the fabrication and electrical characterization of InGaN solar cells. The epitaxial growth of solar cell designs with p-GaN/i-InGaN/n-GaN structures were performed by metal-organic vapor phase epitaxy (MOCVD) by the company NovaGaN.

One of the main objectives is to investigate the influence of the active region design on the crystalline quality of the solar cells structures. To do so, structural and optical characterization techniques such as X-Ray diffraction (XRD), scanning transmission electron microscopy (STEM), atomic force microscopy (AFM) and photoluminescence (PL) spectroscopy were carried out. A structural comparison of solar cell designs including bulk 200 nm thick InGaN layer and InGaN/GaN multiple quantum wells (MQWs) with similar indium compositions is presented. Furthermore, structural quality of designs with InGaN/GaN MQWs were analyzed with variation of the indium content, thickness of InGaN quantum wells and type of the substrate, i.e. sapphire or bulk GaN substrate.

The second principal objective of this study is to develop and optimize the device fabrication process. In addition, an optimization study of transparent and conductive Ni/Au current spreading layer is presented. Also, the influence of using grid schemes for p-type contacts on the device performance is investigated. The photovoltaic performance of solar cells is analyzed as a function of the indium content and the type of substrate. Furthermore, electron beam induced current analysis (EBIC) and external quantum efficiency (EQE) measurements provided additional information such as electrical activity of the active region and spectral response of the solar cell structures.

This manuscript is organized as follows:

Chapter 1 presents the basics of the solar power and an economic overview of the PV industry. The principals of solar cell operation are explained in order to understand the roadmap and needs of the current high efficiency PV technologies. Crystalline and structural properties of III-Nitrides family as well as the polarization effects in the structures are described. The major breakthroughs in III-Nitrides optoelectronic devices, which led to the introduction of InGaN based PV, are presented afterwards. A brief literature study on InGaN based solar cells is reported, which provided a guidance on the choice of the device design in this work. Finally, the potential application of InGaN material system in harsh environments, i.e. high temperature and irradiation, is discussed.

Chapter 2 describes first the structural material characterization techniques of XRD, STEM and AFM, as well as the optical characterization method of PL spectroscopy. In addition, the electrical measurement methods such as current-voltage, EBIC and EQE characterizations are depicted. In the second section of this chapter, comparative structural and optical characterizations of various solar cell designs, such as the nature of the active region; i.e. bulk InGaN or InGaN/GaN MQWs; the composition of In, thickness of quantum wells, the type of the substrate; i.e. c-plane (0001) sapphire or bulk GaN substrate, are presented.

Chapter 3 shows first the main technological steps of the device fabrication process. Special emphasis is given to challenges in solar cell processing steps such as mesa etching and device sidewall protection. This chapter includes also an optimization study of transparent and conductive current spreading layer consisting of Ni/Au. Besides, some preliminary electrical and photovoltaic characterizations are presented for the solar cells using $In_xGa_{1-x}N$/GaN MQWs with relatively high In content, i.e. x=0.19 and 0.24. Finally, a comparison of device performances of solar cells using $In_{0.15}Ga_{0.85}N$/GaN MQWs grown on sapphire and bulk GaN, which were fabricated with optimized processing conditions, are exhibited and the results are discussed.

The manuscript finishes with general conclusions and possible future works on InGaN based solar cell. Furthermore, perspectives such as integration of InGaN solar cells with the current high efficiency PV and development of multijunction InGaN based solar cells by exploiting tunnel junctions are proposed to achieve higher conversion efficiency photovoltaics.

Chapter 1

Introduction to III-Nitride based solar cells

1.1 Basics of Solar Cells

1.1.1 Harnessing of solar energy

Climate change is one of the most significant phenomena of the 21st century. Most of the climate scientists agree that the global warming is caused by the extensive exploitation of fossil fuels, such as coal, crude oil and natural gas, which produces increased levels of greenhouse gases [14]. Over the last decades, our world has already confronted melting of icecaps and glaciers, accelerated rise of sea level and abrupt changes in weather patterns as a result of the inexorable global warming. In addition to the environmental concerns, it should be seriously considered that the supply of these fossil fuels is finite despite our progressively growing dependence on them due to the increasing energy demand of the world population. Given the environmental, social and economic problems associated with the continued use of the natural resources, it becomes crucial to switch to sustainable and renewable energy sources which can adequately meet the potential energy needs. Fortunately, our earth offers numerous renewable energy sources such as solar, wind, hydro, tidal, geothermal heat and biomass. Hence, now it is the right time to start switching our habit of using conventional energy sources and provide better life quality for next generations.

Among the various options of renewable energy sources as listed above, the sunlight is the most promising. The fact that the solar energy received on the top of the atmosphere in an hour (1.7×10^5 terawatts) is much more than the annual energy consumption of the world, is remarkable [15]. Not only because the sun is the entire origin of almost all of the renewable and conventional energy sources, but it is also an inexhaustible, absolutely safe, omnipresent and free source that is required in the nature to sustain life. In addition to its functionality in heating, photosynthesis and formation of fossil fuels, the sunlight can be also directly converted into electricity by the so-called *photovoltaics* (PV) process. This way of harnessing solar energy is highly reliable, environmentally safe, extremely clean, easy to install and it operates at low costs once the solar technologies are installed without producing any greenhouse-gas emission.

Since the discovery of the photovoltaic effect by the French scientist Becquerel [16], the progress in higher performance and lower cost PV technologies have expanded very rapidly with a significant potential for long-term growth in the world. Today the most impressive and promising example of efficient PV generated electricity is in Germany: On a sunny day around noon, Germans can generate 50.6% of their electricity from solar power! In 2014, the total PV-generated power of 35.2 TWh covered approximately 6.9% of Germany's net electricity consumption [17].

1.1.2 Economic viability of solar energy

Figure 1.1 shows that the world's total PV electricity capacity has doubled each year since 2002 and by 2013 it passed 138.9 gigawatts (GW) [18], which is equivalent to an annual capacity of production of electricity from 32 coal power plants or 53 nuclear reactors.

Even though these numbers seem high, today the total PV market stays rather tiny, i.e. less than 1% of overall energy production of the world. The most optimistic reports claim that by 2020, in Germany and China, which are the world's two leading countries currently investing on the solar power; the PV generated electricity would meet only below 10% and 1% of their annual gross power consumption, respectively [19,20]. The main reason for incompetency of PV still remains to be the elevated manufacturing and installing costs of solar electricity.

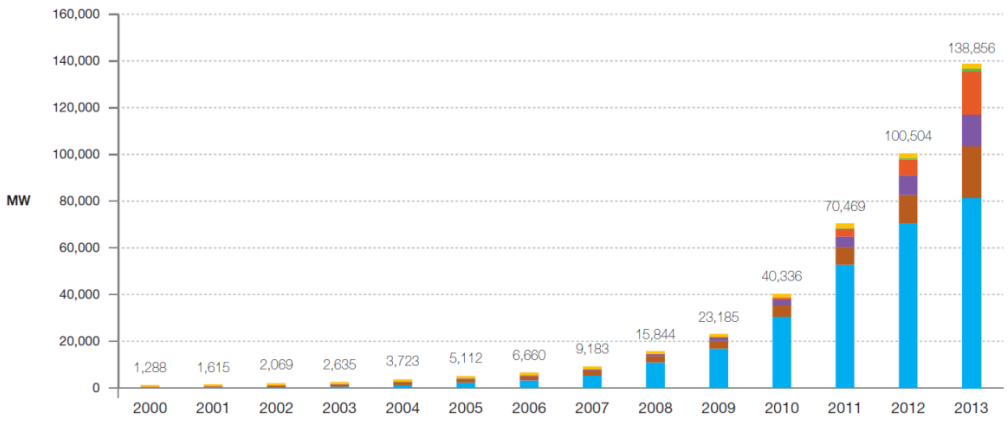

	2000	2001	2002	2003	2004	2005	2006	2007	2008	2009	2010	2011	2012	2013
RoW	751	807	887	964	993	1,003	1,108	1,150	1,226	1,306	1,590	2,098	2,098	2,098
MEA	n/a	n/a	n/a	n/a	1	1	1	2	3	25	80	205	570	953
China	19	24	42	52	62	70	80	100	140	300	800	3,300	6,800	18,600
Americas	21	24	54	102	163	246	355	522	828	1,328	2,410	4,590	8,365	13,727
APAC	368	496	686	916	1,198	1,502	1,827	2,098	2,628	3,373	4,951	7,513	12,159	21,992
Europe	129	265	399	601	1,306	2,291	3,289	5,312	11,020	16,854	30,505	52,764	70,513	81,488
Total	**1,288**	**1,615**	**2,069**	**2,635**	**3,723**	**5,112**	**6,660**	**9,183**	**15,844**	**23,185**	**40,336**	**70,469**	**100,504**	**138,856**

RoW: Rest of the World. MEA: Middle East and Africa. APAC: Asia Pacific.
Methodology used for RoW data collection has changed in 2012.

Figure 1.1 Evolution of global PV cumulative installed capacity between the years 2000-2013 [18].

One way to calculate and compare the cost of different methods of electricity generation is the method of Levelized Cost of Electricity (LCOE). It is an economic model that predicts the overall cost of the energy system including the initial investment, operations and maintenance, taxes and insurance etc. over its lifetime.

Figure 1.2 shows the comparison of levelized costs of different energy technologies to solar energy in two leading countries in current global PV market. In 2013, LCOE for German PV panels varied from 0.078 to 0.142 €/kWh which was twice as much as that of the brown coal (0.038-0.053 €/kWh) which was the cheapest source of German electricity [21]. Similarly, in China, by 2014 LCOE comparison revealed that the solar power price, 0.60¥/kWh, doubled that of nuclear and coal power, 0.23¥/kWh and 0.27¥/kWh [22].

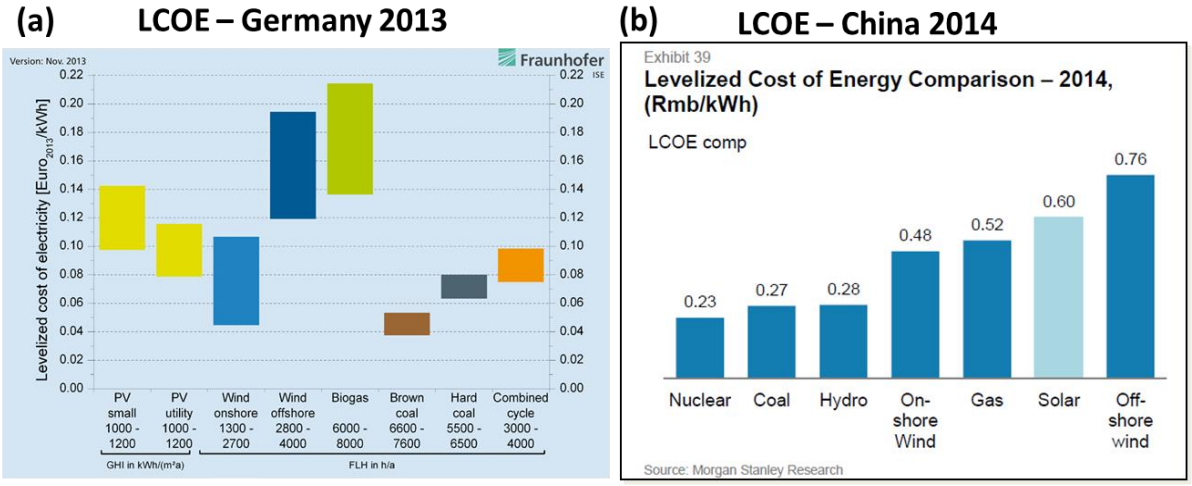

Figure 1.2 Levelized cost of electricity of conventional and renewable energy technologies in (a) in Germany and (b) in China, for 2013 and 2014 respectively [21, 22].

It is argued that to achieve grid parity (i.e. the point at which the PV generated electricity gets competitive with the conventional electricity sources) the performance of PV modules should be enhanced. Hence, the cost and the performance of solar panel directly depend on the energy conversion efficiency of the photovoltaic cells that consist of semiconductor material capturing and transforming the sunlight.

1.1.3 Basics of photovoltaic conversion

A solar cell operates by converting the sunlight directly into electrical energy, using the photovoltaic effect. The photovoltaic energy conversion in semiconductor materials has fundamentally four essential steps;

1. A light absorption process in which the charge carriers are excited from ground state to higher energy states in the light absorbing semiconductor,
2. The energy conversion of the excited states into one pair (at least) of negative and positive charge carriers called *electrons* and *holes*,
3. A charge separation process in which electrons and holes are separated at the p-n junction, and a built-in electric field ensures the flow of electrons in one direction (to *n-type semiconductor*) and the holes in the opposite direction (to *p-type semiconductor*),
4. The collection of the electrons and holes at the n-contact and the p-contact, respectively, thus generating the electrical power.

1.1.3.1 Photon absorption

The energy supply for a solar cell comes from the sunlight, more specifically from the particles called *photons*. The energy of the photons depends on atmospheric conditions, latitude etc. over different wavelengths of sunlight. Figure 1.3 shows the incident spectral radiance of sunlight as a function of photon energy with standardized spectra such as Air Mass 0 (AM0) and Air Mass 1.5 Global (AM1.5G). AM0 corresponds to the solar spectrum outside the atmosphere and used for satellite applications. On the other hand, the AM1.5G spectrum is referred for terrestrial solar cells and it includes direct and diffused light with total integrated intensity of 1000 W/m^2 (known as 1 Sun).

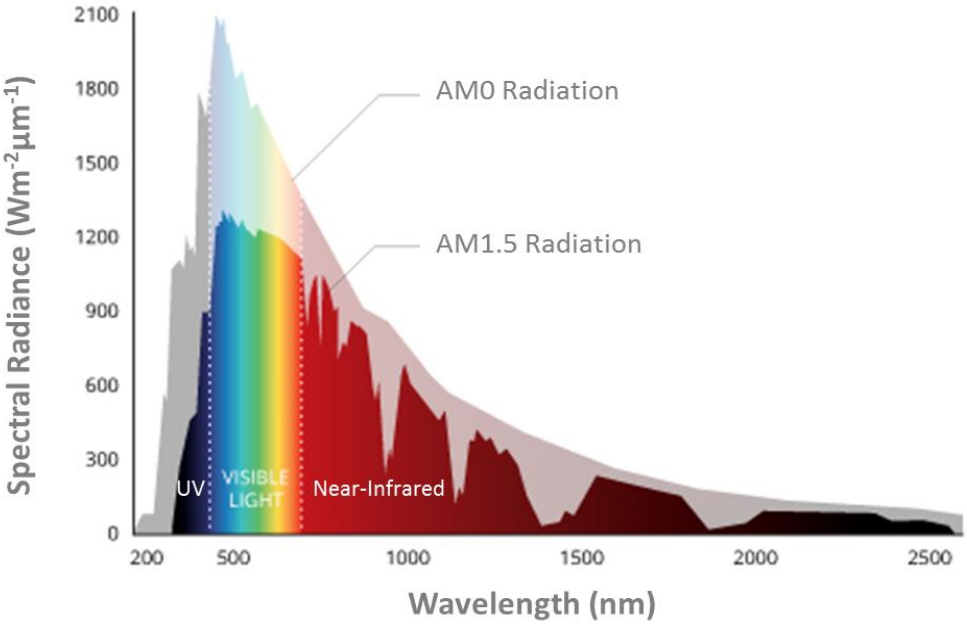

Figure 1.3 Spectral radiance of sunlight as a function of wavelength, AM0 Radiation in the space, AM1.5G Radiation in the Earth's surface.

However, only some part of the energy coming from the sun can be converted into electrical power. Only the photons having equal or higher energy than the bandgap energy of the semiconductor can contribute to efficient absorption and excitation of electrons from valence band to conduction band (Figure 1.4 [b]). The excess energy of high energy photons is lost as heat in the material which causes *thermalization losses* as shown in Figure 1.4 (a). On the contrary, low energy photons are not absorbed and they are the origin of *transmission losses* (Figure 1.4 [c]).

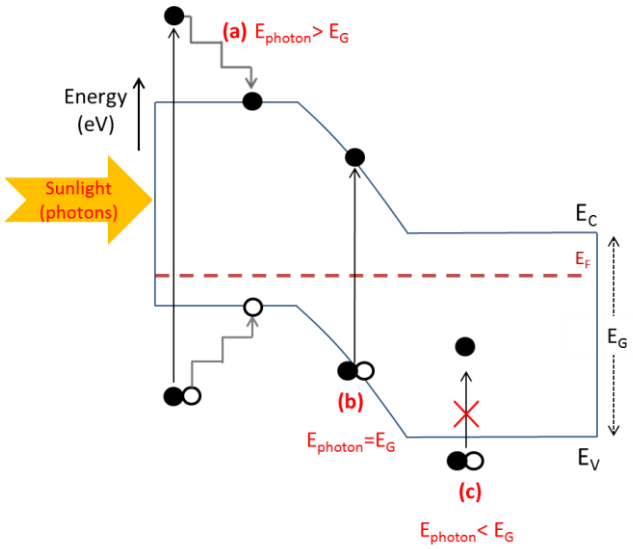

Figure 1.4 Illustration of absorption and loss mechanisms in a solar cell (a) Photons with energy higher than the band gap, E_G (b) Efficient absorption of photons and conversion (c) Photons with insufficient energy for absorption.

The thickness and the absorption coefficient of a semiconductor material determine the amount of light that is absorbed, which is described by Beer-Lambert law [23]. I (0) is the intensity of the incident light, I(x) is the intensity of the light transmitted through the sample, α is the absorption coefficient of the semiconductor and x is the thickness of the material (Equation 1.1).

$$I(x) = I(0)e^{-\alpha x} \tag{1.1}$$

The absorption coefficient determines the penetration distance of the light in the material without being absorbed. It is inversely proportional to the wavelength of the light, resulting in full absorption of shorter wavelength (higher energy) photons at the front of the material, while permitting the longer wavelengths (lower energy) photons penetrate deeper in the substance.

1.1.3.2 Charge separation

Once an electron-hole pair is created, they have to be separated by a driving force before they can relax back to their ground state. This driving force is provided by the p-n junction, which is a junction between same semiconductors having different doping properties. In a p-n junction, upon the connection of p-type and n-type semiconductors, the electrons in the p-type diffuse to n-type leaving positively charged ions behind, whereas the holes in the n-type diffuse into p-type material leaving negatively charged ions behind. As a result, a built-in electric field is created which opposes the diffusion of any charge carriers at the semiconductor interface region which is called *depletion region*. Solar cells are classified depending on the creation of the built-in asymmetry or the formation of the depletion region.

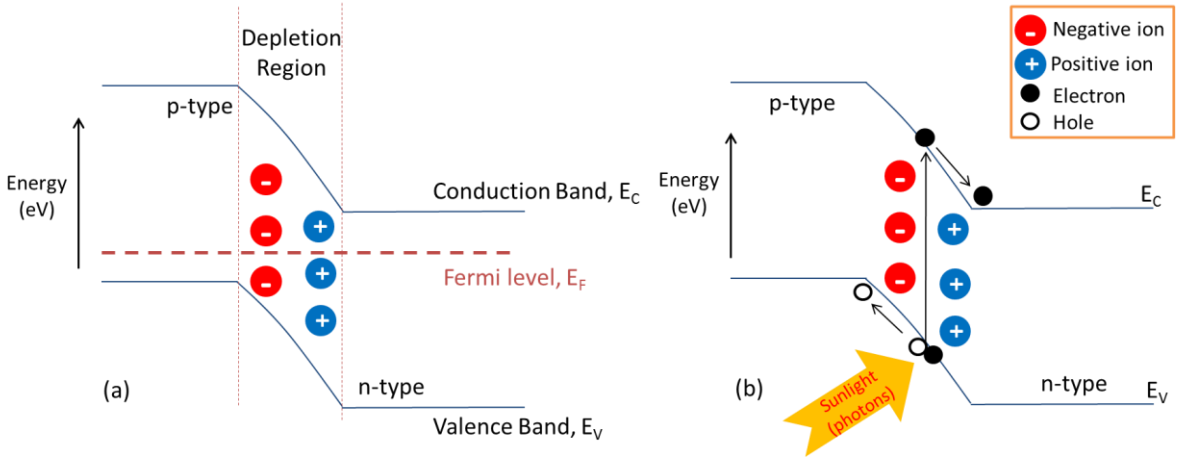

Figure 1.5 Band diagram of a p-n junction (a) in equilibrium condition (b) under illumination.

Figure 1.5 (a) shows the band diagram of a p-n junction in the equilibrium condition. The depletion region and the built-in electric field depend on the relative doping on the either side of the interface. Upon illumination, the photogenerated electrons and holes in the depletion region are separated by the built-in electric field generating a photocurrent. Electrons and holes generated in the vicinity of the depletion region can also contribute to the photocurrent, if their distance is equal or smaller than their *diffusion length*, L_C. Diffusion length is a key parameter, since it determines the average distance that can be travelled by the carriers before getting recombined. It is defined by the Equation 1.2, where D_C is the diffusion coefficient of the carriers and τ_C is the carrier lifetime.

$$L_C = \sqrt{D_C \, \tau_C} \tag{1.2}$$

In order to enhance the sweeping of the minority carriers across the junction, the depletion region width is extended by the use of a p-i-n junction solar cell, where *i* stands for intrinsic semiconductor. Figure 1.5 (b) shows the drift of photogenerated electrons towards the n-type semiconductor, while the photogenerated holes are drifted to the p-type semiconductor. The charge separation is followed by the collection of electrons at the n-contact and holes at the p-contact.

1.1.3.3 Output power of a solar cell

The solar cell is a two terminal device which works like a diode in the dark and generates a photocurrent when illuminated. In dark, when a forward bias is applied to the diode, the majority carriers (holes in the p-type, electrons in the n-type) are pushed towards the junction leading to reduction of the width of depletion region until it is entirely eliminated. Under the reverse bias, the carriers are pulled away from the depletion region causing an increase in the depletion width. In an ideal diode, very small current flows through the junction in reverse bias, which is called the *dark saturation current* (I_0). At very high applied reverse voltage, the carrier leakage appears in the junction eventually leading to reverse breakdown of the diode. Equation 1.3 gives the expression of dark current, I_{dark}, flowing through the diode as a function of applied voltage, V; where q, k and T are electron charge, Boltzmann constant and temperature, respectively.

$$I_{dark} = I_O\left(e^{\frac{qV}{kT}} - 1\right) \tag{1.3}$$

When charged by the sun, the cell develops a photovoltage and generates a photocurrent. The key parameters to describe the photocurrent and photovoltage are the *short-circuit current* (I_{SC}) and the *open-circuit voltage* (V_{OC}). I_{SC} is the photocurrent that flows through the cell when the voltage across the cell is zero (i.e. when the cell is short-circuited). In general, since the I_{SC} is proportional to the area of solar cell (A), the short circuit density, $\boldsymbol{J_{SC}} = \frac{\boldsymbol{I_{SC}}}{\boldsymbol{A}}$, is often used to compare different solar cells. Under illumination, the resulting net current density in the cell is approximated as a superposition of the short circuit current density and the dark current density as shown in Equation 1.4.

$$J = J_{SC} - J_O\left(e^{\frac{qV}{kT}} - 1\right) \tag{1.4}$$

Applying forward bias to an illuminated p-n junction, leads to a decrease in the potential barrier for the carrier diffusion and an increase in the diffusion current. At a certain applied voltage, called V_{OC}, the dark current and photocurrent exactly cancel out, leading to a zero net current in the cell. This is the maximum voltage that can be attained from the cell. The V_{OC} for an ideal solar cell is expressed as shown in Equation 1.5.

$$V_{OC} = \frac{kT}{q} \ln\left(\frac{J_{SC}}{J_O} + 1\right) \tag{1.5}$$

The overall current voltage response of the cell in dark and under illumination, which is called current-voltage characteristics, is shown in Figure 1.6. The parameter that relates the actual maximum power obtained from the cell to the theoretical maximum power is the *fill factor, FF*. Fill factor describes the 'squareness' of the J-V curve and it can be calculated as shown in Equation 1.6. In Figure 1.6, it is the ratio of the area A (indicated by blue color) to the area B (colored by yellow).

$$FF = \frac{J_{MAX} V_{MAX}}{J_{SC} V_{OC}} \tag{1.6}$$

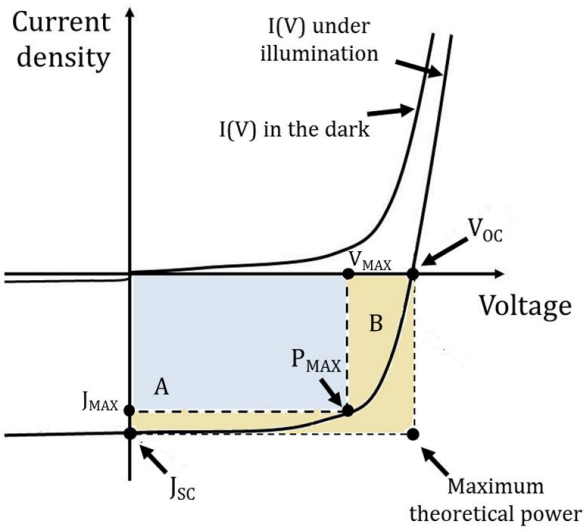

Figure 1.6 Current density- voltage characteristics of a solar cell in dark and under illumination with key parameters, J_{SC}, V_{OC}, J_{MAX}, V_{MAX}, P_{MAX}.

In solar cells, there are three different types of efficiencies: *conversion efficiency* (η), *internal quantum efficiency* (IQE) and *external quantum efficiency* (EQE). The conversion efficiency is described as the ratio of the power delivered from a solar cell to the incident light power density and it can be obtained from Equation 1.7. The conversion efficiency should be

defined by standard test condition for the solar cells, i.e. AM1.5 condition, at 25°C and with incident power density of 1000Wm^{-2} (1 sun).

$$\eta = \frac{J_{MAX}V_{MAX}}{P_S} = \frac{J_{SC}V_{OC}FF}{P_S} \quad (1.7)$$

The internal quantum efficiency corresponds to the ratio between the numbers of charge carriers collected in the solar cell to the number of photons that are absorbed in the cell at a specific wavelength. Whereas, the external quantum efficiency is the ratio of the number of charge carriers collected in the solar cell to the number of incident photons hitting the cell.

Contrary to an ideal solar cell, the power can be dissipated through the parasitic resistances such as *series resistance*, R_{SERIES} and *shunt resistance*, R_{SHUNT} in a real cell. Series resistance arises from the resistance of the cell material to current flow, including the bulk resistance of non-depleted n-type and p-type semiconductors as well as the resistance between the metal contacts and the semiconductors. On the other hand, the shunt resistance is due to the leakage current through the cell and the surface recombination. Increase in R_{SERIES} of the cell causes a reduction in the $J_{SC,}$ while decrease in R_{SHUNT} leads to lower V_{OC} values. Figure 1.7 shows the equivalent circuit for the solar cell, in which the effect of R_{SERIES} and R_{SHUNT} are indicated.

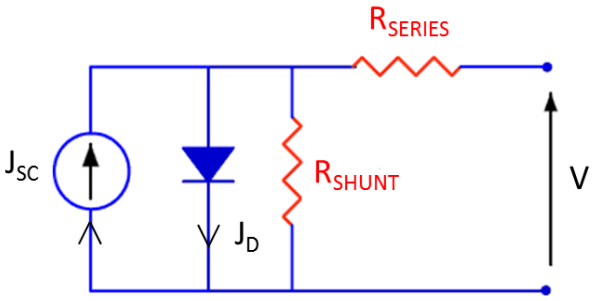

Figure 1.7 The equivalent circuit for a PV cell.

1.1.4. A roadmap to high efficiency solar cells

Since the development of the first silicon SC with 6% efficiency by Chapin *et al.* in 1950's [24], technological leaps and continual innovations both in material science and solar panel production have paved the way for high cell efficiencies close to 50% nowadays. The roadmap of solar cells has been set by two features: conversion efficiency and cost. Figure 1.8 exhibits the progress of best research cell efficiencies of different generations of solar cells (SCs) which have been developed throughout the time [25].

First generation SCs, which consist of solar cells based on crystalline Silicon (c-Si), represent today 90% of the global market. Innovative technologies such as surface texturing [26], using buried contacts [27] and reducing wafer thickness are adopted in order to increase the light absorption. As a result, high efficiencies up to 27.6 % [28] have been achieved by single junction c-Si SCs. However, single junction crystalline Si based solar cells are about to reach their maximum theoretical efficiency limit, which was calculated by Shockley and Queisser's in 1961 [29].

Shockley and Queisser's detailed model for the maximum theoretical efficiency has guided significantly the research and development of high efficiency solar cells. They calculated a theoretical limit of 33.7% for a solar cell having semiconductor with a band gap of 1.34eV by taking the following assumptions into consideration [29];

1. The solar cell is composed of only one semiconductor material (single p-n junction).
2. A single absorbed photon can give rise to only one electron/hole pair.
3. Thermalization and transmission losses are not neglected.
4. All recombination are via radiative processes inside the material.

By taking their model into account, the maximum theoretical efficiency of abundantly used single junction Si solar cells can reach 29.4% under 1 sun AM1.5G illumination [30].

With the purpose of reducing the cost of production and using less material, 2nd generation SCs have been developed in form of thin-film SCs of amorphous silicon (a-Si), polycrystalline silicon (poly-Si), Cadmium telluride (CdTe) or Copper Indium Gallium Selenide (CIGS). However, Si based second generation SCs suffer mostly from the structural defects and stability (for a-Si) that make them less efficient compared to the 1st generation cells. The second best thin film SCs are based on CIGS, which have achieved best research efficiencies of 23.3% [31]. However, toxicity is one of the big obstacles for the production and the recycling of these solar modules.

Even though the costs were progressively reduced as the second-generation SCs became mature, none of them have been able to compete with the bulk crystalline silicon SCs so far in terms of high performance, stability, abundance, and nontoxicity. On the other hand, the single junction crystalline Si solar cells cannot promise very high efficiencies mainly due to the spectral losses (transmission + thermalization losses).

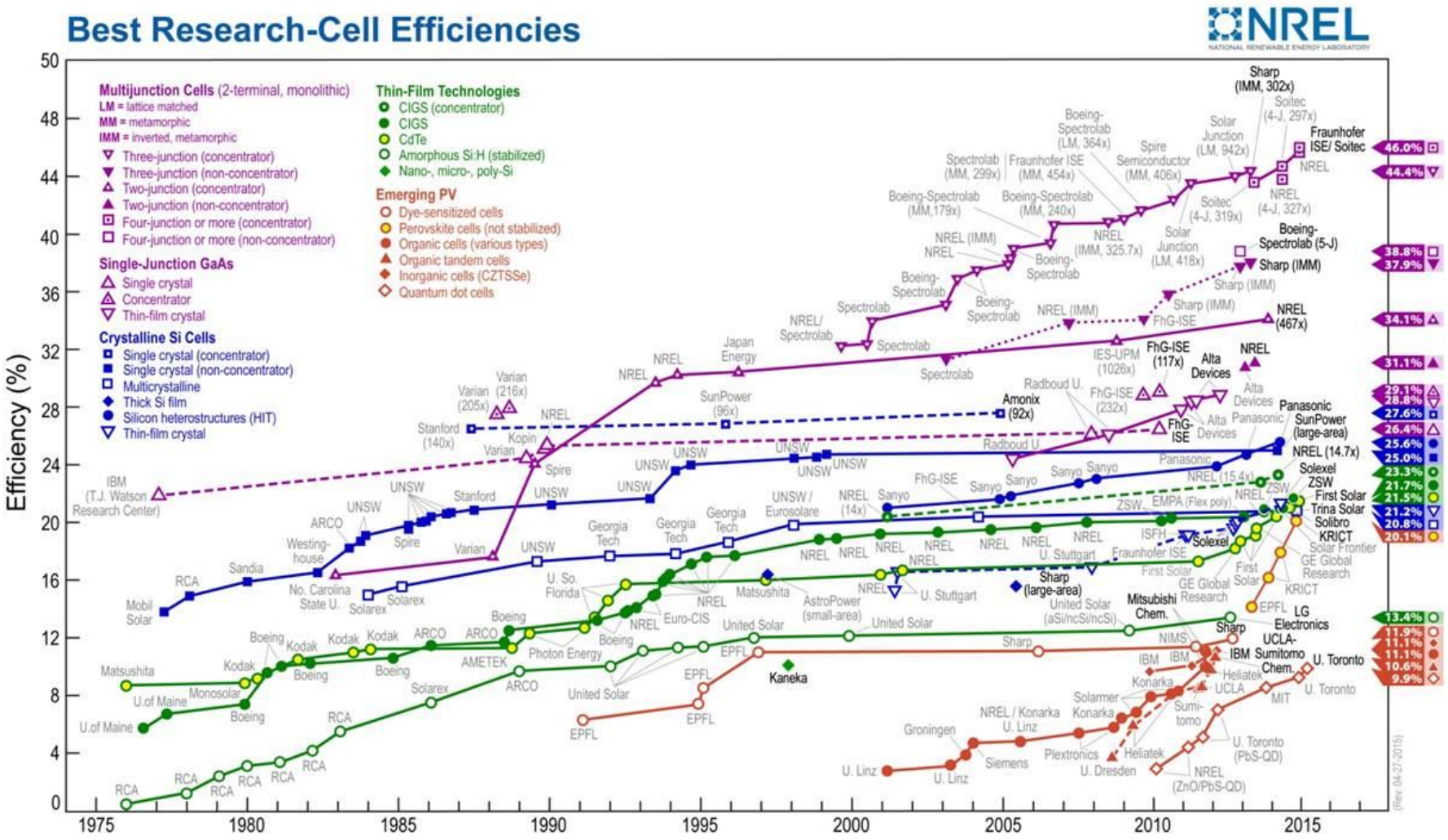

Figure 1.8 Progressive development of best research efficiency SCs from 1977 to 2015 illustrated by NREL [25].

This constituted the main driving force for the generation of two novel configurations:

- Stacking of multiple solar cells of different bandgaps to increase the absorption spectrum, which led to the development of *tandem solar cells,*
- Reducing the area of the solar cell by concentrating the sunlight by using mirrors and lenses, which resulted in formation of *concentrated photovoltaics.*

Tandem solar cells can revolutionarily reduce the thermalization and transmission losses by splitting the spectrum and absorbing efficiently different sections of the spectrum by stacking several cells with different bandgaps. Figure 1.9 illustrates the spectral absorption of a five junction tandem solar cell having sub-cells that can separately absorb the photons with energy close to their band gaps. Semiconductors having higher bandgap are designed to be stacked on top to absorb the high energy photons by filtering and transmitting the lower energy photons to the sub-cells beneath with lower bandgaps. Tandem cells are classified in two groups; *stacked cells* which consist of isolated and individually probed cells, and *monolithic cells* in which the sub-cells are internally series connected by tunnel junctions on one substrate. For an infinite stack of independently operated cells, tandem cell conversion efficiency is calculated to be 86.8% [32]. In addition, the tandem cell performance increases by adding new sub-cells in the stack and by keeping low ohmic contact resistances between the cells.

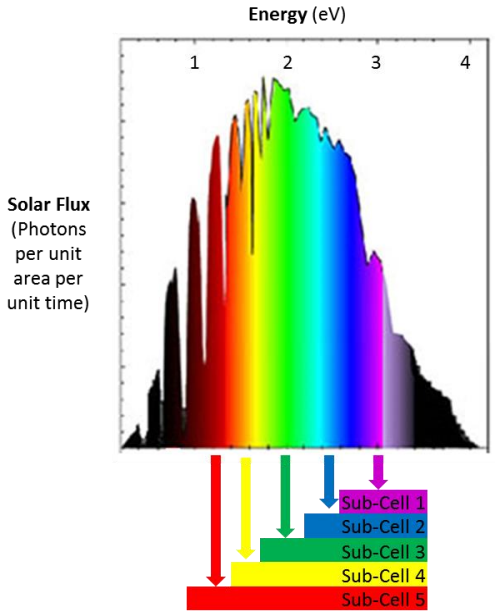

Figure 1.9 Illustration of spectral absorption in five-junction tandem solar cell in which the band gap of subcells decrease from subcell- 1 down to sub-cell 5.

A combination of concepts of tandem and concentrated PV formed the basis of the 3rd generation solar cells. Today an efficiency record of 46% is held by a four-junction tandem solar cell based on III-V semiconductors under concentrated sunlight (x508 Suns) by Soitec and CEA-Leti, France, together with the Fraunhofer Institute for Solar Energy Systems ISE, Germany [12].

Table 1.1 Detailed balance calculations of band gaps and achievable efficiencies of three to eight stack tandem cells [32].

3 to 8 stack tandem solar cells under black body radiation at 6000 K at 500 x										
Number of stacks	**Values of Bandgap (eV)**								**Maximum limit Efficiency η (%)**	**Achievable Efficiency *0.8 x η* (%)**
3	0.7	1.37	2						56	**44.8**
4	0.6	1.11	1.69	2.48					62	**49.6**
5	0.53	0.95	1.4	1.93	2.68				65	**52**
6	0.47	0.84	1.24	1.66	2.18	2.93			67.3	**53.84**
7	0.47	0.82	1.19	1.56	2	2.5	3.21		68.9	**55.12**
8	0.44	0.78	1.09	1.4	1.74	2.14	2.65	3.35	70.2	**56.16**

However, it is important to notice that this value is very close to achievable theoretical efficiency limit of four-junction tandem cells as shown in detailed balance calculations in Table 1.1 [33]. In order to go beyond this limit, new materials and device designs must be investigated.

To overcome the 50% efficiency barrier with tandem cells of four or more junctions requires the exploration of new materials having band gaps higher than 2.4 eV. Over the last decade, one material system has drawn lots of attention for full-solar spectrum PV applications owing to its wide and direct band gap range between 0.65 eV to 3.4 eV: **Indium Gallium Nitride**.

1.2 III-Nitrides for photovoltaic applications

1.2.1 Overview of III-Nitride Materials

1.2.1.1 Crystalline and structural properties of III-Nitrides

III-Nitride materials, GaN, AlN and InN, crystallize in cubic zinc blinde or hexagonal wurtzite phases. The wurtzite phase is more of interest, since it is stable and commonly achieved phase in current high quality III-Nitrides based optoelectronic devices. Figure 1.10(a) shows the structure of wurtzite-GaN which consists of two embedded, closely packed hexagonal arrangements (ABAB…stacking) of Ga ions or N ions along the [0001] growth direction. In the hexagonal plane of the wurtzite structure, the distance between two neighboring atoms is denoted as the *in-plane lattice parameter, a,* while the distance between two identical atoms (two Ga atoms) along the [0001] direction is indicated by *out-of plane lattice parameter, c*. The lattice parameters of GaN, AlN and InN are reported in Table 1.2.

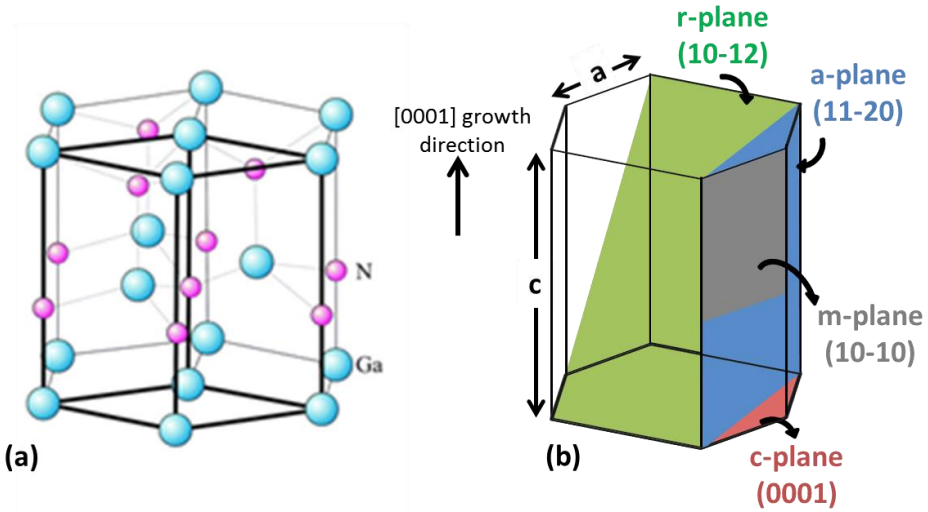

Figure 1.10 (a) Atomic positions of Ga and N in wurtzite GaN structure, Ga and N are indicated as blue and pink balls, respectively; (b) diagram of crystal planes in hexagonal lattice.

Figure 1.10 (b) shows the main crystal planes in hexagonal wurtzite system in four digit Miller Bravais notation {*hkil*}. The c-plane (0001) is referred as *polar* plane. The origin of this polarity is explained by the asymmetry along the c-axis, i.e. the [0001] and [000-1] directions are not equivalent. On the other hand, on the surface of a-(11-20) and m-(10-10) planes, which are perpendicular to the c-plane, there are equal numbers of threefold coordinated Ga and N leading to charge neutrality. Hence these planes are called non-polar. There are also semi-polar atomic planes, (10-12) which make angles with c-plane other than 0° and 90°.

The III-Nitride compounds, especially InGaN ternary alloys, which are the main focus of this thesis, are generally grown heteroepitaxially; i.e. growth of one crystalline material is performed on a foreign crystalline material. The heteroepitaxial growth and its consequences define all the structural, electrical and optical properties of the materials. Therefore, it is important to understand the basics of structural properties and the stress-strain relationship in heteroepitaxially grown structures.

Table 1.2 Lattice parameters and thermal properties of wurtzite GaN, InN and AlN [33, 34].

Material	Lattice parameters (Å)		Energy Bandgap at 300°K (eV)	Thermal expansion coefficient (10^{-6} K^{-1})	Lattice mismatch with GaN (%) (a_{GaN}-$a_{MATERIAL}$)/a_{GaN}
	a	c			
GaN	3.19	5.19	3.42	5.6	0
InN	3.54	5.70	0.65	2.85-3.15 (at 300°K)	+11
AlN	3.10	4.97	6.2	4.2	-2.7

Figure 1.11 shows three possible outcomes of heteroepitaxial growth. In the 1st case, the lattice parameters of the top layer and the underlying layer can be identical or very close leading to a perfect matching of the crystals. In the second and third cases, which are also valid for InGaN/GaN hetero-junctions, there is a large difference in the lattice parameters of the top and the underlying materials. Depending whether the lattice parameter of the top layer (a_T) has smaller or larger than that of the underlying layer (a_S), the top layer can be subjected to tensile or compressive strain, respectively, in order to accommodate the different lattice constant of the underlying layer. For very thin layers, the lattice parameter of the top layer is slightly deformed in the growth direction, i.e. c_T becomes c_{Tp}, creating *strained or pseudomorphically grown* epilayers as shown in Figure 1.11 (b). Whereas, when the growth thickness of the top layer reaches a critical value, it can relax to its own lattice parameter by creating a crystalline defect at the interface which is called a misfit *dislocation*. This type of heteroepitaxial growth causes *relaxed* epilayers (Figure 1.11 (c)).

In this thesis, both strained and relaxed InGaN/GaN heterostructures are studied in terms of their structural, electrical and optical characteristics. Therefore, it is crucial to examine the stress-strain behavior into heteroepitaxially grown structures.

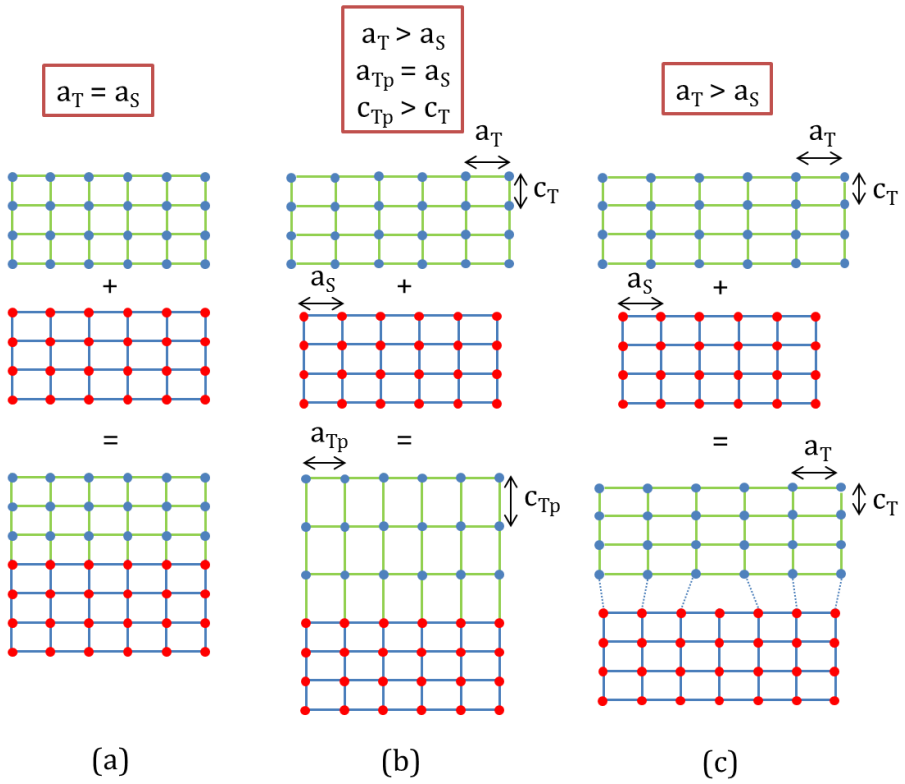

Figure 1.11 Schematic representation of (a) perfectly lattice matched (b) strained and (c) relaxed heterostructures with hexagonal lattice parameters, *a_T = original a of the top layer, c_T= original c of the top layer, a_{Tp}= a of pseudomorphically grown strained layer, c_{Tp} = c of pseudomorphically grown strained layer and a_S = a of the underlying substrate.*

In a pseudomorphically grown wurtzite system, the stress generated in the layers (σ) and the induced strain (ε) is linearly related with the elastic tensor coefficient (C) as $\overrightarrow{\boldsymbol{\sigma_{ij}}} = \boldsymbol{C}.\overrightarrow{\boldsymbol{\varepsilon_{ij}}}$ by Hooke's law. The stress tensor $\vec{\boldsymbol{\sigma}}_{\boldsymbol{ij}}$ corresponds to the pressure that should be applied on the crystal in order to deform it. The strain tensor $\vec{\boldsymbol{\varepsilon}}_{\boldsymbol{ij}}$ describes the distortion in the crystal lattice compared to its equilibrium state. In hexagonal lattices, where an external or internal force causes an elastic deformation, the stress-strain relation is described in Voigt notation as shown in Equation 1.8 [35].

$$\overrightarrow{\sigma_{ij}} = \begin{bmatrix} \sigma_{xx} \\ \sigma_{yy} \\ \sigma_{zz} \\ \sigma_{yz} \\ \sigma_{zx} \\ \sigma_{xy} \end{bmatrix}, C = \begin{bmatrix} c_{11} & c_{12} & c_{13} & 0 & 0 & 0 \\ c_{12} & c_{11} & c_{13} & 0 & 0 & 0 \\ c_{13} & c_{13} & c_{33} & 0 & 0 & 0 \\ 0 & 0 & 0 & c_{44} & 0 & 0 \\ 0 & 0 & 0 & 0 & c_{44} & 0 \\ 0 & 0 & 0 & 0 & 0 & \frac{c_{11} - c_{12}}{2} \end{bmatrix}, \overrightarrow{\varepsilon_{ij}} = \begin{bmatrix} \varepsilon_{xx} \\ \varepsilon_{yy} \\ \varepsilon_{zz} \\ 2\varepsilon_{yz} \\ 2\varepsilon_{zx} \\ 2\varepsilon_{xy} \end{bmatrix} \quad (1.8)$$

When the growth direction is considered along the z axis, the layered material is free to expand (or compress) in the interface plane and compress (or expand) in the perpendicular plane, therefore, the stress in the growth direction is zero $\boldsymbol{\sigma_{zz}} = \mathbf{0}$. The heterostructure in such condition is called to be in-plane *bi-axial stress state*. Biaxial strain situation sets some

constraints, the strain and stress in the in-plane axes are identical, $\boldsymbol{\sigma_{xx} = \sigma_{yy} = \sigma}$ and $\boldsymbol{\varepsilon_{xx} = \varepsilon_{yy} = \varepsilon}$, $\boldsymbol{\sigma_{zz} = 0}$ and $\boldsymbol{\sigma_{ij} = 0}$ (for $\forall i \neq j$) With these constraints, the strain along the z-axis can be related to in-plane strain a in Equation 1.9, by solving the Equation 1.1, where C_{13} and C_{33} are components of elastic stiffness tensor.

$$\varepsilon_{zz} = -2\frac{c_{13}}{c_{33}}\,\varepsilon \tag{1.9}$$

In other terms of in-plane and out-of plane lattice parameters, the strain in in-plane and in the growth direction can be derived as the following:

$$\varepsilon_{xx} = \varepsilon_{yy} = \varepsilon = \frac{a_{T_P} - a_T}{a_T} \tag{1.10}$$

$$\varepsilon_{zz} = \frac{c_{T_P} - c_T}{c_T} \tag{1.11}$$

In III-Nitrides, the lattice parameters of strained alloys at specific compositions can be calculated by Vegard's law [36], which is shown in Equation 1.12. This empirical rule supposes that at constant temperature, there exists a linear relation between the lattice parameters (a and c) of alloys and the concentrations (x) of the constituting elements.

$$\begin{aligned} a_{In_xGa_{1-x}N} &= a_{GaN} + x\,(a_{InN} - a_{GaN}) \\ c_{In_xGa_{1-x}N} &= c_{GaN} + x\,(c_{InN} - c_{GaN}) \end{aligned} \tag{1.12}$$

1.2.1.2 Spontaneous and Piezoelectric Polarization in III-Nitrides

In GaN, the nitrogen ions have higher electronegativity than that of gallium ions leading to greater electron probability density in the vicinity N and strongly ionic Ga-N bonds. As a consequence of the non-centrosymmetry of its wurtzite structure and the high degree of ionicity of the covalent metal–nitrogen bonds, GaN grown along the (0001) axis possesses a large spontaneous polarization (P_{SP}). Vurgaftman *et al.* calculated the spontaneous polarization in GaN, AlN and InN as -0.034 C/m^2, -0.090 C/m^2 and -0.042 C/m^2, respectively [37].

The spontaneous polarization in ternary III-Nitride alloys was reported to show nonlinear dependence on alloy composition and microstructure by Equation 1.13. The parameter b is called bowing parameter, which can be calculated by Equation 1.14 [38]. Experimental and theoretical investigations have shown that macroscopic polarization effects

have a great influence on the characteristics, performance, and response of the low-dimensional nitride heterostructure devices grown on c-plane [39, 40].

$$P_{SP\ In_xGa_{1-x}N} = x\ P_{SP(InN)} + (1-x)P_{SP(GaN)} - bx\ (1-x) \tag{1.13}$$

$$b = 2\ P_{SP(InN)} + 2P_{SP(GaN)} - 4P_{SP(In_xGa_{1-x}N)} \tag{1.14}$$

When an external strain leads to crystalline deformation along the polar axis, another type of polarization will be present in the structure: Piezoelectric polarization. In III-Nitrides, the piezoelectric polarization along the c-axis is given by as $\overrightarrow{\boldsymbol{P_{PZ}}} = \boldsymbol{E}.\overrightarrow{\boldsymbol{\varepsilon_{ij}}}$, where e_{ij} are piezoelectric coefficients of the material and ε_{ij} is the strain tensor as represented in Equation 1.15.

$$E = \begin{bmatrix} 0 & 0 & 0 & 0 & e_{15} & 0 \\ 0 & 0 & 0 & e_{15} & 0 & 0 \\ e_{31} & e_{31} & e_{33} & 0 & 0 & 0 \end{bmatrix} \tag{1.15}$$

In biaxially strained heterostructures, the value of P_{PZ} can be simplified to Equation 1.16 by assuming $\boldsymbol{\sigma_{xx} = \sigma_{yy} = \sigma}$, $\boldsymbol{\sigma_{zz} = 0}$ and $\boldsymbol{\sigma_{ij} = 0}$.

$$P_{PZ} = 2\ \varepsilon\ \left(e_{31} - \frac{C_{13}}{C_{33}}\ e_{33}\right) \tag{1.16}$$

The coefficients pertaining to piezoelectric polarization of III-Nitride compounds are tabulated in Table 1.3 [41]. The piezoelectric polarization of InGaN can be derived from Vegard's law, as shown in Equation 1.17.

$$P_{PZ\ In_xGa_{1-x}N} = x\ P_{PZ\ (InN)} + (1-x)P_{PZ(GaN)} \tag{1.17}$$

Table 1.3 Values of piezoelectric and elastic constants of InN, GaN and AlN [41].

Materials and constants	InN	GaN	AlN
Elastic constant, C_{13} (GPa)	92	103	108
Elastic constant, C_{33} (GPa)	224	405	373
Piezoelectric constant, e_{31} (C/m^2)	-057	-0.49	-0.60
Piezoelectric constant, e_{33} (C/m^2)	0.97	0.73	1.46
Spontaneous pol. coefficient (C/m^2)	-0.042	-0.034	-0.09

The total polarization can be expressed by the sum of spontaneous and piezoelectric polarization as $\boldsymbol{\vec{P}_T = \vec{P}_{PZ} + \vec{P}_{SP}}$, it becomes more pronounced when InGaN/GaN layers are grown in quantum well based heterostructures, which will be detailed in the next section.

1.2.1.3 Growth of InGaN/GaN heterostructures

The epitaxial growth is a key parameter that significantly affects the structural, optical and electronic properties of III-Nitrides heterostructures. Currently two developed growth methods are commonly utilized for this purpose: MBE and MOCVD.

In MBE growth, the elements are separately sublimed and their gaseous forms condense on the substrate where they react with each other. The typical MBE growth temperature range is 800-850°C. The growth in MBE depends entirely upon the arrival of the atoms at the surface. In order to increase their arrival probability, this technique requires ultra-high vacuum (~10^{-11} Torr). The high vacuum condition enables also performing extensive material analyses during the epitaxy (*in situ*). The low growth rate (~0.5µ/h) and precise control over the layer-by-layer growth provide capability of growing various heterostructures with homogenous doping, composition and abrupt surfaces. However, low growth rates and need for ultra-high vacuum prevent MBE growth for mass-production purposes in the industry.

On the other hand, MOCVD is a chemical vapor deposition method in which high vacuum is not necessary. High purity metal-organic precursors are injected into the reactor where they mix and react with carrier gases (H_2 or N_2) to create and deposit thin layers of atoms on a substrate. In the optoelectronics industry MOCVD is the major growth technique owing to its higher growth rate (>2µ/h) and multi-wafer capability under no vacuum. In addition, the MOCVD growth of GaN is carried out at much higher temperatures compared to MBE, typically at 1000-1100°C.

In general, the chemical reaction for III-Nitride compounds in MOCVD growth is shown Equation (1.18) where A is the organic radical (CH_3 or C_2H_5), M is the group III-metal element (Ga, Al or In), and B is the group V element (N) [42].

$$A_3\mathrm{M\ (g)} + BH_3\ \mathrm{(g)} \longrightarrow \mathrm{MB\ (s)} + 3\mathrm{AH}\uparrow \qquad (1.18)$$

In MOCVD, the metal organic precursors for III-Nitrides are trimethylgallium (TMGa) or Triethylgallium (TEGa), trimethylindium (TMIn). For doping of n-type and p-type GaN, dopant elements Si and Mg are transported to the reactor through organometallics, i.e. Bis (cyclopentadienyl)-magnesium (Cp_2Mg) and hydrides i.e. Silane (SiH_4).

In this study, all the InGaN/GaN heterostructures have been grown by the company NovaGaN by MOCVD technique. Therefore, it is vital to investigate the MOCVD growth in terms

of crystalline quality in order to understand the main challenges in achieving high quality InGaN active layers for solar cells and correlate the results of material characterization, which are addressed in Chapter 2. To do so, the choice of the substrate, the design and growth parameters of different types of active regions will be examined hereafter.

1.2.1.3.1 Choice of the substrate

The high melting points (>2500°C for GaN) and low decomposition temperatures at low pressures (~1000°C for GaN at 1 atmosphere) of III-Nitride compounds stand as the main obstacles for their large single crystal growth [43]. Therefore, many of single crystalline films are currently grown heteroepitaxially on various substrates such as sapphire, 6H-SiC, Si as shown in Table 1.4 even though extensive work on growth of bulk GaN substrates is currently on-going in many laboratories and companies.

Therefore, the choice of the substrate is done by minimalizing the difference between lattice parameters as well as the thermal expansion coefficients (TEC) of the epilayers and the substrates. The thermal expansion coefficient is also an important parameter, which plays a main role in choosing the right substrate, since a large difference in the TEC of the thin film and the substrate would cause the development of strains and cracking on the surface after cooling following the MOCVD at high temperatures.

Table 1.4 Lattice parameters and thermal properties of possible substrates and their lattice mismatch with GaN [33].

Material	Lattice parameters (Å) a	c	Energy Bandgap at 300°K (eV)	Thermal expansion coefficient (10^{-6} K^{-1})	Lattice mismatch with GaN (%) $(a_{GaN}-a_{MATERIAL})/a_{GaN}$
Sapphire (0001)	4.76	12.99	8.8	7.5	-13.8
6H-SiC	3.08	15.11	2.9	4.2	-3.4
Si (111)	5.43	-	1.12	3.6	+20.4

Si is a potential substrate, which offers low cost, large substrate possibility and direct integration with mature Si technology. However, GaN epilayers grown on Si substrates display poor crystalline quality due to high thermal strain and lattice mismatch with GaN epilayers. Generally, several low temperature AlN interlayers are employed as buffer layers between GaN and Si substrates for strain compensation. Currently, there is a tremendous amount of interest on GaN-on-Si LEDs in the industry. Recently, 8" GaN on Silicon LEDs with decent quality were demonstrated and announced to be released into the market soon [44]. 6H-SiC has nearly

similar thermal expansion coefficient and lattice parameters related to GaN, but due to its high cost, the conventional III-N based optoelectronics devices are grown on sapphire substrates.

Sapphire is still the most commonly used substrate for optoelectronic devices owing to its wide availability, hexagonal symmetry and high temperature stability (above 800°C) which is required for GaN epilayer growth by MOCVD. On the other hand, it exhibits a higher thermal expansion coefficient than that of GaN, which causes a dislocation density of around 10^9 cm^{-2}. Amano *et al.* suggested growth of low temperature AlN buffer layer on sapphire which allowed significantly higher quality and crack-free GaN layers [3]. Besides, the nitridation of the sapphire surface prior to GaN growth was proposed as a solution by Keller *et al.*, which reduced the defect density to $4x10^8$ cm^{-2} [10]. Therefore, currently the growth of III-Nitride compounds on sapphire usually includes nitridation and thin AlN buffer layer deposition on sapphire following the surface preparation to remove the organic contaminants. A low temperature GaN layer is usually grown between 450 °C and 600°C, which serves as a buffer and nucleation layer afterwards [4]. Finally, the growth of un-doped or n-type GaN layer, depending on the application, is conducted at high temperature (1000°C to 1050°C).

In order to obtain high crystalline quality GaN with low defect density, research on development of bulk GaN substrates has attracted considerable interest to be used in homoepitaxial growth. Over the last decade, thick bulk GaN was reported to be grown by hydride vapor-phase epitaxy (HVPE) with very low dislocation density regions in the orders of 10^6 cm^2 [45, 46]. This is about 3 orders of magnitude lower than that of the conventional heteroepitaxial growth. In the upcoming years, the volume of bulk GaN substrate is expected to grow rapidly to come with larger size, higher quality, and lower cost.

In this study, most of the InGaN/GaN heterostructures were grown on c-face (0001) sapphire substrates. In one generation of the solar cells, bulk GaN was used as a substrate. Their structural and device analyses have been studied and compared to that of samples on sapphire substrate in Chapters 2 and 3.

1.2.1.3.2 Challenges in InGaN growth

The InGaN ternary alloy can exhibit bandgaps from 0.65 (E_G of InN) to 3.4 eV (E_G of GaN) and the band gap can be changed by varying the In content. The value of band gap of InGaN ternary alloy can be calculated by Equation 1.19, where b is the bowing parameter indicating the nonlinear dependence of band gap, E_G, on fraction of indium in the InGaN alloys, *x.*

$$E_{G\ (In_xGa_{1-x}N)} = x\ E_{G(InN)} + (1-x)E_{G(GaN)} - bx\ (1-x) \qquad (1.19)$$

For high efficiency solar applications, the InGaN alloy is attractive when it can provide band gaps of more than 2.4 eV. This corresponds to InGaN material having more than 15% of indium. However, the growth of $In_xGa_{1-x}N$ alloys (x>0.15), so called *high In content InGaN* in this thesis, is much more challenging than that of GaN due to different lattice parameters and thermal stability of InN and GaN compounds. The growth of high quality InGaN layers depends on two vital parameters: the growth temperatures and ratio of group III/V elements.

First of all, the elemental vapor pressure of In is much higher than that of Ga which causes evaporation of In from the growing surface, making the control over the composition of InGaN more difficult [47]. This is why the growth of $In_xGa_{1-x}N$ is usually done at lower temperatures (600°C-850°C) compared to GaN. As a matter of fact, the low growth temperature suppresses the indium desorption from the surface, as well as increasing the indium incorporation. However, decreasing the growth temperature causes a trade-off between the incorporation of In and the quality of the InGaN layer. Low growth temperature reduces the cracking efficiency of ammonia leading to formation of indium clusters on the surface and nitrogen vacancies in the InGaN alloy. Piner *et al.* reported avoiding H_2 during the growth can enhance the incorporation of In [48]. In addition, it was shown that large III-V ratios increase the In incorporation in In-rich InGaN alloys [49].

Secondly, there exists a large difference in inter-atomic spacing between InN and GaN which leads to solid phase miscibility gap [50] and lattice mismatch between InN and GaN (+11%). For the growth of $In_xGa_{1-x}N$ epilayers with x > 0.2, the low immiscibility of InN in GaN causes great challenges such as phase separation and fluctuation of In content within the InGaN epilayer. Phase separation in InGaN layers is reported as the segregation of In-rich and Ga-rich domains in macro or nano scales, which cause band gap variations within the InGaN layer. Lai *et al.* reported severe In fluctuations $In_{0.3}Ga_{0.7}N$/GaN MQW solar cells which led to trapping of carriers in low-In content domains. This formed shallow potential depths across the thin InGaN epilayers [51]. It has been shown that the phase separation in low (high)-In content InGaN can be alleviated by decreasing (increasing) the growth temperatures [52]. Moreover, strained InGaN layers were reported to suppress the phase separation [53].

In addition, the lattice mismatch and the thermal strain between InN and GaN can cause formation of threading dislocations (TD) at the interface between high In content $In_xGa_{1-x}N$ and GaN, The TDs nucleate at the interface and terminate at the surface of the layer in the form of V-

shaped defects. The V-shaped pits act as non-radiative recombination centers (NRCs) which are detrimental to device performances [54]. As a solution, thin and strained InGaN epilayers can be embedded in GaN layers repetitively in structures called *InGaN/GaN multiple quantum wells.*

1.2.1.3.3 InGaN/GaN multiple quantum wells (MQWs)

For InGaN/GaN heterostructures, it was shown that an InGaN layer can be grown pseudomorphically on a GaN below a critical thickness (h_C), while beyond the h_C, plastic relaxation occurs resulting in misfit dislocations [55]. They showed that the h_C decreases rapidly with increasing indium contents. In order to achieve defect-free materials, multiple quantum well (MQW) or superlattice (SL) structures using few nanometers of InGaN layers have been exploited as an alternative for the active regions of the solar cells. Such structures aim to reduce the defect density in devices by incorporating very thin InGaN layers below the h_C depending on the composition of In. Figure 1.12 (a) displays the band diagram of i-InGaN/GaN MQWs heterostructures sandwiched between n-GaN and p-GaN.

The concept of exploiting quantum well based solar cells is not specific to InGaN based solar cells. The quantum confinement approach that uses quantum dots (QDs) and quantum wells (QWs) having lower bandgap material in a higher bandgap host material is quite promising for efficiency improvements in the devices. To allow sub-bandgap absorption in the solar cells, multiple quasi-Fermi levels can be created by the incorporation of defects, impurities [56], QDs or quantum wells (QWs) [57]. In 1990, Barhnam *et al.* suggested employing a p-i-n junction with QWs located in the intrinsic region to confine the carriers into two dimensions [58]. The QWs generate quantized energy levels, at which lower energy photons are captured and they shift the spectral response of the cell to lower energy ranges. As a consequence, higher overall power output is achieved by the increased photocurrent leading to higher conversion efficiencies. The absorption edge and efficiency of the quantum well-based solar cells can be tailored by bandgap, size, and number of incorporated QWs.

In solar cell applications, it is important to have thick absorbing material for efficient absorption of the photons and hence high conversion efficiencies. The need to keep QW thicknesses below the h_C imposes growth of high number of InGaN/GaN MQWs. However, the growth of high number of InGaN MQWs is also challenging since it may lead to a transition of the growth mode of QWs over growth time as investigated in detail in this study.

As a matter of fact, in this study, two different types of InGaN layers are studied of which the structural and optical characterization will be detailed in the next chapters: bulk and relaxed InGaN layers (200 nm) and very thin InGaN quantum wells (2 to 4 nm) embedded in GaN barriers.

Polarization effects in InGaN/GaN MQWs

The above mentioned spontaneous and piezoelectric polarizations have significant effects on the electrical and optical properties of InGaN/GaN MQWs grown on c-plane polar GaN. The total polarization, $\vec{P}_T = \vec{P}_{PZ} + \vec{P}_{SP}$, leads to accumulation of electrical charges at the InGaN/GaN interfaces creating an electric field in the QWs. Figure 1.12 (b) shows that the P_{SP} is always in the opposite direction to the [0001] in InGaN wells and GaN barriers grown on polar c-plane (0001), leading to building up charges with alternative signs at the well/barrier interfaces. Since the strained InGaN wells have higher in-plane lattice parameter than that of GaN barriers (by Equation 1.5), they will be subjected to compressive stress, that causes P_{PZ} in the opposite direction to that of P_{SP}.

The P_T in the wells can be calculated by addition of $P_{SP(InGaN)}$ (Equation 1.13) and $P_{PZ(InGaN)}$ (Equation 1.17), while in the barriers $P_{T(GaN)} = P_{SP(GaN)}$ since GaN barriers are assumed to be strain free ($P_{PZ\ (GaN)} = 0$). It was shown that the P_T in InGaN/GaN heterostructures is mostly dominated by the piezoelectric component and it increases as a function of In content in InGaN [59]. For instance, the polarization field was reported around 1.4 MV/cm in $In_{0.15}Ga_{0.85}N$/GaN MQWs structures [60]. High internal electric fields in InGaN/GaN heterostructures were reported to cause a strong reduction in the overlap of the electron and hole wavefunctions and hence lead to band bending as shown in Figure 1.12 (c). As a result, the emitted wavelength is redshifted. Such effect is called *Quantum Confined Stark Effect* (QCSE). QCSE becomes more pronounced by increasing the well thickness, d_{WELL}, and/or the In content, since the change in energy (E), is directly proportional to d_{WELL} and the P_{PZ} as simplified to $\boldsymbol{E = qP_{PZ}d_{WELL}}$, where q is the electron charge.

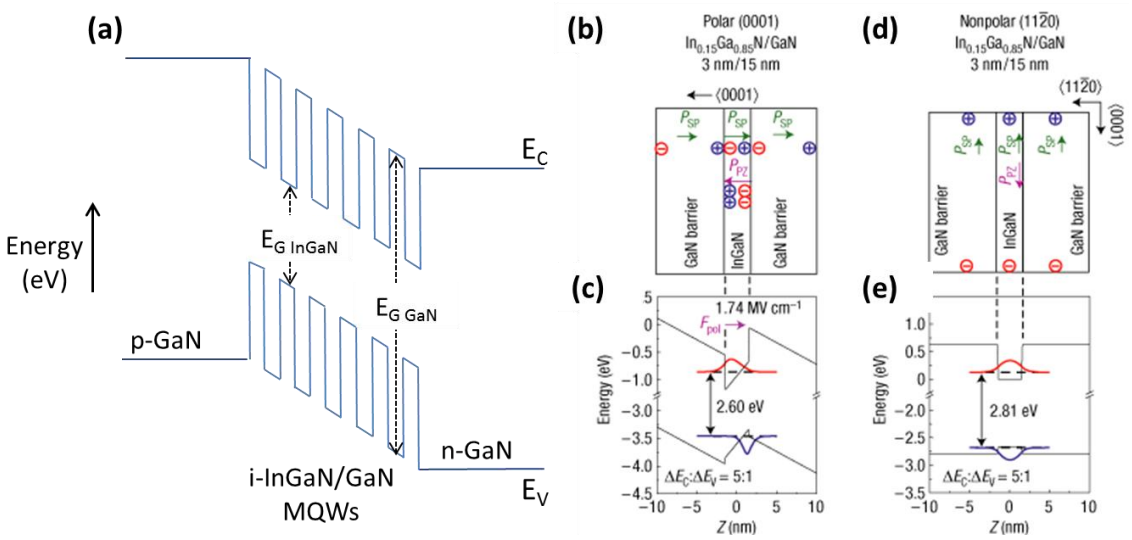

Figure 1.12 (a) Band diagram of InGaN/GaN MQWs. Representation of P_{SP} and P_{PZ} directions inside the bi-axially strained MQWs grown on a (b) polar (0001) plane and (d) non-polar (11-20) and their band structures (c) and (e), respectively [60].

On the other hand, the polarization effects can be entirely eliminated in InGaN/GaN heterostructures grown on non-polar a-plane (11-20). In such structures, the piezoelectric fields are perpendicular to the growth direction as shown in Figure 1.12 (d). As a matter of fact, there is no charge accumulation at the interfaces; hence the structures exhibit flat-band profile without any spatial separation of wavefunctions (Figure 1.12 (e)).

1.2.2 Major breakthroughs in III-Nitrides optoelectronic devices

Over the last decade, solid state lighting technologies have emerged rapidly and penetrated deeply into various segments of market such as automotive, medical applications, aviation lighting, indoor and outdoor lighting as well as lifestyle products. The global light-emitting diode (LED) market volume in general lightening is currently around US$26 billion and it is expected to grow much more than US$72 billion by 2020 [61]. This is driven by advances in key materials called III-Nitrides materials and remarkable progress in their growth and device fabrication.

Since the discovery of electroluminescence phenomenon in inorganic semiconductors by H. Round [62] and O. V. Losev [63], which created the basis of light generation in LEDs, the first red LED was developed in 1960's by N. Holonyak *et al.* [64], followed by the invention of yellow-orange LEDs by G. Craford *et al.* [65]. These LEDs, which were realized by III-V semiconductors such as InGaP or GaAlAs, delivered too low efficiencies and brightness to be used in general lightning applications.

The development of efficient blue LEDs was only possible three decades later by using wide-band gap materials such as GaN and its ternary alloys, InGaN and AlGaN. The first demonstration of single crystal GaN growth on sapphire was shown by hydride vapor-phase epitaxy (HVPE) by Maruska and Tietjen [1]. After significant attempts of GaN growth on sapphire using AlN buffer by reactive molecular beam epitaxy (MBE) and metalorganic chemical vapor deposition (MOCVD) by Yoshida *et al.* [2] and Amano *et al.* [3], respectively, Nakamura achieved remarkably high-quality GaN film growth using low temperature GaN buffer layers on sapphire in 1991 [4]. However, due to high n-doping background of undoped GaN, obtaining p-type conductivity in GaN films remained challenging for a long time. In addition to enhancing the growth quality, Nakamura *et al.* clarified this difficulty by the influence of hydrogen atoms which create acceptor-H complexes causing hole compensation in p-doped GaN films [6]. They also proposed a NH_3 post-thermal annealing to prevent the formation of atomic H and thus demonstrated p-GaN films with hole concentration of 3×10^{17} cm^{-3} together with a hole mobility of 10 cm^2/Vs [7]. This achievement paved the way for the creation of LEDs based on p-n junction GaN [5] and p-GaN/i-InGaN/n-GaN by inserting Ga-rich InGaN which served as the active region [8]. Later in 1995, Nakamura *et al.* demonstrated high brightness blue, yellow and green LEDs based on single InGaN quantum well (QW) by adjusting the indium content in InGaN alloy [9], which enabled the foundation of commercially available first-generation blue and green LEDs. In 2014, for the invention of efficient blue light-emitting diodes which has enabled bright and energy-saving white light sources, S. Nakamura, I. Akasaki and H. Amano were honored by the Nobel Prize.

On the other hand, the growth of InN and In-rich InGaN alloys has been more challenging than that of the Ga-rich InGaN alloys. Earlier, InN which was deposited by radio-frequency sputtering showed high electron concentrations (>10^{19} cm^{-3}), significant oxygen contamination and hence relatively low electron mobilities (10-100 cm^2/Vs) [66, 67]. Such materials showed a strong absorption at 1.9eV due to impurities and free carrier absorption. Similar to GaN, as grown InN is unintentionally n-type. The origin of high n-type conductivity was suggested as native defects such as Nitrogen vacancy, point defects and edge-type threading dislocations that generate sources of free electrons in InN [68].

The band gap of intrinsic InN was accepted as 1.9 eV, until the growth quality of III-Nitrides by MOCVD and MBE was significantly improved. The enhanced material quality corresponded to lower carrier concentrations allowing the intrinsic optical properties free from any influence of unintentional doping. Yamaguchi *et al.* reported for the first time the decrease of band gap of InGaN below 1.9 eV for the compositions of indium much higher than 50% [69].

Since then, the major breakthrough in growth of high quality InN by MBE provided much reduced electron concentrations (<10^{18} cm^{-3}) and higher electron mobilities (2000 cm^2/Vs) [70, 71, 72]. As a consequence of further material characterizations on higher quality InN, the room temperature fundamental bandgap of InN was revised from 1.9 eV to a much narrower value of 0.64 eV in 2002 [11].

The reevaluation of the InN band gap revealed that a continuum of wide and direct band gaps (0.64 to 3.4 eV) can be reached only by altering the compositions of indium and gallium in InGaN ternary alloy as seen in Figure 1.13. The outstanding achievements in material growth and device technology of InGaN based blue and green LEDs as well as the progress in revision of InN band gap, made InGaN alloys attractive for other optoelectronic applications; particularly the PV applications. InGaN material system can provide direct band gaps between 0.65 eV and 3.4 eV making them excellent candidates for full-solar spectrum photovoltaic applications.

Furthermore, InGaN alloys possess high absorption coefficient (> 10^5 cm^{-1} at the band edge) allowing 95% of incident light to be efficiently absorbed within the first 300 nm of the material, whereas in traditional Si based solar cells several hundreds of microns are required for equivalent absorption [73, 74].

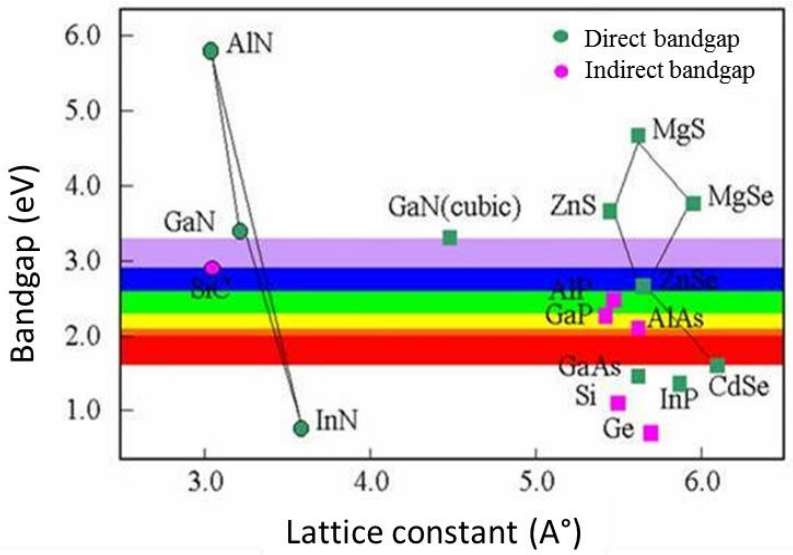

Figure 1.13 Bandgap versus lattice constant of common semiconductor materials.

Since the first demonstration of InGaN based solar cells in 2006, they have captured attention of many researchers. However, InGaN solar cells have not taken their place in the NREL's best research cell efficiency chart (Figure 1.8) due to some significant challenges in material quality and device processing issues. In InGaN based optoelectronics, there is still room for study and resolution of several scientific and technological issues in the domains of material

physics (lattice mismatch, high dislocation densities, etc.) and material chemistry (segregation of In, phase separation, difficulties in doping, strong polarization etc.). Figure 1.14 summarizes the major breakthroughs in the (In)GaN based optoelectronic devices, i.e. specifically for LEDs and solar cells.

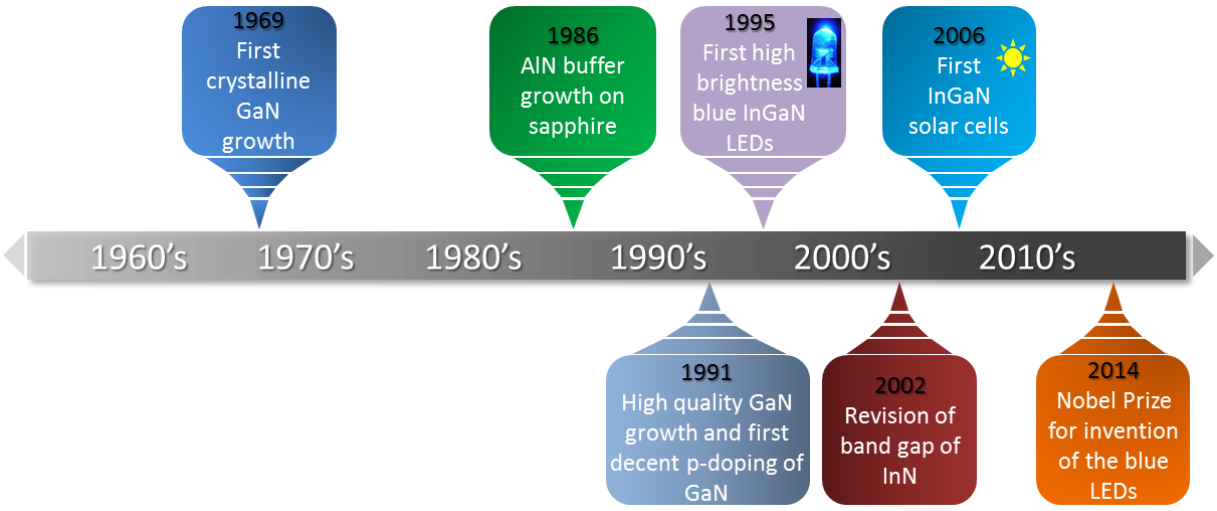

Figure 1.14 Major breakthroughs in (In) GaN based LEDs and solar cells.

1.2.3 Literature Overview of InGaN based Solar Cells

1.2.3.1 State of the art of InGaN based solar cells

Since the InGaN was proposed as a potential material for solar cells (SCs) by Wu *et al.* [11] in 2003, significant progress has been established while many challenges remain to be overcome to meet the requirements of high-efficiency III-nitride PV. In the initial stages, InGaN alloy was examined extensively for single junction SC applications with Ga-rich materials owing to mature growth and doping technologies of GaN.

The first clear demonstrations of PV effect were achieved by designs of Jani *et al.* [74] and Yang *et al.* [75] having Ga-rich p-n $In_xGa_{1-x}N$ homojunction and p-GaN/InGaN/n-GaN heterojunctions [76] grown by metal-organic vapor phase epitaxy (MOCVD) in 2006 and 2007. These preliminary studies resulted in the evolution of the fabrication of InGaN-based SCs in two different axes: *homojunction InGaN solar cells* (i.e. p-$In_xGa_{1-x}N$/n- $In_xGa_{1-x}N$) and *heterojunction solar cells* (i.e. $In_xGa_{1-x}N$ sandwiched between p-GaN and n-GaN). Further advances and efforts, which will be detailed throughout this chapter, include the growth of In-rich InGaN layers by molecular beam epitaxy (MBE) [77, 78], the introduction of InGaN/GaN multiple quantum wells (MQWs) in the absorption region [79], the optimization of the top contact grids [74], the formation of low-resistance p-type ohmic contacts by the introduction of different current spreading layers (CSL) [80, 81], and the utilization of different substrates with various antireflection methods to enhance the external quantum efficiencies (EQE) and internal quantum efficiencies (IQE) of the devices [82, 83].

1.2.3.1.1Homojunction InGaN Solar Cells

High-efficiency SCs based on InGaN can be achieved only by exploiting $In_xGa_{1-x}N$ layers incorporating In contents higher than 0.15 [84]. Due to the large mismatch between InGaN with x>0.15 and GaN, the primary studies were mostly based on p-InGaN/n-InGaN homojunction and p-InGaN/i-InGaN/n-InGaN homojunction SCs, which are summarized in Table 1.5.

Jani *et al.* demonstrated the first single-junction 100-nm-thick MOCVD grown $In_{0.28}Ga_{0.72}N$ SC with an open-circuit voltage (V_{OC}) of 2.1 V, which successfully corresponds to its bandgap of 2.5 eV [76]. They reported the degradation of SC performance by the phase separation in InGaN layers thicker than 200 nm and poor p-type InGaN doping. Yamamoto *et al.* [85] reported a MOCVD grown p-n $In_xGa_{1-x}N$ homojunction SC with high In content (25%) that

showed a clear photo-response with open-circuit voltage V_{OC} of 1.5 V and a short-circuit current density (J_{SC}) of 0.5 mA/cm^2. The origin of such low values of V_{OC} and J_{SC} were explained by radiative and non-radiative recombination of carriers due to highly defective thick InGaN layers (700 nm). The SCs suffered also from the low-doping capability of p-InGaN causing high series resistance, R_{series}, in the device. On the other hand, MBE grown p-n $In_{0.31}Ga_{0.69}N$ SC by Misra *et al.* [78] showed very poor performances of V_{OC} of 0.55 V and J_{SC} of 0.24 mA/cm^2 under one sun of AM0 illumination. Chen *et al.* [77] observed very poor photo-response with high leakage current in MBE grown p-i-n InGaN devices with 20% and 30% In compositions. Boney *et al.* [86], who reported the highest In content, 39%, in InGaN homojunction SCs so far, mentioned an increase in Jsc while an overall degradation in other SC characteristics with increasing In contents. The major challenges of epitaxial growth and p-type doping of In-rich InGaN layers caused the limitation of the In contents to lower values in further studies with homojunction InGaN SCs. Jampana *et al.* [87] reported p-n junction $In_{0.17}Ga_{0.83}N$ SC that had V_{OC} of 1.73 V and J_{SC} of 0.91 mA/ cm^2 under concentrated AM0 illumination.

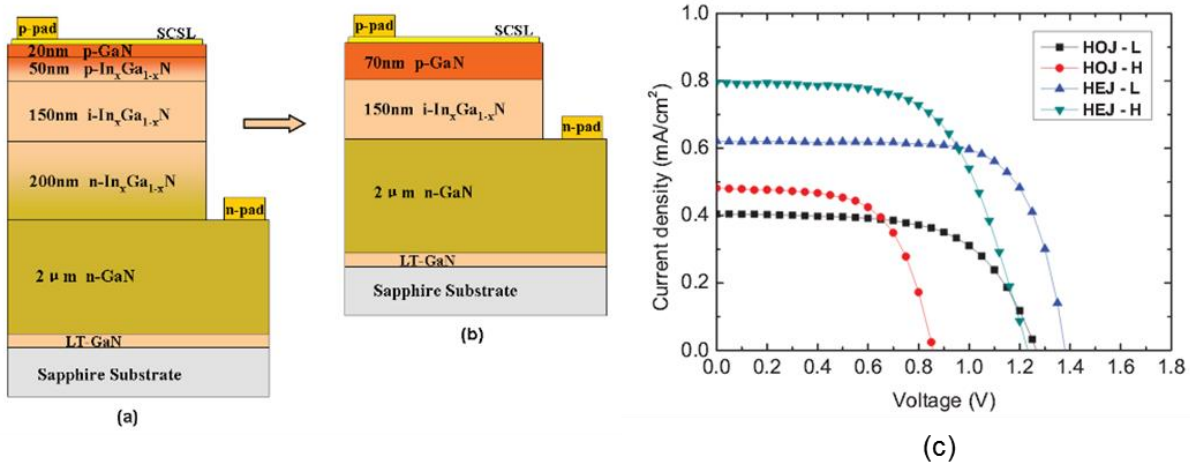

Figure 1.15 Structure of a) homojunction; b) heterojunction InGaN-based solar cells c) PV characteristics of homojunction and heterojunction solar cells with 12–16% In contents [88].

In 2013, Cai *et al.* reported a performance comparison of p-InGaN/i-InGaN/n-IGaN homojunction and p-GaN/i-InGaN/n-GaN heterojunction solar cells [88] Figure 1.15 (a) shows the design of the homojunction SCs, HOJ-L and HOJ-H, with x=0.12 and x=0.15, respectively. Figure 1.15 (b) displays the heterojunction SCS, HEJ-L and HEJ-H, with x=0.135 and x=0.16, respectively. As seen in Figure 1.15 (c) heterojunctions are demonstrated to be a better choice for active region of solar cells, as they exhibited much higher efficiencies (η =0.62% and η =0.6% for HEJ-L and HEJ-H, respectively) than that of homojunction based SCs under 1 sun AM1.5G illumination (η =0.32% and η =0.26% for HOJ-L and HOJ-H, respectively). The poor performances of HOJ SCs were related to high density of defects in thick InGaN layers and

insufficient doping p-InGaN. It was indeed reported that the degradation in the crystalline quality by increasing the Indium content in p-InGaN material, leads to lower acceptor concentrations and hence reduces p-type InGaN doping capability [86]. As a result, the performance of InGaN homojunction solar cells degrades.

Table 1.5 State-of-the-art for InGaN homojunction based solar cells [84].

Characteristics of reported $In_xGa_{1-x}N$ homojunction based solar cells			
Structure ***(Growth method)***	**Content of Indium** ***(Substrate)***	**Performance** ***(Excitation)***	**Reference/author year**
p-n InGaN *(MOCVD)*	0.18 *(0001)sapphire*	V_{OC}=0.43V, J_{SC}=0.04mA/cm^2 *(360 nm illumination)*	[75] Yang 2007
p-n InGaN *(MOCVD)*	0.28 *(0001)sapphire*	V_{OC}=2.13V *(additional UV bias)*	[76] Jani 2007
p-i-n InGaN *(MBE)*	0-0.3 *(0001)sapphire*	V_{OC}=2.5V, J_{SC}=0.04mA/cm^2 *(325 nm laser, 200mW/cm^2)*	[77] Chen 2008
p-n InGaN *(MBE)*	0.31 *(0001)sapphire*	V_{OC}=0.78V, J_{SC}=1.99mA/cm^2 *(3 suns AM0)*	[78] Misra 2008
p-n InGaN *(MOCVD)*	0.12 *(0001)sapphire*	V_{OC}=1.5-2V, J_{SC}=0.04mA/cm^2 *(1 sun AM15G)*	[90] Jani 2008
p-i-n InGaN *(MOCVD)*	0.02-0.1 *(0001)sapphire*	V_{OC}=2.24-0.96V, J_{SC}=1.4-1.87mA/cm^2 *(Xe lamp illumination)*	[89] Cai 2009
p-i-n InGaN *(MOCVD)*	0.148-0.168 *(0001)sapphire*	V_{OC}=1.73V, J_{SC}=0.91mA/cm^2 *(AM0)*	[87] Jampana 2010
p-n InGaN *(MBE)*	0.14-0.54 *GaN template*	V_{OC}=1.8-0.02V, J_{SC}=1-2.2mA/cm^2 *(AM0)*	[86] Boney 2011
p-i-n InGaN *(MOCVD)*	0.12-0.15 *(0001)sapphire*	η=0.32-0.26% *(AM1.5, 100mW/cm^2)*	[88] Cai 2013

1.2.3.1.2 Heterojunction InGaN Solar Cells

III-Nitride-based SCs with heterojunction structures, p-GaN/ InGaN/n-GaN, have been extensively studied and most of the notable progress and promising results have been accomplished in this type of SCs. The development of InGaN based solar cells with the active layers in the form of bulk $In_xGa_{1-x}N$ or MQW/superlattice (SL) structures, which is sandwiched between p-GaN and n-GaN layers, benefited mostly from the mature growth and fabrication of InGaN/GaN LED technology. Table 1.6 summarizes the state-of the art of InGaN heterojunction solar cells.

First of all, Jani *et al.* [91] demonstrated a clear photo-response in a p-GaN/i-$In_xGa_{1-x}N$/n-GaN single-layer heterojunction cell with an In fraction of 0.04–0.05 on sapphire substrate. The devices resulted in high V_{OC} of 2.4 V and consistent internal quantum efficiency of 60% at their band edge but showed relatively low J_{SC}. Zheng *et al.* [92] then reported an improvement in the same structure with increased In content of 10% that demonstrated a high V_{OC} of 2.1 V and high fill factor (FF) of up to 81% under an illumination of AM 1.5 solar light.

The high dislocation density in bulk InGaN layers was the main obstacle in getting higher conversion efficiencies. This is why many researchers tried improving light absorption by surface roughening or backside reflection methods. Matioli *et al.* reported heterojunction InGaN solar cells with bulk $In_{0.12}Ga_{0.88}N$ active layer (60 nm thick) [93]. They demonstrated that the surface roughened devices have enhanced peak external quantum efficiency of 72%, owing to improved light incoupling by textured surface. Horng *et al.* [94] and Tsai *et al.* [95] both reported the laser lift-off technique to remove the sapphire substrate of the thin-film p-i-n $In_xGa_{1-x}N$ /GaN SCs with In content of 10% and 8.5%, respectively. Horng *et al.* [94] then transferred the device on Ti/Ag mirror-coated Si substrate via wafer bonding and observed an increment in efficiency from 0.55% to 0.8%, whereas Tsai *et al.* [95] mounted the device on AlN carrier by using an Ag reflector in between. They achieved 13.6% increase in short-circuit current density.

Establishing low resistance and transparent ohmic contacts to p-type GaN plays a key role in InGaN-based SCs. However, low resistivity ohmic contacts to p-GaN still remain challenging due to relatively deep Mg acceptor levels and low incorporation/activation efficiency. In addition to challenges in doping, there is readily no available metal that could form low ohmic contact resistivity on p-GaN and p-InGaN, which possess both high work functions and high electron affinity. As a solution, semi-transparent p-type ohmic contacts are generally realized by metals (e.g. Ni/Au) or transparent conductive oxide (e.g. ITO) based current spreading layer schemes which result in specific contact resistance in the range of 10^{-4} to 10^{-6} $\Omega.cm^2$. This method requires deposition of grid form metal electrodes to increase carrier collection whereas it strongly reduces the efficient photo absorption in InGaN active layer. Neufeld et al studied the optimization of the p-contact grid spacing on MOCVD grown $In_{0.12}Ga_{0.88}N$/GaN p-i-n double heterojunction SCs grown on sapphire [74]. As a result, the absorption of a larger fraction of incident light allowed the demonstration of a FF of 75%, high external quantum efficiency of 63%, V_{OC} of 1.81 V, and J_{SC} of 4.2 mA/cm^2 under concentrated AM0 illumination. Besides, Shim *et al.* [80] compared performances of the p-i-n $In_xGa_{1-x}N$ /GaN (x~0.108) SCs with the current spreading layers (CSL) of Ni/Au and ITO under AM 1.5 conditions. The devices with ITO showed superior V_{OC} characteristics of 2.0 V, J_{SC} of 0.64 mA/cm^2, and 1% conversion efficiency while

devices without any CSL and Ni/Au CSL resulted in η=0.93 and η=0.75, respectively. In a further study, Shim *et al.* reported an improved η (1.2%) and J_{SC} (0.83 mA/cm^2) by utilizing a CSL of graphene on the same structure [81].

However, the studies revealing poor crystalline quality and high dislocation density in thick single layers of InGaN (with In content ≥0.15) grown on GaN pointed out the fact that the thickness of InGaN should be below a critical thickness to suppress the defects. As an alternative, MQWs or SL structure consisting of few nanometers InGaN layers has been proposed as the active region of InGaN-based SCs. Dahal *et al.* fabricated the first $In_xGa_{1-x}N$/GaN MQW (x~0.30) SCs that delivered unprecedented external quantum efficiency of 40% at long operating wavelength of 450 nm [79]. Then, they reported $In_xGa_{1-x}N$/GaN MQW (x~0.35) concentrator SCs having 12 periods of 3-nm-thick InGaN QWs and 17-nm-thick GaN barriers, the design of which is displayed in Figure 1.16 (a). Figure 1.16 (b) shows that the device demonstrated V_{OC}, J_{SC}, and maximum power of 1.80 V, 2.56 mA/cm^2, and 2.95 mW/cm^2, respectively under one sun [96].

The novel approach of InGaN/GaN MQWs certainly led to an improvement of overall performance of the InGaN-based SCs by enabling growth of high In content $In_xGa_{1-x}N$ (x~0.35) material. The device was reported to achieve overall efficiency of 2.95 % and 3.03 % under one sun and 30 suns, respectively. In this paper, the total thicknessof the InGaN wells (36 nm) was mentioned to be insufficient for efficient light absorption limiting the conversion efficiencies lower than expected theoretically when using a single junction SC at the same optical energy bandgap (8%). This was evidenced by the increase in photocurrent density by more than 15% when an aluminum back reflector was deposited on the sapphire side of the device. It was also stated that it is rather challenging to obtain In-rich InGaN/GaN MQW structures with total InGaN absorption thicker than 150 nm. Growing higher numbers of quantum wells in order to increase the photo-absorption led to higher external quantum efficiency solar cell as reported by Farrell *et al.* They demonstrated solar cells with 30 pairs of $In_{0.28}Ga_{0.72}N$/GaN MQWs achieving conversion efficiency of 2.29% and peak external quantum efficiency of 70.6% under 1.2 sun AM1.5G illumination [97].

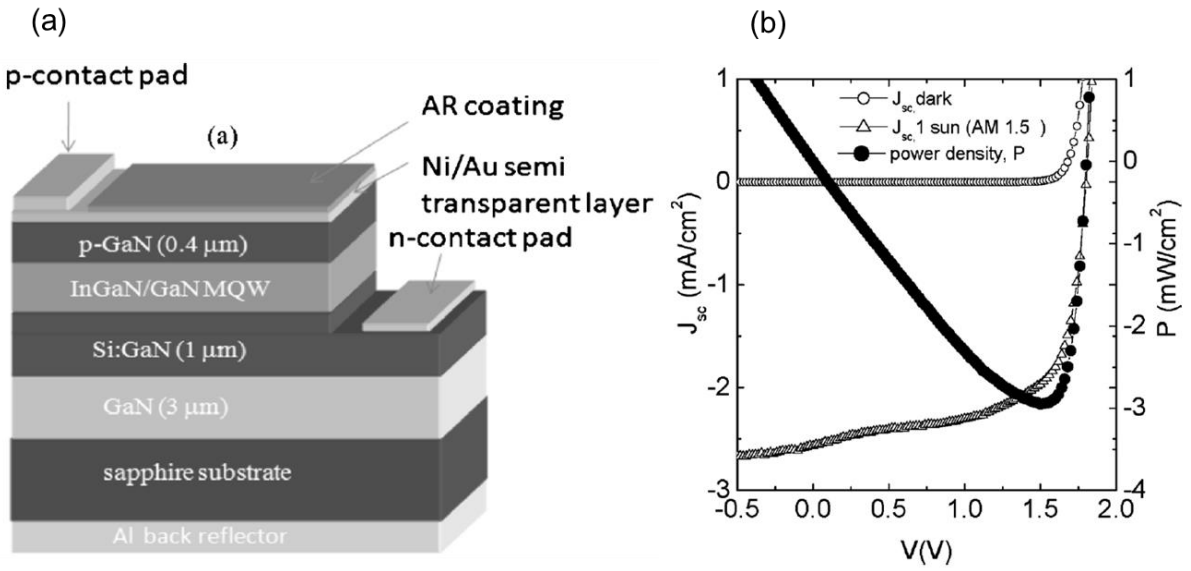

Figure 1.16 a) Design of $In_xGa_{1-x}N$/GaN MQW-based solar cells with (x~0.35)b) Current density-voltage characteristics of the solar cell in dark and under 1 Sun AM1.5G irradiation [96].

All above mentioned solar cells with active regions including either bulk InGaN or InGaN/GaN MQWs were grown on c-plane sapphire substrates. There were several attempts to grow heterojunction InGaN solar on r-plane sapphire substrate, Silicon substrate and free standing bulk GaN substrates. Nakao *et al.* reported the growth of 30 periods $In_{0.15}Ga_{0.85}N$/GaN MQWs on non-polar a-plane GaN template on r-plane sapphire which demonstrated conversion efficiency of 1.6% [98]. The growth of InGaN solar cells on Si substrates is significant as it opens up the possibility for tandem InGaN-Si solar cells. In addition, the use of silicon substrate promises cost reduction in InGaN based solar cells. Jampana *et al.* was first to report the growth of 4 periods of $In_{0.155}Ga_{0.845}N$/GaN MQWs grown on Si (111) using GaN/AlN superlattice structure to reduce the density of threading dislocations at the AlN/Si interface [99]. Then, Liu *et al.* [100] demonstrated 6 pairs of $In_{0.15}Ga_{0.85}N$/GaN MQWs grown on Si (111) substrates using AlGaN/AlN superlattice buffer layers to accommodate the lattice mismatch between GaN and Si. These solar cells achieved conversion efficiency of 0.2% under 1 sun AM1.5G illumination.

Kuwahara *et al.* [82] reported for the first time $In_{0.11}Ga_{0.89}N$/GaN p-i-n double heterojunction SCs grown on freestanding c-plane GaN substrate and on c-plane sapphire substrate covered with a low-temperature-deposited buffer layer. The device on GaN substrate showed a superior performance with a conversion efficiency of 1.41% under 1.5 suns owing to lower pit density and higher shunt resistance (R_{shunt}) compared to sapphire substrates. They also fabricated SCs with active region including 50 pairs of $In_{0.17}Ga_{0.83}N$ (3 nm)/$In_{0.07}Ga_{0.93}N$ (0.6 nm) and 10 pairs of doped $In_{0.17}Ga_{0.83}N$: Si (3 nm)/GaN: Si (3 nm) after optimizing the InGaN barrier thickness for the pit density [101]. As a result, the device exhibited V_{OC}, J_{SC}, FF, and η of 1.78V,

3.08 mA/cm², 70%, and 2.5%, respectively, under 1.5 suns. Young *et al.* demonstrated the highest conversion efficiency so far, η=3.33%, for single junction InGaN based solar cells [102]. Figure 1.17 (a and c) shows the design and the performance of their solar cells, which included 30 periods of $In_{0.2}Ga_{0.8}N$/GaN MQWs on (0001) GaN substrate. The device had anti-reflective coating and back-side dichroic mirror in order to minimize the reflection from the surface and maximize the rear reflection, respectively, which enhance the external quantum efficiencies as shown in Figure 1.17 (b).

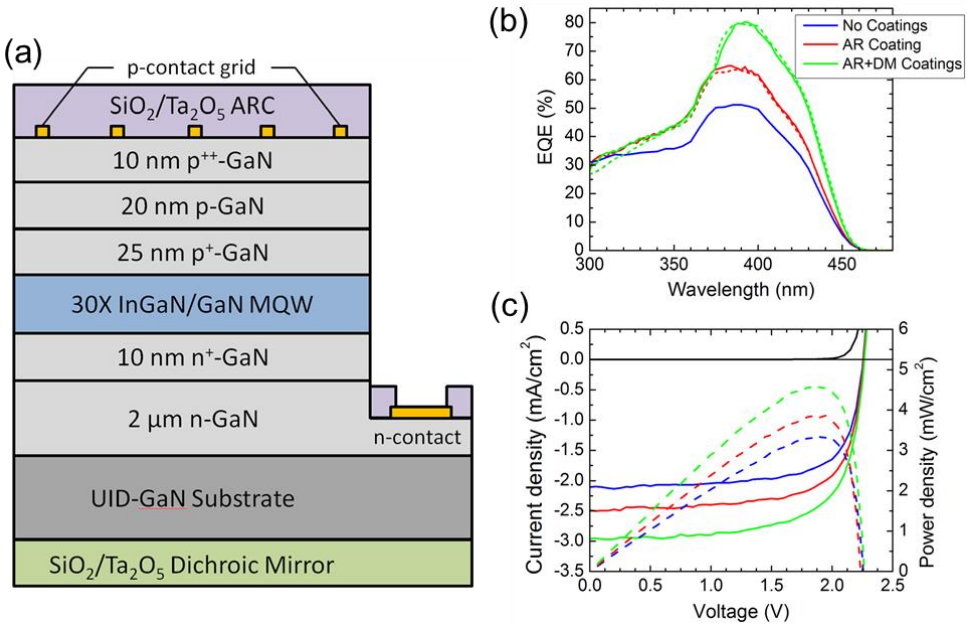

Figure 1.17 Design of the solar cell which achieved 3.33% efficiency. The effect of antireflective (AR) and dichroic mirror (DM) coatings on (b) the external quantum efficiency (EQE), and (c) the 1 sun AM0 illuminated I-V curves of the devices [102].

It can be concluded that several promising single junction InGaN-based SC results have been established so far, but to compete with mature existing PV technologies, higher conversion efficiencies need to be achieved.

On the other hand, InGaN material system is promising to be integrated with low-cost and mature Si technology to develop higher efficiency PV cells. As a matter of fact, the ohmic junction between n-$In_{0.45}Ga_{0.55}N$ and p-Si was reported to exhibit low resistance; enabling integration of p-n junction InGaN with p-n Si solar cell without the need of any tunnel junction [102]. This fact can boost the efficiencies up to 31% for two-junction InGaN/Si tandem cells as modeled by Hsu and Walukiewicz [102] and Ager III *et al.* [103].

Demonstration of n-$In_{0.4}Ga_{0.6}N$/p-Si tandem cells was reported by Tran *et al.* [104] in which 300 nm $In_{0.4}Ga_{0.6}N$ was grown on GaN on the top of Si substrate by using 50 nm thick AlN

buffer layer. ITO and Ti/Al/Ni/Au were investigated as n-type contacts. The solar cells with ITO as n-type contact were reported to demonstrate an enhanced J_{SC} due to the increased amount of absorbed light compared to the device using Ti/Al/Ni/Au as n-type contact. The device with ITO contact showed good PV performances and clear spectral response with an FF of about 54%, an external quantum efficiency of 20.8 and 14% at 375 and 390 nm, respectively and the overall conversion efficiency of 7.12%. However, this study does not take into account the contribution of Si on overall spectral response of the tandem cell. Therefore, it would be reasonable to credit such high efficiency partly to the silicon sub-cell itself. Nevertheless, this study is very promising for future applications to achieve efficiencies up to 31% for two-junction InGaN/Si tandem cells. Further advances in high quality growth of In-rich InGaN layers as well as in the GaN-on-Silicon technology would hopefully lead to effective merging of high efficiency InGaN and low cost Si PV technologies.

Table 1.6 State-of-the-art for InGaN heterojunction based solar cells [84].

$In_xGa_{1-x}N$ heterojunction based solar cells (p-GaN/i-InGaN/n-GaN)				
Structure ***(Growth method)***	**Content of Indium** ***(Thickness)***	**Type of the active region** ***(Substrate)***	**Performance** ***(Excitation)***	**Reference / author year**
p-i-n InGaN *(MOCVD)*	0.04-0.05 *(200nm)*	Bulk *(0001) sapphire*	V_{OC}=2.4V *((additional UV bias)*	[91] Jani 2007
p-i-n InGaN *(MOCVD)*	0.12 *(200nm)*	Bulk *(0001)sapphire*	V_{OC}=1.81V, J_{SC}=4.2mA/cm^2 *(additional UV bias)*	[74] Neufeld 2008
p-i-n InGaN *(MOCVD)*	0.1 *(150 nm)*	Bulk *(0001)sapphire*	V_{OC}=2.1V, J_{SC}=0.46mA/cm^2 *(325 nm laser, 200mW/cm^2)*	[92] Zheng 2008
p-i-n InGaN *(MOCVD)*	0.3 *(24 nm)*	8 pairs of MQWs *(0001)sapphire*	V_{OC}=2V, J_{SC}=1.5mA/cm^2 *(white light illumination)*	[79] Dahal 2009
p-i-n InGaN *(MOCVD)*	0.19 *(84 nm)*	28 pairs of SL *(0001)sapphire*	η=0.58% *(1 sun AM1.5G)*	[105] Sheu 2009
p-i-n InGaN *(MOCVD)*	0.2-0.28 *(15 nm-15nm)*	5 pairs of MQWs *(0001)sapphire*	η=1.06-1.02% *Wafer bonding on Ti/Ag coated Si*	[106] Jeng 2009
p-i-n InGaN *(MOCVD)*	0.1 *(150 nm)*	Bulk *(0001)sapphire*	η=0.8% *(AM1.5)* *Wafer bonding on Ti/Ag coated Si*	[94] Horng 2010
p-i-n InGaN *(MOCVD)*	0.08 *(150 nm)*	Bulk *(0001)sapphire*	η=0.57% (AM1.5G) *Mounted on Ag coated AlN*	[95] Tsai 2010
p-i-n InGaN *(MOCVD)*	0.35 *(36 nm)*	12 pairs of MQWs *(0001)sapphire*	η=2.95% *(AM1.5G, 100mW/cm^2)*	[96] Dahal 2010
p-i-n InGaN *(MOCVD)*	0.1 *(250 nm)*	Bulk *(0001)GaN substrate*	η=1.41 % *(1.5 suns AM1.5G)*	[82] Kuwahara 2010
p-i-n InGaN *(MOCVD)*	0.17/0.1 (240 nm)	50 pairs of SL / 10 SL pairs of SL *(0001)GaN substrate*	η=2.5% *(1.5 suns AM1.5G)*	[101] Kuwahara 2011
p-i-n InGaN *(MOCVD)*	0.15 (90 nm)	30 pairs of MQWs *r-plane sapphire*	η=1.6% *(AM1.5G, 155mW/cm^2)*	[98] Nakao 2011

$In_xGa_{1-x}N$ heterojunction based solar cells (p-GaN/i-InGaN/n-GaN) -continued				
Structure *(Growth method)*	**Content of Indium *(Thickness)***	**Type of the active region *(Substrate)***	**Performance *(Excitation)***	**Reference/author year**
p-i-n InGaN *(MOCVD)*	0.12 *(0001)sapphire*	Bulk 60nm thick InGaN	Peak external quantum efficiency 72% *(1 sun AM1.5)*	[93] Matioli 2011
p-i-n InGaN *(MOCVD)*	0.11 *(200nm)*	*Graded InGaN bulk layers (0001)sapphire*	η=0.51% *(AM1.5G)*	[107] Lee 2011
p-i-n InGaN *(MBE)*	0.11 *(90nm)*	Bulk *(0001)sapphire*	V_{OC}=1.75V, J_{SC}=1.11mA/cm^2 *(1 sun AM0)*	[108] Lang 2011
p-i-n InGaN *(MOCVD)*	0.108 *(200 nm)*	Bulk *(0001)sapphire*	η=1.2% *(1 sun AM1.5G)*	[81] Shim 2011
p-i-n InGaN *(MOCVD)*	0.28 *(66 nm)*	30 pairs of MQWs *(0001)sapphire*	V_{OC}=1.93V, J_{SC}=2.53mA/cm^2 *(1.2 sun AM1.5G)*	[97] Farrell 2011
p-i-n InGaN *(MOCVD)*	0.21 *(40.5)*	15 pairs of MQWs *(0001)sapphire*	η=1.66% *(1 sun AM1.5G)*	[109] Wierer 2012
p-i-n InGaN *(MOCVD)*	0.2 *(69 nm)*	30 pairs of MQWs *(0001)GaN substrate*	η=2.4% *(1 sun AM1.5)*	[110] Young 2013
p-i-n InGaN *(MOCVD)*	0.15 *(15 nm)*	6 pairs of MQWs *(0001)sapphire*	η=0.2% *(1 sun AM0)*	[100] Liu 2013
p-i-n InGaN *(MOCVD)*	0.19 *(30nm)*	15 pairs of MQWs *(0001)sapphire*	η=2.0% *(1 sun AM1.5G)*	[111] Valdueza 2014
p-i-n InGaN *(MOCVD)*	0.2 *(90 nm)*	30 pairs of MQWs *(0001)GaN substrate*	η=3.33 % *(AM1.50)*	[102] Young 2014

1.2.3.2 InGaN material for PV applications in harsh environments

Harsh environments such as near-sun missions, orbits of planets, deserts, volcanoes or outer space require self-powered and independently operated systems since they are not easily accessible by human. In all of these environments, where elevated temperatures or high radiation damage is present, the solar power would be the most suitable way to sustain efficient electricity generation. Currently, high efficiency solar cells are readily used for two main applications, in which the reliability at high temperature and high radiation resistance is of great interest: *concentrator photovoltaic (CPV)* and *space applications*. However, most of the semiconductors show poor reliability in harsh environments i.e. extreme temperatures and high energy radiation. As a matter of fact, it is important to explore the reliability issues of current semiconductors for high efficiency PV applications, which makes InGaN-based solar cells an attractive candidate for harsh environment sustainable PV.

Concentrator photovoltaic offers a low-cost and viable technology by using cost-efficient concentrating optics. The concentrated sunlight can boost the efficiency of the solar cells beyond their theoretical efficiency limits as well as reducing the area of expensive semiconductor material. The CPV market is not mature and small compared to the conventional PV, but its market segment is expected to grow fast with compound annual growth rate (CAGR) of +22% and reach 5.4GW by 2017 [112]. Currently, more than 90% of the CPV capacity is reported to be in the form of high concentration PV (HCPV) in which the sunlight is concentrated by a factor of x300 to x1000 onto a small area. HCPV uses multi-junction solar cells based on III-V semiconductors e.g. GaInP/InGaAs/Ge triple junction solar cells. Today the state-of-the-art four-junction tandem solar cells (GaInP/GaAs//GaInAsP/GaInAs) indeed benefit from CPV; they deliver 46% efficiency under x508 Suns. Crystalline silicon (c-Si) solar cells are also used in CPV applications so-called low concentration PV (LCPV), in which the concentration ratios are below x100 [113].

Similarly, in space, the solar cells are supposed to achieve higher efficiencies due to the fact that they receive more solar radiation ($1353W/m^2$) than in terrestrial applications ($1000W/m^2$) and without any interruption; i.e. absence of clouds or night time. In space, the satellites solar array generation of electricity from solar power plays a significant role. Today, nearly all satellites, which are equipped with solar arrays, are powered by solar energy. The real breakthrough in space solar cells were achieved when III-V based multijunctions was introduced in 1990's. Since then, satellites continued to grow in size and power requirement, which triggered the research and development of higher efficiency solar cells.

However, the sunlight is as beneficial as it is harmful on the performance of the PV cells. After transforming some part of the solar energy into electrical energy, the remaining fraction of the absorbed sunlight is converted into thermal energy which causes an increase in the solar cell temperature. The thermal environments in CPV systems and in space are indeed highly severe, which should be taken into consideration in design and material selection of the solar cells. For instance, in the orbit of Earth the temperatures can reach 85°C, for near-sun missions the temperatures would rise up more drastically. In terrestrial applications, the solar cells are exposed to temperatures from 15°C to 50°C. On the other hand, when the sunlight is concentrated by a factor of x500 suns, the solar cells would heat up to 1400°C, if insulated [114]. Although the concentrated PV systems generally possess cooling precautions, they cannot completely suppress the temperature effects.

Many of the key performance parameters (J_{SC}, V_{OC}, FF and η) of solar cells degrade with temperature. To start with, the band gap of a semiconductor decreases as the temperature increases. Equation 1.20 shows the dependence of a semiconductor band gap (E_G) on temperature, T by Varshni's Law, where α and β are the Varshni thermal coefficients [115]. Table 1.7 lists the values of E_G, α and β for typical solar cell semiconductors including GaN and InN.

$$\boldsymbol{E_G(T) = E_G\,(0) - \frac{\alpha\, T^2}{\beta + T}} \qquad (1.20)$$

Table 1.7 Energy gap parameters for the semiconductor materials Si, Ge, GaAs, InP, GaN and InN [115, 37].

Material	Energy Bandgap at 0°K (eV)	α ($eV.K^{-1}$) x 10^{-4}	β (K)
Si	1.156	7.021	1108
Ge	0.741	4.561	210
GaAs	1.522	8.871	572
InP	1.421	4.906	93
GaN	3.510	0.909	830
InN	0.780	0.245	624

Dark saturation current, J_0, is a measurement of the leakage of minority carriers across the p-n junction when reverse biased. The origin of this leakage is the carrier recombination on the either side of the junction. As a result of increasing temperatures, the minority carriers are thermally generated leading to an increase in J_0. It was shown that J_0 depends both on temperature and band gap of the material. Singh *et al.* concluded theoretically that the higher the band gap, the lower will be J_0 [116]. J_0 is a critical parameter that controls the V_{OC}, as mentioned

already in Equation 1.5 as well as the conversion efficiency of the solar cells. As a consequence, the dependence of conversion efficiency on temperature is described by a parameter called temperature coefficient of the conversion efficiency $\{(d\eta/dT)/\eta_{25°C}\}$.

The temperature coefficient of the conversion efficiency of crystalline Si-solar cells is around -0.5%/C° under 1 sun, meaning that by 100°C, the solar cell would lose around 40% of its original efficiency at 25°C [114]. On the other hand, InGaP/InGaAs/Ge triple-junction solar cells are more advantageous over Si solar cells with a conversion efficiency temperature coefficient of -0.053%/C°. However, their conversion efficiency reduces with increasing temperatures. In addition, the solar cell loses more than 1% of efficiency after only 2-minutes of sunlight radiation [117].

On the other hand, GaN has been the correct choice for many high temperature device applications owing to its excellent thermal stability [118,119]. Consequently, the reliability of InGaN based solar cells has been studied at concentrated sunlight and high temperatures. Yamamoto *et al.* reported a monotonic increase in conversion efficiency of InGaN/GaN solar cells up to 200 suns without any cooling implementation [120]. Recently, InGaN based solar cells with increasing power conversion efficiency were demonstrated up to 250°C by Zhao *et al.* [121] It was also revealed that the devices were still operational at 400°C which proves the great potential of InGaN based PV in concentrated sunlight applications and high temperature environments as compared to any other semiconductors. Finally, Lien *et al.* reported enhanced conversion efficiency with increasing temperatures with a conversion efficiency temperature coefficient of +0.52%/K° contrary to Si and GaAs based solar cells [122]. The high thermal stability of GaN is owing to its strong atomic bonds, i.e. 8.92 eV/atom for GaN against 2.34 eV/atom for Silicon. Indeed, InGaN/GaN based solar cells face less losses in V_{OC} leading to higher FF and hence greater conversion efficiency with increasing temperatures.

For the space PV applications, the resistance to high irradiation and relatively high temperature becomes crucial. The exposure to electron and proton radiation produces defects in the semiconductor materials, which eventually cause a reduction in the output power of the solar cell. In the case of crystalline silicon solar cells, the mutual effect of elevated temperature and high radiation damage in space degrades severely their performances. Direct band gap semiconductors were reported to be more radiation resistant over indirect band-gap Si based solar cells [123]. Nevertheless, GaAs/Ge based MJ solar cells suffer from severe power reduction (~90%) and increase in resistivity after an intermediate proton radiation, which adversely affect the long term sustainability of space cells [124].

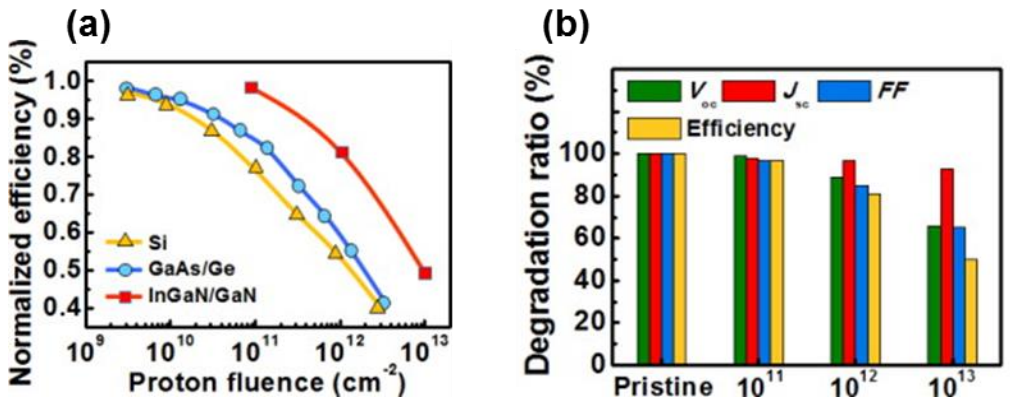

Figure 1.18 (a) Degradation ratio of InGaN solar cells as a function of irradiated proton fluence (b) Comparison of radiation resistance of Si, GaAs/Ge, and InGaN solar cells at different proton fluences [122].

On the other hand, InGaN alloy was reported to withstand radiation damage doses at least two orders of magnitude greater than the damage threshold of the current semiconductors i.e., GaAs or GaInP, which are used in high efficiency tandem space solar cells [124]. The radiation dependent PV performance of $In_{0.15}Ga_{0.85}N$ solar cells (absorption range of 350nm to 450 nm) was recently studied by Lien *et al.* in comparison to that of Si and GaAs/Ge solar cells [122]. Figure 1.18 (a) shows that after proton irradiation of 2 MeV with proton fluence of 3 x 10^{12} cm^{-2}, the Si and GaAs/Ge solar cells lose 59% and 55% of their pristine performance, respectively whereas the degradation ratio of InGaN/GaN based solar cells is 33%. It is important to notice that proton irradiation of 2 MeV is the common dose of irradiation exposed in satellites and national space stations. In addition, Figure 1.18 (b) presents that InGaN based solar cells can maintain up to 50% of their performance at irradiation flux as high as 10^{13} cm^{-2}.

1.3 Conclusions

In this chapter InGaN alloy is introduced as a promising candidate for high efficiency PV applications where they can provide band gaps of more than 2.4 eV. The III-Nitride materials have been described with respect to their unique crystalline and structural properties, which lead to spontaneous and piezoelectric polarization effects in the structures and influence their electrical and optical properties. The major challenges in growing high quality InGaN epilayers have been examined and the alternative of InGaN/GaN MQWs adoption has been proposed. A brief literature overview of the InGaN based solar cells have pointed out that the p-GaN/i-InGaN/n-GaN heterojunctions are more advantageous over p-InGaN/n-InGaN homojunction structures in terms of crystalline quality, capability of p-type GaN doping and hence higher solar cell conversion efficiencies. The potential integration of InGaN alloy with low cost and mature Si technology is stressed and some preliminary literature results have been discussed. Finally,

1.3 Conclusions

InGaN material system is presented as a highly promising candidate for potential use in integration with the mature PV technologies and to achieve higher efficiency sun-harvesting applications in harsh environment owing to their superior thermal stability and resistance to high radiation damage.

Chapter 2

Structural and optical characterization of InGaN/GaN heterojunctions

This chapter presents comparative structural and optical characterizations of solar cell (SC) structures with different active region designs: bulk InGaN and InGaN/GaN MQWs; the composition of In, the type of the substrate; i.e. c-plane (0001) sapphire and bulk GaN substrate. The solar cell designs, which are sandwiched between p-GaN ([Mg] ~ 5×10^{17} cm^{-3}) and n-GaN ([Si] ~5×10^{18} cm^{-3}), were grown by MOCVD by the company NovaGaN.

The material characterization of the SC structures is a crucial part of this study since it provided key information to optimize the design of the active region. To do so, each set of samples, so called "generations" of solar cells, were studied in terms of their material properties as a function of different design parameters. In addition, the characterization results of each generation served as guidance to develop the next generation solar cells. The characteristic features such as targeted indium content, *x*, the number of InGaN/GaN MQWs pairs, *n*, targeted thickness of InGaN wells, t_W, targeted thickness of GaN barriers, t_B, and the type of the substrate in each generations of solar cells are exhibited in Table 2.1.

Table 2.1 The design parameters and characteristic features of solar cell designs in different generations.

Generation of solar cell designs	The design parameter to be studied	Characteristics of the active region				
		x	N	t_W (nm)	t_B (nm)	Type of the substrate
1	Nature of the active layer	~ 0.3	200 nm bulk InGaN layer			Sapphire
2	Thickness of InGaN quantum wells, t_W	~ 0.3	35 25	~ **4** ~ **3**	~ 10	Sapphire
3	Indium content in the InGaN layer	~ **0.1** ~ **0.2** ~ **0.3**	25	~ 2.5	~ 10	Sapphire
4	Type of the substrate	~ 0.15	25	~ 2	~ 5	**Sapphire** **Bulk GaN**

The surface and structural quality of InGaN epilayers in bulk and MQWs forms were assessed by High Resolution X-Ray Diffraction (HRXRD) and Atomic Force Microscopy (AFM). The analysis of the morphological evolution and micro-compositional study of the designs with bulk InGaN and InGaN/GaN MQWs were carried out through Transmission Electron Microscopy (TEM) and High Angle Annular Dark Field-Scanning Transmission Electron Microscopy (HAADF-

STEM), respectively. In addition, Energy dispersive X-Ray (EDX) analyses provided elemental analysis within the layers. The optical analyses of the un-processed epilayers were performed by Photoluminescence (PL) spectroscopy. In addition, electrical characterizations on the processed samples were assessed by Current-Voltage (I-V), External Quantum Efficiency (EQE) and Electron-beam Induced Current (EBIC) measurements. In this chapter, first the characterization methods will be presented; then the material analyses of each set of samples will be detailed.

2.1 Characterization techniques

2.1.1 High resolution X-Ray diffraction analysis

The analysis by X-Ray diffraction is one of the most significant non-destructive characterization techniques in order to assess the crystalline quality as well as the composition and the morphology of the thin films. X-Rays are electromagnetic waves, which possess wavelengths (10^{-9} to 10^{-10} m) in the order of atomic distances in condensed matter. When the electromagnetic radiation impinges on the periodic arrays of atoms in a crystal, the X-Rays are scattered by the electronic shells producing diffraction patterns. The maximal intensity of scattered radiation is achieved in Bragg condition in which the reflected rays from the atoms in successive planes, spaced by a distance *d*, interfere constructively. The Bragg's law is satisfied for this reflection given by Equation 2.1, where λ is the incident wavelength of X-Rays, *n* is the order of the reflection, θ is the angle of diffraction and *d* is the inter-planar spacing.

$$n\lambda = 2d \sin\theta \tag{2.1}$$

X-Ray diffraction is performed by rotating a detector and the sample to be analyzed in a diffractometer. Incident X-ray beams, which are produced in a vacuum tube, are conditioned by the double monochromators to select the $K_{\alpha 1}$ radiation. Resulting from the interaction of the incident beam and the set of atoms in the crystal, the diffracted beam is received by the detector as shown in Figure 2.1 (a). Figure 2.1 (b) presents the different rotational angles, which can be changed to obtain different configurations and various types of information from the crystalline structure. The ω and χ axes lie within the surface of the sample, while φ axis is perpendicular to the sample surface. The sample and the detector can be rotated by certain angles of ω and Θ, respectively, to assess a 3D array of diffraction spots produced by each set of crystal planes in the *real space*. The *reciprocal space* corresponds to the diffraction spots, in which the position of

each diffraction maxima is inversely related to the inter-planar spacing of the crystal planes in the real space.

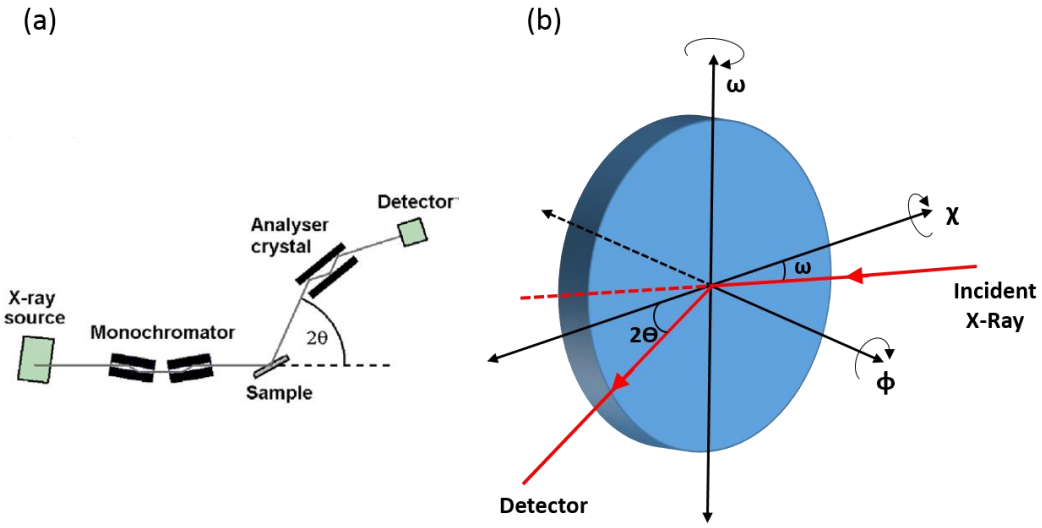

Figure 2.1 (a) High resolution diffraction geometry used in this study [125], and (b) illustration of different axes of rotation of the sample.

The III-Nitrides present many challenges for XRD analyses due to high levels of strain and numerous types of defects in the epilayers resulting from the heteroepitaxial growth, i.e. InGaN/GaN MQWs and GaN on sapphire, and high lattice mismatches. This necessitates high resolution diffraction set up which includes incident beam monochromator, precision goniometer and analyzer crystal as shown Figure 2.1 (a) [125]. The diffraction geometry with an open detector is called the *double-axis geometry*, while the *triple-axis geometry* includes an analyzer crystal before the detector to condition the diffracted beam. The double axis geometry provides information about the defect density, since it is more sensitive to detect the structural defects. On the other hand, the triple axis geometry enables to measure precisely the lattice parameters of the strained epilayers, where the peak broadening due to the dislocations is avoided by the use of a monochromator. The ω/2Θ scan done in the triple axis geometry can be treated as 1D measurement in the reciprocal space. It provides the extraction of the out-of plane lattice parameter (parameter *c*) of the strained layer, the layer thicknesses and the alloy composition. Even though the morphological defects i.e. mosaicity, 3D shape etc. are hidden in triple axis geometry, ω/2Θ scans enable to deduce the periodicity of the superlattice structures in the growth direction and the alloy composition.

A symmetrical ω/2Θ scan of strained InGaN/GaN MQWs heterostructures reveals a sharp main peak of the GaN template, a zero-order peak and series of satellite peaks centered along the zero order peak. The zero-order peak belongs to the average mixture of GaN and

InGaN in the whole MQW stack. Therefore, its angular position corresponds to a diffraction from a lattice which has the mean lattice parameter of the entire MQW superlattice. As a matter of fact, the angular mismatch between the zero-order and substrate peaks provides the average lattice mismatch of the MQWs. Besides, the broadening and intensity of the satellite peaks give information about the structural quality.

Symmetric and Asymmetric Reciprocal Space Mappings of strained InGaN/GaN MQWs

For the analysis of strained InGaN/GaN MQWs heterostructures, study of reciprocal space maps (RSM) in triple axis geometry is a very useful tool to get more information about the crystalline quality and deduce the lattice parameters. The RSMs correspond to 2D sections of the reciprocal space and obtained by performing a series of $\omega/2\theta$ scans at successive ω values. RSMs can be done in two different geometries, i.e. *symmetric and asymmetric geometries,* as shown in Figure 2.2(a) and (b), respectively. First of all, the RSMs are collected in symmetric geometry in which the sample is not tilted, i.e. $2\omega=2\theta$, in order to examine the crystallographic planes parallel or nearly parallel to the surface i.e. any *(00.l)* planes. In the hexagonal crystal system, the distance between the adjacent lattice planes with *hkl* Miller indices can be found by Equation 2.2. In symmetric geometry, Equation 2.2 is simplified to Equation 2.3, which enables the extraction of the out of plane lattice parameter (parameter *c*).

$$\frac{1}{d^2}=\frac{4}{3}\left(\frac{h^2+hk+k^2}{a^2}\right)+\frac{l^2}{c^2} \qquad (2.2)$$

$$d=\frac{c}{l} \qquad (2.3)$$

Secondly, asymmetrical RSMs are collected by tilting the sample about omega, i.e. $2\omega\neq2\theta$, to investigate the mismatch along the a-plane and hence to deduce the in-plane lattice parameter (parameter *a*) by Equation 2.2. Both symmetric and asymmetric RSMs can be done at several azimuthal (φ) angles in order to take into account the relative tilts between the layers, where φ stands for the angle of in-plane rotation around the center of the sample as shown in Figure 2.1 (b). Consequently, an average lattice parameter (*a* or *c*) is obtained from these scans at several azimuthal directions.

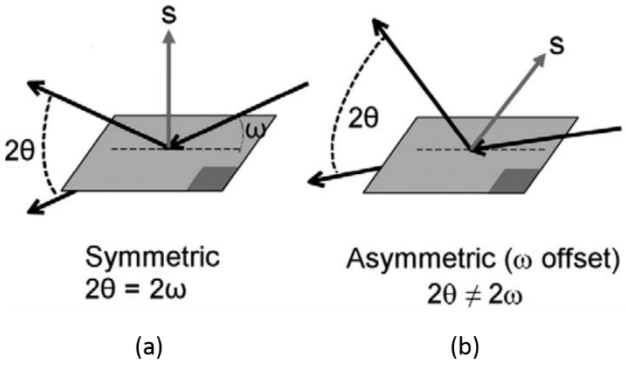

Figure 2.2 (a) Symmetric and (b) asymmetric diffraction geometries used to obtain lattice parameters [125].

Once the average lattice parameters *a* and *c* of the $In_xGa_{1-x}N$ superlattice are found, the indium content can be extracted by Vegard's Law (Equation 1.12)) which assumes a linear dependence of the lattice parameters on the composition [36]. Another approach to determine the alloy composition in InGaN/GaN MQWs is to make use of the simulation XPert once the strain state of the heterostructures is known. In this study, this simulation software is used to interpret the cut lines of symmetric scans at several azimuthal angles in order to obtain the indium content in InGaN quantum wells. The thickness of the InGaN wells and GaN barriers are deduced from the high resolution STEM images. For the fully strained superlattice structures, the relaxation parameter is taken as zero.

2.1.2 Transmission Electron Microscopy analysis

In this study, two different methods of transmission electron microscopy are used to assess the crystalline quality of the InGaN/GaN heterostructures. For the 1st generation solar cells, where the active region is a bulk $In_xGa_{1-x}N$ with x~0.3, conventional TEM (CTEM) is employed. Conventional TEM achieves highly improved spatial resolution (on the atomic scale) compared to optical and scanning electron microscopy (SEM). Briefly, an electron beam illuminates the sample and the diffracted and transmitted electrons are projected onto a screen or a camera for observation. In CTEM, the diffracted electrons and the scattered electron beams are used to create dark field (DF) and bright field (BF) imaging, respectively. Dark field imaging is used to analyze the extended defects in the structure, while BF imaging provides a combination of contrast associated with the defects and thickness. In a BF image, an element with higher atomic number or a thicker region would appear darker since they scatter more the electrons. Furthermore, as a result of the interaction between the parallel beam and the crystalline structure, selected area diffraction (SAED) patterns, which are similar to XRD diffraction but on a much smaller area, i.e. several hundreds of nanometers, are formed. The SAED patterns are of great use to evaluate the crystalline quality of an interface between two

epilayers. In addition, high resolution TEM (HRTEM) enables atomically resolved characterization of the dislocations and interfaces [126].

For the characterization of all other solar cell generations, i.e. with InGaN/GaN MQWs as the active regions, Scanning TEM (STEM) tool is exploited. Contrary to CTEM and HRTEM, STEM mode operates by scanning the sample with a highly focused electron beam. Similar to BF imaging mode in TEM, STEM BF images are sensitive to different phases and diffraction contrasts. The STEM offers a significant characterization tool in dark field operation which is called High Angle Annular Dark Field (HAADF) or Z-contrast imaging. This method is possible by detection and collection of incoherently scattered (not Bragg-diffracted electrons) by an annular dark field detector. As a result, the contrast in the images is governed by the thickness and the chemical composition of the structure. The HAADF signal is directly proportional to tZ^2, where t is the thickness and Z is the mean atomic number.

In addition, by Energy Dispersive X-Ray (EDX) measurement in STEM, elemental analysis can be performed at a nanometer scale. In this method, the number and the energy of the X-Rays emitted from the sample are measured by an EDX detector, and it provides a microanalysis of the heterostructure.

2.1.3 Photoluminescence spectroscopy

Photoluminescence (PL) is the light emission from a matter subsequent to an optical excitation with a high energy laser source. The electrons in the valence band are excited to conduction band with incident photons, which have energy equal or higher than the band gap of the semiconductor. As a result of the photoexcitation, an electron-hole pair is created and the relaxation process occurs via radiative recombination of the carriers and a photon is emitted. The emitted photons, energy of which is generally equal to the bandgap of the material, are then detected and their intensity is counted.

The PL analysis provides various information about the structural quality and purity of the heterostructures in addition to the bandgap of the semiconductor. The PL setup from Prof. M. Stutzmann's group at Walter Schottky Institute (WSI-TUM) (Figure 2.3 has been used for all solar cell generations with InGaN/GaN MQWs. An Argon ion laser (488 nm) in combination with a frequency doubler is excited at 244 nm. The light with 488 nm was separated from the beam by a prism monochromator and then produced a 300μm diameter spot on the sample. The emitted light is then detected by a photomultiplier after passing through the spectrometer. The

PL measurements of all generations of solar cells containing InGaN/GaN MQWs, i.e. generations 2, 3 and 4; are performed at room temperature with incident power of 2mW.

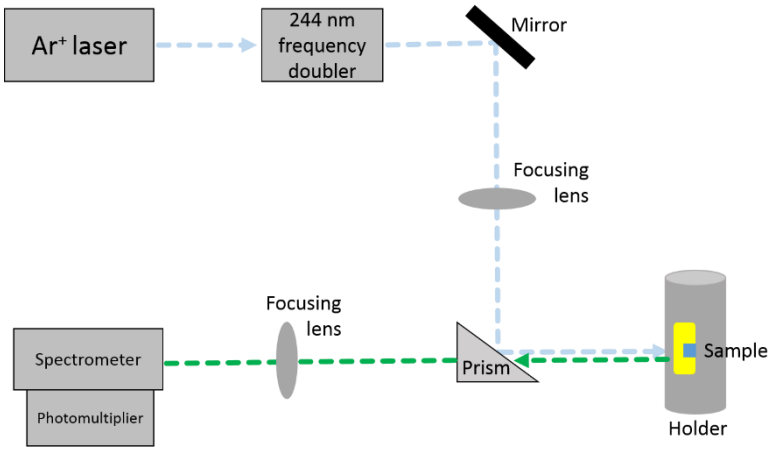

Figure 2.3 The photoluminescence set up used in this study.

2.1.3 Electrical Characterization Techniques

Electrical characterization techniques include Current-Voltage (in dark and illuminated under 1 sun AM1.5G), External Quantum Efficiency and EBIC measurements. The results of all electrical characterizations are presented and discussed in Chapter 3.

2.1.3.1 Current-voltage measurements

Current-voltage measurements were performed during the device processing with KEITHLEY 2614 at IEMN clean room facility. Oriel Sol3A solar simulator under AM1.5G illumination with intensity of 1kW/m2 (1 sun) was exploited for the photovoltaic characterizations.

2.1.3.2 External Quantum Efficiency measurements

External quantum efficiency (EQE) is the ratio of the number of charge carriers collected in the solar cell to the number of incident photons impinging the cell. Basically, to measure the EQE, the intensity of the monochromatic incident light and the generated current by the solar cells should be quantified. In this study, the thermally stabilized EQE measurements were performed in Laboratoire de Physique des Interfaces et Couches Minces (LPCIM) under the supervision of Dr. Martin Foldyna. The experimental setup, which is exhibited in Figure 2.4, includes a light source of 300 W Xenon arc lamp. The intensity of the incident light beam is modified by a two aperture chopper controlled by a lock-in amplifier. The light is then coupled

by Oriel Cornerstone 260 monochromator for the measurements in spectral range of 300 to 800nm. A calibrated Si photodetector (Newport 70356 module) is used as a reference diode. The software displays the measured EQE as a function of wavelength.

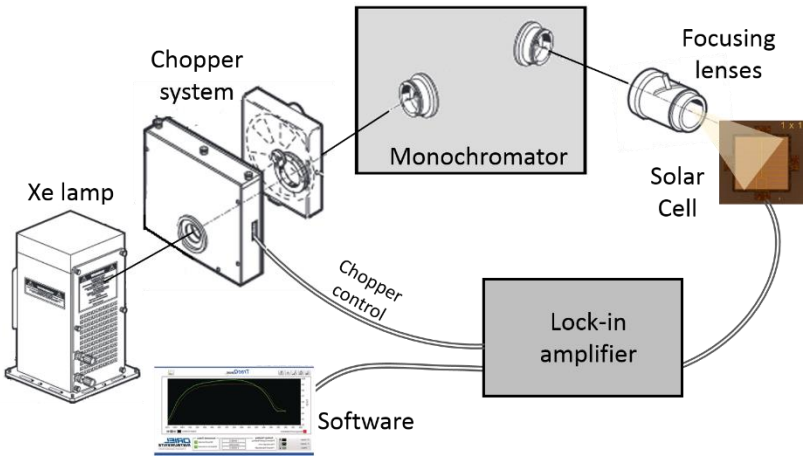

Figure 2.4 The setup of the EQE measurement system used in this study.

2.1.3.3 Electron beam induced current measurements

Electron beam induced current (EBIC) microscopy is a unique tool which allows to study the electrical activity in devices at a nanometer scale. In principal, the incident electron beam of a Scanning Electron Microscopy (SEM) generates electron-hole pairs which will be dissociated by the build-in electric field of the junction and collected at the contacts. The EBIC analysis is of great importance to identify the minority carrier traps such as crystal defects, dislocations [127]. EBIC measurements, which were done at room temperature in a Hitachi SU8000 SEM tool, are performed by the group of Dr. Maria Tchernycheva at Institut d'Electronique Fondamentale. The electron beam was at normal incidence and its acceleration voltage was varied between 1 kV and 15 kV.

2.2 Material Characterization of solar cell design with bulk InGaN epilayers

InGaN alloys possess high absorption coefficient (> 10^5 cm^{-1} at the band edge) allowing 95% of incident light to be efficiently absorbed within the first 300 nm of the active layer. This stands for the main driving force for growing thick (>200 nm) $In_xGa_{1-x}N$ layers with x>0.2 to attain attractive band gap regions unreachable by current high efficiency PV technologies. However, as mentioned before, the high lattice mismatch and the thermal strain between InN and GaN cause formation of threading dislocations, which act as non-radiative recombination centers (NRCs) and are detrimental to device performances. Nevertheless, it is important to investigate the structural and optical properties of InGaN/GaN heterostructures with bulk InGaN

epilayers, which constitute our 1st generation solar cell designs. Figure 2.5 exhibits the schematic design of the 1st generation solar cell with an active region of 200nm thick $In_{\sim 0.3}Ga_{\sim 0.7}N$ sandwiched between 100 nm thick p-GaN [Mg~ $5x10^{17}$ cm^{-3}] and 2 µm thick n-GaN [Si ~ $5x10^{18}$ cm^{-3}] grown on c-plane (0001) sapphire substrate by MOCVD. The XRD, TEM and PL analyses of this generation solar cells were conducted in the facilities of the University of Lille.

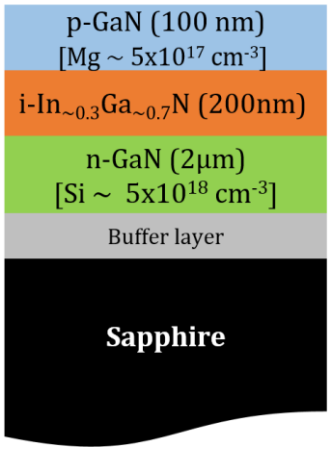

Figure 2.5 Schematic of the 1st generation solar cell design having an active region of bulk $In_xGa_{1-x}N$ layer with x~0.3.

2.2.1 Estimation of indium content and study of crystalline quality by XRD, HRTEM and AFM analyses

The XRD analysis was assessed using a Rigaku SmartLab X-Ray Diffractometer by Dr. Pascal Roussel at Unité de Catalyse et Chimie du Solide (UCCS) at Lille University. The symmetric (000.l) measurements were done at Cu $K_{\alpha 1}$ radiation (λ=1.54056 Å) delivered by the combination of an elliptic mirror and a 2 bounce Ge (220) monochromator. Figure 2.6 (a) shows in plane Θ-2Θ scan of GaN and InGaN (0004) diffraction peaks from the InGaN/GaN double heterostructure. The out-of-plane lattice constants (parameter *c*) of GaN and different InGaN phases can be derived from the Bragg's law as shown in Equation (2.4)

$$c = \frac{l\lambda}{2\ sin\theta_B} \qquad (2.4)$$

The XRD scan around 004 reflection reveals a clear peak for GaN and two peaks for InGaN phases as seen in Figure 2.6 (a). In Figure 2.6 (b), curve fitting of the two peaks is performed in order to determine the lattice constant c and eventually the indium composition of these two InGaN phases. On the other hand, there are no peaks corresponding to pure InN phase or metallic In in the XRD scans.

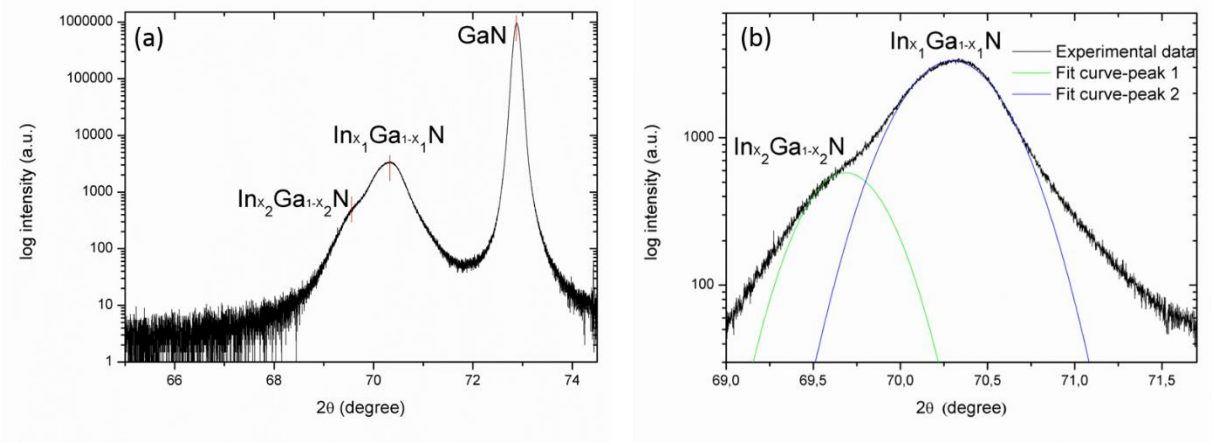

Figure 2.6 004 Θ-2Θ XRD scans of (a) InGaN and GaN bilayers; (b) thick InGaN layers with different contents of indium x_1 and x_2.

The symmetric XRD reflections provide only measurement of out of plane lattice parameter. In the absence of further information, i.e. the asymmetric reflection, the content of Indium in the InGaN phases can be determined by assuming extreme cases for the InGaN/GaN bilayers: fully relaxed or pseudomorphic [128].

- For fully relaxed layers, the fraction of In, *x*, can be determined by Vegard's law as shown in Equation 2.5, where $c_{In_xGa_{1-x}N}$ is the lattice parameter measured from the XRD analysis; while c_{GaN} and c_{InN} are the lattice constants of GaN and InN as tabulated in Table 1.2 in the previous chapter.

$$x = \frac{c, a_{In_xGa_{1-x}N} - c, a_{GaN}}{c, a_{InN} - c, a_{GaN}} \quad (2.5)$$

- When the InGaN layer is assumed to grow on GaN in a pseudomorphic manner, the in-plane lattice parameter of the top layer is supposed to be equal to that of the underlying layer, i.e. $a_{InGaN} = a_{GaN}$. In this case, the biaxial strain state should be taken into consideration, where the in-plane strain vectors; $\varepsilon_{xx} = \varepsilon_{yy} = \varepsilon$, and the strain along the z-axis, ε_{zz} are related to each other by Poisson's ratio i.e. $v(x) = \frac{2\,C_{13}(x)}{C_{33}(x)}$. The detailed information about the bi-axial strain state can be found in the section 1.2.1.1.By assuming a linear dependency of v(x) on the composition between GaN and InN, the fraction of indium in strained InGaN layers can be determined as in Equation 2.6 [128].

Equation 2.7 summarizes the variables used in Equation 2.6 such as Δc, Δa, δc, δa, Δξ and ξ_{GaN}.

$$x = \frac{(\Delta\xi\delta a - \Delta c - \xi_{GaN}\Delta a) + \sqrt{(\Delta\xi\delta a - \Delta c - \xi_{GaN}\Delta a)^2 + 4\Delta\xi\Delta a\,(\delta a\xi_{GaN} + \delta c)}}{2\Delta\xi\Delta a} \quad (2.6)$$

$$\Delta c, a = c, a_{InN} - c, a_{GaN}$$

$$\delta c, a = c, a_{In_xGa_{1-x}N} - c, a_{GaN}$$

$$\Delta\xi = v_{InN}\left(\frac{c_{InN}}{a_{InN}}\right) - v_{GaN}\left(\frac{c_{GaN}}{c_{InN}}\right) \quad (2.7)$$

$$\xi_{GaN} = v_{GaN}\left(\frac{c_{GaN}}{a_{GaN}}\right)$$

Table 2.2 presents the measured lattice parameters and derived fractions of In in InGaN phases when the InGaN layer is assumed to be fully relaxed and pseudomorphically grown on GaN. Figure 2.7 exhibits the ranges for x resulting from the assumptions of fully relaxed and fully strained InGaN layers. The curves for relaxed and pseudomorphic layers are calculated by Equations 2.5 and 2.6, respectively.

Table 2.2 The measured values of 2Θ for the XRD peaks and lattice parameters c of the two InGaN phases, in addition to their estimated values of x, fraction of In, for the assumptions of fully relaxed and fully strained InGaN layers.

InGaN layer	2Θ value for the XRD peak (°)	Lattice parameter *c* (Å)	Estimation of *x*	
			Fully relaxed InGaN	Fully strained InGaN
$In_{X1}Ga_{1-X1}N$ phase	70.30	5.3519	0.32	0.189
$In_{X2}Ga_{1-X2}N$ phase	69.62	5.3970	0.41	0.238

It can be noticed that when the degree of strain is not known and only lattice constant c is measured, the composition of In can be overestimated since the range for x is very large. The range becomes broader as the In content increases. However, it is known that InGaN can be grown pseudomorphically on GaN only below a critical thickness (h_C), which is inversely proportional with the indium content [50]. Beyond this critical thickness, the creation of a misfit dislocation at the interface results in a fully relaxed structure. The critical thickness of a defect free $In_{\sim 0.3}Ga_{\sim 0.7}N$ layer that can be grown on GaN is around 2-4 nm. Therefore, it is plausible to assume a fully relaxed growth of $In_xGa_{1-X}N$ phases with x~0.3 on GaN layer for this generation of SC. As a result, the In contents in two fully relaxed InGaN phases are 0.32 and 0.41. It can be concluded that when growing bulk and high In content (x>0.25) InGaN on GaN, In-rich InGaN tends to form within the InGaN layer.

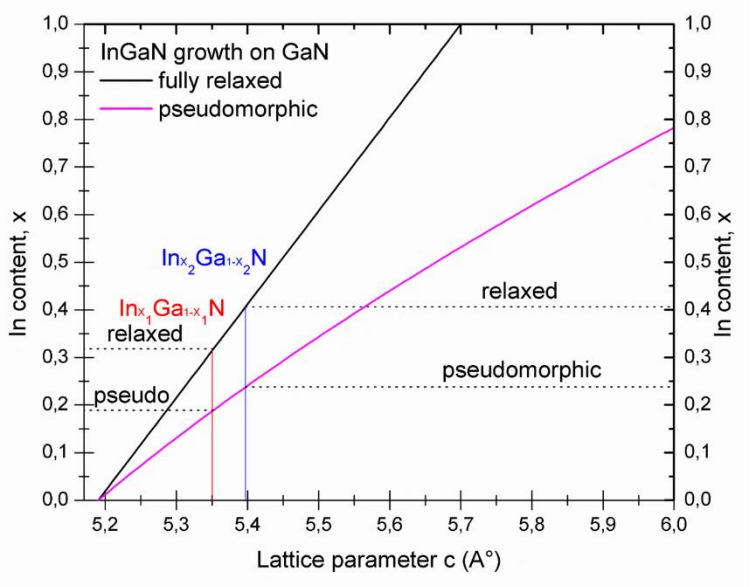

Figure 2.7 Calculated indium content in two InGaN phases as a function of lattice constant c, for the assumptions of fully relaxed and pseudomorphic InGaN layers.

Furthermore, cross sectional TEM samples were prepared by focused ion beam (FIB) method resulting in a cross section thickness lower than 200 nm after depositing Ti-Pt to protect the sample surface. The structural quality of the epilayers was analyzed by TEM-FEI Tecnai G2 20 with the support of Dr. Ahmed Addad at Unité Matériaux et Transformations (UMET) at the University of Lille.

Figure 2.8 (a) and (b) display TEM cross section images of 1st generation solar cell design without p-GaN cap layer and having bulk $In_xGa_{1-x}N$ layer with x~0.3, at higher and lower magnification respectively. In Figure 2.8 (b) the threading dislocations, which originate from the high lattice mismatch between the InGaN and GaN layers, are easily perceived. Figure 2.8 (a) presents the evolution of the defects which create V-shaped pits on the surface of the sample. In addition, inhomogeneities in the contrast of InGaN layer may indicate possible segregation of In-rich InGaN phases, which confirm the XRD analysis.

Figure 2.8 (d) and (e) present clear and identical spots on Selection Area Electron Diffraction (SAED) patterns from InGaN and GaN layers, respectively and confirm the good interface quality between monocrystalline InGaN and GaN films. It can be concluded that the first InGaN monolayers tend to grow pseudomorphically on GaN. On the other hand, high density of stacking faults is observed in Figure 2.8 (c), when InGaN layer thickness exceeds some critical value. Similarly, Pantzas *et al.* [129] reported a 2D/3D transition in growth mode of thick InGaN layers, where first InGaN monolayers are grown pseudomorphically on GaN. The increasing

strain and compositional fluctuations in In content trigger a 2D/3D transition and subsequent InGaN layers are grown in a 3D mode.

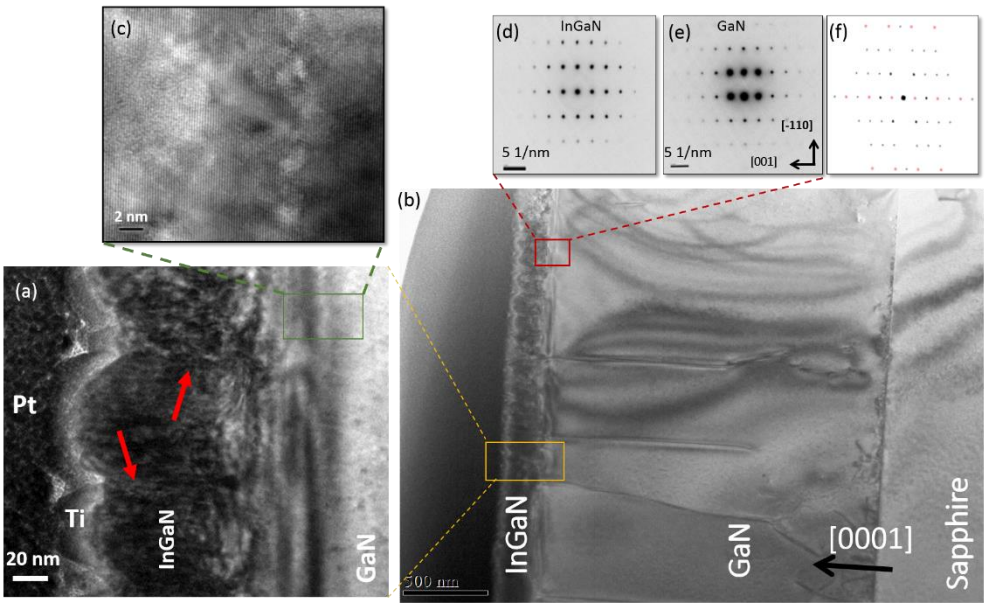

Figure 2.8 Bright-field TEM cross section images of bulk $In_xGa_{1-x}N$/GaN layer with x~0.3 (a) at higher and (b) lower magnification. (c) High Resolution TEM image of the InGaN/GaN interface, Selection Area Electron Diffraction patterns of (d) InGaN layer and (e) GaN layer close to the InGaN/GaN interface, and (f) Diffraction simulation along the (0001) direction.

Furthermore, the surface quality of the samples was evaluated with Atomic Force Microscopy (AFM) by Dimension 3100 tool in tapping mode in air. The topographical image in AFM provides information about the average dislocation density in the InGaN/GaN heterostructures by counting the V-shaped pits, which are the terminations of the threading dislocations at the epilayer surface. Even though this technique may give an underestimated value of actual dislocations densities, it can be used to compare the structural quality of different SC designs. Figure 2.9 (a) and (b) show representative 5×5 μm^2 and 10×10 μm^2 AFM topographical images of the 1st generation solar cell design, respectively. The AFM analysis provides information from a larger area in the structure compared to the TEM investigations. The calculated dislocation density from the AFM images is around 6×10^8 cm^{-2}. The root-mean-square (rms) surface roughness of the structure is 28 nm. On the other hand, Figure 2.9 (c) and (d) exhibit the AFM characterizations on reference sample, which includes only 2µm thick GaN grown on sapphire. The root-mean-square surface roughness of this structure is only 0.6 nm. The AFM analyses from two different zones indicate that the growth of GaN is well optimized by the company and the defects in Figure 2.9 (a) and (b) are originated from the thick InGaN layer.

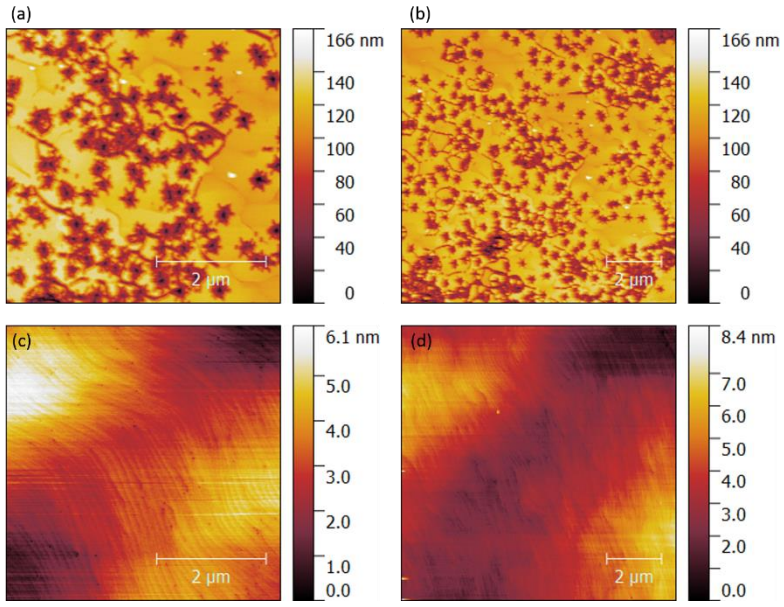

Figure 2.9 Representative AFM images of (a) 5×5 µm² and (b) 10×10 µm² areas on the 1st generation solar cell design, and (c) 5×5 µm² and (b) 10×10 µm² areas on 2µm thick GaN grown on sapphire.

2.2.2 Photoluminescence analysis

The PL measurements were performed with the support of Dr. Brigitte Sieber at Unité Matériaux et Transformations (UMET) at the University of Lille. The samples were excited with 333.6nm line of 30 mW Argon laser focused on the sample to produce a 30µm diameter spot. The luminescence emitted by the samples was analyzed by a triple monochromator DilorRT30 and then detected by a Hamamatsu R943 photomultiplier in the photon counting mode. The PL spectra were corrected for the detection response. The incident power on the sample was 0.35 mW and the PL analysis was carried out at room temperature.

Figure 2.10 presents the room temperature PL spectra of unprocessed 1st generation SC design. The bulk InGaN layer exhibits a peak emission energy of around 2.25 eV and FWHM (Full-width at half maximum) of 900meV. Very high FWHM value is a strong indication of poor crystalline quality and phase separation within the InGaN layer. By using the Equation 1.19, the corresponding In content for the PL peak can be derived as 31% by taking the bowing factor as 1.40, which agrees with the XRD analysis [37]. In addition, the spectrum exhibits possible peaks at around 2.85 and 1.75 eV, which would be associated with InGaN phases with different In compositions. Such PL behavior has been explained by compositional fluctuations and strain relaxation in thin InGaN films with relatively high In contents [130, 131].

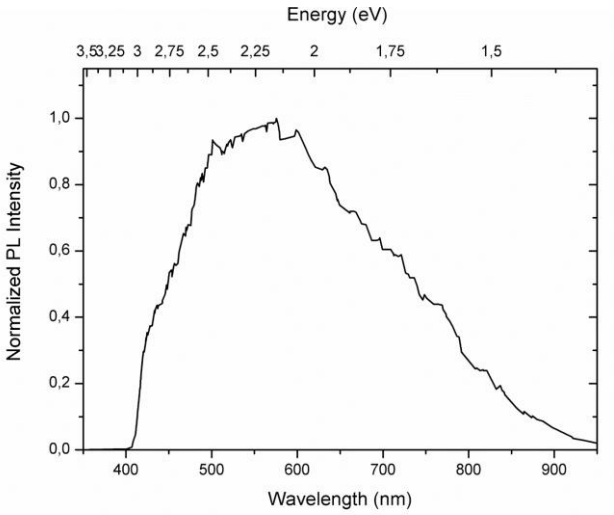

Figure 2.10 Room temperature photoluminescence spectra of 1st generation solar cell having an active region of 200 nm of $In_xGa_{1-x}N$ with x~0.3.

As a conclusion, the design having thick InGaN layer as an active region have demonstrated in our case two significant drawbacks to be used for solar cells; very high dislocation density and phase separation within the InGaN layer. The structural and optical analyses confirm that the InGaN layer is grown in a fully relaxed manner on GaN resulting in creation of high misfit and threading dislocations. The threading dislocations are detrimental to solar cell, since they cause recombination of carriers and reduce the charge collection efficiency. The studies with single thick layers of InGaN using In contents above 20% similarly reported high dislocation density and phase separation that resulted in poor device performances [84-86]. The phase separation and fluctuation in the In composition within the InGaN layer would result in highly inhomogeneous absorption spectrum of the solar cells. Jani *et al.* reported that the phase separated domains act as recombination centers and reduce the short circuit density since their size and distribution are not optimal [91]. Consequently, we considered that thick and fully relaxed InGaN layers are not suitable for solar cell applications.

2.3 Material Characterization of solar cell designs with InGaN/GaN MQWs

In order to improve the structural quality, MQW or superlattice (SL) structures using few nanometers of InGaN layers have been exploited as an alternative for the active regions of the SCs. Moreover, the absorption of light and the short-circuit density of the solar cells can be tailored by introducing low band gap quantum well between the wider band gap barriers. Such structures aim to reduce the defect density in devices by incorporating very thin InGaN layers below the h_C depending on the composition of indium. However, h_C for the formation of misfit dislocations in $In_{0.3}Ga_{0.7}N$/GaN systems is only around 3-4 nm [50], while hundred nanometers

of InGaN are required for full absorption in the active region. As a result, in InGaN/GaN MQW SCs, higher number of InGaN QWs would be needed for efficient absorption of the photons.

As a matter of fact, in this study, InGaN/GaN MQWs heterostructures have been adopted as the active region of the solar cells in different generations. In the 2nd generation solar cell designs, the effect of InGaN well thickness on the structural quality is studied, while the 3rd generation material characterizations included various In contents. Finally, the 4th generation SC designs present a study of crystalline and optical properties for two types of substrates.

2.3.1 Study of crystalline quality with variation of InGaN well thickness

The 2nd generation solar cell includes two SC designs, in which the thickness of InGaN wells was targeted to be 4 nm and 3 nm, by keeping the same In content (x~0.3) as the 1st generation design. The design with thicker wells, which represents our first attempt to grow MQW structures, have 35 pairs of InGaN/GaN MQWs. Then, in the second attempt, a design with thinner wells (~ 3nm) was preferred as well as reducing the number of pairs to 25. The comparative HRXRD, HAADF-STEM, EDX, AFM and PL analyses of these structures, of which the designs are shown in Figure 2.11, will be presented and the results will be discussed hereafter.

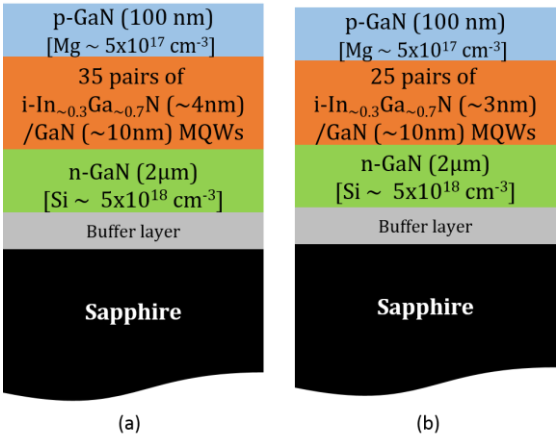

Figure 2.11 Schematic of the 2nd generation SC designs having $In_xGa_{1-x}N$/GaN MQWs where x~0.3 with (a) n=35, t_W~4 nm; and (b) n=25, t_W~3 nm, respectively.

2.3.1.1 Estimation of In content by HRXRD and STEM analyses

The HRXRD analysis by rotating anode Rigaku SmartLab X-Ray Diffractometer and all STEM analyses were assessed by Dr. Ludovic Largeau at Laboratoire de Photonique et de Nanostructures (LPN). The symmetric (000.l) and asymmetric (10-15) RSM measurements were done at Cu $K_{\alpha 1}$ radiation (λ=1.54056 Å) delivered by the double Ge (400) monochromator. The

HRXRD measurements of the 2nd generation solar cells were carried out in double axis geometry, i.e. no monochromator in the diffracted beam.

The procedure to estimate the thickness of InGaN wells and GaN barriers as well as the In content can be briefly described as follows: Firstly symmetric ω/2θ scans and reciprocal space maps (RSM) are measured to deduce the c lattice parameter and the thickness of one period ($T=t_{WELL}+ t_{BARRIER}$). Then, asymmetric RSM are performed to decide the strain state of the samples. Once the strain state is known, In content is extracted using Equation 2.5 or 2.6, according to the Vegard's law. Finally, the thicknesses of GaN and InGaN epilayers are measured by HAADF-STEM analysis and these values are used for simulation of XRD profiles by X'Pert Epitaxy software. In addition, possible fluctuations of In in the InGaN wells are investigated by EDX analyses and then compared to the average In content derived from the HRXRD analyses. Finally, AFM characterizations provided comparison of surface quality of the samples in terms of rms surface roughness as well as dislocation density.

Figure 2.12 (a) and (b) show the complete symmetric ω/2θ scans and ω/2θ scan around (0004) reflections, respectively, for the 2nd generation SC designs. The highest peak corresponds to thick GaN buffer layer. The peak at lower angle compared to that of GaN, called 0th order peak, is associated with the average In content in InGaN and provides the average lattice mismatch of the whole periodic structure. The satellite peaks centered around the 0th order peak are due to superlattice structure of InGaN/GaN MQWs. The thickness of one period can be derived by Equation 2.8 where θ_i and θ_j are the corresponding angles of *i* and *j*, two order superlattice satellites.

$$T = \frac{(n_i - n_j)\lambda}{2\,(sin\theta_i - sin\theta_j)} \qquad (2.8)$$

The period thicknesses are derived to be 15.7nm and 11.4 nm (±0.2 nm) for the designs with t_W~4 nm and t_W~3 nm, respectively. The diffraction peaks of SC design with thicker wells are broader that those of SC design with thinner wells, which points out a more defective structure for the former. Different reflections angles of the satellite peaks of two SC designs indicate that the composition of In in the InGaN layers are different, although the same content, i.e. x~0.3, was targeted for both generations.

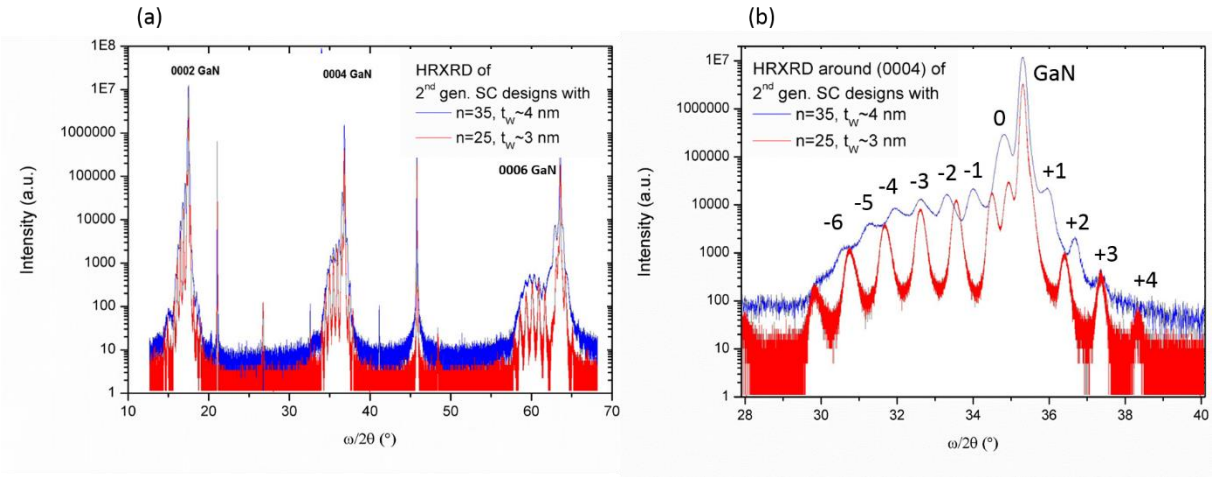

Figure 2.12 Comparison of (a) complete ω/2θ scans and (b) ω/2θ scans around (0004) reflections of the 2nd generation solar cells having $In_{\sim 0.3}Ga_{\sim 0.3}N$/GaN MQWs.

Figure 2.13 presents the symmetrical (0002) RSMs along each m-plane (10-10) that corresponds to various φ (azimuthal) angles of the SC design with t_W~4 nm. From these six Q_Z vs Q_y plots, where the coordinates are in reciprocal lattice units (1/λ), an average out-of plane lattice parameter is deduced. However, to do so, the strain state of the heterostructures should be first clarified by asymmetric RSM, which will be presented in the following part.

A striking feature about the symmetric RSMs of the design with t_W~4 nm is the presence of broadening of the peaks that are elongated over several degrees in Q_y for the most intense satellite peaks. This phenomenon is associated with broadening of the Bragg points perpendicular to the surface [132]. They indicate the presence of crystalline interfaces where the crystal is faceted.

On the other hand, the symmetrical (0002) reciprocal space mappings along each m-plane (10-10) of the SC design with t_W~3 nm, which are presented in Figure 2.14, do not exhibit the same broadening due to facetted crystal behavior. The pronounced broadening features point out more faceted structure in thicker well SC design compared to the SC design with thinner wells. Analysis of STEM would provide further information about the morphological evolution of the epilayers.

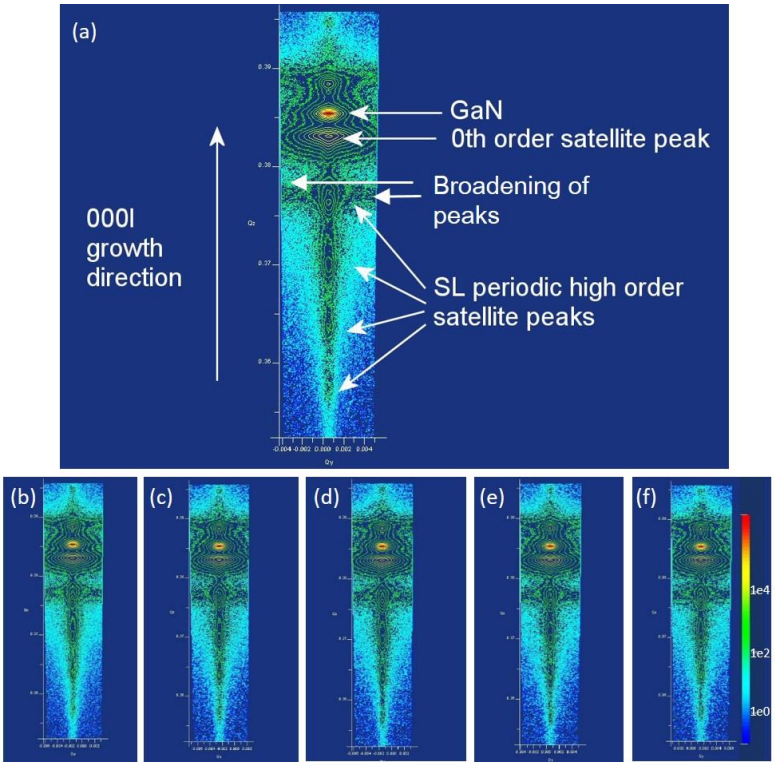

Figure 2.13 Symmetrical 0002 RSM of the SC design with t_W~4 nm at several azimuthal rotations of (a) φ=0°, (b) φ=60°, (c) φ=120°, (d) φ=180°, (e) φ=240°, (f) φ=300°.

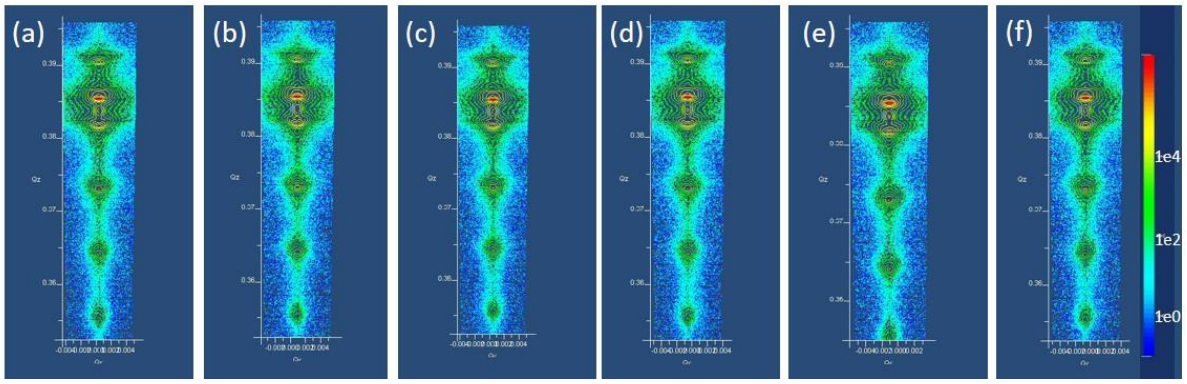

Figure 2.14 Symmetrical 0002 RSM of the SC design with t_W~3 nm at several azimuthal rotations of (a) φ=0°, (b) φ=60°, (c) φ=120°, (d) φ=180°, (e) φ=240°, (f) φ=300°.

In order to determine the strain state of the heterostructures, asymmetric RSMs around (10-15) reflections along each m-plane (10-10) have been performed for 2nd generation solar cells. As seen in Figure 2.15 (a), there exists no vertical alignment of the GaN peak (in red) with the superlattice peaks, indicating that the heterostructure is not fully strained. It is possible that t_W~4 nm is above the critical thickness to grow pseudomorphic InGaN layers.

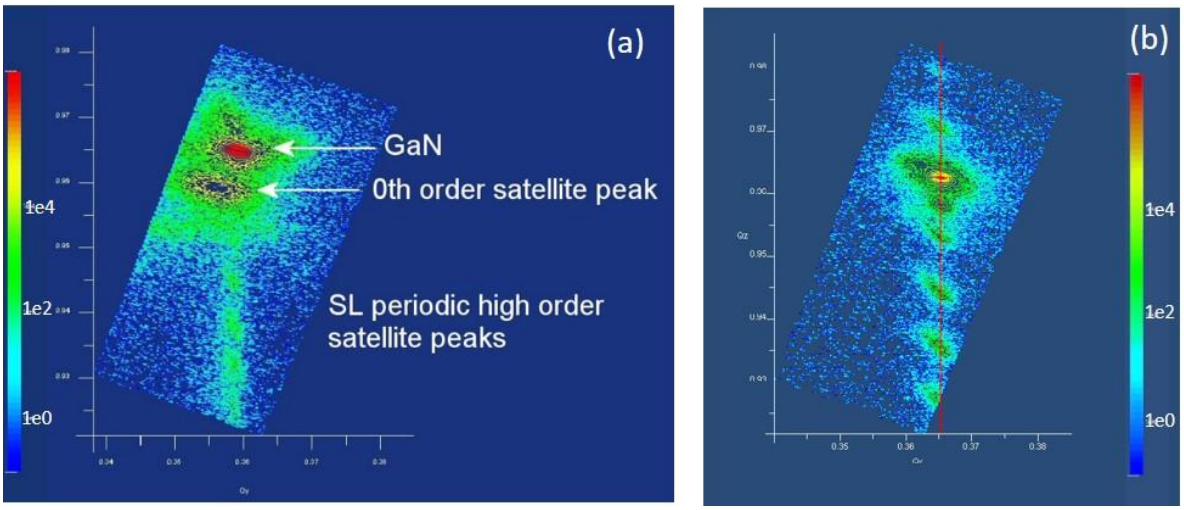

Figure 2.15 Asymmetric reciprocal space maps around (10-15) reflections for the 2nd generation SC designs with (a) n=35, t_W~4 nm at φ=0°; and (b) n=25, t_W~3 nm at φ=60°; respectively.

On the contrary, for the SC design with t_W~3 nm, Figure 2.15 (b) show that all the satellite peaks are aligned vertically with the GaN peak, pointing out a fully pseudomorphic growth of this structure. Consequently, Equation 2.6 has been used to estimate the In content in the InGaN epilayers by assuming a biaxial strain state, i.e. $a_{InxGa1-xN} = a_{GaN}$, and deducing the $c_{InxGa1-xN}$ from the relative misorientation between GaN peak and 0th order SL peak. Table 2.3 summarizes the thickness of one period and estimated In contents in the 2nd generation solar cell designs assuming the corresponding strain states.

Table 2.3 Indium content and thickness of superlattice period of the 2nd generation solar cell designs extracted form HRXRD analyses.

Targeted t_W (nm)	Number of pairs of InGaN/GaN MQWs, n	Thickness of one period (nm)	x, content of In	Strain state
4	35	15.7	-	Fully relaxed
3	25	11.4	0.24	Biaxially strained

Further investigation on the crystalline quality of the samples are conducted by Jeol 2200FS TEM equipped with a corrector of spherical aberrations on the STEM probe and with an ultra-high resolution objective lens. Prior to STEM observation of this sample, Ti was deposited on the top surface and a sample with cross section thickness of 100 nm were prepared with the FIB method. Figure 2.16 (a) presents BF STEM image of the p-GaN/I-InGaN/n-GaN stack of the SC design with t_W~4 nm where the p-GaN is partially damaged and even vanished, i.e. thickness less than 100 nm. It is believed that during the Ti deposition, some Ga ions in the FIB process damage the surface, which partially destroys the top p-GaN surface. In addition, the threading

dislocations (shown with red arrows), which evolve into V-shaped pits, create a highly rough surface for the growth of p-GaN. They also play a role in formation of such irregular surfaces. It is important to notice that the threading dislocations initiate after growth of different number of MQWs, which indicate irregularities in the growth conditions.

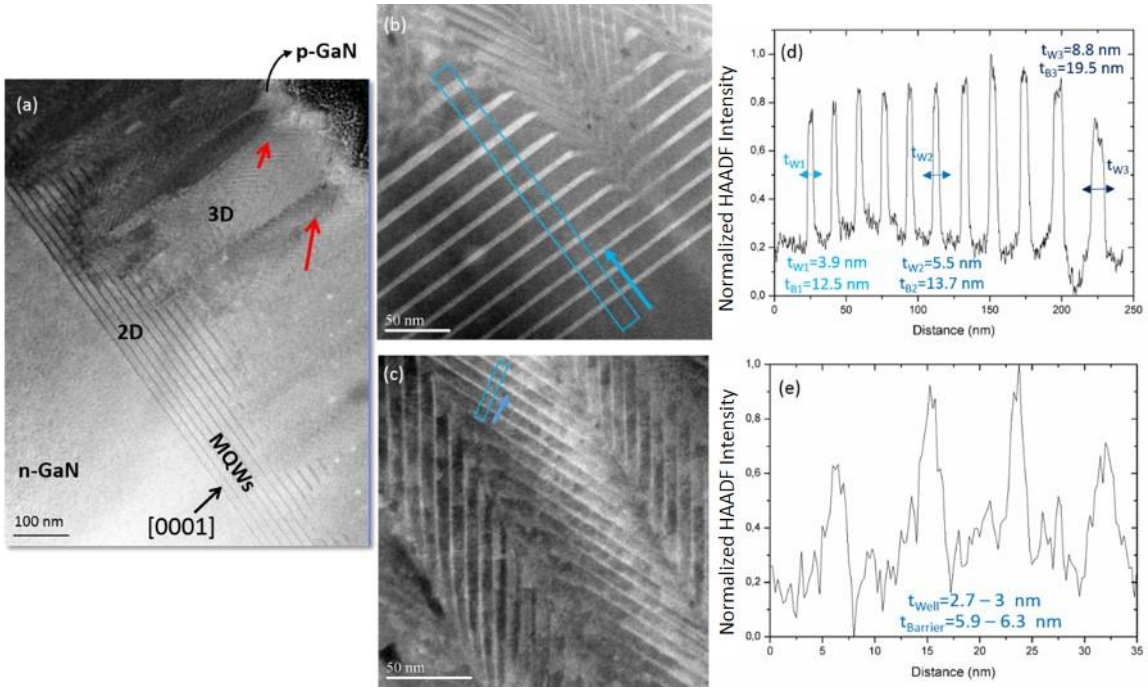

Figure 2.16 For the 2nd generation SC design with t_W~4 nm: (a) BF STEM image of the p-i-n stack, HAADF- STEM images of (b) 2D grown InGaN/GaN MQWs, (c) 3D grown InGaN/GaN MQWs and (d) and (e) corresponding normalized EDX signal intensity vs distance plots, respectively.

Figure 2.16 (b) exhibits an interesting phenomenon in the growth of high number of pairs of InGaN/GaN MQWs with relatively thick InGaN wells. The cross sectional HAADF-STEM characterization points out that the first InGaN/GaN MQWs seem to be grown in pseudomorphic manner. In Figure 2.16 (d), the HAADF analysis with respect to the distance shows that during growth, the fully strained or 2D grown InGaN epilayers and the GaN barriers tend to grow thicker. Figure 2.17 (a) present an EDX study on several InGaN QWs in the 2D grown InGaN/GaN MQWs region. The EDX analysis reveals that the primary 2D pseudomorphic InGaN QWs demonstrate strong lateral fluctuations in In composition over growth time with an average of 20 % causing an increase in both the growth rate and the elastic strain at In-rich regions. Eventually, the structure is plastically relaxed, since the well thickness exceeds the critical thickness and threading dislocations are produced. Interestingly, the periodic growth of InGaN and GaN layers continues on the inclined planes, which is referred as 3D growth in this study. Similarly, it was reported that the lateral fluctuations and increase in elastic strain in 2D grown InGaN MQWs which trigger the faceting of the growth surface and the transition to a 3D growth

mode [129]. Besides, the highly faceted structures in this mixed 2D/3D MQW structures confirm the presence of the elongated broadening of the peaks in symmetric (0002) RSMs.

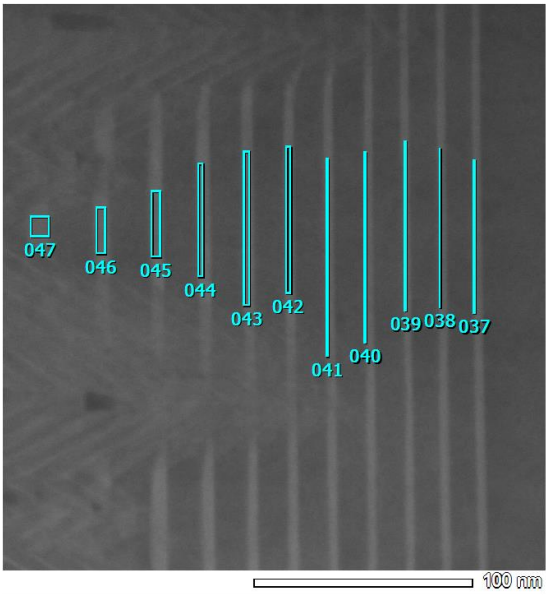

EDX Line	Atoms (%) Ga	In
37	81	19
38	80	20
39	84	16
40	80	20
41	79	21
42	79	21
43	76	24
44	76	24
45	78	22
46	79	21
47	85	15

Figure 2.17 For the 2nd generation SC design with t_W~4 nm: (a) HAADF- STEM images of 2D grown InGaN/GaN MQWs with EDX lines. Inset table: Analysis of atomic concentration of In and Ga analysis for the corresponding EDX lines.

The 3D grown InGaN/GaN MQWs on the inclined planes and the evolution of thicknesses of wells and barriers of the corresponding layers are displayed in Figure 2.16 (c) and (d), respectively. The fluctuation in the thickness of the InGaN wells and GaN barriers are less pronounced compared to the 2D grown MQWs.

The HAADF-STEM analysis of the 2nd generation SC design with t_W~3 nm is shown in Figure 2.18. To start with, a smoother and less defective p-GaN layer is observed, which can be associated to two following factors. Prior to the FIB procedure, a thin layer of C is deposited instead of Ti, which did not cause any damage of the top p-GaN layer. Secondly, less defect density and decent 2D growth quality which led to smooth surface properties. On the other hand, Figure 2.18 (a) reveals various defects within the active region of the SC design. First of all, Figure 2.18 (b) exhibits a possible threading dislocation initiation within the MQW stack and transition to 3D growth mode. Moreover, some local thickness fluctuations within the InGaN epilayers are displayed at the top MQWs in Figure 2.18 (c). In addition, the EDX line analysis conducted on the top MQW layers of the active region indicates that the In content varies between 19 and 24%.

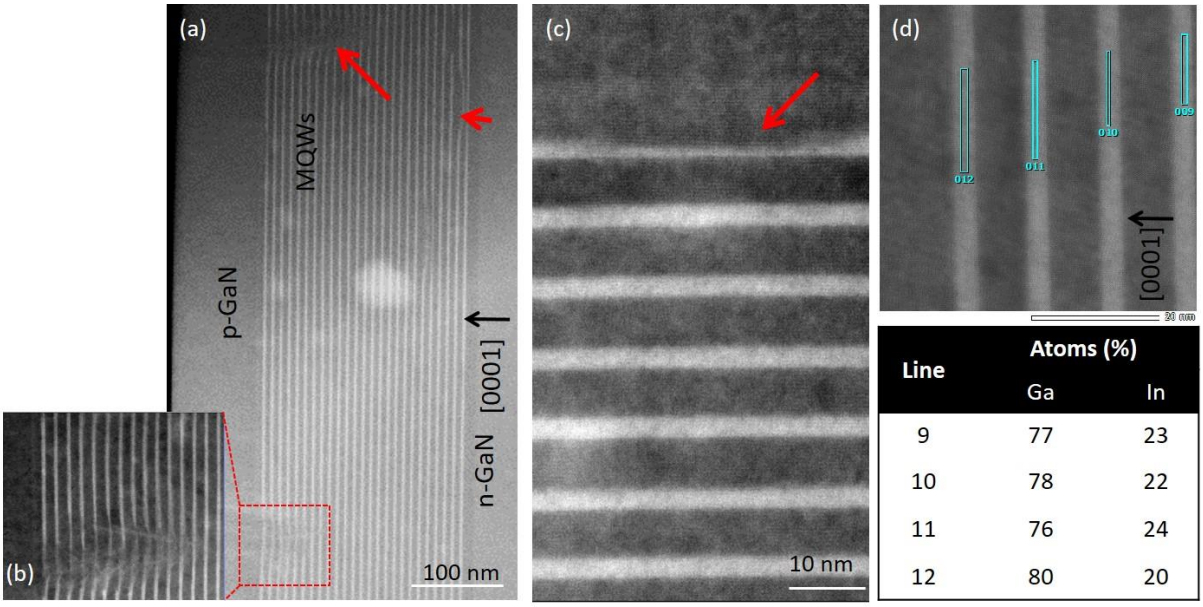

Line	Atoms (%)	
	Ga	In
9	77	23
10	78	22
11	76	24
12	80	20

Figure 2.18 For the 2nd generation SC design with t_W~3 nm: HAADF- STEM images of (a) the complete p-i-n stack, the top InGaN/GaN MQWs layers with (b) possible transition to 3D growth mode, (c) local thinning of the quantum well and (d) evidence of In fluctuation with EDX line analysis. Inset table: Analysis of atomic concentration of In and Ga analysis for the corresponding EDX lines.

According to the HAADF-STEM analysis, the average thickness of the InGaN quantum wells and GaN quantum barriers were measured to be 3.1 nm and 8.3 nm for this design, which provided the necessary information to simulate XRD profiles by the X'Pert Epitaxy software. Consequently, Figure 2.19 displays the experimental and simulated $\omega/2\Theta$ scans around (0004) reflections of the 2nd generation SCs design with thinner wells. Two scans fit well confirming that the indium content is 24% in the InGaN layer. The peaks of the experimental scan are broader than those of the simulated curve, since the simulation does not take into account the structural defects in the epilayers. As the XRD probe has a footprint of size of $2mm^2$, it is very sensitive to any kind of defect in the structure.

On the other hand, for the SC design with t_W~4 nm, the simulation of XRD profiles is very challenging since this structure shows a great inhomogeneity in thickness of the well as well as the barriers. In addition, the HRXRD and STEM analyses point out possible phase separation within the InGaN layers since average In content is 20% for the 2D grown domains while it is around 28% for the 3D grown part.

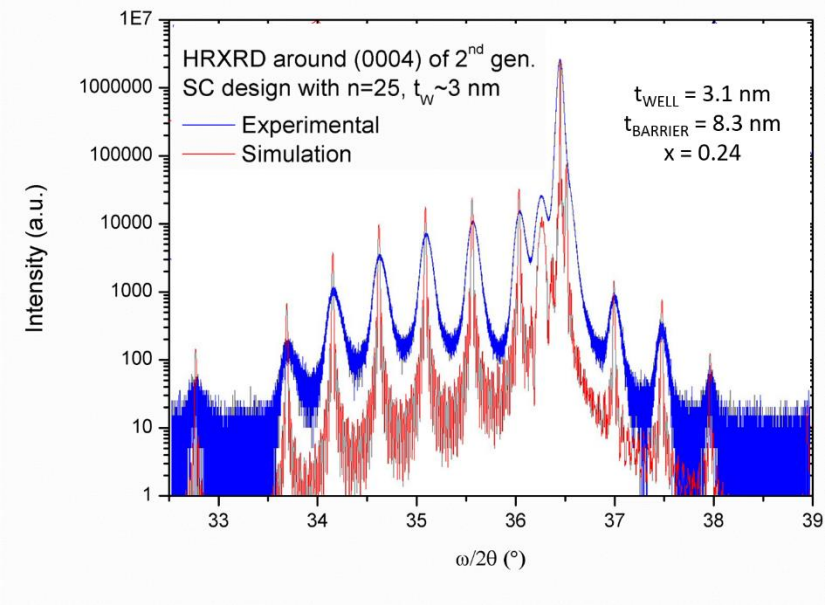

Figure 2.19 Experimental ω/2Θ scans around (0004) reflections of the 2nd generation SC design with n=25, tw~3 nm and the corresponding XRD simulation curve.

2.3.1.2 Assessment of surface quality by AFM analysis

The surface quality of the 2nd generation SC designs was assessed by AFM. Figure 2.20 (a) and (b) show representative 5×5 μm^2 AFM topographical images of the SC designs with t_W~4 nm and t_W~3 nm, respectively. The SC design with thicker wells has rms surface roughness of 41 nm, which agrees with the high density of defects and mixed structure (2D/3D grown InGaN/GaN) observed in TEM observations. On the other hand, the SC design with t_W~3 nm exhibits very low roughness of 6.4 nm. The calculated dislocation density for the latter is around 4×10^8 cm^{-2}, which is lower than that of the 1st generation SC design using bulk $In_xGa_{1-x}N$ with x~0.3.

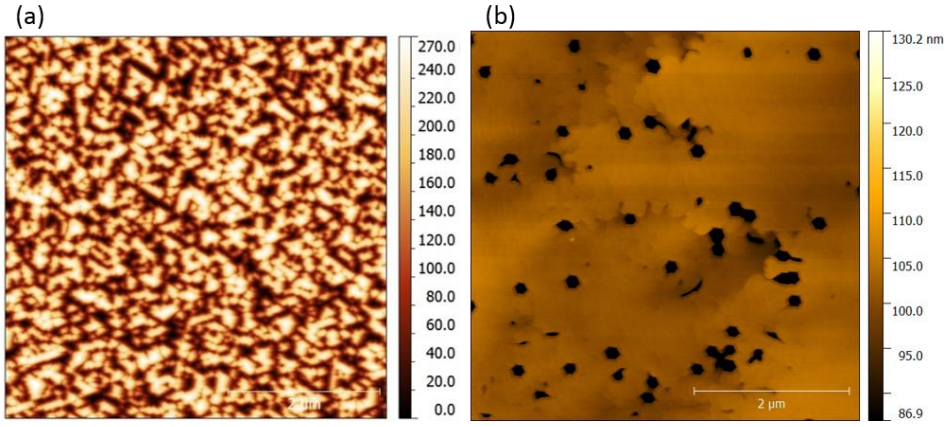

Figure 2.20 Representative AFM images of 5×5 μm^2 areas on the 2nd generation SC designs with (a) n=35, tw~4 nm, and (b) n=25, tw~3 nm.

2.3.1.2 PL Analysis

Room temperature PL spectra of 2nd generation SC designs are exhibited in Figure 2.21. The peak emission wavelengths of designs with t_W~4 nm and t_W~3 nm are 556.1 nm (2.23 eV) and 543.9 nm (2.28 eV). The red shift of emission wavelength of about 12 nm is due to higher average In content and thicker wells in the former structure. The design with t_W~4 nm exhibited much higher FWHM value, i.e. 288 meV, than that of the design with t_W~3 nm which is around 263 meV. This is originated from higher defect density and mixed grown structure in the former. Both of the designs exhibited emission spectra with clear peaks delivering lower FWHM, compared to the 1st generation SC designs, which point out an improvement in the crystalline structure by growing InGaN/GaN MQWs.

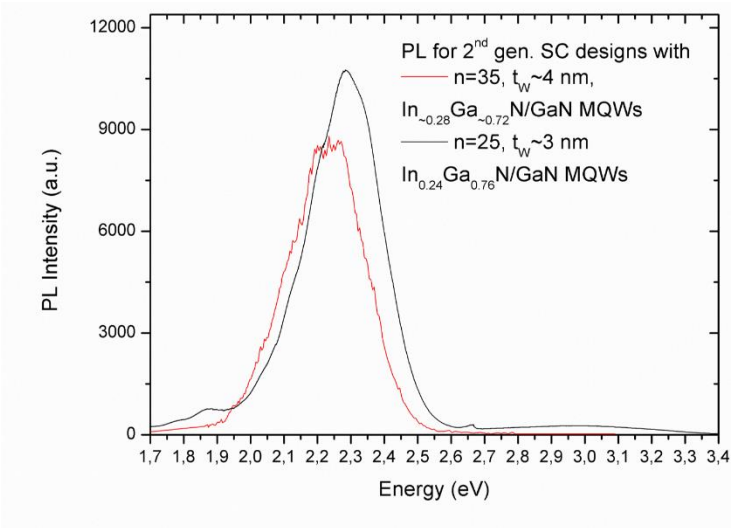

Figure 2.21 Room temperature PL spectra for 2nd generation SC designs with n=35, t_W~4 nm $In_{\sim 0.28}Ga_{\sim 0.72}N$/GaN MQWs, and n=25, t_W~3 nm $In_{0.24}Ga_{0.76}N$/GaN MQWs.

To conclude, the structural analysis by means of HRXRD, STEM, AFM and PL measurements have shown that 2nd generation SC designs with t_W~4 nm, which include 35 pairs of $In_{\sim 0.3}Ga_{\sim 0.7}N$/GaN MQWs exhibit great irregularities in indium content and thickness of quantum wells and barriers. The well thickness and the indium content increase as a function of the growth time, leading to higher elastic strain and eventual plastic relaxation in the structure. As a result, the subsequent periodic structures are grown on inclined planes and causes formation of a mixed (2D and 3D) heterostructures. This would point out that the growth parameters are not sufficiently optimized. Similarly, Wu *et al.* reported that the formation of V-defects is promoted by the increase in the inelastic relaxation in strain as a result of increase in the number of QWs in a MQW structure or increase in the In content in the QWs [133]. On the other hand, for the SC design with thinner wells a better control over the growth characteristics is obtained. The well thickness and the integrity of the MQWs are well preserved throughout the

structure, which indicates a better growth quality compared to the former design. It is noticed that the targeted InGaN well thickness (3.1 nm) is nearly achieved, while for other design the well thickness fluctuates significantly. The relatively low surface roughness and evidence of pseudomorphic growth by asymmetric RSMs also confirm the improved quality. As it is remarked, in this generation of SCs, two design parameters have been varied: the number of InGaN/GaN MQW pairs and the thickness of InGaN wells. However, since the structures with targeted $t_W \sim 4$ nm, undergo a plastic relaxation and the MQWs show a transition in growth mode after several pseudomorphically grown epilayers, the factor of improvement in crystalline quality is finally owing to the design parameter of well thickness, even though the number of MQW pairs should also play a role.

Furthermore, it can be concluded that compared to the 1st generation solar cells with bulk and phase separated $In_{\sim 0.3}Ga_{\sim 0.7}N$, the adoption of MQWs provided better structural quality and less dislocation density (retrieved from the AFM analyses). However, local discontinuities in In content is observed as well as the structural defects such as thinning of QWs and imitation of threading dislocations, which could stimulate the 3D growth.

2.3.2 Study of crystalline quality with variation of indium content

The 3rd generation solar cell designs offer a comparison of crystalline quality for similarly grown samples as a function of indium content. The solar cells, of which the identical designs are presented in Figure 2.22, include 25 pairs of $In_xGa_{1-x}N$/GaN MQWs with various indium contents of $x \sim 0.1$, $x \sim 0.2$ and $x \sim 0.3$. The thickness of quantum wells and quantum barriers were targeted to be 2.5 nm and 10 nm, respectively. Firstly, symmetric $\omega/2\theta$ XRD scans were taken to determine the thickness of one period and the lattice parameter c. Then, by asymmetric RSMs along several azimuthal angles, the strain state of the heterostructures was investigated. The HAADF-STEM analyses provided measurements of GaN and InGaN epilayer thicknesses, which then enabled the estimation of the In content in the corresponding SC design. In addition, EDX analyses allowed examination of possible fluctuations of In in the InGaN wells for the highest In content SC design; i.e. $x \sim 0.3$.

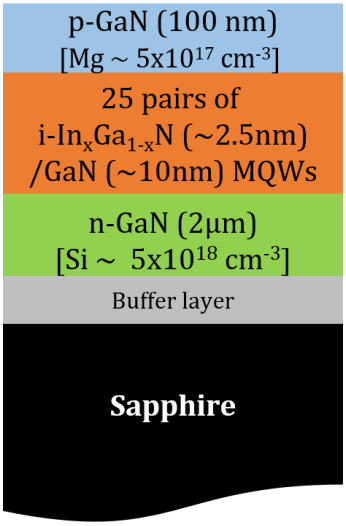

Figure 2.22 Schematic of the 3rd generation solar cell design having 25 pairs of $In_xGa_{1-x}N$/GaN MQWs with various In contents (x~0.1, x~0.2 and x~0.3) grown on sapphire.

2.3.2.1 Estimation of In content by HRXRD and STEM analyses

The HRXRD analysis was performed in double axis geometry, with Cu $K_{\alpha 1}$ radiation (λ=1.54056 Å) delivered by the double Ge (400) monochromator, similar to the analysis of the 2nd generation SC designs. Figure 2.23 (a) presents the symmetric 0002 RSM of 3rd generation SC design with $In_{\sim 0.3}Ga_{\sim 0.7}N$/GaN MQWs, which does not exhibit any CTR features for the superlattice peaks, unlike the 2nd generation SC design with thicker wells. In addition, Figure 2.23 (b) displays a vertical alignment of the GaN peak (in red) with the superlattice peaks, pointing out fully pseudomorphic growth of InGaN/GaN MQWs on GaN layer. Similarly, the SC designs with $In_{\sim 0.1}Ga_{\sim 0.9}N$/GaN and $In_{\sim 0.2}Ga_{\sim 0.8}N$/GaN MQWs, exhibit the identical asymmetric RSM behavior (not shown here). Therefore, the biaxial strain state can be assumed for all designs in this generation of SCs.

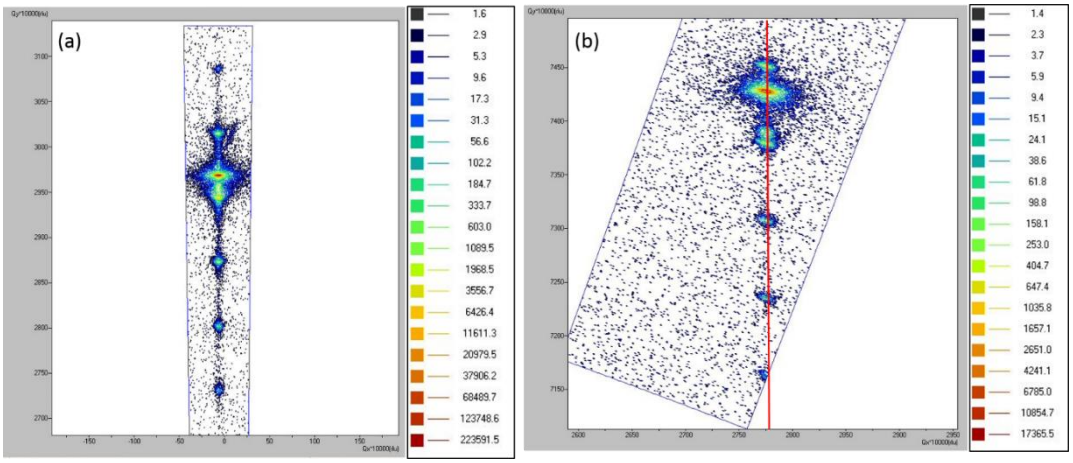

Figure 2.23 (a) Symmetric 0002 RSM at φ=60° and (b) Asymmetric RSM around (10-15) reflections at φ=120° for the 3rd generation solar cell design with $In_{\sim 0.3}Ga_{\sim 0.7}N$/GaN MQWs.

Another evidence for the pseudomorphic growth and well preserved 2D grown MQW integrity can be seen in HAADF-STEM images of SC designs with $In_{\sim 0.1}Ga_{\sim 0.9}N$/GaN and $In_{\sim 0.2}Ga_{\sim 0.8}N$/GaN MQWs in Figure 2.24. The thicknesses of bottom and top InGaN QWs and GaN barriers in SC design with $In_{\sim 0.1}Ga_{\sim 0.9}N$/GaN heterostructures were measured to be 2.6±0.2 nm and 12±0.2 nm. Similarly, the top and bottom InGaN QWs and GaN barriers have thicknesses of 2.5±0.2 nm and 8.3±0.3 nm in SC design with $In_{\sim 0.2}Ga_{\sim 0.8}N$/GaN heterostructures.

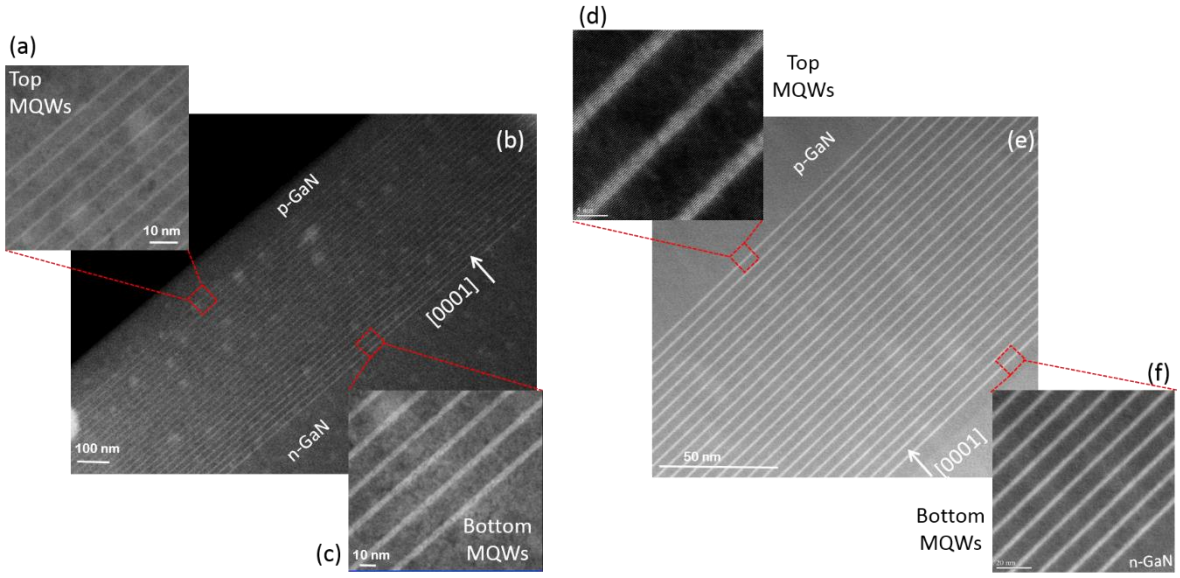

Figure 2.24 HAADF-STEM images of (a) top MQWs (b) the complete active region and (c) bottom MQWs in SC design with $In_{\sim 0.1}Ga_{\sim 0.9}N$/GaN MQWs, and (d) top MQWs (e) the p-i-n stack and (f) bottom MQWs in SC design with $In_{\sim 0.2}Ga_{\sim 0.8}N$/GaN MQWs.

On the other hand, for the 3rd generation SC design with $In_{\sim 0.3}Ga_{\sim 0.7}N$/GaN MQWs, Figure 2.25 (a) and (b) reveal some structural defects such as local thinning of InGaN QWs and an initiation of a threading dislocation and eventual 3D growth of the InGaN/GaN structures on the

dislocation site. The average thickness of InGaN QWs and GaN barriers were estimated to be 2.6 nm and 8.2 nm. However, it is important to notice that the average fluctuation of well widths can reach up to 4-5 monolayers (ML), where 1 ML=0.259 nm for GaN. It was reported that for an InGaN/GaN MQW system with In fraction of 0.25 and well thickness of 3.3 nm, one monolayer change can lead to energy band gap change of 58 meV and cause carrier localization by potential fluctuations in the MQW region [134]. In addition, the EDX analysis shown in Figure 2.25 (c), exhibits variation of In composition between 20% and 24% in this structure.

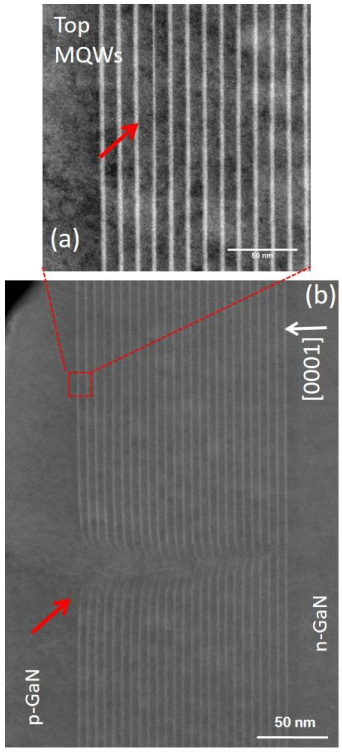

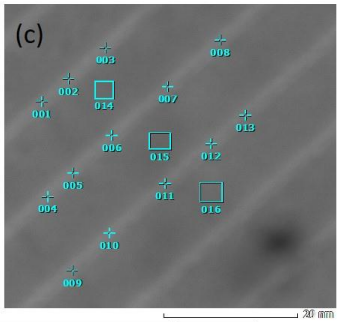

EDX Line	Atoms (%) Ga	In
1	78	22
2	77	23
3	75	25
4	75	25
5	77	23
6	76	24
7	77	23
8	78	22

EDX Line	Atoms (%) Ga	In
9	75	25
10	80	20
11	78	22
12	77	23
13	79	21
14	100	0
15	100	0
16	100	0

Figure 2.25 For the 3rd generation SC design with $In_{\sim 0.3}Ga_{\sim 0.7}N$/GaN MQWs: HAADF-STEM images of (a) top MQWs (b) the complete active region with a defect, and (c) evidence of In fluctuation with EDX. Table inset: Analysis of atomic concentration of In and Ga analysis for the corresponding EDX features.

As a result of the thickness measurements by high-resolution STEM analyses, the indium content was derived as 10%, 19% and 24% for the 3rd generation SCs designs. The ω/2Θ XRD scans of SC designs around (0004) are presented in Figure 2.26. The period thickness is measured as 14.6±0.2 nm, 10.7±0.2 nm and 10.8±0.2 nm for designs having $In_xGa_{1-x}N$/GaN MQWs with x=0.10, x=0.19 and x=0.24, respectively. The large difference in period thicknesses of the designs with x=0.10 and those of designs with richer In, explains the different periodicity of the XRD scans. In addition, the relative broadening of the satellite peaks in the XRD scans as a function of increasing In contents, reveals the degradation in crystalline quality due to defects and In content fluctuations for richer In InGaN/GaN MQWs.

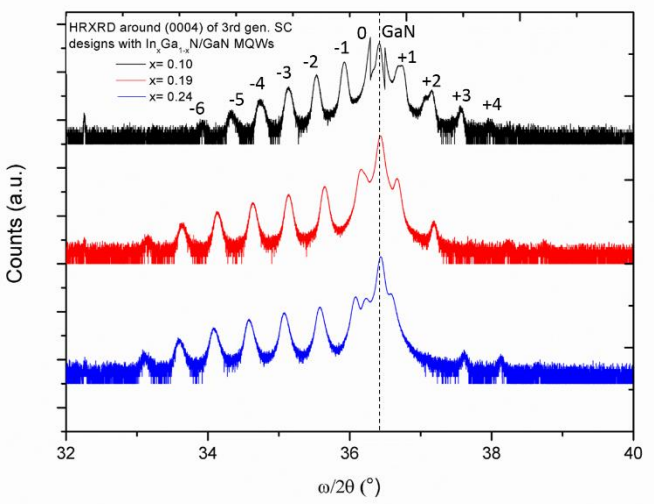

Figure 2.26 Comparison of ω/2Θ scans around (0004) reflections of the 3rd generation solar cells having $In_{\sim 0.3}Ga_{\sim 0.3}N$/GaN MQWs.

2.3.2.2 Assessment of surface quality by AFM analysis

Moreover, the surface quality of the 3rd SC designs was evaluated by AFM analyses. Figure 2.27 show representative 5×5 μm² AFM topographical images of the 3rd generations SC designs. The rms surface roughness values of 0.45 nm, 3.5 nm and 5.6 nm were recorded for SC designs having $In_xGa_{1-x}N$/GaN MQWs with x=0.1, x=0.19 and x=0.24, respectively. The calculated dislocation densities were also approximately 2.5×10^8 cm^{-2}, 3.1×10^8 cm^{-2}, and 3.6×10^8 cm^{-2}, respectively. The degradation in crystalline quality is confirmed by the increase in rms surface roughness as well as the dislocation density as a function of the In composition.

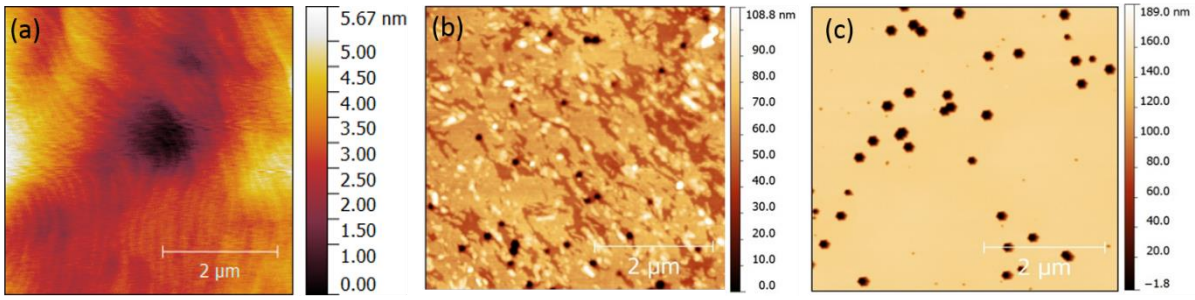

Figure 2.27 Representative AFM images of 5x5 μm² areas on the 3rd generation SC designs having 25 pairs of $In_xGa_{1-x}N$/GaN MQWs with (a) x=0.1, (b) x=0.19, and (c) x=0.24.

2.3.2.3 PL Analysis

Room temperature PL spectra of 3rd generation SC designs are exhibited in Figure 2.28. A redshift in peak emission wavelengths is clearly seen as the In content increases in the SC design. The peak emission energies are 3.1 eV, 2.58 and 2.33 eV for the designs with x=0.1, x=0.19 and x=0.24, respectively. It is remarked that as the fraction of In increases, the intensity

of the PL emission is reduced and the FWHM of the peaks increases, due to higher defect density, compositional fluctuations and carrier localization effects in richer In structures. In addition, Figure 2.28 provides a comparison of PL spectra of the 2nd and 3rd generation SC designs with $In_{0.24}Ga_{0.76}N$/GaN MQWs with t_W=3.1 nm and t_W=2.5 nm. The red shift of emission energy of about 50 meV and drop in PL emission efficiency in the former structure can be explained by reduction in the overlap of the electron and hole wavefunctions. As a result, for the thicker InGaN wells the QCSE effect is more pronounced. In addition, the FWHM of the PL peak increases significantly as the well thickness is increased, indicating a degradation in the crystalline structure, which is also confirmed by the higher rms surface roughness in the AFM analyses.

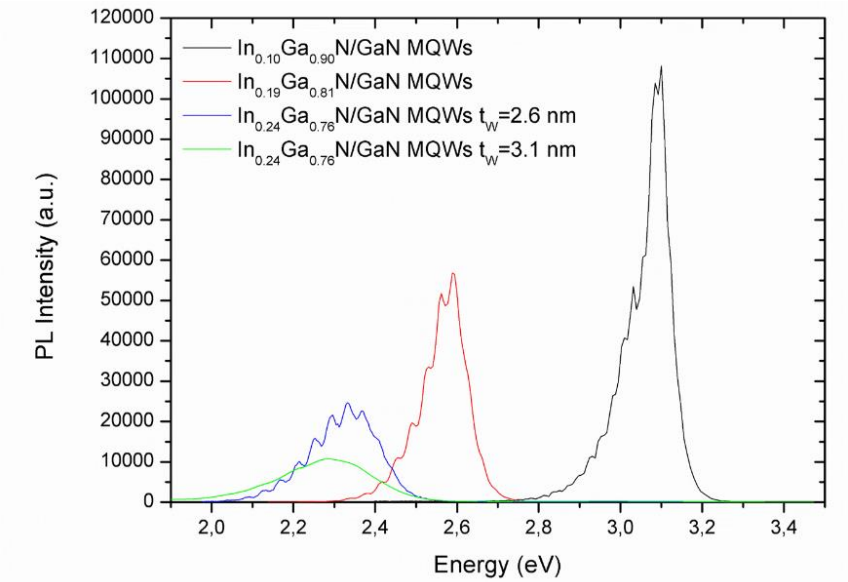

Figure 2.28 Room temperature PL spectra for 3rd generation SC designs having $In_xGa_{1-x}N$/GaN MQWs with x=0.10, 0.19 and 0.24, and 2nd generation SC design with n=25, t_W=3.1 nm $In_{0.24}Ga_{0.76}N$/GaN MQWs.

As a conclusion, the HRXRD, STEM, AFM and PL analyses have presented a comparison of structural quality of 3rd generation SC designs with respect to the In content. The $In_xGa_{1-x}N$/GaN MQWs, x from 0.1 to 0.24, have been shown to exhibit fully pseudomorphic growth on GaN layers. Table 2.4 summarizes the structural parameters such as the estimated In content, thickness of InGaN wells (t_{WELL}) and GaN barriers ($t_{BARRIER}$), as well as the roughness, PL emission peaks and the FWHM of the corresponding PL peaks. It is clearly seen that as the In content increases, the structural quality degrades, which would deteriorate significantly the SC performances.

Table 2 4 Structural parameters of 2nd and 3rd generation solar cells obtained from HRXRD, STEM, AFM and PL analyses.

x, content of In	Thickness of one period (nm)	t_W (nm)	t_B (nm)	RMS surface roughness by AFM (nm)	RT PL emission peak (eV)	FWHM of the RT PL peak (meV)
0.1	14.6	2.6	12	0.45	3.1	92
0.19	10.7	2.5	8.3	3.5	2.58	114
0.24	10.8	2.6	8.2	5.6	2.33	178
0.24	11.4	3.1	8.3	6.4	2.28	263

When 2nd and 3rd generation SC designs with identical In content, i.e. x=0.24, are compared in terms of PL and AFM analyses, the improvement in structural quality in 3rd generation SC design, with thinner quantum wells, is easily noticed. In addition, it is remarkable to preserve the integrity of high numbers of InGaN/GaN MQWs for such high In contents. Nevertheless, fluctuations in well widths and/or in indium composition within the wells, which were observed for this design, can favor the localization of carriers and cause eventual trapping of the carriers in the PV devices [51]. On the other hand, it is worth noting that only InGaN based SCs with more than 20% In can provide unreachable bandgaps by traditional PV devices, i.e. E_g > 2.4 eV. In addition, thicker total active region, i.e. higher numbers of MQWs, is necessary to obtain efficient absorption of photons. This study reveals that it is highly challenging to achieve defect free and high number of pairs of InGaN/GaN MQWs with attractive In content, i.e. x>0.19.

2.3.4 Study of crystalline quality for different types of substrate

The 4th generation solar cell designs offer a comparison of crystalline quality for similarly grown samples as a function of substrate. The design of the solar cells, which include 25 pairs of $In_{\sim 0.15}Ga_{\sim 0.85}N$/GaN MQWs, grown on sapphire and bulk GaN substrates (from Sumimoto®) are presented in Figure 2.29 (a) and (b), respectively. The thickness of quantum wells and quantum barriers were targeted to be 2 nm and 5 nm, respectively. The thickness of GaN barrier was decreased from 10 nm to 5 nm. Young *et al*. reported two reasons to decrease the thickness of the GaN barrier [110]. Firstly, reducing the total thickness of the InGaN/GaN MQWs stack would facilitate to sustain a fully depleted active region and provide efficient drift transport. Secondly, decreasing $t_{BARRIER}$ increases significantly the tunneling rate of carriers, which is the dominant escape mechanism from InGaN quantum wells at room temperature [108].

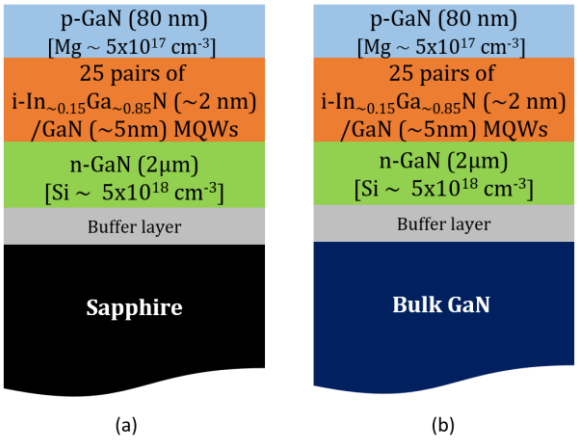

Figure 2.29 Schematic of the 4th generation SC designs with 25 pairs of $In_xGa_{1-x}N$/GaN MQWs with x~0.15 grown on (a) sapphire and (b) bulk GaN substrates.

2.3.4.1 Estimation of In content by HRXRD and STEM analyses

The HRXRD analysis was performed in double axis geometry, with Cu $K_{\alpha 1}$ radiation (λ=1.54056 Å) delivered by the double Ge (400) monochromator, similar to the analysis of the previous generation SC designs. Figure 2.30 (a) and (b) present the symmetric 0002 RSMs of both 4th generation SC designs, which do not exhibit any elongated broadening for the superlattice peaks due to faceted crystal. In addition, Figure 2.30 (c) and (d) display a vertical alignment of the GaN peak with the superlattice peaks, indicating fully pseudomorphic growth of InGaN/GaN MQWs on GaN layer in both samples. Consequently, the biaxial strain state can be assumed for both of the designs in this generation of SCs.

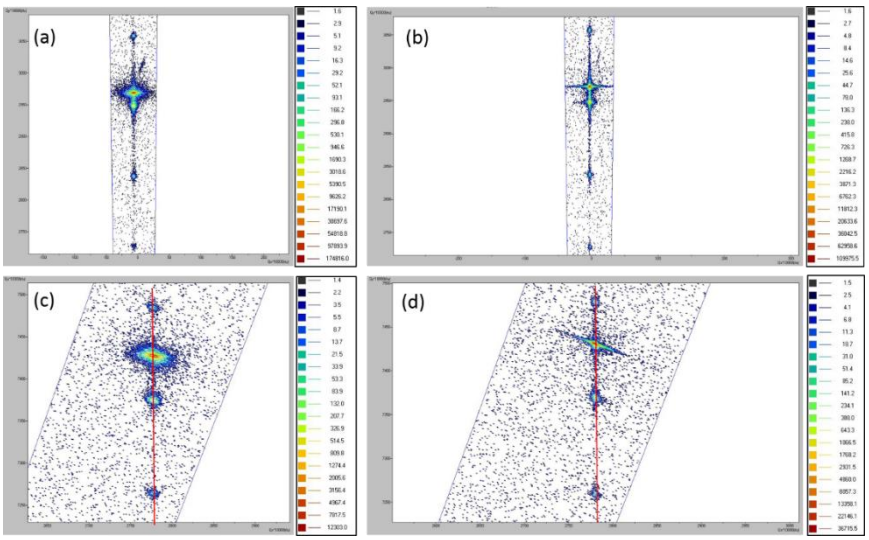

Figure 2.30 For the 4th generation SC designs: Symmetric 0002 RSM (a) at φ=0°for the design grown on sapphire, and (b) at φ=270° for the design grown on bulk GaN substrate. Asymmetric RSM around (10-15) reflections (c) at φ=0° for the design grown on sapphire, and (d) at φ=270° for the design grown on bulk GaN substrate.

The pseudomorphic growth of InGaN/GaN MQWs is also confirmed in HAADF-STEM images of SC designs grown on bulk GaN substrate in Figure 2.31 (c). The STEM analyses have been performed using a Cs-probe aberration corrected FEI Titan Themis TEM/STEM. The thickness measurements of top and bottom InGaN QWs and GaN barriers shown in Figure 2.31 (a) and (d) in SC design grown on bulk GaN substrate revealed that the well widths exhibit very low fluctuations, as seen in Figure 2.31 (b) and (e), respectively,. The average t_w and t_B are 2.5±0.2 nm and 4.5±0.3 nm, respectively. The thickness of one period is derived to be 7±0.2 nm from HRXRD analysis.

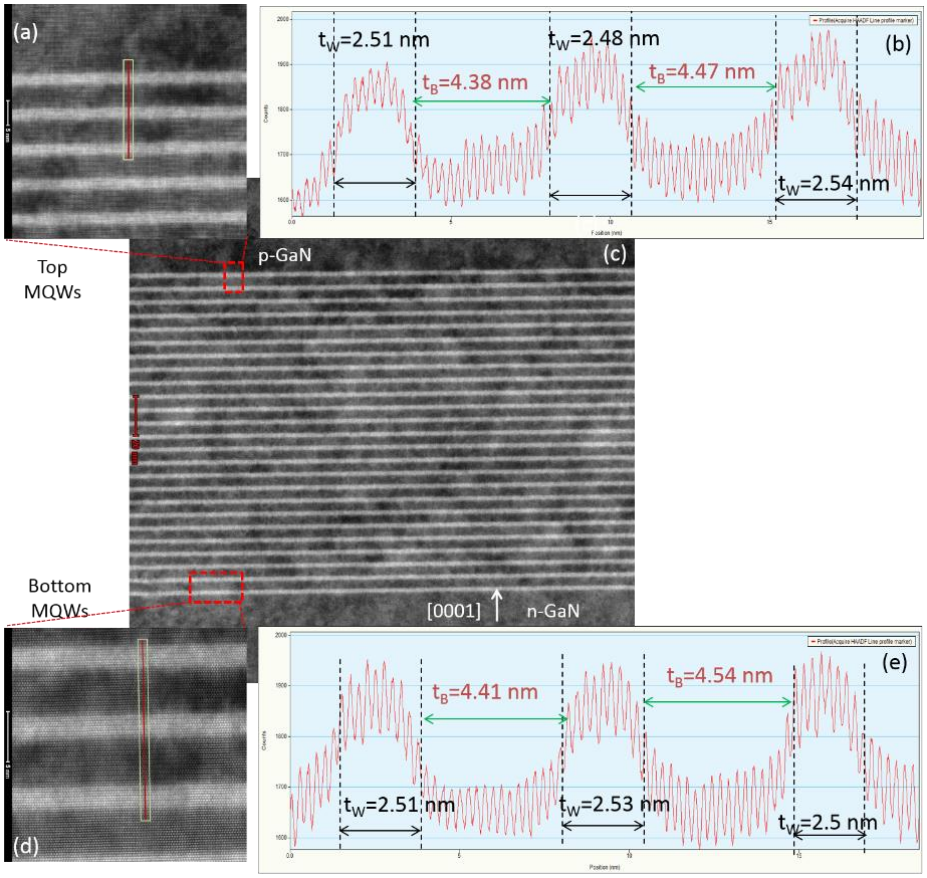

Figure 2.31 For the 4th generation SC design grown on bulk GaN: (a) HAADF-STEM images of top MQWs and (b) the corresponding thickness profiles of wells and barriers; HAADF-STEM images of (c) the p-i-n stack and (d) the bottom MQWs and (e) the corresponding thickness profiles of wells and barriers.

The Figure 2.32 (c) shows that the InGaN/GaN MQWs are grown pseudomorphically on GaN layer grown on sapphire substrate and the integrity 2D grown are well preserved in this structure. Slight variation in thickness of InGaN wells and GaN barriers on the top and bottom MQWs are presented in Figure 2.32 (b) and (e). The average t_w and t_B are deduced to be 2.2±0.2 nm and 4.8±0.3, respectively. For this design, the thickness of one period is calculated to be 7±0.2 nm from the HRXRD analysis.

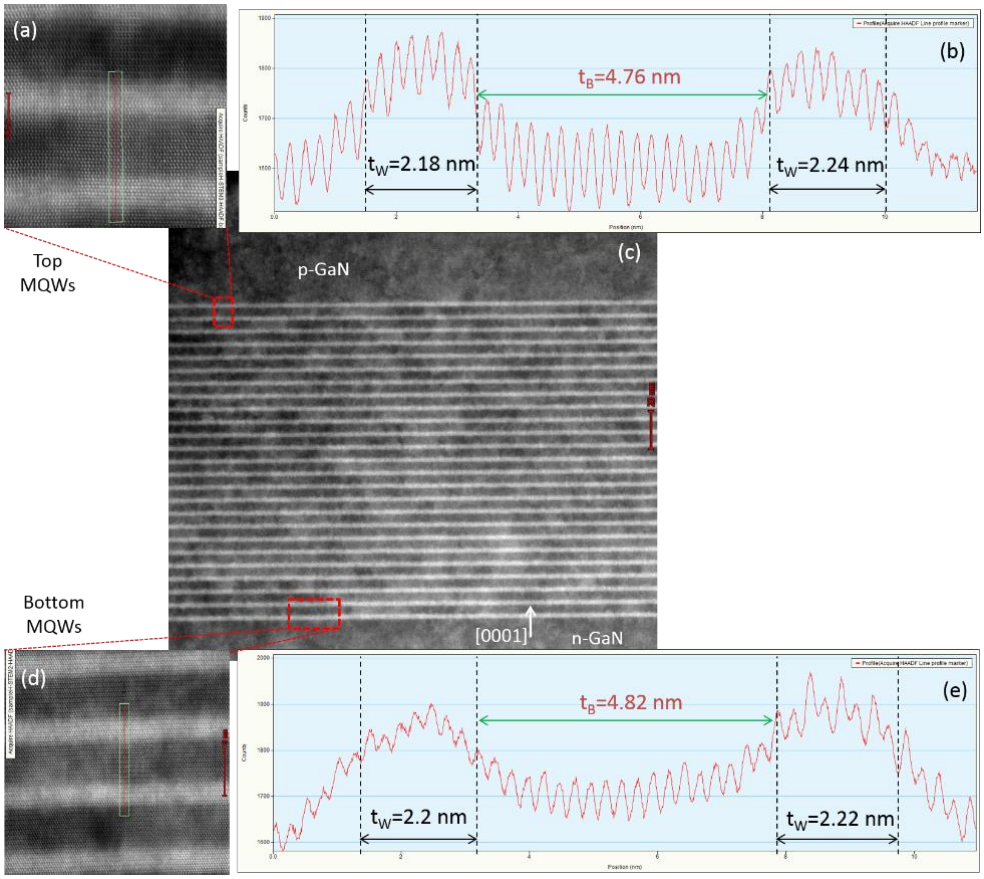

Figure 2.32 For the 4th generation SC design grown on sapphire: (a) HAADF-STEM images of top MQWs and (b) the corresponding thickness profiles of wells and barriers; HAADF-STEM images of (c) the p-i-n stack and (d) the bottom MQWs and (e) the corresponding thickness profiles of wells and barriers.

In the light of the thickness measurements by the STEM analyses, the In contents were anticipated to be 15% for both designs by XRD simulations. The fitting of the experimental and simulation curves are presented in Figure 2.33. The broadening of the peaks from the experimental scans with respect to the simulations indicates the presence of structural defects such as threading dislocations as well as the fluctuations in indium composition and thickness of InGaN wells and GaN barriers. It is important to note that XRD analysis performed in double geometry is more sensitive to detect the crystalline defects unlike the STEM analysis, which represents highly local elemental and structural analyses of the samples.

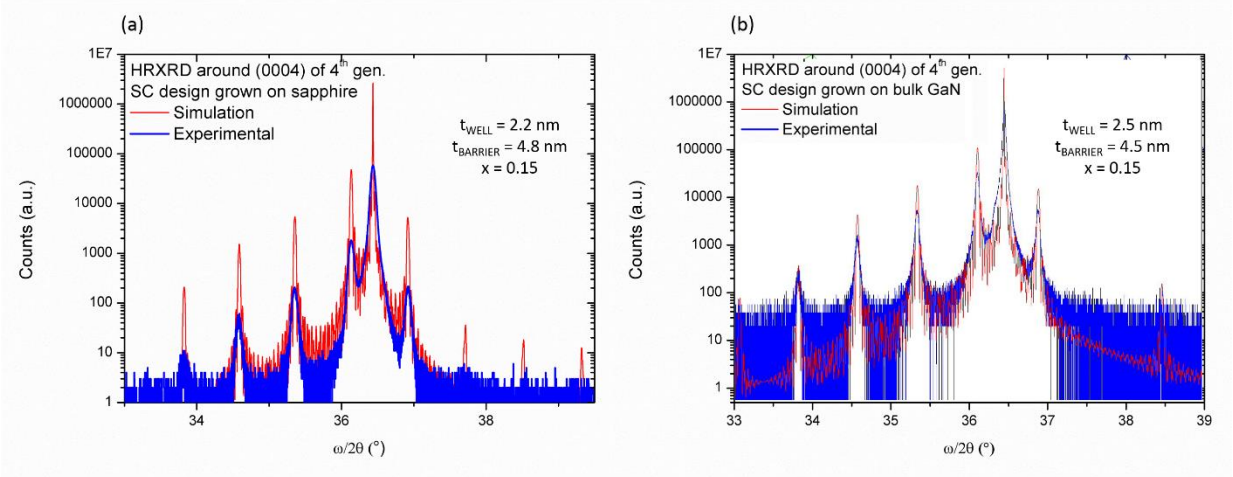

Figure 2.33 Experimental ω/2Θ scans around (0004) reflections of the 4th generation SC designs grown on (a) sapphire, and (b) bulk GaN substrate and their corresponding XRD simulation curves.

Furthermore, as it has been already mentioned in the 1st chapter, InGaN alloy possesses a very large miscibility gap, which can cause formation of In-rich clusters within the material. Even though small scale statistical fluctuations are expected in any random ternary alloy, In-rich clusters were supposed to have size of 1-3 nm and exhibit a large compositional variation from the nominal In content, which gets more pronounced for richer In layers. [135]. However, the existence of In-rich clusters in as-grown InGaN alloys is still under debate since they are very challenging to be precisely detected. Smeeton *et al*. suggested that exposure to an electron beam with 200 keV or more could cause irreversible irradiation damage in the InGaN alloy and cause formation of In-rich clusters [136]. Similarly, introduction of inhomogeneous strain due to formation of In-clusters only after 20 seconds of e-beam irradiation was reported [137, 138]. Thus, the existence of In-clustering in as-grown InGaN has been shown to be challenging with standard STEM used for imaging.

In this study, similar interesting phenomenon has been observed after 2 minutes of exposure to e-beam of 200keV, which is presented in Table 2.5. The BF-STEM images, which are sensitive to phase and diffraction differences, show large contrast after irradiation in both samples. The inhomogeneity of strain could be associated indeed with the electron beam induced formation of new phase in the material, which can be In-rich clusters. On the other hand, the corresponding HAADF images do not reveal these local contrasts in a pronounced manner. However, it is important to note that this study presents preliminary results that need further investigation.

Therefore, it is significant to bear in mind that genuine In content of the materials is not trivial to distinguish by STEM analysis with more than 200 keV electron-beam. An additional

method such as STEM analysis below the knock-on threshold voltage or three dimensional atom probe (3DAP) [139] can be employed for investigating local compositional variations in InGaN alloy.

Table 2.5 HAADF-STEM and BF-STEM micrographs of 4th generation SC designs before and after 2 minutes exposure to 200keV electron beam exposure.

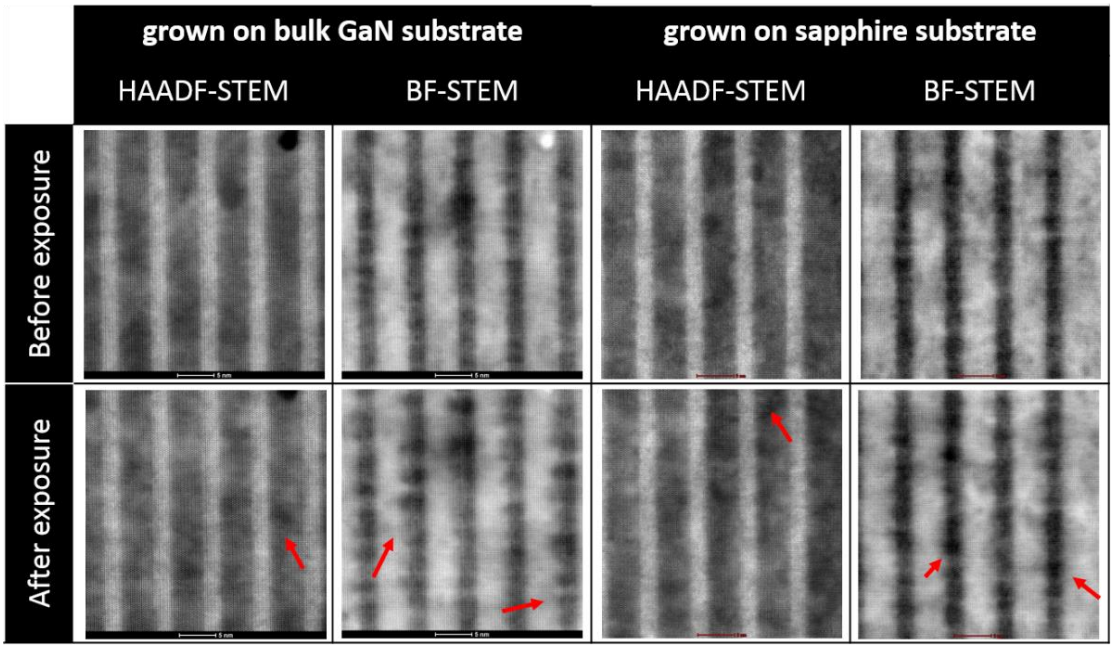

2.3.4.1 Assessment of surface quality by AFM analysis

The AFM analysis provides structural information from a larger scale area on the samples. Figure 2.34 presents the AFM images taken at different regions of 4th generation SC designs grown on sapphire and bulk GaN substrates. Figure 2.34 (a) and (b) display very similar rms surface roughness and surface quality for samples grown on sapphire. The average rms surface roughness and approximate density of dislocation for this sample have been derived as 3nm and 2.7 $\times 10^8$ cm^{-2}, respectively. On the other hand, AFM analyses at different parts of the un-processed samples grown on bulk GaN substrates have revealed inhomogeneous surface roughness and quality. As a result, an average rms surface roughness of 3.8 nm and approximate dislocation density of 2.8 $\times 10^8$ cm^{-2} have been measured.

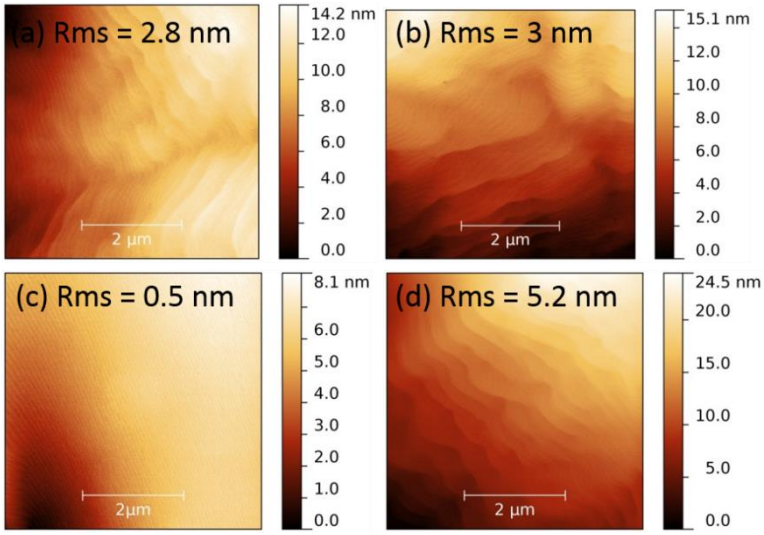

Figure 2.34 AFM images of 5x5 µm² areas on the 4th generation SC designs grown on (a),(b) on sapphire substrate; and (c), (d) on bulk GaN substrate.

2.3.4.1 PL Analysis

Room temperature PL spectra of 4th generation SC designs (analysis done at the center of the wafers) are exhibited in Figure 2.35. The peak emission energies are 2.883 eV and 2.857 eV; for the designs grown on sapphire and bulk GaN substrates, respectively. The FWHM values of the PL peak of the structure grown on sapphire, i.e. 83 meV, is slightly lower than that of the grown on bulk GaN, i.e. 87 meV. Even though the In contents are exactly the same in two designs, there exists a slight difference between the peak emission energies, i.e. 26 meV. By taking into account the similar crystalline quality and equivalent homogeneity in well thicknesses as well as the In contents in the InGaN/GaN MQWs; the origin of this redshift in the peak emission wavelengths for the design grown on bulk GaN substrate can be explained by more pronounced QCSE effect due to its thicker InGaN wells. This can be also confirmed with the slight drop in the PL intensity and relatively higher FWHM of the PL peak for this structure compared to the design grown on sapphire. Therefore, the PL analysis agree with the AFM observations, which has indicated a better crystalline quality for the SC design grown on sapphire by relatively lower rms surface roughness. On the other hand, the design grown on bulk GaN could show higher short current density owing to its thicker active region and slightly lower absorption cut off.

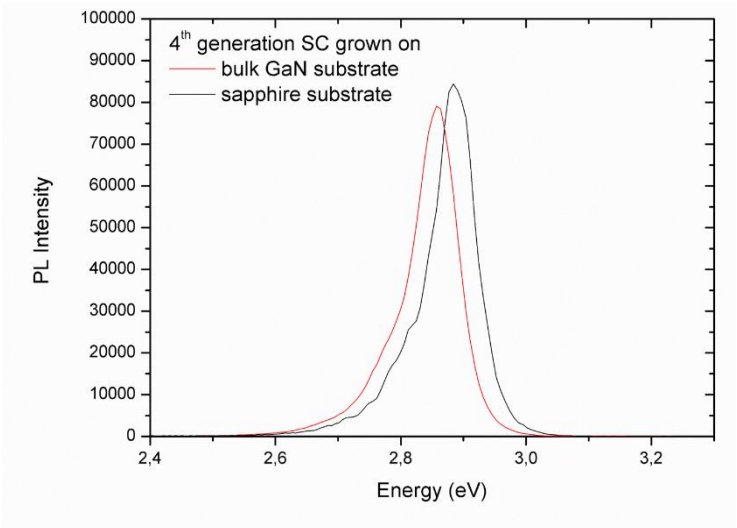

Figure 2.35 Room temperature PL spectra for 4th generation SC designs having 25 pairs of $In_{0.15}Ga_{0.85}N$/GaN MQWs grown on sapphire and bulk GaN substrates.

Table 2.6 presents a summary of structural parameters such as estimated In content, thickness of one SL period as well as the thickness of InGaN wells (t_W) and GaN barriers (t_B). Even though STEM analyses have exhibited very similar and high quality epitaxial growth on both substrates, AFM and PL analyses have revealed that the structures grown on GaN substrates exhibit slightly higher dislocation density and surface roughness compared to the ones grown on sapphire.

Table 2.6 Structural parameters of 4th generation solar cells obtained from HRXRD, STEM and AFM analyses.

Type of substrate	x, content of In	Period thickness (nm)	t_W (nm)	t_B (nm)	RMS surface roughness (nm)	PL emission peak energy (eV)	FWHM of the PL peak (meV)
Sapphire	0.15	7.0	2.2±0.2	4.8±0.3	3	2.883	83
Bulk GaN	0.15	7.0	2.5±0.2	4.5±0.3	3.8	2.857	87

In addition, it is significant to note that the surface characteristics of the structure grown on bulk GaN is very inhomogeneous. In the literature, InGaN/GaN MQWs grown on bulk GaN substrates have shown superior growth quality and very low dislocation density in the orders of 10^6 cm^2 as a result of homoepitaxial growth [101, 110]. On the other hand, these studies have not reported on the homogeneity of the structural and PV characteristics of the devices grown on bulk GaN substrates. However, in our study, this was a first attempt to grow InGaN/GaN heterostructure on this new type of substrate and the growth parameters are not fully optimized. Further electrical information such as spectral response by EQE analysis and photovoltaic performance of these designs would give more idea about this generation of solar cells.

2.4 Conclusions

This chapter presents a summary of material characterization of InGaN based solar cell with respect to different design parameters by means of HRXRD, STEM, EDX, AFM and PL analyses. The main motivation axis of the material analysis is centered around the investigation of the crystalline quality of InGaN alloy having more than 20% indium, which can provide E_g>2.4 eV and serve as a candidate material system for integration with the mature PV technologies. Nonetheless, achieving decent growth quality of In rich InGaN alloys, which can be fabricated into fully functional solar cells is highly challenging due to major issues explained earlier in the previous chapter, i.e. large lattice mismatch, phase separation and In fluctuation in the InGaN layers, etc. Therefore, the material characterization and optimization of the active region are key parameters to reach high quality InGaN epilayers. Consequently, each set of samples, i.e. generations of solar cell designs, were studied in terms of their material properties as a function of different design parameters, such as the indium content, the thicknesses and the characteristic features of the active region and the type of the substrate. However, due to the limited number of available samples, namely because of their high growth costs, many of the parameters had to be simultaneously altered among the generations and hence this study does not exhibit complete comparison of structural and optical parameters. Nevertheless, we believe that this work includes many enlightening information about the structural quality of In-rich InGaN layers and presents coherent results in agreement with the literature.

Table 2.7 provides a summary of the material characterization results and characteristic features such as the estimated indium content, *x*, the number of InGaN/GaN MQWs pairs, *n*, the measured thickness of InGaN wells, t_W, the hickness of GaN barriers, t_B, and the type of the substrate in each generations of SC designs. The 1st generation of SC designs provided valuable evidence about the crystalline quality of bulk 200 nm thick InGaN layers with x~0.3 as the active region. Two significant disadvantages have been observed in our case: very high dislocation density and phase separation within the InGaN layer. This showed that such thick InGaN layers are not suitable to be used in solar cell applications. As an alternative, InGaN/GaN MQW heterostructures were adopted for the active regions of the 2nd generation SC designs, where few nanometers of InGaN epilayers were embedded between relatively thicker GaN barrier layers.

Table 2.7 Structural and optical parameters of all generations of solar cell designs such as fraction of Indium, *x*, number of pairs of InGaN/GaN MQWs, n, thickness of InGaN wells, t_W, thickness of GaN barriers t_B, type of the substrate, rms surface roughness by AFM, room temperature PL emission peak, and FWHM of the PL peak.

Generation of solar cell designs	The design parameter to be studied	Characteristics of the active region					Rms surface roughness by AFM (nm)	RT PL emission peak (eV)	FWHM of the PL peak (meV)
		x	*n*	t_W *(nm) (±0.2)*	t_B *(nm) (±0.3)*	Type of the substrate			
1	The nature of the active layer	~ 0.32	200 nm **bulk** InGaN layer			Sapphire	28	2.25	900
2	Thickness of InGaN quantum wells, t_W	~ 0.28	35	**mixed**	mixed	Sapphire	41	2.23	288
		0.24	25	**3.1**	8.3	Sapphire	64	2.28	263
3	Indium content in the InGaN layer	**0.1**	25	2.6	12	Sapphire	0.43	3.1	92
		0.2	25	2.5	8.3	Sapphire	3.5	2.58	114
		0.3	25	2.6	8.2	Sapphire	5.6	2.33	178
4	Type of the substrate	0.15	25	2.2	4.8	**Sapphire**	8.3	6.4	2.28
		0.15	25	2.5	4.5	**Bulk GaN**	3.8	2.857	87

By keeping in mind that, the critical thickness for the formation of misfit dislocations in $In_{\sim 0.3}Ga_{\sim 0.7}N$/GaN systems is only around 3-4 nm, two SC designs with $t_W \sim 4$ nm and $t_W \sim 3$ nm were analyzed. The SC designs with $t_W \sim 4$ nm exhibited great irregularities both in the indium content as well as in the thickness of quantum wells and barriers. It was found that the growth rate increased over time and resulted in elevated elastic strain and eventual plastic deformation in the structure. It was concluded that 4 nm of well width is already quite close to the critical thickness and it stimulates formation of mixed (2D and 3D) grown MQW heterostructures when growing high number of MQWs. On the other hand, pseudomorphic growth and less defect density were obtained for thinner wells, i.e. t_W=3.1 nm by targeting the same In content $x \sim 0.3$. However, this design also exhibited some local discontinuities in In content as well as structural defects such as thinning of QWs and/or formation of threading dislocations, which could initiate 3D growth.

The 3rd generation SC designs presented the influence of the In content on the structural quality of the InGaN/GaN heterostructures. The main conclusion is that the crystalline quality of the epilayers degrades significantly as a function of increasing the In content due to higher levels of strain between the InGaN and GaN. The SC design with x=0.1 showed the best structural quality meaning very low compositional and thickness fluctuations in addition to low dislocation density. However, this design is not really interesting for PV applications because of its relatively high absorption band gap, $E_g \sim 3.1$ eV. On the other hand, the design with x=0.19, which exhibited good crystalline quality, is a promising candidate for SC applications owing to its attractive band gap of around 2.5 eV. The well thickness can be further decreased to improve the growth quality, but in this case higher numbers of MQWs would be necessary for more efficient absorption.

The comparison between 2nd and 3rd generation SC designs with identical In content, i.e. x=0.24, revealed the effect of piezoelectric polarization and redshift of the emission peak wavelengths. It can be concluded that the well widths can be tuned to reach lower band gaps without the necessity of increasing In contents. However, it is also important to note that thicker wells threaten significantly the crystalline quality. Therefore, an important compromise between the well thickness and the growth quality should be established to reach the desired absorption band gaps, as reported by Redaelli *et al.* [140].

The last generation of SCs provided a comparison of crystalline quality between two different types of substrates, i.e. sapphire and bulk GaN. The surface characterization by AFM revealed an inhomogeneous quality for the structure grown on bulk GaN. In addition, relatively higher FWHM and thicker well thicknesses in this structure can indicate a slight degradation on the crystalline quality. However, the best evaluation would be provided with the electrical characterization and the photovoltaic performance of this generation of solar cells as shown in the next chapter.

Chapter 3

Fabrication and characterization of InGaN based solar cells

The fabrication of the solar cells was performed at IEMN Clean Room facilities. Briefly, the development of p-GaN/i-InGaN/n-GaN based solar cell includes Chlorine based dry mesa etching of the stack followed by formation of n-type and p-type ohmic metallic contacts. However, the greatest challenge in the device processing is to optimize each single technological step and then perform the most suitable process flow in order to achieve the best device performances. Another important challenge, which is specific to this study, is the limited number of samples (pieces of 2 inch wafers), due to high growth costs of unoptimized InGaN/GaN heterojunctions on sapphire (~2500€ /wafer) and on bulk GaN substrate (~3000€ /wafer). As a matter of fact, many of the samples from different generations of solar cell designs were used as tests for technology optimization, but were not transformed into fully functional devices.

In this chapter, the technological fabrication steps of InGaN based solar cells will be detailed in terms of challenges and solutions that were proposed in the optimization of the process parameters. Furthermore, the influence of p-type contacts quality on the device performances is investigated. Finally, comparison of electrical and photovoltaic characterizations of the solar cells as a function of the indium content in InGaN/GaN heterostructures as well as the type of the substrate are presented and discussed.

3.1 Processing steps of the solar cells

The typical device processing sequence for InGaN based solar cell is shown in Figure 3.1. This fabrication sequence was used to develop all InGaN solar cell structures in this work.

- ***Surface preparation of the wafers***

  The surface of the p-GaN/i-InGaN/n-GaN solar cell (Figure 3.1 (a)) is cleaned first by acetone and then isopropyl alcohol (IPA) in order to get rid of any organic contaminations. The sample is dried by nitrogen afterwards. Finally, the sample is heated to 150°C for 10 minutes to remove any moisture on the surface, which is called dehydration. This cleaning step is repeated prior to each photolithography process.

- ***Mesa etch***

  As shown in Figure 3.1 (b), a mesa etch is performed in order to define the size of the devices and expose the n-type GaN. This involves uniform spin coating of light sensitive photoresist on the wafer surface and then alignment and exposition with UV light (365 nm) of the photoresist through a mask, which is in hard contact with the substrate. The photoresist patterns, which are exposed to UV light, is removed away in the developer solution. For the mesa etch step, different types of photoresists are used and finally a SiO_2 mask approach has been adopted. The reasons and results will be detailed in the next section. After the development of the photoresist, low power (50 Watts) and low pressure (50 mTorr) O_2 based Reactive Ion Etching (RIE) is carried out for 30 seconds in order to get rid of some resist residues on the surface to be etched. Then, the stack is etched till the n-GaN using Cl_2/Ar based Inductive Coupling Plasma (ICP) by ICP-RIE etching tool (SI 500 Sentech tool or Oxford Plasmalab 80plus). Finally, the photoresist or SiO_2 mask is removed by hot (at 70°C) resist stripper solution (SVC14) or Buffered Oxide Etch (BOE) (7:1 H_2O: HF) solution, respectively. Following the removal of the photo resist, the wafers are cleaned by standard cleaning process, which involves soaking in acetone and then isopropyl alcohol (IPA), and drying by N_2 gas afterwards.

- ***Formation of the n-type ohmic contacts***

  A second photolithography pattern is created with 3.4µm thick bilayer photoresist structure including LOR10A and S1818, in order to deposit the electrical contacts to the n-type GaN, as shown in Figure 3.1 (c). Prior to metallization, the wafer undergoes some surface pretreatments. First the resist residues are etched away by O_2 based RIE etching (50W, 50mT) for 30 seconds. Secondly, the wafer is treated in the BOE7:1 solution for 1 minute in order to strip off the native oxide of GaN (or any existing SiO_2 layer) on the n-type GaN, which is basically *deoxidation*. Then, Argon based dry etching with a power of 200 eV is performed for 2 minutes in order to facilitate the adhesion of metal stack on the n-type layer. The deposition of Ti (12 nm)/Al (200nm)/Ni (40nm)/Au (100nm) is done by electron-beam evaporation technique in high vacuum environment. After the deposition, metal lift-off is carried out in hot SVC14 solution for 2 hours, followed by a treatment of ultra-sonic bath for 20 minutes. The wafer is finally cleaned with standard cleaning procedure. The formation of ohmic-contacts to n-GaN requires thermal annealing, which will be explained in next sections. Hence, the contacts undergo a rapid thermal annealing (RTA) at 850°C for 30 seconds in N_2 ambient.

3.1 Processing steps of the solar cells

- ***Formation of the current spreading layer***

  A third photolithography step by using 1µm thick bilayer photoresist structure LOR10A and S1805, is needed for the deposition and lift-off of a thin semitransparent current spreading layer of Ni/Au. Following the photolithography, O_2 based RIE etching (50W, 50mT, 30") and the BOE7:1 treatment for 1 minute, a thin layer of Ni (5nm) /Au (5nm) is deposited on p-type GaN by e-beam evaporation, as seen in Figure 3.1 (d). Prior to deposition of the layer, Ar based dry etching (power of 200eV for 2') is conducted. Subsequent to the lift-off process in hot SVC14 solution and the standard cleaning procedure of the wafers, Ni/Au layer is annealed at 500°C in air in order to get the best combination of highest transmittance and highest conductivity. The influence of time annealing of this thin layer upon its transmittance and the photovoltaic characteristics of the cells is discussed in the upcoming section.

- ***Deposition of the p-contact grids***

  A final photolithography step (1µm thick bilayer photoresists, i.e. LOR10A+S1805) is performed for the deposition of the interdigitated p-contact grids on top of the semitransparent Ni/Au current spreading layer. After the formation of photolithography patterns and O_2 based RIE etching (50W, 50mT, 30"), followed by dry etching with Argon (200eV for 2'), the deposition of metal stack of Ni (50nm)/Au (200nm) is carried out in an e-beam evaporator as shown in Figure 3.1 (e). The process is finalized by the lift-off in hot SVC14 solution and standard cleaning procedure of the wafer.

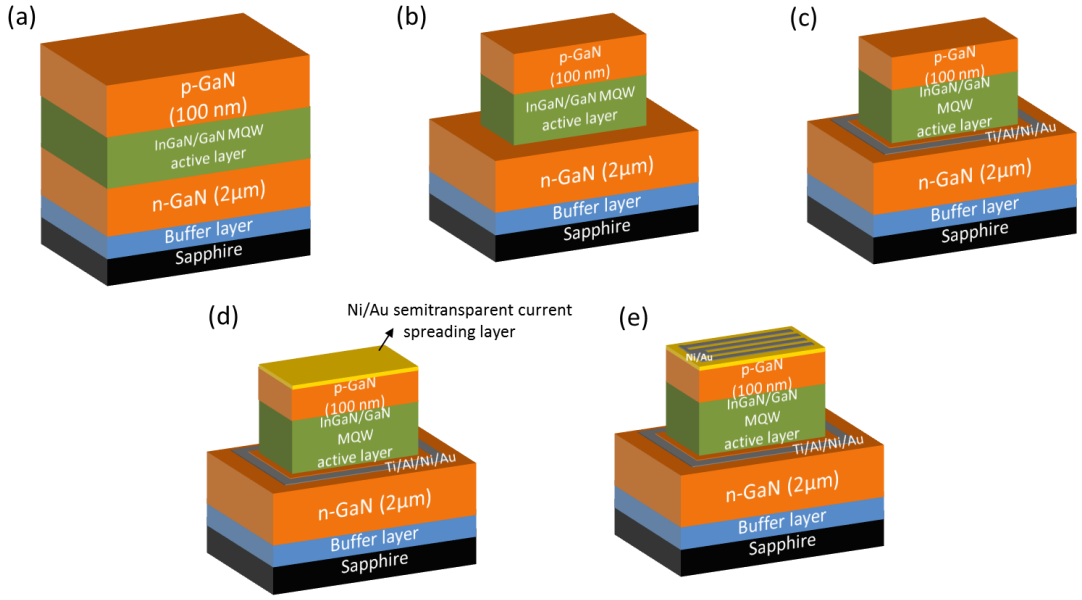

Figure 3.1 Fabrication process sequence for (a) a p-GaN/i-InGaN/n-GaN based solar cell including (b) mesa etch, (c) n-contact formation, (d) current spreading layer formation, and (e) p-contact grids deposition.

3.1 Processing steps of the solar cells

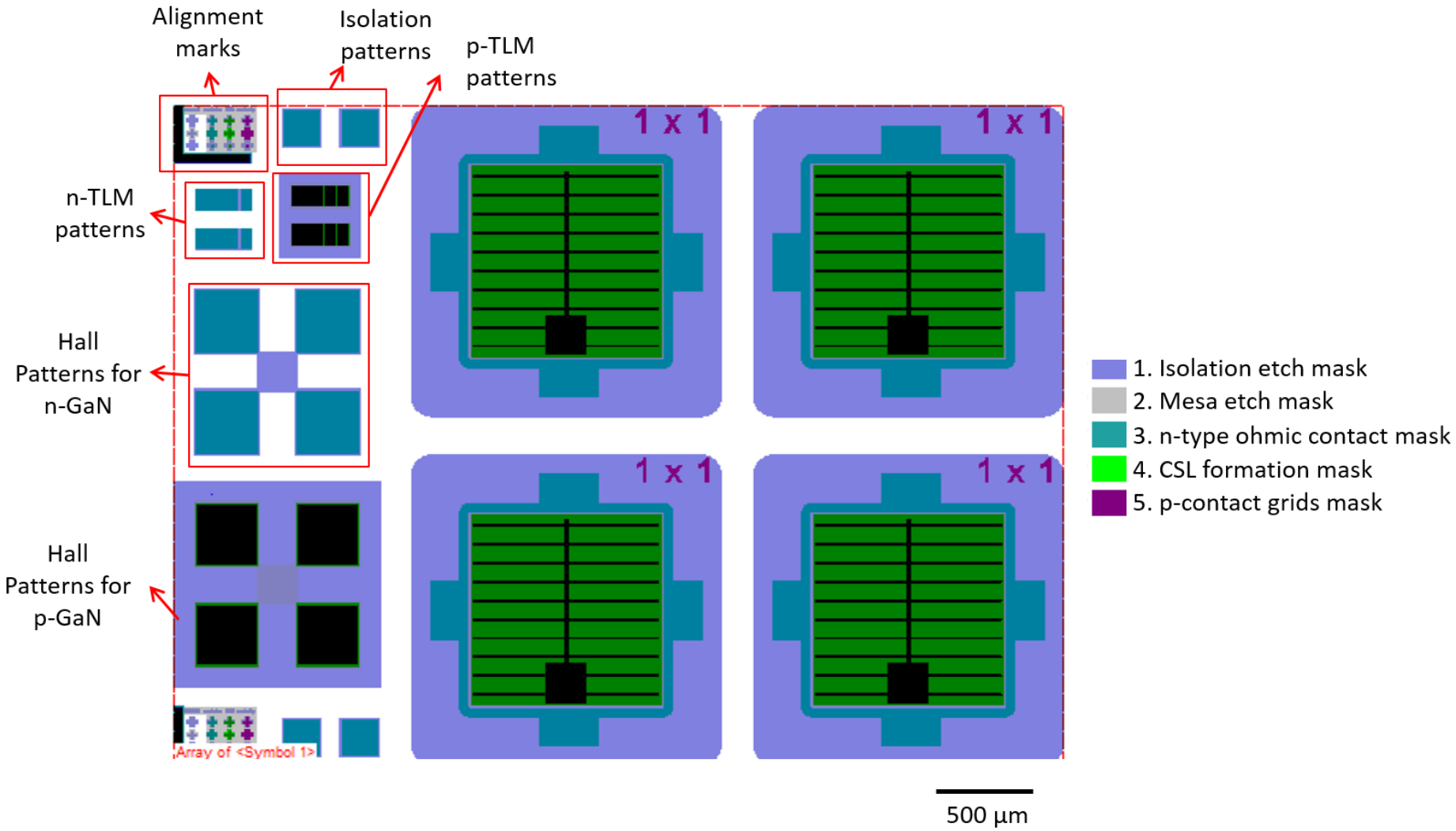

Figure 3.2 The description of the optical mask set used for the fabrication of the InGaN based solar cells.

A description of the mask set is presented in Figure 3.2. It includes 5 optical masks which are indicated in different colors as shown in the legend. The first mask is the isolation etch, which provides the isolation of the devices by etching till the insulating sapphire substrate. The isolation of the devices can also be verified by simple I-V characterization on the isolation patterns of 200×200 μm^2 with a separation distance of 100 µm after the deposition of the n-type ohmic metallic contacts. The second optical mask belongs to mesa etch step, which is used to expose the n-GaN and create mesas with the size of 1×1 mm^2. The third optical mask has been used for the formation of n-type ohmic contacts. This mask also allows measurement of the resistivity of the n-type contacts by Transmission length method (TLM). The rectangular n-TLM patterns with size of 100×50 μm^2 are separated from each other with interspacing distances of 2.5, 5, 10 and 20 µm. The fourth and fifth optical masks correspond to the technological steps of current spreading layer (CSL) deposition and the p-type contact grids. These masks enable determination of the resistivity of the CSL owing to the p-TLM patterns, which will be detailed in section 3.3.2.1. The p-TLM patterns have the same size and interspacing distances as the n-TLM patterns. In addition, the mask sets include Hall patterns which provide electrical characteristics of the layers such as carrier concentration, mobility and resistivity. Furthermore, in each process step, the alignment marks are used to align properly the wafer to the corresponding optical mask.

3.2 Device processing issues

In any device fabrication, the choice of right processing conditions is not trivial and therefore needs careful optimization. Since this thesis work was the first attempt to develop InGaN based solar cells at IEMN, no processing recipe was readily existing, except for the formation of the n-type ohmic contacts to n-doped GaN. Consequently, two critical steps were developed: the mesa etch of the InGaN/GaN stack and the formation of the current spreading layer for p-type contacts. In this part, the challenges in the development of InGaN based solar cells will be described and the solutions that were proposed will be detailed.

3.2.1 Mesa etch using SiO_2 mask

The mesa on GaN is formed by Cl_2/Ar based ICP etching which provides a good selectivity and high etching rate of the InGaN/GaN stack. ICP etching provides a combination of chemical and physical etching, which can achieve high etching rates despite the strong bond energy of III-Nitrides. ICP power determines the plasma density that influences the chemical

component of the etching, while RF power controls the energy of the ions that dominates the physical component of the etching. The parameters of the etching processes that were developed in two different ICP-RIE plasma etching tools, i.e. Sentech SI500 and Oxford Plasmalab, present at IEMN clean room facilities, are listed in Table 3.1. This indicates that the mesa etch of InGaN/GaN can be developed in any ICP-RIE plasma etch tool equipped with Cl_2 gas.

Table 3.1 The parameters of ICP assisted etching processes developed in two plasma etching tools in the clean room of IEMN.

ICP-RIE tool	ICP Power (W)	RF Power (W)	Gas flow (sscm)		Pressure (mT)	Temperature of deposition (°C)
			Cl_2	Ar		
Sentech SI500	150	50	5	15	5	20
Oxford Plasma lab 80plus	100	35	10	30	2	20

The etching rate of InGaN/GaN stack is around 125 nm/min and 80 nm/min in the etch processes developed in Sentech SI500 and Oxford ICP tools, respectively. The rate of etching increases slightly with increasing indium contents in InGaN. Table 3.2 summarizes the rate of etching of the different masks used in this process. In order to expose the n-GaN, a mesa etch of around 500-600 nm is necessary, which corresponds to a time of etching around 5 minutes and 8 minutes in Sentech SI500 and Oxford ICP tools, respectively.

Table 3.2 The rate of etching of $In_xGa_{1-x}N$/GaN stack with different In compositions and different masks by using Sentech and Oxford ICP-RIE tools.

ICP-RIE tool	Rate of etching (nm/min)			
	InGaN/GaN stack	Type of Mask		
		S1828	SPR	SiO_2
Sentech SI500	125	80	125	25
Oxford Plasmalab 80plus	80	40	75	10

The high plasma flux, which is generated to enhance the bond-breaking efficiency in nitrides, may have some adverse effects on the structure of the photoresist mask. Photoresists such as S1828 or SPR220 are polymer-based materials that can heat up and get burnt during an ordinary plasma etching process. In addition, their isotropic etch may lead to formation of slanted sidewall formation, which could cause re-deposition of the etched photoresist on the edges of the device.

After the etching process, the wafers were cleaned in the standard resist stripper solution (SVC14) at 70°C for 2 hours followed by cleaning in ultra-sonic bath. However, this cleaning procedure was found out to be insufficient by SEM characterization as seen in Figure

3.3 (a). It can be noted that increasing the time of cleaning treatment does not necessarily provide complete removal of the residues. The same wafer was then cleaned by using a basic resist stripper solution called EKC265, which is a stronger post-etch organic residue remover and known to etch some metals. The cleaning treatment involves soaking the wafers in already heated (at 65°C) EKC265 solution for 20 minutes and then cleaning with IPA and distilled water. Figure 3.3 (b) shows that the treatment with the EKC265 solution improved the residue removal considerably, but still not totally efficient to eliminate everything. Further cleaning in severe environment; i.e. heated ultra-sonic bath, does not provide complete cleaning either. However, the photoresist contamination on the sidewalls threatens the functionality of the devices to a great extent. Any thermal treatment in the following processing steps can cause immediate polymerization of the photoresist creating conductive residues between the p-type and the n-type materials. As a result, the solar cell suffers from high leakage currents through the sidewalls and eventual device failure.

Another approach to remove the redeposits of photoresist from the device edges is to perform an O_2 based ICP plasma etching subsequent to the mesa etching in Sentech tool. The plasma of 20sscm of O_2 with 150W ICP power, 10W RF power at pressure of 10mT was carried out for 5 minutes. In semiconductor processing, oxygen is frequently used to burn off the organic residues such as photoresists [141]. The high ICP power of the plasma can provide isotropic etching and burning of the resist on the sidewalls. As a matter of fact, Figure 3.3 (c) and 3.3 (d) display clean device edges after O_2 based ICP etching followed by cleaning in SVC14 solution. However, the wafers are still not resist-free; some residues are observed on top of the p-GaN close to the border. These remaining residues can diffuse and contaminate the sidewalls of the devices in any thermal annealing in the next technological steps.

In addition, 4.5µm thick monolayer SPR220 resists were also used as masks in mesa etching. Figure 3.4 (a) and (c) show the sidewalls of the devices after cleaning only in hot SVC14 solution. It is observed that the burnt resist is redeposited on the edges and standard cleaning cannot achieve efficient removal. Figure 3.4 (b) displays the results after cleaning in EKC265 which removed the residues significantly. Similarly, ICP assisted O_2 plasma etching following the mesa etching provides considerable amount of cleaning on the device edges as shown in Figure 3.4 (d). However, none of these techniques are efficient enough to afford complete cleaning of the redeposited residues which can eventually be at the origin of the device failure.

3.2 Device processing issues

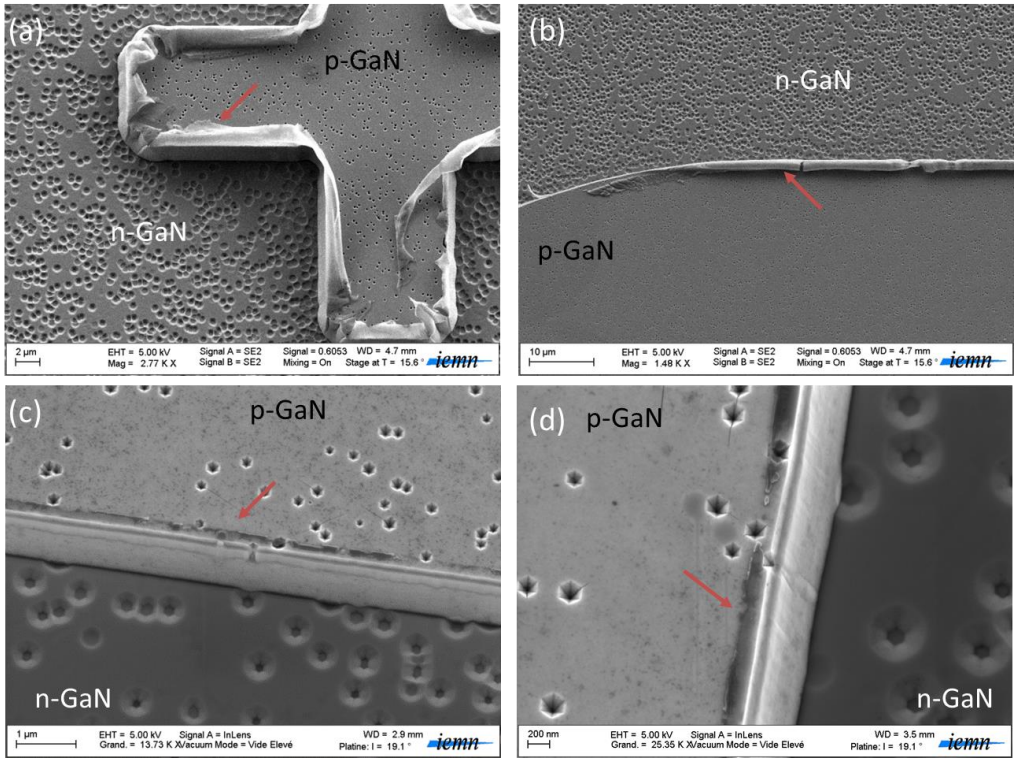

Figure 3.3 SEM images of the device sidewalls after ICP etching when using bilayer LOR10A+S1828 followed by (a) standard cleaning in SVC 14 solution at 70°C, (b) and cleaning of the same sample in EKC265 stripper solution at 65°C; (c and d) another etched sample cleaned with O_2 based ICP plasma treatment and then in SVC14 solution at different magnifications.

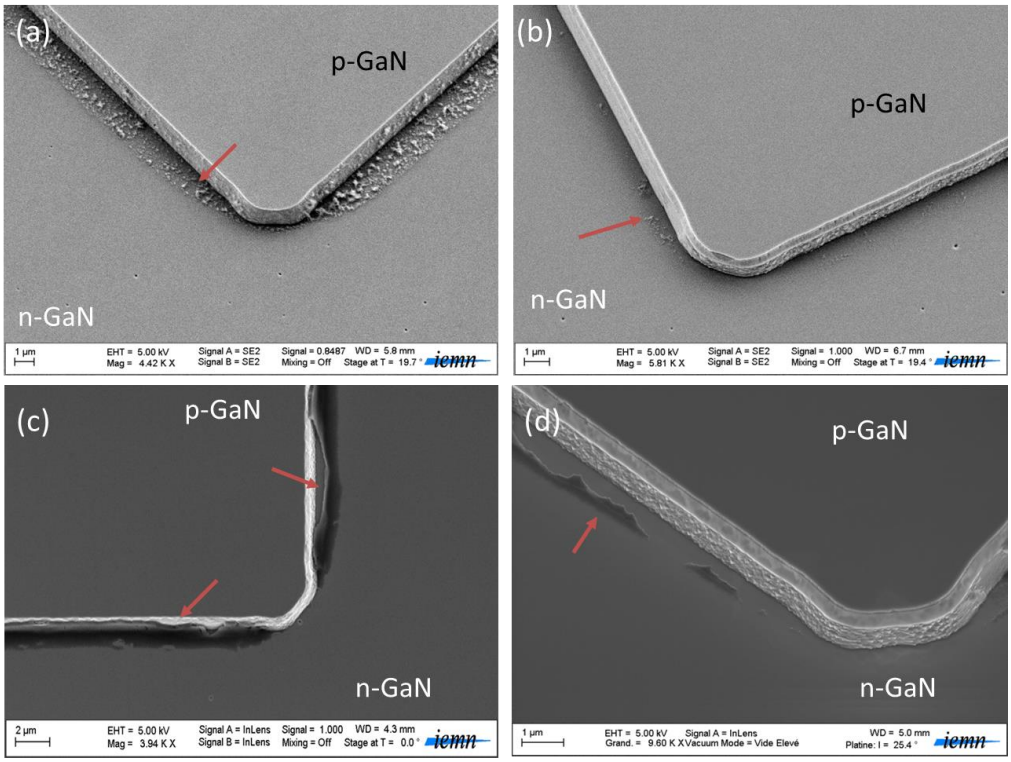

Figure 3.4 SEM images of the device sidewalls after ICP etching with monolayer resist SPR220 followed by (a) standard cleaning in SVC 14 solution at 70°C, (b) and cleaning of the same sample in EKC265 stripper solution at 65°C; another etched sample (c) cleaned only in SVC14 solution and (d) cleaned with O_2 based ICP plasma treatment and then in SVC14 solution.

3.2 Device processing issues

As a solution, the photoresist can be replaced by a SiO_2 mask. The preparation of the SiO_2 mask is explained hereafter.

1. Any native oxide or former contamination on p-i-n InGaN/GaN heterostructures is removed by deoxidation by using BOE7:1 solution.

2. 300 nm thick SiO_2 layer is deposited by Plasma-Enhanced Chemical Vapor Deposition (PECVD), parameters of which are summarized in Table 3.3.

Table 3.3 The parameters of deposition of SiO_2 layers by PECVD.

Precursors (sccm)		Pressure (mT)	RF Power (W)	Temperature of deposition (°C)
SiH_4	N_2O			
150	700	1000	20	340

3. Mesa etch pattern is defined by photolithography using 2.5µm thick S1828 photoresist.

4. O_2 based RIE etching is performed (20sccm/50 W/50 mT) for 30 seconds in order to get rid of resist residues on the surface to be etched.

5. Definition of SiO_2 mask is performed with SF_6 based RIE etching as shown in Figure 3.7(c). Laser end-point detection is used to monitor the etch-back of the SiO_2 layer, which provided selective etching of the dielectric but not the layer below, i.e. GaN. The etching rates of SiO_2 layer as a function of the RF power of the plasma are summarized in Table 3.5. In this work, the recipe with the highest etching rate is adopted.

6. Subsequent to SF_6 based dry etching of SiO_2, the top burnt resist is removed by strong O_2 plasma etching during 10 minutes (20sccm/100W/100mT). The wafer is cleaned in hot SVC14 solution afterwards.

7. Finally, the mesa etch is performed, in which the etching rate of SiO_2 was found to be 25nm/min. The selectivity with the SiO_2 mask was found to be 1:5.

8. After the ICP etch, the remaining SiO_2 mask can be easily removed by BOE7:1 solution. The etch rate of SiO_2 in BOE solution is around 100 nm/min. Figure 3.7(d) displays the wafer after mesa formation.

3.2 Device processing issues

Table 3.4 The etching rate of SiO_2 as a function of the RF power by SF_6 based Reactive Ion Etching.

Pressure (mT)	Gas flow of SF_6 (sscm)	RF Power (W)	Etching rate of SiO_2 (nm/min)
50	30	50	8
		100	30
		150	50

The SEM observation shown in Figure 3.5 revealed very smooth and contamination-free sidewalls when mesa etching is performed by using SiO_2 mask, for different generations of solar cell structures. In Figure 3.5 (a), where the SEM image of sidewalls from a non-tilted wafer is exhibited, it is noticed that the mesa etch is not completely anisotropic, which leads to slanted sidewalls. However, when the size of devices ($1mm^2$) is taken into consideration, the etching depth in horizontal direction (400nm) is negligible.

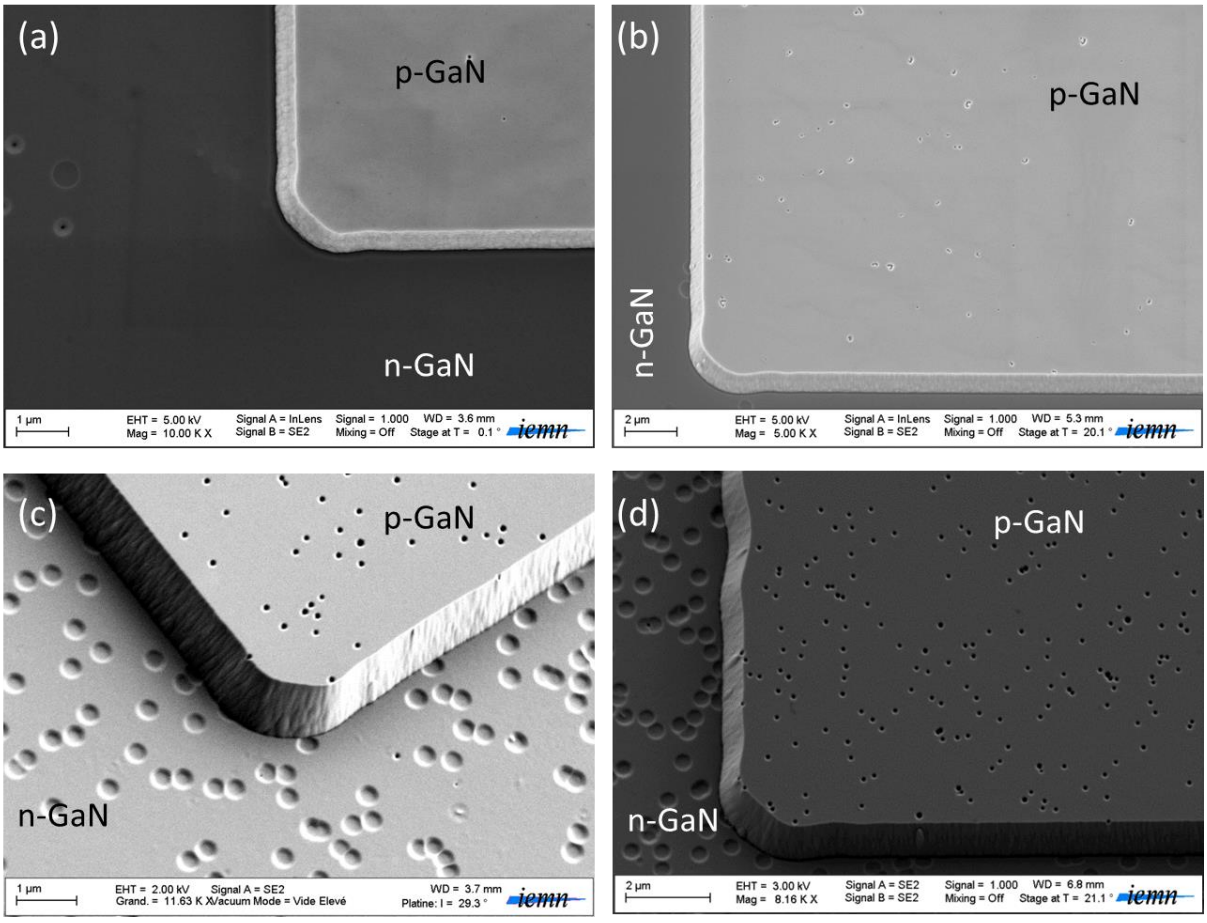

Figure 3.5 SEM images of the device sidewalls after ICP etching using SiO_2 mask of samples with (a) $In_{0.15}Ga_{0.85}N$/GaN MQWs grown on sapphire (b) $In_{0.15}Ga_{0.85}N$/GaN MQWs grown on GaN substrate (c) $In_{0.19}Ga_{0.81}N$/GaN MQWs grown on sapphire, and (d) $In_{0.24}Ga_{0.76}N$/GaN MQWs grown on sapphire.

As a result of the adoption of the SiO_2 mask in mesa etch step, the dependence of the reverse leakage current on device processing is eliminated. Figure 3.6 displays the measurement

of dark current as a function of the reverse bias, which is performed after the mesa etch of the solar cell structure with $In_{0.15}Ga_{0.85}N$/GaN MQWs on sapphire substrate. When the mesa etch was carried out by using the photoresist mask (LOR10/S1828 or SPR), the leakage through the conductive polymerized resist residues on the sidewalls generates very high dark currents (tenths of µA). On the other hand, in the case of etching with SiO_2 mask, the very low dark current under reverse bias (tenths of nA) reflects the resist-free sidewalls. As a matter of fact, the dark current generation is entirely due to the bulk contribution, which depends on the material quality. Figure 3.6 also indicates very low defect density in the solar cell structure with $In_{0.15}Ga_{0.85}N$/GaN MQWs grown on sapphire, leading to very low leakage currents. As a result, the optimization of this significant step of processing allows reliable assessment of photovoltaic characterization of devices as a function of the In content and the crystalline quality, which will be discussed in the next section.

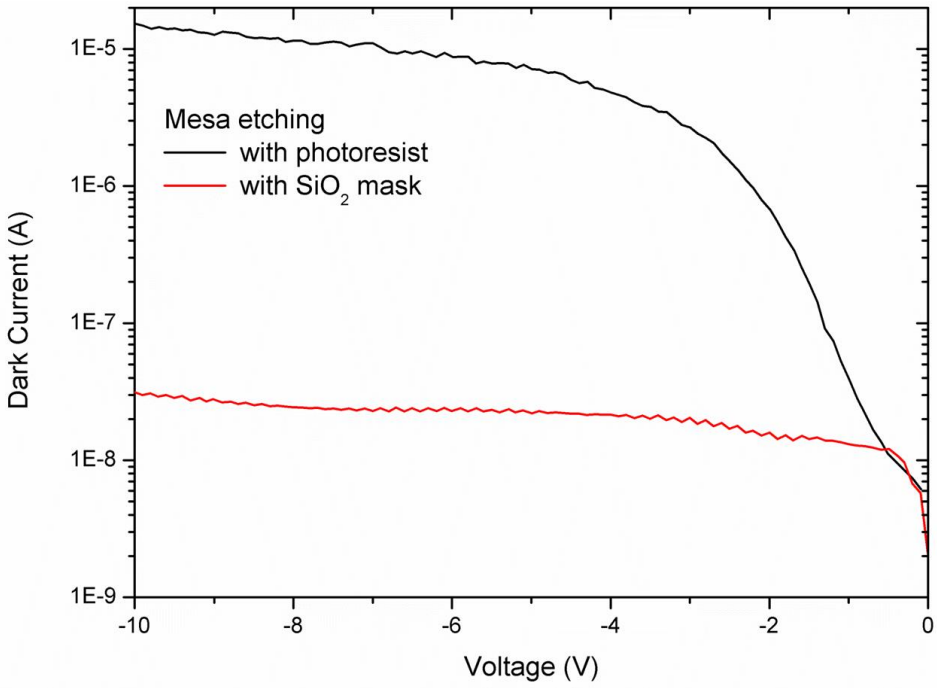

Figure 3.6 Comparison of dark current versus voltage under reverse bias performed after the mesa etching with photoresist and SiO_2 masks.

3.2.2 SiO_2 sidewall protection

Once formed with the mesa etch, the device sidewalls are always vulnerable to any contamination or re-deposition of the photoresists, which are required for patterning of the devices in the next technological steps. Residues of the resist, which cling to the sidewalls during any lift-off process, can get polymerized when the wafers are thermally treated, causing short circuiting of the devices.

An alternative processing sequence is developed including deposition of thin inert SiO_2 layers in the intermediate processing steps, in order to protect the device sidewalls from re-deposition of the residues. Figure 3.7 describes all the steps of this alternative fabrication process. Figure 3.7 (a) displays the patterning of a SiO_2 mask which is deposited by PEVCD for the isolation of the devices. Figure 3.7 (b) shows the isolated devices after the ICP etch and removal of SiO_2 mask. The same procedure is applied for mesa etching as mentioned in the previous section and shown in Figures 3.7 (c) and (d).

After the formation of the mesa, a thin sacrificial layer (50nm) of SiO_2 is deposited by PECVD as shown in Figure 3.7 (e) with the parameters indicated in Table 3.3. Prior to deposition of Ti/Al/Ni/Au metal stack for the n-contact, O_2 based RIE etching (50W, 50mT, 30") and a BOE7:1 treatment of 1 minute is needed to remove the SiO_2 protection layer by wet etching. This treatment also eliminates the native oxide of GaN and facilitates the formation of ohmic contacts on n-type GaN. Figure 3.7 (f) shows the wafers after the metal lift-off and formation of ohmic contacts by RTA, which is carried at 850°C for 30 seconds in N_2 ambient.

Similarly, the SiO_2 layer on top of the p-GaN is exposed by O_2 based RIE etching (50W, 50mT, 30") and BOE7:1 wet etching for 1 minute. Following the lift-off of thin Ni/Au current spreading layer, the wafer is subjected to thermal annealing in order to form semi-transparent Ni/Au layer as shown in Figures 3.7 (g). The device fabrication is finalized by the deposition of Ni/Au grids as seen in Figure 3.7 (h).

3.2 Device processing issues

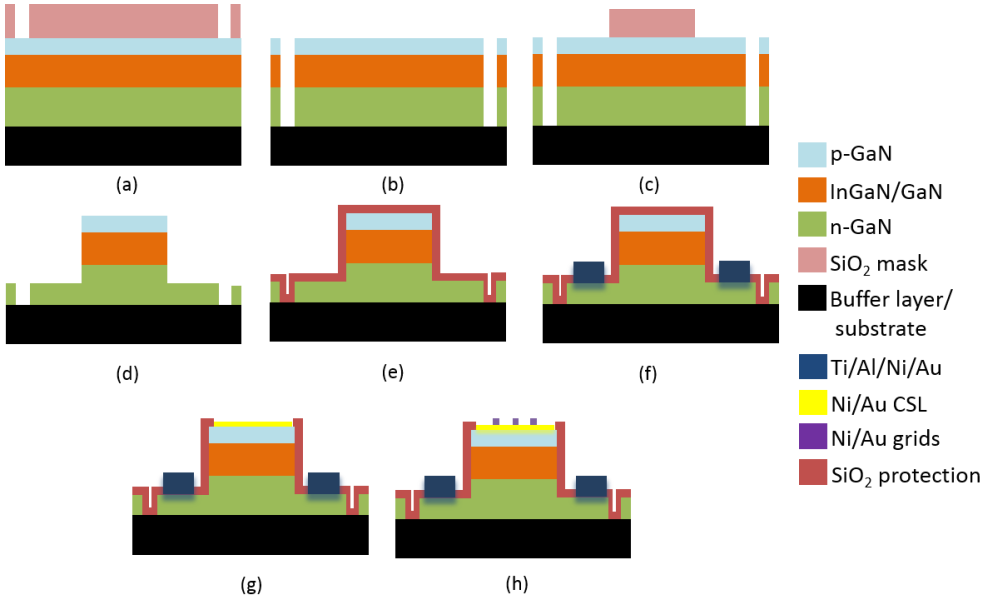

Figure 3.7 (a) Definition of SiO_2 mask for isolation etching, (b) The stack after the isolation etch, (c) Definition of the SiO_2 mask for the mesa etch (d) The stack after the mesa formation, (e) Deposition of the SiO_2 protection layer, (f) Exposition of n-GaN, lift-off of Ti/Al/Ni/Au for n-contacts and RTA of n-contacts, (g) Exposition of p-GaN, lift-off of Ni/Au current spreading layer (CSL) and thermal annealing of Ni/Au CSL, and (h) Lift-off of Ni/Au grids.

It is possible that some persistent residues remain on the SiO_2 protection layer during n-contacts metal lift-off and degrade the devices after the RTA treatment (at 850°C). In this case, the wafer can be soaked in BOE7:1 solution to wet etch the entire SiO_2 protection layer and eventually remove any residues by lift-off effect. In order to sustain further protection of the sidewalls in the consecutive processing steps, new SiO_2 layer can be redeposited on the device. However, in this case, it is important to note that the SiO_2 layer; which would be deposited on the n-contacts, should be removed by dry or wet etching techniques, in order to prevent diffusion of the dielectric into the n-contact metal stack during the thermal treatment of the p-contacts, which would cause deterioration of the ohmic quality.

Figures 3.8 (a) and (b) point out the improvement of SiO_2 sidewall protection on the reverse biased dark currents of the diodes after some thermal treatments. They present an evidence for the diffusion and polymerization of the resist on the device sidewalls by means of electrical characterization, when the sidewalls are not protected. Prior to the thermal treatment, the devices in $In_{0.15}Ga_{0.85}N$/GaN MQWs solar cell structures on sapphire and GaN substrates, demonstrate very low leakage currents under reverse bias, as shown in Figure 3.8 (a) and (b), respectively.

3.2 Device processing issues

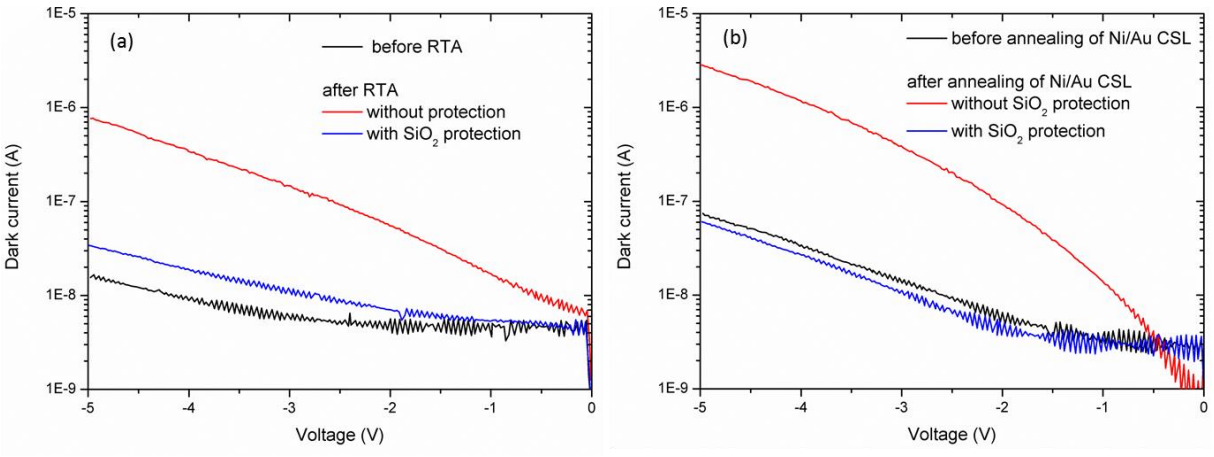

Figure 3.8 The influence of SiO_2 sidewall protection on dark current-voltage characteristics under reverse bias after thermal treatments of the solar cell structures with (a) $In_{0.15}Ga_{0.85}N$/GaN MQWs grown on sapphire substrate; and (b) $In_{0.15}Ga_{0.85}N$/GaN MQWs grown on bulk GaN substrate.

On the other hand, when the sidewalls are not protected, both devices suffer from high leakage (tenths of µA) through the sidewalls (curves shown in red) after the thermal treatments; i.e. RTA of n-contacts and annealing of the Ni/Au current spreading layers, respectively. On the other hand, when the sidewalls are covered with SiO_2, the dependence of the dark current on the sidewall leakage is eliminated as presented in blue curves. As a consequence, the electrical analyses are reliable since they are only dominated by the characteristics of the p-i-n junction. Figure 3.9 displays the top view image of a fabricated solar cell with 1x1 mm^2 mesa size.

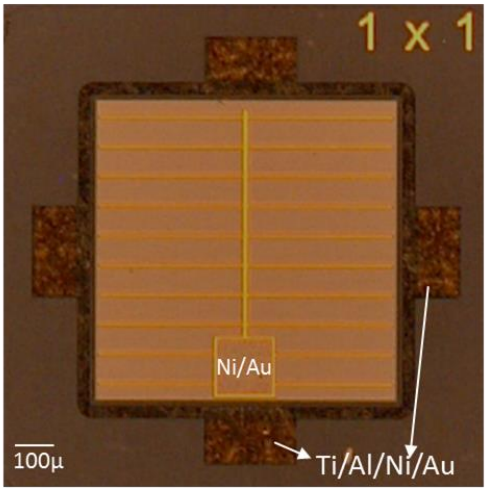

Figure 3.9 Optical microscopy image of fabricated InGaN based solar cell.

3.3 Electrical and photovoltaic characterization of the devices

3.3.1 Device isolation and n-type contact characteristics

The isolation between the devices was obtained by ICP etching till the insulating sapphire substrate. Figure 3.10 (a) exhibits the current-voltage measurement for isolation, which was carried out after the lift-off of n-type contacts, on metal isolation patterns separated by 100µm as shown in Figure 3.10 (b). Very low current levels (tenths of nA) in the applied voltage range of -5V to +5V confirm the device isolation.

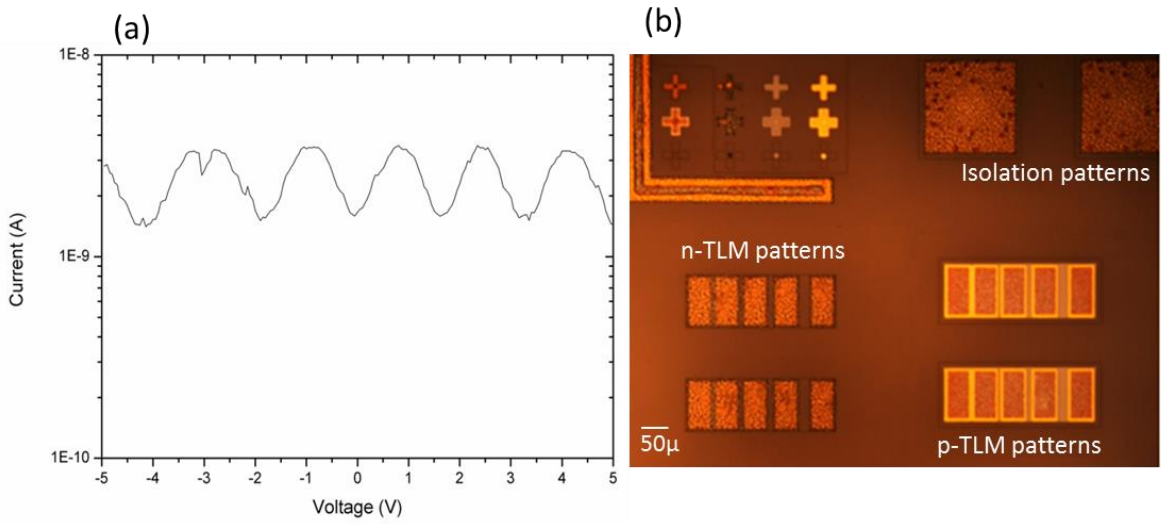

Figure 3.10 (a) I-V characteristics for the device isolation and (b) optical microscopy image displaying the isolation, n-Tranmission line method (TLM) and p-TLM patterns.

Formation of ohmic contacts plays a key role in fabrication of InGaN based solar cells. N-type ohmic contact formation to GaN is relatively well-controlled with a good understanding. Ti and Al thin films are generally employed for n-type metallization schemes owing to their low workfunctions. Deposition of Ti is believed to lead the out-diffusion of N from the GaN lattice and formation of nitrogen vacancies in the crystal structure. The nitrogen vacancies act as electron donors, which greatly increase the n-type character of the material by generating free electrons. As a result, the metal/semiconductor interface becomes heavily doped creating very low specific contact resistances [142]. Al is, on the other hand, used to prevent Ga diffusion from the lattice structure. The contact resistance is further decreased by using the metal stack of Ti/Al/Ni/Au and performing an oxygen-free ambient thermal annealing around 850°C [143]. The Au layer on the top is introduced to prevent any oxidation of the Ti or Al layer and it also serves as the top electrical contact layer. Ni is employed to prevent Au diffusion to n-GaN through the Ti/Al layers.

In this study, Ti (12 nm)/Al (200nm)/Ni (40nm)/Au (100nm) stack treated with RTA at 850°C in N_2 ambient is used as n-type metallic contact. The current-voltage characteristics which is shown in Figure 3.11 displays very good ohmic quality. The contact resistance (R_C) was extracted to be 0.05 Ω.mm by transmission line method (TLM) measurements.

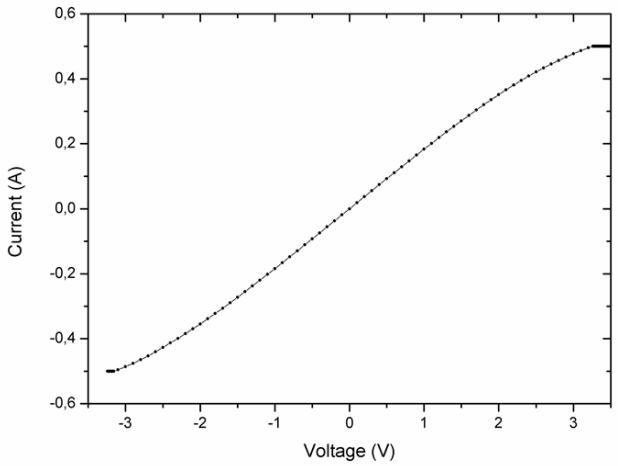

Figure 3.11 Current voltage characteristics of Ti/Al/Ni/Au metal stack used as n-type ohmic contacts in InGaN based solar cells.

3.3.2 Influence of p-type contact quality on the device performance

Contrary to n-type GaN, it is extremely difficult to achieve a decent quality of ohmic contacts to p-type GaN. This is mainly due to the lack of conducting oxides or metals with high workfunction (more than 5eV) and low hole concentration in p-GaN as a result of its poor Mg doping activation capability. As a solution, semitransparent and conductive thin Ni/Au layers are employed as a current spreading layer in conventional InGaN based LEDs and solar cells. The current spreading layer should exhibit high transmittance and low resistivity. However, the formation of such layers is still not well understood in the literature. In this study, the evolution of transmittance and conductivity of a thin Ni/Au (5/5nm) layer deposited on top of the p-type GaN has been investigated at different annealing conditions. In addition, the need of larger Ni/Au grids deposited on the current spreading layers is questioned. As a matter of fact, in this section, the influence of the p-contact quality on the device performances is investigated through two following studies;

- The optimization of thermal annealing time of Ni/Au current spreading layers in terms of their optical and electrical properties.
- The effect of Ni/Au grid schemes deposited on top of Ni/Au CSLs for p-contacts on the device performances.

3.3.2.1 Optimization of thermal annealing of semitransparent Ni/Au current spreading layers

Ni/Au contact schemes are generally used as p-type contacts on p-type GaN owing to Ni's large workfunction (5.15 eV). Annealing of Ni/Au contacts around 500°C in air or in O_2 ambient was reported to result in specific contact resistances between 10^{-4} and 10^{-6} Ωcm^2 [74, 80, 104]. Different mechanisms of improved conductivity of annealing Ni/Au layers were proposed by several groups. Koide *et al.* [144] reported that the annealed Ni/Au contacts could form an intermediate semiconductor layer with high hole concentration, since it causes removal of hydrogen atoms which were bonded to Mg or N in p-GaN. Ho *et al.* [145] and Smalc *et al.* [146] stated that during the annealing the Ni out-diffuses and gets oxidized by creating transparent and conductive NiO_X layers in different surface morphologies on top of Au. The annealing in oxygen ambient is believed to lead to formation of three types of domains: crystalline NiO_X grains on the top, crystalline Au grains in the middle and an amorphous compound of Ni-Ga-O close to the p-GaN. Another interpretation proposes an in-diffusion of Au atoms towards the p-GaN and dissolution of Ga in Au, leading to creation of Ga vacancies that lowers the p-type resistivity.

In this study, the transmittance of 500°C annealed Ni/Au layers on glass was measured as a function of annealing time in air ambient. It should be noticed that glass substrates were preferred for this investigation due to the limited number of p-i-n InGaN/GaN heterostructure samples. Figure 3.12 (a) shows the transmittance of Ni/Au layers at 400 nm after annealing for different durations. The highest transmittance values are obtained for samples which were annealed for 3, 10 and 30 minutes. The transmittance of the annealed layers was observed to get stabilized after 30 minutes of thermal treatment. Figure 3.12 (b) exhibits the transmittance of as-deposited and annealed samples as a function of wavelength. For the wavelength range between 350-550 nm, which corresponds to the absorption range of InGaN active layers, the transmittance is improved from 40-45% to 60-65% as a possible consequence of the formation of semi-transparent NiO_x layers after annealing. It is important to note that the transmittance spectra of annealed Ni/Au layers are not exactly the same for 3, 10 and 30 minutes; indicating possible formation of different phases of NiO_x. The range of possible non-stoichiometry, x, of NiO_X phase was reported to be between 1 and 1.2 at 500°C, at equilibrium with atmospheric air Po_2= 0.21 bar [147]. Nevertheless, it can be concluded that 3 minutes of annealing in air is sufficient to create a NiO_x layer that provides 60-65% transmittance in the absorption wavelength range of InGaN active region.

Therefore, it is crucial to assess the electrical characteristics of the semi-transparent Ni/Au current spreading layers which are annealed for short, intermediate and long durations, (3, 10 and 30 minutes). In order to determine the resistivity of the annealed NiO_x/Au/Ni layers, TLM measurements are performed after the deposition of Ni/Au (50/200nm) grid schemes.

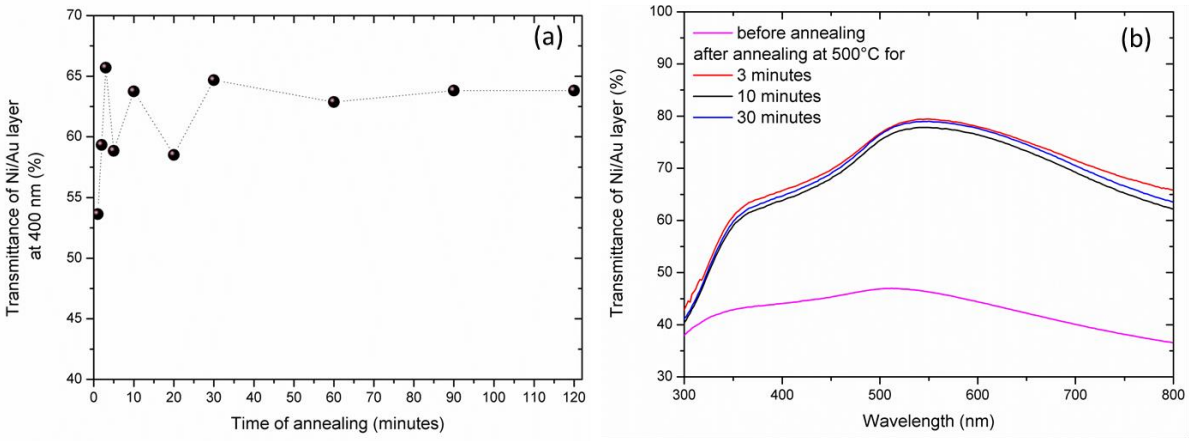

Figure 3.12 Measurements of transmittance of 500°C annealed Ni/Au layers on glass substrate in air (a) at 400nm as a function of annealing time , and (b) as a function of wavelength for three different annealing durations.

Figure 3.13 (a) shows the specific contact resistivity of the current spreading layer as a function of the annealing time. As the time of annealing is increased, the resistivity of Ni/Au layers slightly increases. Figure 3.13 (b) displays the measured total resistance with respect to the distance between the p-TLM patterns that were presented in Figure 3.13 (b). The total measured resistance can be assumed as the sum of the resistance associated with the metal (Ni/Au)/semiconductor (NiO_x) interface, R_1, and the resistance between the contact metals, R_2, as shown in Equation 3.1.

$$R_{\text{Total measured}} = R_1 + R_2 \qquad (3.1)$$

A possible explanation for the increase in specific contact resistivity with respect to the annealing time is a further oxidation and creation of more resistive NiO_x phases on the top surface. Horak reported an increase in the concentration of oxygen in the NiO_x alloy, as a function of the annealing time [148]. The resistivity of annealed thin Ni films in air was reported to increase slightly with time due to formation of richer oxygen NiO_X compounds. Indeed, in our study, it is plausible to create several NiO_x phases, which contribute to degrade R_2 and thus increase the overall resistivity of the contacts when the layers are annealed for longer durations. It is important to note that the measured resistivity values correspond only to that of the annealed Ni/Au current spreading layer (R_1), but not that of p-type GaN layer (R_1+R_2).

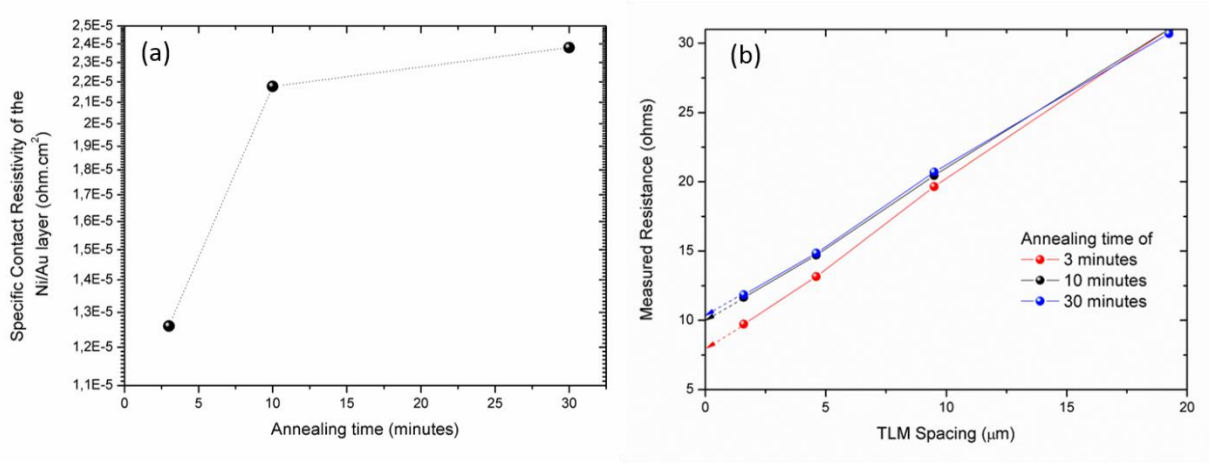

Figure 3.13 (a) Specific contact resistivity of annealed Ni/Au contact layer with respect to the time of annealing and (b) measured resistance of the contacts as a function of TLM spacing for different annealing durations.

In order to analyze the influence of the annealing time of Ni/Au current spreading layer (CSL) over the device performances, the current-voltage characteristics of solar cells in dark and under 1 sun illumination (AM1.5G) are presented in Figure 3.14, in which the Ni/Au layers were annealed at 500°C in air for 3, 10 and 30 minutes. It should be noticed that these solar cells including $In_{0.15}Ga_{0.85}N$/GaN MQWs grown on sapphire substrates had been fabricated using identical processing until this thermal treatment step. The S-shape behavior, which is present in the illuminated J-V curves of the solar cells, will be discussed in the next section.

Table 3.5 summarizes the electrical parameters such as open-circuit voltage V_{OC}, short-circuit current J_{SC}, fill factor FF, conversion efficiency η, and the resistances at V_{OC} and J_{SC}. The series (R_S) and shunt (R_{SH}) resistances of the solar cells can be approximated from the slopes of the I-V curves at V_{OC} and J_{SC}, respectively [149]. The series resistance of a solar cell is due to the vertical transport of the current through the p-i-n materials of the cells and the contact resistances between the metals and n-type and p-type semiconductors.

Table 3.5 Electrical parameters of $In_{0.15}Ga_{0.85}N$/GaN MQWs solar cells grown on sapphire substrate for different annealing times of Ni/Au current spreading layers

Time of annealing of Ni/Au CSL (min)	V_{OC} (V)	J_{SC} (mA/cm²)	FF (%)	η (%)	R at V_{OC} ~ R_S Ω.cm²	R at J_{SC} ~ R_{SH} kΩ.cm²
3	1.76	0.637	53.92	0.56	1137.89	24.62
10	1.80	0.586	56.77	0.59	1500.63	41.43
30	1.64	0.585	50.93	0.51	1814.99	20.75

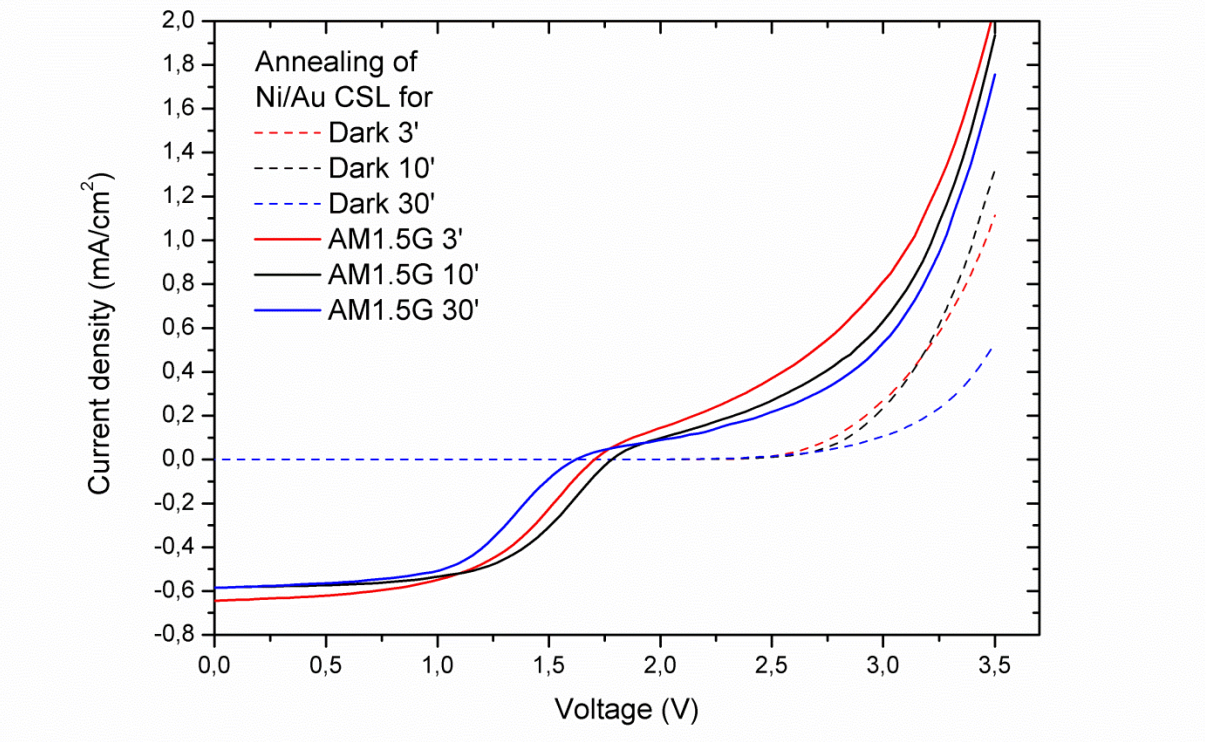

Figure 3.14 Current-voltage characteristics of solar cells with $In_{0.15}Ga_{0.85}N$/GaN MQWs grown on sapphire substrates in dark and under 1 sun illumination (AM1.5G) for different annealing times of Ni/Au current spreading layers for p-contacts.

Figure 3.15 exhibits the contact resistances contributing to R_S in the InGaN based solar cells with Ni/Au current spreading layers. R_1 is the resistance between the metal (Ni/Au) and the semiconductor (NiO_x) interface and R_2 is the resistance of the contact metals used for p-contacts. $R_{C,P}$ and $R_{C,N}$ are the contact resistance between the metal contacts and p-type and n-type GaN, respectively. As mentioned earlier, $R_{C,N}$ is 0.05 Ω.mm which is negligible compared to the p-contact resistance. As a result, very high R_S of the solar cell, which is estimated from the value of resistance at V_{OC} in Table 3.5, can be attributed to high $R_{C,P}$ and high bulk resistivity of the p-type GaN. In this study, the value of $R_{C,P}$ cannot be assessed by any TLM or Hall measurements since the stack includes a less resistive n-type GaN which allow the lateral charge transport. Therefore, in order to measure the value of $R_{C,P}$, TLM measurements should have been performed on bare p-type GaN grown only on insulating sapphire substrates.

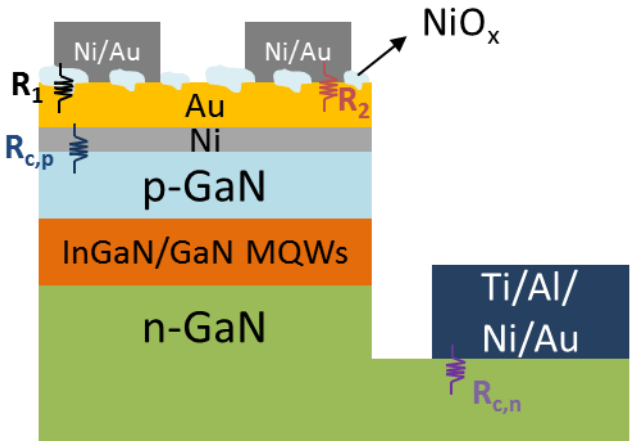

Figure 3.15 The contact resistances of the p and n-contacts contributing to overall series resistance of the solar cells (figure not drawn to scale).

It is clearly seen that the series resistance increases as the annealing time of the Ni/Au CSL increases. Since the solar cells have identical p-i-n structures and n-type ohmic quality, the difference in R_S can be attributed to different characteristics of p-type contacts. Similar phenomenon, i.e. increase in resistance with respect to increase in annealing time of Ni/Au CSLs, was observed earlier by TLM measurements in Figure 3.13. However, the strong increase in R_S as a function of the annealing time can be attributed to the creation of a more resistive NiO_X phase, which has certainly a strong influence on the vertical charge transport. The R_1 component increases as a consequence of a further oxidation and formation of more resistive NiO_X alloy. On the other hand, for the TLM measurements, the increase in R_1 component would not cause the same influence since the measurements are carried out laterally. Consequently, the overall effect of increase in R_1 is more pronounced, when assessing the vertical charge transport. It can be concluded that the time of annealing has to be minimized in order to reduce the series resistance which would lead to enhanced FF and J_{SC} of the solar cells.

On the other hand, the shunt resistance, which is approximated as the R at J_{SC}, is the highest for the solar cells with Ni/Au current spreading layers annealed for intermediate durations, i.e. 10 minutes. Low R_{SH} is attributed to power losses in the cell due to leakage current inside the device or surface recombination. A possible explanation is that annealing in air ambient provides oxidation on the surface of the solar cells, which can reduce the surface recombination. Indeed, the annealing of Ni/Au CSL for 10 minutes can be considered as a slightly better compromise between R_S and R_{SH}, leading to the highest FF and conversion efficiency.

3.3.2.2 The influence of using Ni/Au grid schemes for p-contacts

Figure 3.16 displays a comparison of photovoltaic performances and External Quantum Efficiencies (EQE) for the solar cells including $In_{0.15}Ga_{0.85}N$/GaN MQWs grown on sapphire substrates with and without Ni/Au grids. The electrical parameters of the solar cells, which are illuminated under 1 sun (AM1.5G), are tabulated in Table 3.6. Both of the solar cells have Ni/Au current spreading layers annealed at 500°C for 3 minutes in air. The solar cells in Figure 3.16(c) have Ni (50nm)/Au (200nm) contact pattern of 200×200μm^2 which is deposited on top of the Ni/Au CSL, while in Figure 3.16 (d), the Ni (50nm)/Au (200nm) p-contacts are in the form of 7μm width finger grids with a separation distance of 90μm.

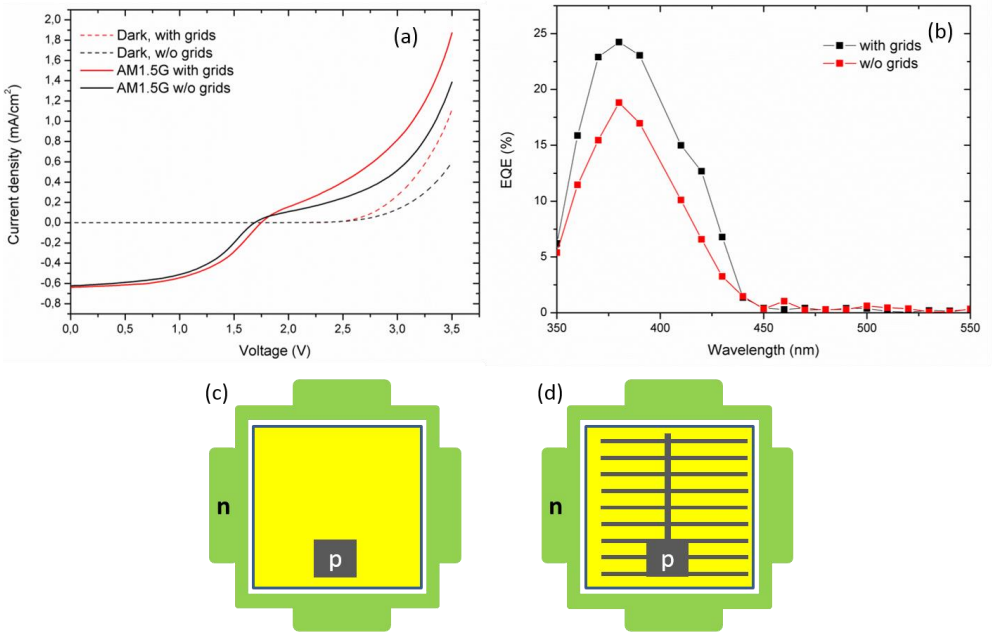

Figure 3.16 For $In_{0.15}Ga_{0.85}N$/GaN MQWs solar cells grown on sapphire substrates with and without grids (a) Comparison of J-V characteristics in dark and under 1 sun illumination (AM1.5G), and (b) Comparison of external quantum efficiencies (EQE). Top view of the solar cells (c) without Ni/Au grids, and (d) with grids.

The cell without grids has lower EQE than that of the cell with the grids, due to losses in carrier collection and higher R_S. The current-voltage characteristics of the solar cells also confirm reduced R_S, when the grid schemes are adopted. Despite the high difference in R_S, the solar cells exhibit similar J_{SC} values, which can be attributed to possible shadowing of the grids and less light absorption. It indicates that the spacing between the grids needs a careful optimization to achieve the best combination of light absorption and carrier collection efficiency. Nonetheless, this study points out the necessity of Ni/Au grids, since it provides an improvement in the whole electrical parameters as well as the external quantum efficiency.

Table 3.6 Electrical parameters of $In_{0.15}Ga_{0.85}N$/GaN MQWs solar cells grown on sapphire substrate with and without Ni/Au grid schemes.

Solar cell	V_{OC} (V)	J_{SC} (mA/cm²)	FF (%)	η (%)	R at V_{OC} ~ R_S Ω.cm²	R at J_{SC} ~ R_{SH} kΩ.cm²
With Ni/Au grids	1.76	0.637	53.92	0.56	1137.89	24.62
Without Ni/Au grids	1.71	0.623	49.73	0.51	1528.84	16.65

3.3.3 Preliminary device results of $In_xGa_{1-x}N$/GaN MQWs solar cells with high indium content

In this section, the development and photovoltaic performance of 3rd generation of solar cells, which have high indium content i.e. 19% and 24% In InGaN/GaN MQWs, are addressed. In chronological point of view, the development and optimization of mesa etching with SiO_2 mask were performed by using this generation of solar cells, which led to first functional devices in this work. Table 3.7 presents the important processing steps in fabrication of the solar cells including 25 pairs of $In_{0.19}Ga_{0.81}N$ (2.5 nm)/GaN (8.9nm) MQWs and $In_{0.24}Ga_{0.76}N$ (2.5 nm)/GaN (9nm) MQWs grown on sapphire substrates. It should be noted that the sidewalls of the devices were not protected after the mesa etch step, which caused very low yield of functional devices. As mentioned earlier, during the thermal treatments for the formation of n-type and p-type contacts, some resist residues from the lift-off processes can be re-deposited on the edges of the devices creating short circuit. As a solution, subsequent to thermal annealing treatments of the n- and p-type contacts, the wafers were treated by O_2 based ICP cleaning (150W ICP power, 10W RF power, 10mT of pressure) for 5 minutes and then cleaned with EKC265 solution. This severe cleaning procedure helped cleaning of the residues and provided electrical characterization of some devices. However, it is important to notice that such a cleaning process can degrade the R_S of the devices to a great extent. Nevertheless, since both wafers are processed identically, the results can provide a comparison of device performances as a function of indium content.

In addition, the Ni/Au current spreading layers are annealed at 500°C for 30 minutes in air. Both of the samples have Ni/Au grids for the p-type contacts.

Table 3.7 specifications of key processing steps in the fabrication of $In_xGa_{1-x}N$/GaN MQWs solar cells grown on sapphire substrate with x=0.19 and 0.24.

Mesa etching	Performed with SiO_2 mask
Sidewall protection	No protection in intermediate steps (instead : O_2 based ICP + EKC265 cleaning)
Thermal treatment of Ni/Au CSL	30 minutes of annealing at 500°C in air

Figure 3.17 exhibits the spectral response of the solar cells having $In_xGa_{1-x}N$/GaN MQWs with x=0.19 and 0.24. The external quantum efficiency peak values of the solar cells with 19% and 24% indium are 13.3% and 11.7%, respectively. The drop in EQE peak efficiency with the increase in In content, x from 0.19 to 0.24, can be explained by higher dislocation density [150] and compositional fluctuations [151] in higher In content InGaN, which lead to trapping of photo-generated carriers either in crystalline defects or shallow InGaN wells. It can be remarked that owing to InGaN/GaN MQWs with x=0.19 and 0.24, the spectral cut-off of GaN (~365 nm) is redshifted to 496 nm and 530 nm, respectively.

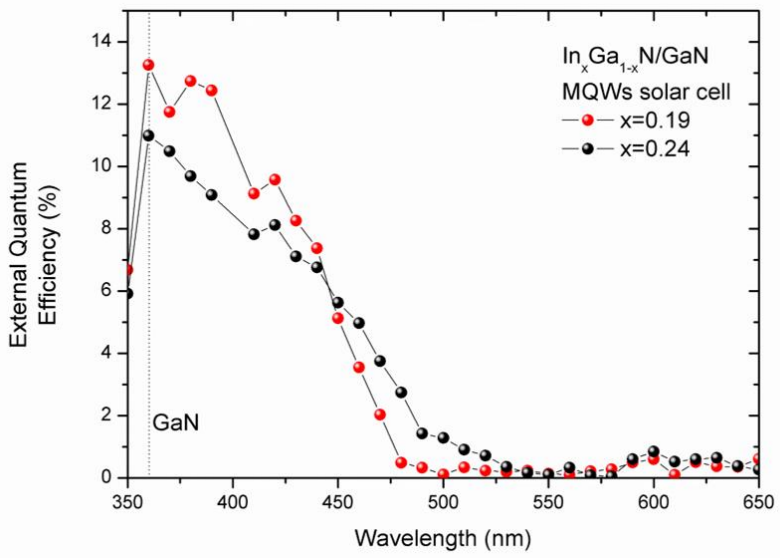

Figure 3.17 Comparison of external quantum efficiencies of the solar cells having 25 pairs of $In_xGa_{1-x}N$/GaN MQWs with x=0.19 and 0.24.

Figure 3.18 (a) represents the dependence of the dark current density on the composition of indium, when the devices are reverse biased. The reverse dark current is related to the defect density in the structures when the processing of the devices is well optimized. High reverse leakage currents; i.e. around 1µA and 1mA at -5V for x=0.19 and 0.24, respectively; indicate the high defect density in both cells and explain the low EQE values. The solar cell with x=0.24 displays higher dark reverse leakage than that of the cell with x=0.19. The increase in reverse leakage current as a function of increasing the In content, is an indication of the degraded crystalline quality in solar cell structures with higher In composition.

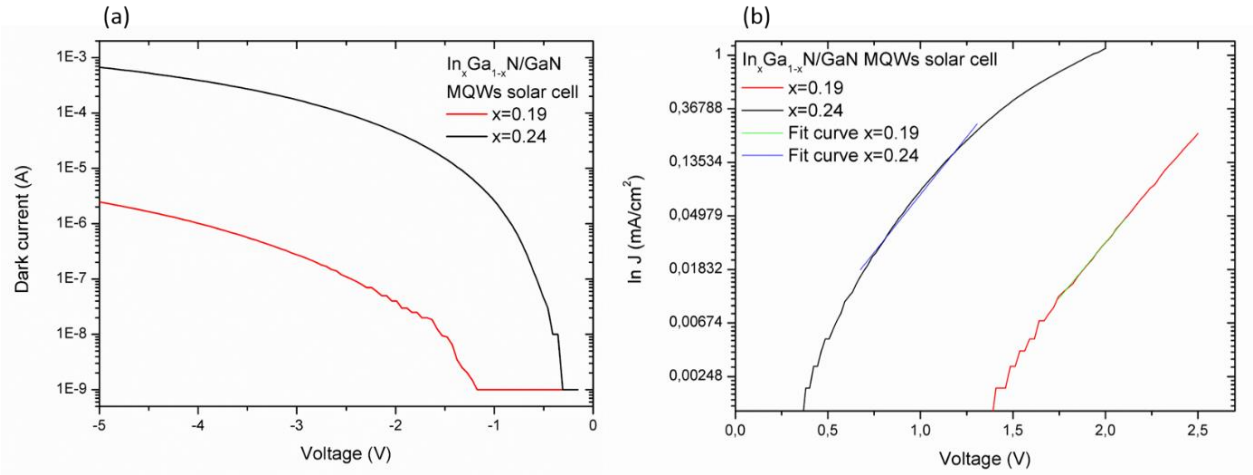

Figure 3.18 $In_xGa_{1-x}N$/GaN MQWs with x=0.19 and 0.24 solar cells: (a) Comparison of dark reverse leakage current vs voltage and (b) dark current density (ln J) vs. voltage characteristics in forward bias.

Furthermore, Figure 3.18 (b) shows the plot of dark current density – voltage of the diodes from which the ideality factor (n) and dark saturation current (J_0) can be extracted. The ideality factor can be derived from the slope of ln (J) –V plot, while the intercept gives the J_0 as shown in Equation 1.3 in the first chapter. The values of J_0 extracted from dark ln (J) –V curves of $In_xGa_{1-x}N$/GaN MQWs solar cells are 7.73×10^{-6} and 9.84×10^{-4} mA/cm^2 for x=0.19 and 0.24, respectively. The increase in dark saturation current in the devices with higher In content is attributed to a more pronounced effect of recombination of the charge carriers due to higher defect density in the structure. On the other hand, the ideality factors are derived to be 9.13 and 8.97, respectively, for $In_{0.19}Ga_{0.81}N$/GaN and $In_{0.24}Ga_{0.76}N$/GaN MQWs solar cells. It is important to note that ideality factors of more than 2 were also reported in literature for GaN based optoelectronic devices. The origin of anomalously high ideality factor (n>5) in III-Nitrides was reported to be deep level assisted tunneling. Cao *et al.* [152] showed that in InGaN/GaN heterostructures, negatively charged defects can be generated in the vicinity of the dislocations and introduce deep-level states in the depletion region. The carriers can tunnel into deeply lying defect states in the band gap of In(GaN) and non-radiatively recombine leading to internal quantum efficiency drop in InGaN/GaN based LEDs. Possible sources of deep level traps were reported to be Oxygen impurities, N vacancies, Mg-H complexes or structural defects due to the lattice mismatch in InGaN/GaN MQWs [152]. In addition, Zhu *et al.* [153] proposed that the externally measured ideality factor of a p–n junction diode is the sum of the ideality factors of the individual rectifying junctions within the diode. Therefore, such high ideality factors can be associated with the combined effect of the non-radiative deep-state tunneling through the p-i-n junction of the diode and the non-ohmic metal–semiconductor junction, i.e. the low quality of p-type contact.

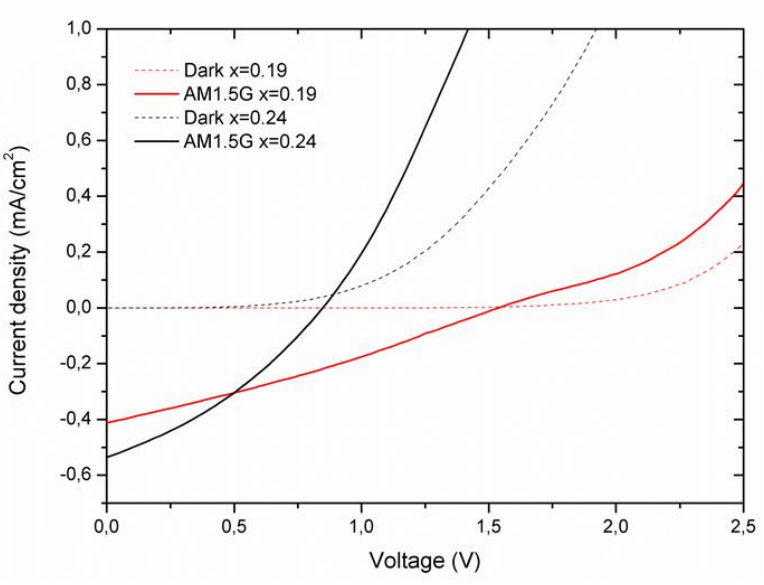

Figure 3.19 J-V characteristics of solar cell having $In_xGa_{1-x}N$/GaN MQWs with x=0.19 and 0.24 in dark and under 1 sun illumination (AM1.5G).

Table 3.8 Electrical parameters of $In_{0.19}Ga_{0.81}N$/GaN MQWs and $In_{0.24}Ga_{0.76}N$/GaN MQWs solar cells grown on sapphire substrate.

x in $In_xGa_{1-x}N$/GaN MQWs solar cell	V_{OC} (V)	J_{SC} (mA/cm²)	J_O (mA/cm²)	FF (%)	η (%)	R at V_{OC} ~ R_S Ω.cm²	R at J_{SC} ~ R_{SH} kΩ.cm²
0.19	1.47	0.481	$7.73x10^{-6}$	29.24	0.18	3185.39	49.48
0.24	0.84	0.560	$9.84x10^{-4}$	33.54	0.16	875.84	30.42

Figure 3.19 presents a comparison of current density-voltage characteristics of $In_xGa_{1-x}N$/GaN MQWs solar cells with x=0.19 and 0.24 in dark and under 1 sun illumination (AM1.5G). Table 3.8 summarizes the electrical parameters of these solar cells. The solar cell with x=0.24 exhibits slightly better J_{SC} than that of the cell with x=0.19, which can be attributed to its broader absorption range and greater number of created charge carriers owing to its higher In content, x=0.24. However, most of the photogenerated carriers recombine due to the structural defects and cannot contribute to efficient energy conversion, which severely degrades the V_{OC} and results in low conversion efficiency, η of 0.16%. Surprisingly, this device exhibits lower R_S than that of lower In content solar cell. However, it should be noted that due to highly defective epilayers and possible In segregation within the InGaN QWs as well as the non-optimized processing conditions, the electrical characteristics of the devices in this batch were highly inhomogeneous. It can be concluded that the results obtained for the $In_{0.24}Ga_{0.76}N$/GaN MQWs solar cells are not entirely representative for this In content.

On the other hand, for the solar cells with $In_{0.19}Ga_{0.81}N$/GaN MQWs, a different phenomenon is revealed. The illuminated J-V plot displays a slightly distorted S-shaped behavior

with a bias around 1.5V. The distorted J-V curve under illuminated measurement and very low value of FF indicate that collection of most of the photogenerated charge carriers at the contacts are inhibited due to high contact resistances and piezoelectric polarization induced effects in the InGaN/GaN MQWs. Furthermore, the high dislocation and defect density, which act as non-radiative recombination centers, reduce the carrier lifetime and degrade the solar cell performances. Regarding the very high series resistance and low FF value of this device, it is important to notice that the p-type contact quality of this generation of solar cells was not optimized, i.e. annealing time of Ni/Au CSL is 30 minutes. The effect of piezoelectric and spontaneous polarization will be detailed in the next section.

To conclude, pseudomorphically grown $In_xGa_{1-x}N$/GaN MQWs with x=0.19 and 0.24 are fabricated into fully functional solar cells. Even though the processing conditions were not fully optimized for these devices, the electrical characterization analyses provided a comparison of performances of identically processed solar cells as a function of In contents. EQE analyses indicate that for the samples with 19% In and 24% In, the spectral cutoff wavelength is extended up to 496 nm and 530 nm, respectively. The photovoltaic characterization under 1 sun revealed that the J_{SC} is enhanced for the solar cell with higher In content owing to an improved absorption range. However, V_{OC} and η degrade by increasing the In content as a result of higher density of dislocations and possible segregation of Indium clusters, which act as recombination centers. High dark saturation currents and anomalously elevated ideality factors confirm the degraded crystalline quality and low photovoltaic performances. In addition, it can be noticed that for the devices with higher indium content, the yield of functional devices are very low and photovoltaic characteristics exhibit inhomogeneity, due to non-optimized processing and high defect density.

3.3.4 Comparison of device performances on sapphire and on bulk GaN substrates

In this section, the development and comparison of photovoltaic performances of 4th generation of solar cells using $In_{0.15}Ga_{0.85}N$/GaN MQWs grown on sapphire and bulk GaN substrates are investigated. Table 3.9 presents the important processing steps in fabrication of the solar cells including 25 pairs of $In_{0.15}Ga_{0.85}N$ (2.2 nm)/GaN (4.8 nm) MQWs and $In_{0.15}Ga_{0.85}N$ (2.5 nm)/GaN (4.5 nm) MQWs grown on sapphire and bulk GaN substrates, respectively. After the mesa formation, the device sidewalls are protected by deposition of SiO_2 layers, which led to a high yield of functional devices and homogeneous PV characteristics within the batch. The Ni/Au current spreading layer for p-type contacts were prepared by applying 10 minutes of thermal treatment at 500°C in air.

Table 3.9 Specifications of key processing steps in the fabrication of $In_{0.15}Ga_{0.85}N$/GaN MQWs solar cells grown on sapphire and bulk GaN substrates.

Mesa etching	Performed with SiO_2 mask
Sidewall protection	Protection with sacrificial SiO_2 layer in intermediate processing steps
Thermal treatment of Ni/Au CSL	10 minutes of annealing at 500°C in air

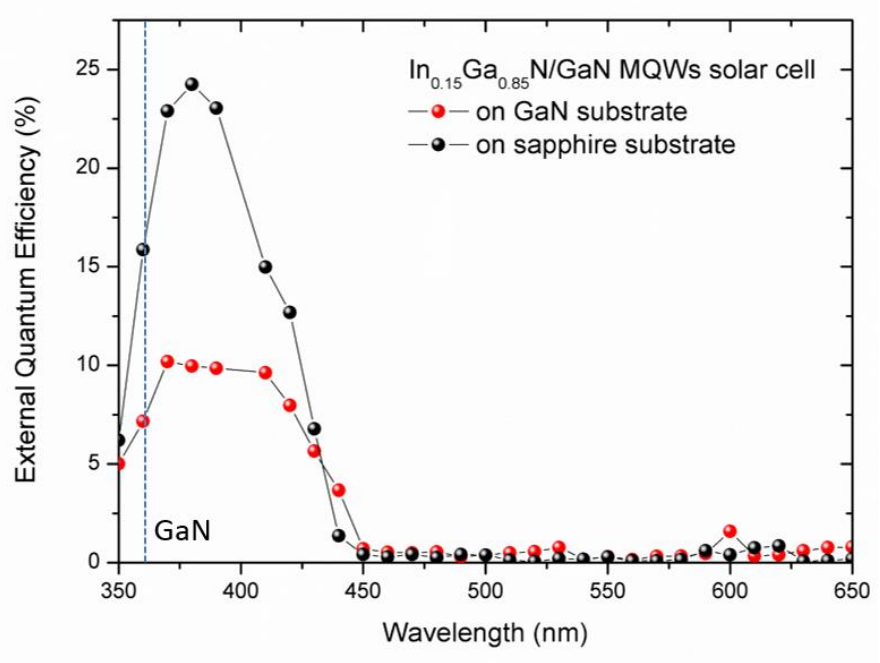

Figure 3.20 Comparison of external quantum efficiencies of the solar cells including 25 pairs of $In_{0.15}Ga_{0.15}N$/GaN MQWs grown on sapphire and bulk GaN substrates.

Figure 3.20 exhibits the spectral response of the solar cells including 25 pairs of $In_{0.15}Ga_{0.85}N$/GaN MQWs grown on sapphire and bulk GaN substrates. It can be observed in the spectral cut offs that both of the solar cell structures are redshifted to 450 nm owing to $In_xGa_{1-x}N$/GaN MQWs with identical indium contents, i.e. x =0.15. The external quantum efficiency peak value of the solar cells grown on sapphire is 24.2 against 10.1 for the solar cells grown on bulk GaN substrate. In theory, the EQE depends on the absorption efficiency, charge separation and carrier collection at the contacts. Since the thickness of quantum wells in the structure grown on GaN substrate (2.5 nm) is slightly higher than that of the structure grown on sapphire (2.2 nm), the total number of absorbed photons is expected to be greater in solar cells grown on GaN substrate owing to its higher effective total active region thickness. However, the EQE values of cells grown on GaN substrate is less than half of that of cells grown on sapphire indicating that the charge separation and the carrier collection are significantly shadowed. Taking into account the identical processing and ohmic contact quality of the solar cells, as well as assuming similar P_{SP} and P_{PZ} effects in both structures, it is reasonable to consider that the significant difference in

EQE peaks is originated from the crystalline quality. Contrary to the structural characterization by means of HRXRD and TEM presented in the previous chapter, EQE analyses indicate more defective structure for the devices grown on bulk GaN substrates. Further electrical characterization will provide more information about the structural quality with respect to the type of the substrates.

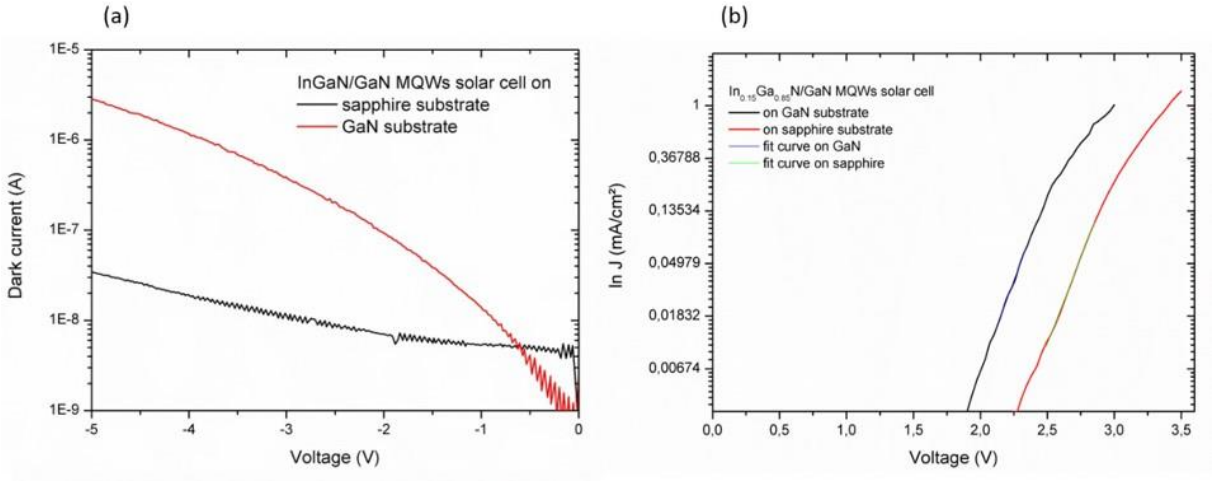

Figure 3.21 For $In_{0.15}Ga_{0.85}N$/GaN MQWs solar cells grown on sapphire and bulk GaN substrates; (a) Comparison of dark reverse leakage current vs voltage and (b) dark current density (lnJ) vs. voltage characteristics in forward bias.

Figure 3.21 displays the dark current-voltage characteristics of $In_{0.15}Ga_{0.85}N$/GaN MQWs solar cells grown on sapphire and GaN substrates in forward and reverse bias. In Figure 3.21 (a), the dependence of the reverse leakage current on the type of substrate is presented. The reverse bias leakage current of the devices grown on GaN substrate is higher by two orders of magnitude than those grown on sapphire substrate. This would once again point out higher density of dislocations, which cause leakage paths in the p-i-n junction within the solar cell structure grown on bulk GaN substrate and is in agreement with the low EQE values. In Figure 3.21 (b), the values of J_0 extracted from dark ln (J) –V curves of $In_{0.15}Ga_{0.85}N$/GaN MQWs solar cells grown on sapphire and GaN substrates are 5.54 $x10^{-8}$ and 3.78$x10^{-6}$ mA/cm^2, respectively. Higher dark saturation current in the devices grown on GaN substrate is consistent with its lower EQE peak. It can be pointed out that the J_0 of these solar cells are much lower than those of the solar cells with higher In contents, i.e. x =0.19 and 0.24. Even though the processing and the configuration of InGaN/GaN MQWs are not the same for these two generations of solar cells, the reduction in J_0 by several orders of magnitude can confirm better crystalline quality for lower In content in InGaN/GaN heterostructures. Similar ideality factors are derived, i.e. 5.94 and 5.66, for the devices with $In_{0.15}Ga_{0.85}N$/GaN MQWs grown on sapphire and GaN substrates, respectively. Anomalously high ideality factors indicate that the charge transport is dominated by deep level assisted tunneling. In addition, relatively low barrier thickness in this generation of solar cells,

i.e. 4-5 nm, can facilitate tunneling of carriers through the GaN barriers. Deep localized states can be associated with the presence of crystalline defects as well as the formation of indium-rich nanoclusters in InGaN QWs due to phase separation [154]. In addition, such high ideality factor can be related to high series resistance of the solar cells due to the low ohmic quality of the p-type contact. It is important to note that the quality of p-type contact can be further improved by using a current spreading layer, which provides higher conductivity and transmittance than the present Ni/Au CSL used in this study.

Figure 3.22 presents a comparison of current density-voltage characteristics of $In_{0.15}Ga_{0.85}N$/GaN MQWs solar cells grown on sapphire and GaN substrates in dark and under 1 sun illumination (AM1.5G). Table 3.10 summarizes the electrical parameters of these solar cells. The solar cell grown on sapphire exhibits much better J_{SC} than that of the cell grown on bulk GaN substrate; in spite of the slightly thicker absorption thickness in the latter. This is consistent with the EQE analyses of these solar cells. The superior V_{OC}, FF and conversion efficiency values of the solar cells grown on sapphire substrate point out that most of the photogenerated carriers recombine due to the structural defects and cannot contribute to efficient energy conversion in the solar cells grown on GaN substrate. These results contradict significantly with the literature, which predicts an enhanced photovoltaic performance for the homoepitaxial growth on bulk GaN substrates [101, 110]. However, it is important to notice that the growth on bulk GaN substrate is currently at an early stage resulting in an immature technology compared to the heteroepitaxial growth on sapphire. Our results indicate that the growth quality on bulk GaN substrates is not trivial and needs further optimization in order to be fabricated into solar cells with enhanced characteristics.

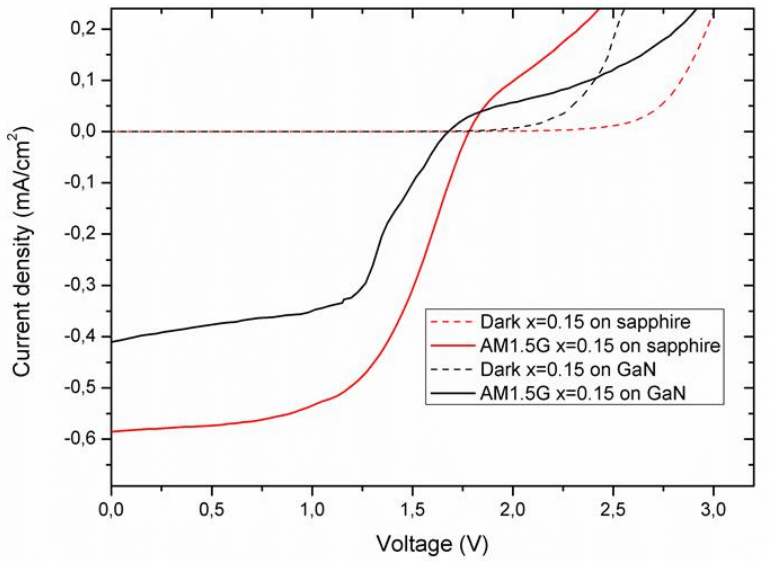

Figure 3.22 Comparison of J-V characteristics of solar cells with $In_{0.15}Ga_{0.85}N$/GaN MQWs grown on sapphire and bulk GaN substrates in dark and under 1 sun illumination (AM1.5G).

Table 3.10 Electrical parameters of solar cells with $In_{0.15}Ga_{0.85}N$/GaN MQWs grown on sapphire and bulk GaN substrates.

Substrate of $In_{0.15}Ga_{0.85}N$/GaN MQWs solar cell	V_{OC} (V)	J_{SC} (mA/cm²)	J_O (mA/cm²)	FF (%)	η (%)	R at V_{OC} ~ R_S Ω.cm²	R at J_{SC} ~ R_{SH} kΩ.cm²
Sapphire	1.80	0.586	$9.35x10^{-10}$	56.77	0.59	1500.63	41.43
Bulk GaN	1.69	0.410	$7.48x10^{-9}$	55.19	0.38	2557.40	13.76

Figure 3.23 provides a comparison of electrical responses in the active regions of these two solar cells by means of top surface electron beam induced current (EBIC) analysis. Figure 3.23 (a) and (b) present the SEM image and top surface EBIC analysis of $In_{0.15}Ga_{0.85}N$/GaN MQWs solar cells grown on sapphire, while Figure 3.23 (c) and (d) exhibit the SEM image and top surface EBIC analysis of solar cells grown on bulk GaN substrate, respectively. The top surface EBIC characterization at acceleration voltage of 5keV creates penetration depth of around 250 nm [155]. It corresponds to current generation from the p-type GaN and InGaN/GaN MQWs in the analyses of both substrates. In addition, it is important to notice that EBIC measurements provide highly complementary characterization of the samples with HRTEM, which displays a more localized scan of a particular zone. Indeed, the top surface EBIC analysis at low magnification gives significant information about the homogeneity of the p-n junction over large sample area.

In Figure 3.23 (b), the homogeneous EBIC signal from the surface confirms the absence of any electrically active defects inside the active region of the cell grown on sapphire substrate. Contrarily, Figure 3.23 (d) shows non-uniformities such as bright and dark dots for the sample grown on GaN substrate. In EBIC analysis, the incident electron beam of the SEM generates electron-hole pairs within the depletion region of the p-n junction. The generated carriers are separated by the internal field and collected at the contacts inducing a current, which is measured and transformed into an EBIC signal. The dark contrast in an EBIC image indicate that the electrons in that region are not collected due to non-radiative recombination and charge trapping, thus it is generally associated with extended defects in the structures.

On the other hand, the origin of the formation of bright spots in InGaN/GaN heterostructures is still not well understood. The bright EBIC contrast formation was reported to be related to enhanced carrier transport through the defects across the active region [156]. Finally, Vergeles *et al.* reported similar bright spots on the surface of 5 pairs of $In_{0.2}Ga_{0.8}N$/GaN MQWs capped with 100nm thick p-type GaN grown on sapphire [157]. First, they assumed that the bright contrast is originated from the structural defects such as micropipes, dislocations or

V-shaped pits; which can provide channels of excess carrier transport across the active region and prevent the recombination in QWs to a great extent. However, this assumption is unlikely since the corresponding SEM images do not reveal any pits or hillocks at the so called defect positions. Similar phenomenon exists in our analysis: bright spots on the EBIC image in Figure 3.23 (d) do not correspond to any noticeable defects in the SEM image in Figure 3.23 (c). Interestingly, in the same publication, they observed an increase and then a slight reduction in brightness of the EBIC signal as a function of exposure time under low-energy e-beam energy irradiation (LEEBI). The origin of such behavior was reported to be a local change in indium content by exposure to e-beam irradiation and possible suppression of carrier recombination inside the QWs from the electric field arising at the boundary of between irradiated and non-irradiated zones. As a result, the carrier recombination within the quantum wells can be prevented and carrier tunneling can be induced by formation of conductive channels, which increases the EBIC signal. In addition, they proposed that the irradiation can passivate the recombination centers since the LEEBI is known to destroy the Mg-H bonds in p-type GaN [158] and lead to healing effect in defective regions and hence create the bright EBIC contrast.

To conclude, preliminary EBIC analyses revealed significant information about the electrical activity in the active regions in both samples and the presence of dark spots pointed out a more defective structure for the GaN substrates. Another interesting result is the formation of bright EBIC contrast, which was associated with a local In change in the irradiated zone and possible formation of conductive channels within the active region in the literature. In the solar cell grown on GaN substrate the bright spots are more pronounced than that of grown on sapphire substrates. This could indicate that the growth of high numbers of pairs (n=25) of $In_xGa_{1-x}N$/GaN MQWs heterostructures with relatively high indium content x=0.15 on sapphire substrate is well optimized and results in decent structural integrity and homogeneity. On the other hand, for the solar cells grown on GaN substrates, non-uniformity of the active region points out the vulnerability and instability of the growth on this new kind of substrate. Besides, the top-surface EBIC analyses showed that the current spreading semi-transparent Ni/Au layer serves well as a p-type contact in InGaN/GaN MQW solar cells. As a future study, it would be interesting to investigate the effect of irradiation time on the evolution of bright spots as well as the range of acceleration voltage of the e-beam exposure.

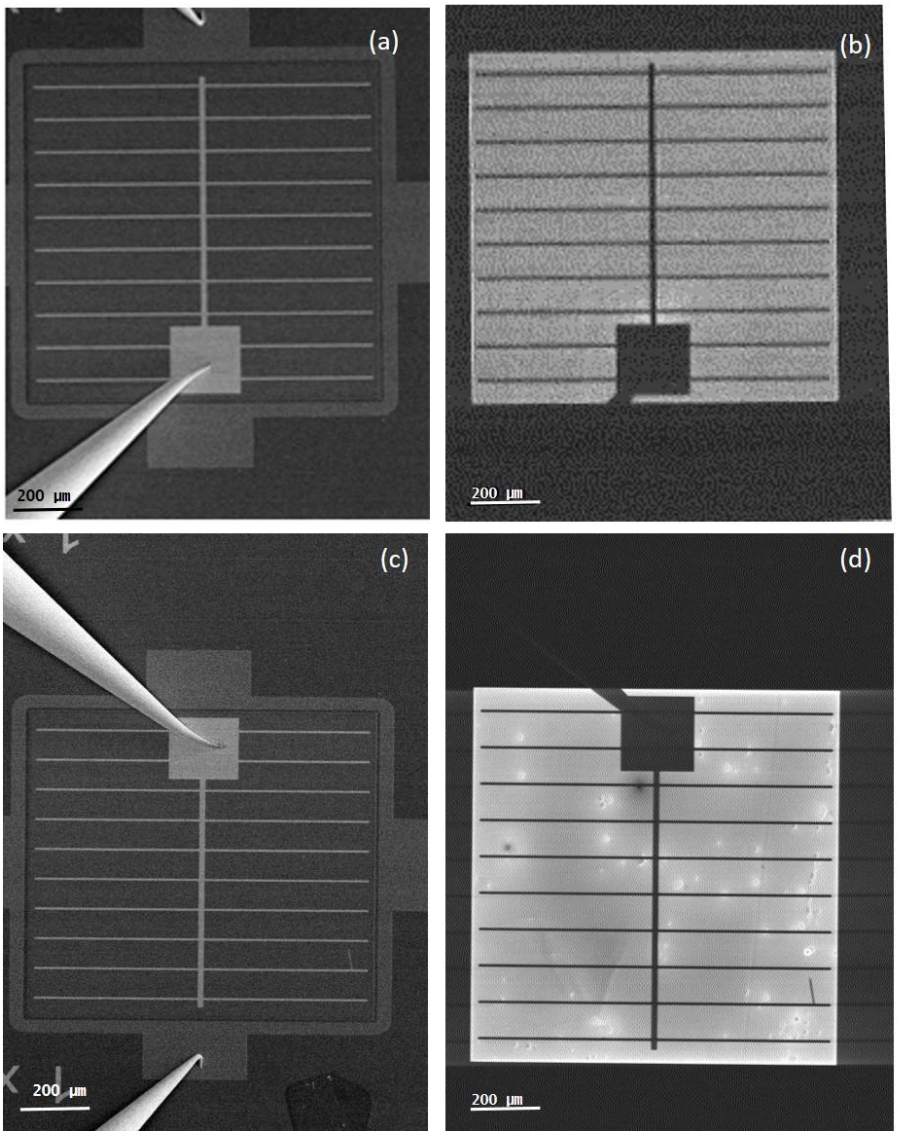

Figure 3.23 (a) SEM image, and (b) top surface EBIC image of $In_{0.15}Ga_{0.85}N$/GaN MQWs solar cells grown on sapphire and ; (c) SEM image, and (d) top surface EBIC image of $In_{0.15}Ga_{0.85}N$/GaN MQWs solar cells grown on bulk GaN at acceleration voltage of 5 keV.

3.3.4.1 Discussion on the S-shape behavior of the illuminated I-V curves

The current-voltage characteristics of the $In_xGa_{1-x}N$/GaN MQWs solar cells with x=0.15 and 0.19 in Figures 3.22 and 3.19, respectively, highlight an S-shape behavior when measured under AM1.5G illumination. Moreover, compared to solar cells with similar indium contents in the literature [110, 111], these solar cell exhibit lower V_{OC} and photovoltaic performances. Therefore, it is crucial to investigate the possible reasons of insufficient PV characteristics. In this context, cross-sectional EBIC analyses are of great interest to observe the electrical response in and around the active region. Figure 3.24 illustrates SEM and cross-sectional EBIC images of the $In_{0.15}Ga_{0.85}N$/GaN MQWs solar cells grown on sapphire at lower (Fig.3.24 a and b) and higher magnifications (Fig. 3.24 c and d).

In the cross sectional EBIC images, a bright contrast is observed in the p-i junction and the active region including InGaN/GaN MQWs, which confirms the efficient charge generation and separation in this zone. However, a dark strip is revealed at the i-n junction, which corresponds to carrier recombination at the interface. Figure 3.25 exhibits a similar electrical response in the active region of $In_{0.15}Ga_{0.85}N$/GaN MQWs solar cells grown on bulk GaN substrates. The recombination of photo-generated carriers at the i-InGaN/ n-type GaN interface could be due to formation of misfit dislocations between the two materials. However, this is very unlikely since the dark strip is homogeneous in the horizontal direction throughout the structure and there exists no evidence of such defects in HRTEM analyses. In addition, misfit and threading dislocations are known to be created in the growth direction in InGaN/GaN heterostructures grown on the c-polar GaN structures. As a consequence, this analysis brings up the question of polarization effects in InGaN/GaN heterostructures.

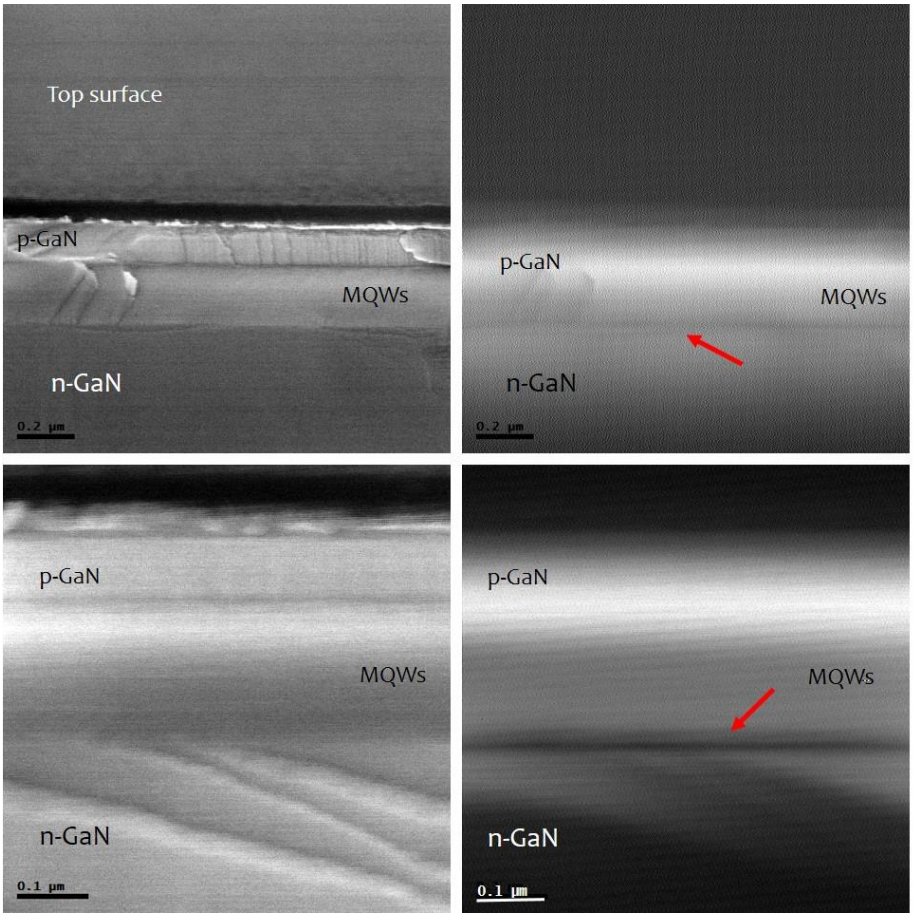

Figure 3.24 (a) SEM image, and (b) cross-sectional EBIC image of $In_{0.15}Ga_{0.85}N$/GaN MQWs solar cells grown on sapphire and; (c) SEM image, and (d) top surface EBIC image of the same structure at higher magnification at acceleration voltage of 5 keV.

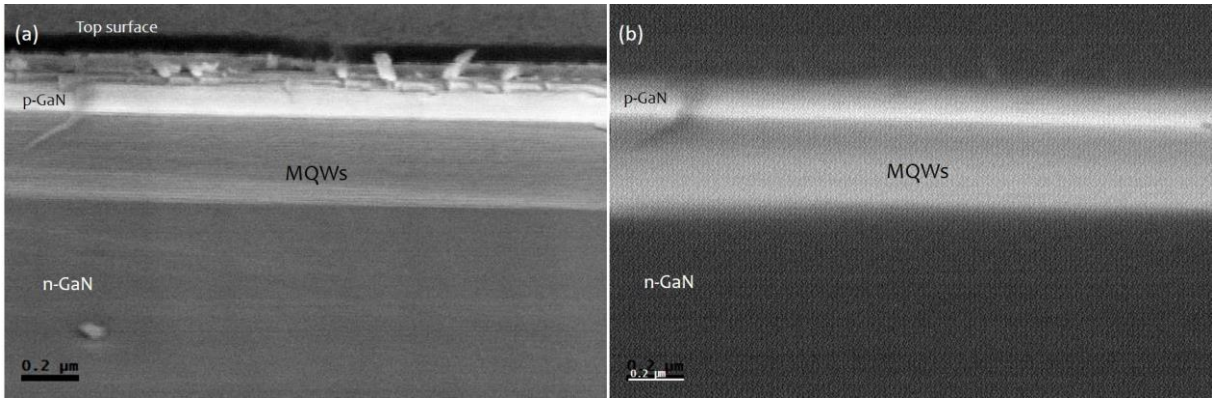

Figure 3.25 (a) SEM image and (b) cross-sectional EBIC image of $In_{0.15}Ga_{0.85}N$/GaN MQWs solar cells grown on bulk GaN substrate at acceleration voltage of 5 keV.

Sumiya *et al.* reported similar S-shape behavior in I-V characteristics of p-GaN/i-$In_{0.20}Ga_{0.80}N$/n–GaN solar cell structures with p-GaN [Mg: 3 x 10^{19} cm^{-3}] and n-GaN with Si doping varied between 3 × 10^{18} cm^{-3} and 3 × 10^{19} cm^{-3} [159]. Figure 3.26 (a) presents the simulated illuminated I-V plots of relaxed and strained p-i-n solar cells with several Si doping concentrations in n-type GaN. They stated that as the concentration of the Si-doping is reduced in the n-type GaN, the potential of the band profile at the i-InGaN/n-GaN interface is pulled up due to piezoelectric field induced by strain effect as shown in Figure 3.26 (b). Carrier recombination occurs at the i/n junction at 0V bias due to the accumulation of electrons at the interface. When the Si-doping concentration is increased up to 3 × 10^{19} cm^{-3}, the band profile and the IV characteristics become comparable to that of the relaxed model with 7 × 10^{18} cm^{-3} of Si doping where no strain effect is present. Therefore, higher levels of doping in n-type GaN layer is proposed as a solution to overcome the adverse effects of induced P_{PZ} and allow the flow of electrons into the n^+ layer without recombination.

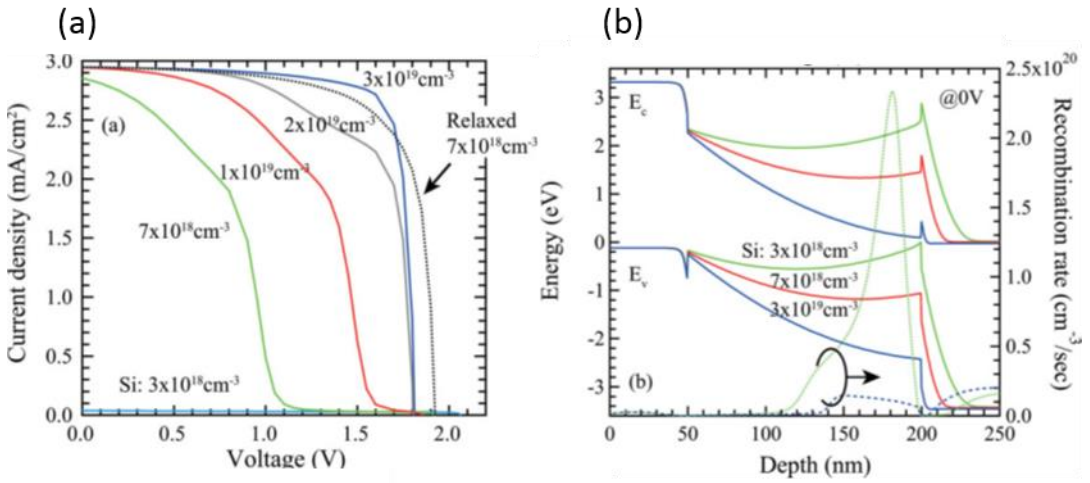

Figure 3.26 (a) Simulated I–V characteristics of the strained and relaxed p–i–n heterostructures for various Si-doping of the n-GaN layer. (b) The corresponding band profiles and recombination rate calculated at 0V [159].

Similarly, in our study, the doping level of the n-type GaN is 5×10^{18} cm^{-3}, which could create such large internal piezoelectric field at the strained i-InGaN/n-GaN interface. The strain effect due to insufficient doping of the n-GaN also explains the carrier recombination revealed as dark strip at the i/n interface in the cross-sectional EBIC analyses. As a consequence of the deficient carrier collection at the contacts, the illuminated IV curves are pulled upwards causing an S-shape behavior.

To conclude, fully strained pseudomorphic 25 pairs of $In_{0.15}Ga_{0.85}N$/GaN MQWs structures grown on sapphire and bulk GaN substrates are processed by using the mesa etch with SiO_2 mask and sidewall protection giving rise to fully functional solar cells with high yield and homogeneous characteristics. EQE analyses revealed that for both samples the spectral cut-off wavelength is extended up to around 450 nm owing to $In_{0.15}Ga_{0.85}N$/GaN MQWs. The solar cells grown on GaN substrates exhibit lower EQE peak and relatively high dark saturation current compared to the devices grown on sapphire substrates. The photovoltaic characterization under 1 sun resulted in degraded V_{OC}, J_{SC}, FF and η for the solar cells grown on bulk GaN substrate confirming the EQE and dark I-V characteristics. Unlike the defect-free HRTEM analyses which were nearly identical for these two samples, the top surface EBIC characterizations revealed a defective structure for the solar cells grown on GaN substrate. Contrary to the literature, where devices on GaN substrates exhibit superior performance that those on sapphire, this study showed that the epitaxial growth of InGaN/GaN MQWs on GaN resulted in inhomogeneity and poor crystalline quality. Moreover, the cross sectional EBIC analyses enlightened the origin of S-shape character of the illuminated I-V curves of the $In_xGa_{1-x}N$/GaN MQWs solar cells with x=0.15 and 0.19. The dark contrast, which is observed at the interface of the i-InGaN/n-GaN is associated with carrier recombination. The reason for such behavior can be explained by insufficient doping of the n-GaN (5×10^{18} cm^{-3}), which creates piezoelectric field induced by strain effect and causes accumulation of the electrons at the i/n interface. The carrier recombination and hence the S-shape behavior of the I-V curves could be suppressed by increasing the level of doping in the n-type GaN close to the interface.

Conclusions and outlooks

This thesis focused on fabrication and both material and device characterization of InGaN based solar cells absorbing in green-violet spectral range. The epitaxial growth of all solar cell designs using p-GaN/i-InGaN/n-GaN structures were performed by metal-organic vapor phase epitaxy (MOCVD) by the company NovaGaN. Two main objectives of this work were to investigate the influence of the active region design and the type of substrate on the crystalline quality of the solar cell structures as well as the development and the optimization of a full device fabrication process.

The principal motivation of the development of InGaN based solar cells is to go beyond the photovoltaic conversion limit of 50% by possible integration of InGaN with the current PV technologies. Furthermore, InGaN alloy, which has emerged as a promising candidate for harsh environment-sustainable solar cells that can be used in space or concentrated sunlight applications, is certainly worth being investigated. However, the growth of high quality InGaN layers with more than 20% of indium, which can achieve the attractive band gaps unreachable by current high efficiency PV technologies, is very challenging due to formation of extended crystalline defects and phase separation within the alloy. As a result, InGaN based solar cells have not yet demonstrated high efficiencies as expected. As a matter of fact, the design of the active region using InGaN with desired band gaps should take the particularities of this material system into consideration to enhance the conversion efficiencies. Besides, a reproducible and reliable processing sequence should be developed to fabricate fully functional and efficient InGaN based solar cells. This is why, in this study many of the samples were used for technology optimization purposes, but were not converted into fully functional devices.

The first part of the thesis mainly reports an investigation on the influence of the nature of the active region and the type of substrate of the solar cell designs on their structural and optical properties. The analysis of crystalline quality of bulk 200 nm thick InGaN layers with $x \sim 0.3$ as the active region showed very high dislocation density and phase separation within the InGaN layer, indicating that thick InGaN layers are extremely challenging to be used in solar cell applications. As an alternative, InGaN/GaN multiple-quantum well heterostructures were adopted as the active region, where few nanometers of defect free InGaN epilayers and relatively thicker GaN barrier layers were grown repetitively. The structural analysis as a function of different design parameters such as the indium content and the thickness of the quantum wells

in InGaN/GaN MQWs provided interesting information about the morphological evolution of the epitaxial layers.

It can be concluded that the crystalline quality of the epilayers degrades significantly as a function of increasing the In content due to higher levels of strain between InGaN and GaN. As the content of In gets higher, the lattice mismatch between InGaN and GaN increases and the critical thickness to grow defect free InGaN on GaN decreases rapidly. As a matter of fact, the solar cell design having 25 pairs of InGaN (2.6 nm)/GaN (12 nm) MQWs with x=0.1 showed the best structural quality with very low compositional and thickness fluctuations as well as fully pseudomorphic growth quality. In addition, this structure exhibited very low rms surface roughness indicating low dislocation density. However, due to its relatively high absorption band gap, E_g~3.1 eV, this design is not really attractive for high efficiency PV applications.

On the other hand, the design having 25 pairs of InGaN (2.5 nm)/GaN (8.3 nm) MQWs with x=0.19 is a promising candidate for SC applications owing to its spectral response extended to 495 nm (2.5 eV), obtained by the EQE measurements. The structural analysis by STEM showed well strained layers and low fluctuation in the well thicknesses. However, by AFM and PL analyses, which provide information from larger areas, it was seen that this design includes some structural defects due to strain relaxation. The existence of these defects is the primary reason for low V_{OC}, η and EQE values and, hence low performances of the solar cells fabricated from these structures. On the other hand, as it was mentioned, the fabrication process of this solar cell design was not fully optimized, which causes dark saturation current values of $7.73x10^{-6}$ mA/cm^{-2} and shadows significantly the device performances. The well thickness of this design can be further decreased to improve the growth quality, but in this case higher numbers of MQWs would be necessary for more efficient absorption.

In addition, this study reports on comparative structural and optical characterization of solar cell designs with 25 and 35 pairs of InGaN/GaN MQWs with relatively high targeted In content, i.e. x~0.3, as a function of InGaN well thickness. The SC design with t_W~4 nm, which include 35 pairs of $In_{\sim 0.3}Ga_{\sim 0.7}N$/GaN MQWs exhibited great irregularities in In content and thickness of quantum wells and barriers. It was found out that the well thickness and the indium content increase as a function of the growth time, leading to increase in elastic strain and formation of dislocation in the structure. As a result, the subsequent periodic structures are grown on inclined planes and causes formation of a mixed (2D and 3D) heterostructures. When a lower well thickness was targeted, the integrity of the $In_{0.24}Ga_{0.76}N$/GaN MQWs were shown to

be well preserved throughout the structure with an average InGaN well thickness of 3.1 nm which indicated a better growth quality compared to the former design. However, STEM and AFM analyses revealed formation of dislocations and several fluctuations in well widths. Further reduction of t_W to 2.6 nm with the same In content of x=0.24, resulted in lower rms surface roughness and FWHM of the PL peaks, pointing out a significant improvement in the structural quality. Furthermore, it is worth noting that the integrity of high numbers of InGaN/GaN MQWs for such high In contents is well preserved. The fabricated solar cells from the latter design exhibited spectral cut-off extending to 530 nm, which corresponds to an absorption band gap of 2.33eV. However, low V_{OC} and EQE values and inhomogeneous PV characteristics of this design were attributed to high density of dislocations, possible segregation of Indium clusters and non-optimized processing parameters. In addition, possible fluctuations in well widths and/or in composition of indium within the wells, can favor the localization of carriers and cause eventual trapping of the carriers in the PV devices. High dark saturation current of 9.84×10^{-4} mA/cm^2 and anomalously elevated ideality factors confirmed also the degraded crystalline quality and low photovoltaic performances.

Moreover, this work includes a comparison of crystalline quality and device performances of two solar cell designs having 25 pairs of $In_{0.15}Ga_{0.85}N$/GaN MQWs grown on two different types of substrates, i.e. sapphire and bulk GaN. The STEM analyses revealed homogeneous well thicknesses of 2.2 nm and 2.5 nm, in addition to barrier thicknesses of 4.8 nm and 4.5 nm for the designs grown on sapphire and bulk GaN, respectively. Both structures exhibited defect free and well strained InGaN/GaN MQWs by STEM and XRD analyses. However, surface characterization by AFM revealed an inhomogeneous quality for the structure grown on bulk GaN. In addition, relatively higher FWHM of the PL peak indicated a slight degradation on the crystalline quality. The solar cells grown on GaN substrate showed indeed lower V_{OC}, EQE and conversion efficiency compared to those grown on sapphire substrate, pointing out that most of the photogenerated carriers recombine due to the structural defects and cannot contribute to efficient energy conversion. Despite the slightly thicker absorption thickness of the device grown on GaN, the solar cell grown on sapphire exhibits much higher J_{SC}. These results were also confirmed with top-surface EBIC analyses, which revealed more pronounced presence of dark and bright spots that correspond to structural defects and local compositional fluctuations for the devices grown on bulk GaN substrates. Consequently, the non-uniformity of the active region points out the vulnerability and instability of the growth on this new type of

substrate. It can be concluded that the growth on bulk GaN substrate requires further optimization in order to be fabricated into solar cells with improved characteristics.

Finally, the best photovoltaic performance was obtained with the solar cell having 25 pairs of $In_{0.15}Ga_{0.85}N$/GaN MQWs grown on sapphire with V_{OC} of 1.80 V, J_{SC} of 0.586 mA/cm^2, FF of 56.77% and a conversion efficiency of 0.59%. This solar cell exhibits an extended spectral response up to 450 nm (2.75 eV) and a peak EQE value of 24.2%. However, compared to the devices with similar characteristics that are reported in the literature, the V_{OC} is relatively low and the illuminated I-V curve exhibits an S-shape feature, indicating a partial failure of the device which can be due to insufficient photogeneration and/or collection. The cross sectional EBIC analyses provided crucial information about the origin of this S-shape behavior. The dark contrast, which is observed at the interface of the i-InGaN/n-GaN was associated with carrier recombination. The reason for such behavior was explained by insufficient doping of the n-GaN layer (5×10^{18} cm^{-3}), which creates piezoelectric field induced by strain effect and causes accumulation of the electrons at the i/n interface. The carrier recombination and hence the S-shape behavior of the I-V curves can be suppressed by increasing the level of doping in the n-type GaN close to the interface.

There are several significant conclusions that can be drawn out from this work and future work to be carried out in order to achieve higher efficiency InGaN based solar cells.

- The comparative structural analyses of the designs with thick InGaN layer and InGaN/GaN MQWs with t_w in the range of 2 to 4 nm, revealed clearly that MQW structures should be adopted by targeting well thicknesses lower than the critical thickness for higher crystalline quality and functional devices.
- The solar cell design with 25 pairs of InGaN (2.5 nm)/GaN (8.3 nm) MQWs with x=0.19 is a promising candidate for integration with the current multi-junction PV technologies, which requires an additional junction near 2.65 eV to achieve higher efficiencies than 50% [160]. For enhanced and homogenous crystalline quality, the thickness of the quantum wells can be further decreased to around 2 nm. This would necessitate growth of higher numbers of InGaN/GaN MQWs pairs for improved photon absorption. In addition, targeting thinner GaN quantum barriers of around 4-5 nm, would also facilitate the carrier tunneling and enhance the short circuit current J_{SC} of the solar cells [161, 162]. It was shown that the development of higher In content InGaN/GaN MQWs (x>0.2)

is much more complicated since it would require better control over the epitaxial growth of thinner InGaN wells and higher number of MQW pairs.

- An optimized and reproducible processing has been developed for fabrication of InGaN based solar cells. The challenges such as mesa etching of GaN and contamination on the device sidewalls, which caused high reverse leakage currents, were studied and solutions of using SiO_2 mask and protection of sidewalls by SiO_2 layers were proposed. These solutions finally resulted in high yield fully functional devices with homogeneous PV characteristics. In addition, the optimization study of thermal treatment of Ni/Au current spreading layer was found to be 10 minutes of annealing at 500°C in air, which led to the best device performances.
- The thermally treated Ni/Au layer in our work was shown to provide 60-65% transmittance in the absorption wavelength range of InGaN active region (400-500 nm). Another alternative for low contact resistance technology with high transmittance would be to use the transparent conductive oxide such as Indium tin oxide (ITO). For instance, the best combination of highest transmittance and conductivity in ITO layers grown on p-GaN were reported by Yan *et al.,* i.e. resistivity of 1.19×10^{-4} Ωcm^2 and transparency of 94.17% at 460 nm [163]. However, it is important to notice that development of ITO layers is a challenging task, since it requires a reproducible deposition procedure and subsequent thermal annealing treatment.
- The S-shape behavior of the illuminated I-V curves of SC designs having $In_xGa_{1-x}N$/GaN MQWs with x=0.15 and x=0.19 was explained to be due to deficient doping of the n-GaN (5×10^{18} cm^{-3}), which builds piezoelectric field and causes accumulation of the electrons at the i/n interface. As a solution, a highly doped n^+-GaN layer of 10-20 nm [Si:10^{19-20} cm^{-3}] can be grown on the n-doped GaN to screen the polarization charges.

An important future perspective of InGaN solar cells is to integrate them with already existing high efficiency multi-junction solar cells. The multijunction solar cells can be developed by formation of monolithic cells, in which the sub-cells are internally series connected by tunnel junctions or development of stacked cells which consist of isolated and individually probed cells. The first technique is possible by establishing current matching between different sub-cells by using tunnel junctions, which requires lattice-matched materials. The direct growth of InGaN/GaN heterostructures on non-nitride based sub-cells, i.e. Si or GaAs solar cells, is very challenging due to large lattice mismatch and need of high temperatures required by MOCVD. Therefore, a simple approach of stacking the sub-cells could be done by flip-chip technology and

bonding by ITO layer. In this case, two solar cells can be developed separately and integrated at the end to achieve higher efficiencies. This designs requires careful simulation for determination of InGaN material parameters to be matched with the underlying sub-cell as well as optimization of the interface quality and doping of the interlayers to obtain the optimum charge transport.

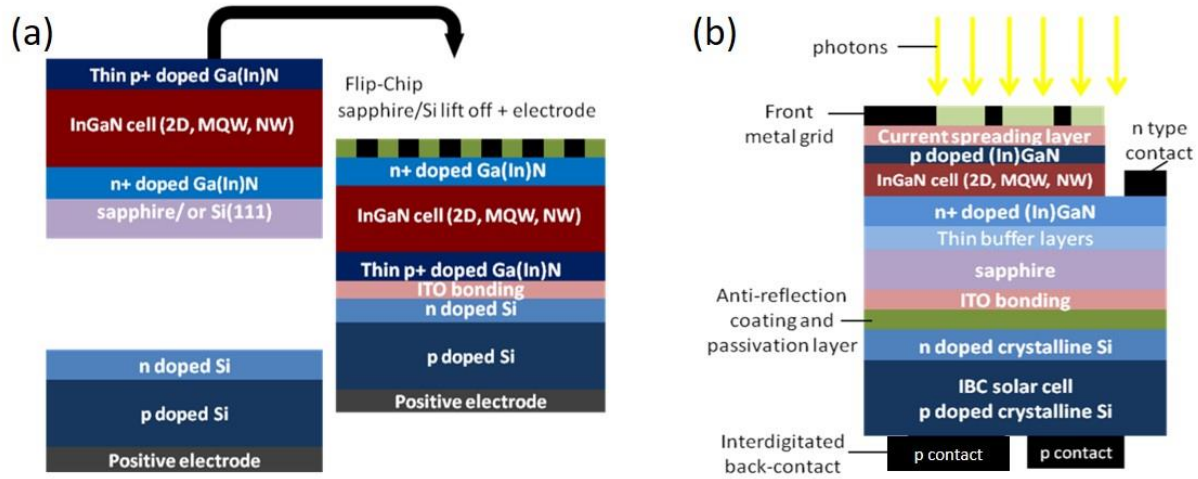

Figure 4.1 Possible design of (a) two terminal current matched InGaN based tandem solar cells, and (b) stacked InGaN-Si tandem solar cell with no need of current matching.

Figure 4.1 (a) displays a 2-junction tandem solar cell based on InGaN with current matching, while Figure 4.1 (b) presents another suggestion for integration where current matching is not needed. The second approach for hybrid integration is stacking of the sub-cells with a bonding layer (i.e. ITO) and anti-reflection layer to enhance the light absorption. Such a tandem cell would have 4 contact terminals, which should be connected to an electronic circuit board by wire bonding to collect the total current. The integration of InGaN with low-cost and mature Si technology can promise efficiencies higher than the theoretical limit of c-Si cells and can achieve around 40% under concentrated sunlight. Even though, this value is lower than the current state of the art, low cost would be a potential advantage for the proposed tandem cells.

Furthermore, the integration of III-nitrides with Si can be possible by nano-selective area growth of (In)GaN on AlN/Si (111) substrates. This technique was proposed using nanoscale growth initiation sites, which can reduce or even eliminate the pre-existing threading dislocations in the defective seed layers leading to high quality re-grown nanostructures [164, 165]. Recently, Sundaram *et al.* reported nano-selective area growth of homogeneously distributed defect free InGaN nanopyramids with 33% In incorporation having average size of 86 nm [166]. Their study showed that it is possible to grow elastically strained 2D InGaN nanopyramids with smooth triangular sidewall semi-polar facets, i.e. (1–101) planes, on AlN/Si

(111) substrates. This approach can be of great interest, since it offers growth of defect free In-rich InGaN nanostructures, which would pave the way for the development of InGaN based multijunction solar cells. In addition, the nano-selective area growth technology can be attractive for realization of InGaN/Si tandem cells, which would benefit from low-cost, large size and high crystalline quality Si wafers, to achieve broad solar spectral absorption and high efficiency PV.

InGaN material system can also be integrated with the high efficiency GaAs based tandem solar cells. McMohan *et al.* suggested a device architecture including InGaN sub-cell providing band gaps of more than 2.65 eV and a 4 junction III-V material based tandem cell covering from 0.74 eV to 2.65 Ev [167]. The cell bonding was proposed to be done with interconnect method, which exploits arrays of metal pillars for charge transport. This four-terminal configuration model can achieve efficiencies around 60%, owing to wide spectral absorption.

Furthermore, owing to its wide and direct band gap, InGaN material system is promising to be developed in the form of multijunction solar cells. However, as already mentioned, current matching between different InGaN sub-cells having different In contents, is not trivial due to issues related to the interfaces and charge transport. As a solution, polarization-engineered p-GaN/InGaN/n-GaN tunnel junction (TJ) with high tunneling probability and low tunneling resistance could be used. This approach of tunneling junctions is possible owing to the polarization induced dipoles, which can generate significantly high electric fields resulting in the band bending over a small distance and hence increase the tunneling probability. Recently, polarization induced TJs have become attractive for III-nitride optoelectronic devices and preliminary demonstrations have been presented in LEDs [168-170] and Vertical-cavity surface emitting laser (VCSELs) [171], since they offer the possibility to replace the highly resistive p-type contact material and result in enhanced light extraction. In addition, they could serve as tunnel junctions to connect multiple active regions in series in LEDs and multijunction solar cells [172]. As a future perspective, this approach requires optimization of growth conditions and interface properties for efficient current matching. This technique can be very promising for possible use of InGaN PV in harsh environments, since it uses only III-Nitride materials, which are known to have excellent thermal stability and high radiation tolerance.

Bibliography

[1] H. P. Maruska and J. J. Tietjen. The preparation and properties of vapor-deposited single-crystal-line GaN. *Appl. Phys. Lett.* 15:327–329, 1969.

[2] S. Yoshida, S. Misawa, and S. Gonda. Improvements on the electrical and luminescent properties of reactivemolecular beam epitaxially grown GaN films by using AlN-coated sapphire substrates. *Appl. Phys. Lett.* 42:427–429, 1983.

[3] H. Amano, N. Sawaki, I. Akasaki, and Y. Toyoda. Metalorganic vapor phase epitaxial growth of a high quality GaN film using an AlN buffer layer. *Appl. Phys. Lett.*48:353–355, 1986.

[4] S. Nakamura. GaN growth using GaN buffer layer. *Jpn. J. Appl. Phys*. 30: L1705–L1707, 1991.

[5] S. Nakamura, T. Mukai, and M. Senoh. High-power GaN p-n junction blue-light-emitting diodes. *Jpn. J. Appl. Phys.*30:L1998–L2001, 1991.

[6] S. Nakamura, N. Iwasa, M. Senoh, and, T. Mukai. Hole Compensation Mechanism of P-Type GaN Films. *Jpn. J. Appl. Phys.* 31:1258-1266, 1992.

[7] S. Nakamura, T. Mukai, M. Senoh, and N. Iwasa. Thermal Annealing Effects on P-Type Mg-Doped GaN Films. *Jpn. J. Appl. Phys.* 31:L139-L142, 1992.

[8] S. Nakamura, M. Senoh, and T. Mukai. p-GaN/n-InGaN/n-GaN double-heterostructure blue-light-emitting diodes. *Jpn. J. Appl. Phys.* 32:L8–L11,1993.

[9] S. Nakamura, M. Senoh, N. Iwasa, S. Nagahama, T. Yamada, and T. Mukai. Superbright green InGaN single-quantum-well-structure light-emitting diodes. *Jpn. J. Appl. Phys.*34:L1332–L1335, 1995.

[10] S. Keller, B. P. Keller, Y.-F. Wu, B. Heying, D. Kapolnek, J. S. Speck, U. K. Mishra, and S. P. DenBaars. Influence of sapphire nitridation on properties of gallium nitride grown by metalorganic chemical vapor deposition. *Applied Physics Letters* 68(11):1525-1527, 1996.

[11] J. Wu, W. Walukiewicz, K. M. Yu, J. W. Ager, E. E. Haller, H. Lu, and W. J. Schaff. Small band gap bowing in In1−x GaxN alloys. Appl. Phys. Lett., 80(25):4741, 2002.

[12] Fraunhofer ISE. 2014. *New world record for solar cell efficiency at 46% French-German cooperation confirms competitive advantage of European photovoltaic industry.* [Press release] 01 December 2014.

[13] A. Marti and G.L. Araujo. Limiting efficiencies for photovoltaic energy conversion in multigap systems.*Sol. Energy Mater. Sol. Cells* 43:203-222, 1996.

[14] I. Allison, N.L. Bindoff, R.A. Bindschadler, P.M. Cox, N. de Noblet, M.H. England, J.E. Francis, N. Gruber, A.M. Haywood, D.J. Karoly, G. Kaser, C. Le Quéré, T.M. Lenton, M.E. Mann, B.I. McNeil, A.J. Pitman, S. Rahmstorf, E. Rignot, H.J. Schellnhuber, S.H. Schneider, S.C. Sherwood, R.C.J. Somerville, K. Steffen, E.J. Steig, M. Visbeck, A.J. Weave. *The Copenhagen Diagnosis: Updating the World on the Latest Climate Science*, UNSW Climate Change Research Center, Sydney, Australia, p. 7, 2009.

[15] K. Tanabe. A Review of Ultrahigh Efficiency III-V Semiconductor Compound Solar Cells: Multijunction Tandem, Lower Dimensional, Photonic Up/Down Conversion and Plasmonic Nanometallic Structures. *Energies*, 2: 504-530. 2009.

[16] A.E. Becquerel. Mémoire sur les effets électriques produits sous l'influence des rayons solaires. *Comt. Rend. Acad. Sci*., 9:561-597, 1839.

[17] Fraunhofer ISE. *Recent Facts about Photovoltaics in Germany*. Last updated on May 19, 2015, (http://www.ise.fraunhofer.de/en/publications/veroeffentlichungen-pdf-dateien-en/studien-und-konzeptpapiere/recent-facts-about-photovoltaics-in-germany.pdf)

[18] European Photovoltaic Industry Association. *Global Market Outlook for Photovoltaics 2014-2018.* Last updated on June 2014, (http://www.epia.org/fileadmin/user_upload/Publications/EPIA_Global_Market_Outlook_for_Photovoltaics_2014-2018_-_Medium_Res.pdf)

[19] T. Henzelmann, J. Schönfelder, P. Hattrup, C. Peters, A. Wiedem, J. Hobohm, F. Peter, L. Krampe, S. Mellahn, F. Sakowski, *Directions for the Solar Economy: PV-Roadmap 2020*. Last updated on December 16, 2010, (http://www.sma.de/fileadmin/content/global/Investor_Relations/Documents/2010-12_16_DT_2_01_10_009_Komplett-02-Kurz_E.pdf)

[20] Y. Wang, S. Zhou, et H. Huo. Cost and CO2 reductions of solar photovoltaic power generation in China: Perspectives for 2020. *Renewable and Sustainable Energy Reviews,* 39:370-380, 2014.

[21] Fraunhofer ISE. *Levelized Cost of Electricity Renewable Energy Technologies.* Last updated on November, 2013, (http://www.ise.fraunhofer.de/en/publications/veroeffentlichungen-pdf-dateien en/studien-und-konzeptpapiere/study-levelized-cost-of-electricity-renewable-energies.pdf)

[22] Morgan Stanley Research. *Solar Power & Energy Storage: Policy Factors vs. Improving Economics*. Last updated on July 28, 2014. (http://forms.greentechmedia.com/Extranet/95679/Morgan%20Stanley%20Solar%20Power%20&%20Energy%20Storage%20Blue%20Paper%20July%2029%202014.pdf)

[23] J. Nelson Physics of Solar cells. Imperial college press, pp 80-98, 2003.

[24] D.M. Chapin, C.S. Fuller, and G.L. Pearson. A New Silicon p-n Junction Photocell for Converting Solar Radiation into Electrical Power. *J. Appl. Phys*., 25:676-677, 1954.

[25] NREL: Best Research Cell Efficiencies 2015. http://www.nrel.gov/ncpv/images/efficiency_chart.jpg. (Accessed July 15th 2014).

[26] J. Zhao, A. Wang, M. A. Green, F. Ferrazza. 19.8% efficient "honeycomb" textured multicrystalline and 24.4% monocrystalline silicon solar cells. *Appl. Phys. Lett.,* 73(14):1991–1993, 1998.

[27] C. B. Honsberg, J. E. Cotter, K. R. McIntosh, S. C. Pritchard, B. S. Richards, S. R. Wenham. Design Strategies for Commercial Solar Cells using the Buried Contact Technology. *IEEE Transactions Electron. Dev*. 46(10):1984-1992, 1999.

[28] A. Slade, V. Garboushian. 27.6% Efficient Silicon Concentrator Solar Cells for Mass Production. Technical Digest of 15th International Photovoltaic Science and Engineering Conference, p.701-702, 2005

[29] W. Shockley and H.J. Queisser. Detailed Balance Limit of Efficiency of p-n Junction Solar Cells. *Journal of Applied Physics,* 32:510-519, 1961.

[30] A. Richter, M. Hermle, and S. W. Glunz. Reassessment of the Limiting Efficiency for Crystalline Silicon Solar Cells. *IEEE Journal of Photovoltaics* 3(4):1184-1191, 2013.

[31] J. S. Ward, B. Egaas, R. Noufi, M. Contreras, K. Ramanathan, C. Osterwald, et K. Emery. Cu(In,Ga)Se2 solar cells measured under low flux optical concentration. Photovoltaic Specialist Conference (PVSC), 2014.

[32] O. K. Jani. Development of wide-band gap InGaN solar cells for high efficiency photovoltaics. PhD thesis, Georgia Instute of Technology. Aug. 2008.

[33] H. Morkoç, Handbook of Nitride Semiconductors and Devices, Materials Properties, Physics and Growth. John Wiley & Sons, 2009.

[34] S. A. Dyer, Wiley Survey of Instrumentation and Measurement. John Wiley & Sons, 2004

[35] J. F. Nye, Physical Properties of Crystals. Oxford University Press, New York, 1985.

[36] O'Donnell, K. P., J. F. W. Mosselmans, R. W. Martin, S. Pereira, and M. E. White. Structural Analysis of InGaN Epilayers. *Journal of Physics: Condensed Matter* 13(32):6977-6991, 2001.

[37] Vurgaftman and J. R. Meyer, Band parameters for nitrogen containing semiconductors. *J. Appl. Phys.* 94(6):3675, 2003.

[38] F. Bernardini, V. Fiorentini, D. Vanderbilt, Nonlinear macroscopic polarization in III-V nitride alloys. *Phys. Review B*, 64:085207, 2001.

[39] Morkoç, R. Cingolani, and B. Gill. Polarization effects in nitride semiconductors and device structures. *Mat. Res. Innovat.* 3:97-106, 1999.

[40] F. Bernardini, V. Fiorentini. Polarization fields in nitride nanostructures: 10 points to think about. *App. Surface Science*. 166:23-29, 2000.

[41] F. Bernardini, V. Fiorentini, D. Vanderbilt. Spontaneous polarization and piezoelectric constants of III-V nitrides. *Phys. Review B*, 56:10024, 1997.

[42] R. D. Dupuis, Epitaxial growth of III–V nitride semiconductors by metalorganic chemical vapor deposition. *Journal of Crystal Growth* 178(1-2):56-73, 1997.

[43] M. Leszczynski, P. Prystawko, T. Suski, B. Lucznik, J. Domagala, J. Bak-Misiuk, A. Stonert, A. Turos, R. Langer, and A. Barski. Lattice parameters of GaN single crystals, homoepitaxial layers and heteroepitaxial layers on sapphire. *Journal of Alloys and Compounds*. 286(1-2):271-275, 1999.

[44] Bridgelux. 2012. *Bridgelux and Toshiba achieve world class performance for 8" GaN-on-silicon LEDs* [Press release] 10 May 2012.

[45] K. Fujito, S. Kubo, and I. Fujimura. Development of bulk GaN crystals and nonpolar/semipolar substrates by HVPE. *MRS Bull*. 34:313–317, 2009.

[46] T. Yoshida, Y. Oshima, T. Eri, K. Ikeda, S. Yamamoto, K. Watanabe, M. Shibata, and T. Mishima. Fabrication of 30 in GaN substrates by hydride vapor phase epitaxy using void-assisted separation method. *J. Crystal Growth,* 310:5–7, 2008.

[47] T. Nagatomo, T. Kuboyama, H. Minamino, and O. Omoto. Properties of $Ga_{1-x}In_xN$ Films Prepared by MOVPE. *Jpn. J. Appl. Phys.*28 (8A): L1334, 1989.

[48] E.L. Piner, M.K. Behbehani, N.A. El Masry, F.G. McIntosh, J.C. Roberts, K.S. Boutros, S.M. Bedair. *Effect of hydrogen on the indium incorporation in InGaN epitaxial films*. *Applied Physics Letters* 70:461, 1997.

[49] Guo, Y., X. L. Liu, H. P. Song, A. L. Yang, X. Q. Xu, G. L. Zheng, H. Y. Wei, S. Y. Yang, Q. S. Zhu, and Z. G. Wang. A Study of Indium Incorporation in In-Rich InGaN Grown by MOVPE. *Applied Surface Science* 256(10):3352–3356, 2010.

[50] I. Ho, and G. B. Stringfellow. Solid phase immiscibility in GaInN. *Appl. Phys. Lett.* 69:2701-2703, 1996.

[51] K. Y. Lai, G. J. Lin, Y. L. Lai, Y. F. Chen, and J. H. He. Effect of indium fluctuation on the photovoltaic characteristics of InGaN/GaN multiple quantum well solar cells. *Appl. Phys. Lett*. 96:081103-1-081103-3, 2010.

[52] B. N. Pantha, J. Li, J. Y. Lin, and H. X. Jiang. Evolution of phase separation in In-rich InGaN alloys. *Appl. Phys. Lett*. 96:232105-1-232105-3, 2010.

[53] R. Singh, D. Doppalapudi, T. D.Moustakas, and L. T. Romano. Phase separation in InGaN thick films and formation of InGaN/GaN double heterostructures in the entire alloy composition, *Appl. Phys. Lett*. V.70**,** 1089, 1997.

[54] I. H. Kim, H. S. Park, Y. J. Park, and T. Kim. Formation of V-shaped pits in InGaN/GaN quantum wells and bulk InGaN films. *Appl. Phys. Lett.*73:1634, 1998.

[55] D. Holec, Y. Zhang, D. V. Sridhara Rao, M. J. Kappers, C. McAleese, and C. J. Humphreys. Equilibrium critical thickness for misfit dislocations in III-nitrides. *J. Appl. Phys.* 104(12):123514-1–123514-7, 2008.

[56] M.J. Keevers and M.A. Green. Extended infrared response of silicon solar cells and the impurity photovoltaic effect. *Sol. Energy Mater. Sol. Cells*, 41(1): 195–204, 1996.

[57] G.F. Brown and J. Wu. Third generation photovoltaics. *Laser Photonics Rev.*, 3(4):394–405, 2009.

[58] K.W.J. Barnham and G. Duggan. A new approach to high-efficiency multi-band-gap solar cells. *J. Appl. Phys.*, 67: 3490–3493, 1990.

[59] Y.-J. Sun, Growth and characterization of m-plane GaN and (In,Ga)N/GaN multiple quantum wells. PhD thesis, 2004.

[60] S. F. Chichibu, A. Uedono, T. Onuma, B. A. Haskell, A. Chakraborty, T. Koyama, P. T. Fini, S. Keller, S. P. DenBaars, J. S. Speck, U. K. Mishra, S. Nakamura, S. Yamaguchi, S. Kamiyama, H. Amano, I. Akasaki, J. Han, and T. Sota. Origin of defect-insensitive emission probability in In-containing (Al, In,Ga)N alloy semiconductors. *Nat Mater*. 5 (10):810-816, 2006.

[61] Pust, Philipp, Peter J. Schmidt, and Wolfgang Schnick. A Revolution in Lighting. *Nature Materials* 14(5):454–58, 2015.

[62] H.J. Round. A note on carborundum. *Electr. World* 19:309–310, 1907.

[63] O. Losev, O. V. *Telegrafiya i Telefoniya bez Provodov (transl. Wireless Telegraphy and Telephony)* 44:485–494, 1927.

[64] N. Holonyak, S.F. Bevacqua. Coherent (Visible) Light Emission from Ga ($As_{1-x}P_x$) Junctions. *Appl. Phys. Lett*. 1:82–83, 1962.

[65] M.G. Craford, R.W. Shaw, AH. Herzog, W.O. Groves. Radiative recombination mechanisms in GaAsP diodes with and without nitrogen doping. *J. Appl. Phys.* 43:4075–4083, 1972.

[66] V. A. Tyagi, V. A. Eustigneev, A. M. Krasilo, A. F. Andreeva, and V. Y.Malatidiou. Optical properties of Indium nitride films. *Sov. Phys. Semicond.* 11:1257 -1259, 1977.

[67] K. L. Westra, R. P. W. Lawson, and M. J. Brett, The effects of oxygen contamination on the properties of reactively sputtered indium nitride films. *J. Vac. Sci. Technol.* A 6:1730-1732, 1988.

[68] J. Wu. When Group-III Nitrides Go Infrared: New Properties and Perspectives*. Journal of Applied Physics* 106(1): 011101, 2009.

[69] Yamaguchi, Shigeo, Michihiko Kariya, Shugo Nitta, Tetsuya Takeuchi, Christian Wetzel, Hiroshi Amano, and Isamu Akasaki. Anomalous Features in the Optical Properties of Al1−xInxN on GaN Grown by Metal Organic Vapor Phase Epitaxy. *Applied Physics Letters* 76(7):876–78, 2000.

[70] H. Lu, W. J. Schaff, J. Hwang, H. Wu, G. Koley, and L. F. Eastman, Effect of an AlN buffer layer on the epitaxial growth of InN by molecular-beam epitaxy. *Appl.Phys. Lett.* 79:1489, 2001.

[71] V. Y. Davydov, A. A. Klochikhin, R. P. Seisyan, V. V. Emtsev, S. V. Ivanov, F. Bechstedt, J. Furthmuller, H. Harima, V. Mudryi, J. Aderhold, O. Semchinova, and J. Graul, Absorption and Emission of Hexagonal InN. Evidence of Narrow Fundamental Band Gap. *Phys. Status Solidi B* 229(3):R1-R3, 2002.

[72] Y. Nanishi, Y. Saito, and T. Yamaguchi, RF-molecular beam epitaxy growth and properties of InN and related alloys. *Jpn. J. Appl. Phys*. 42:2549-2559, 2003.

[73] O. Jani, C. Honsberg, Y. Huang, J.-O.Song, I. Ferguson, G. Namkoong, E. Trybus, A. Doolittle, and S. Kurtz. Design, Growth, Fabrication and Characterization of High-Band GaP InGaN/GaN Solar Cells. Conf. Rec. Proc. 4th World Conf. Photovoltaic. Energy Convers, 2006.

[74] C. J. Neufeld, N. G. Toledo, S. C. Cruz, M. Iza, S. P. DenBaars, and U.K. Mishra. High quantum efficiency InGaN/GaN solar cells with 2.95 eV band gap. *Appl. Phys. Lett.*, 93(14):143502-1–143502-3, 2008.

[75] Yang, X. Wang, H. Xiao, J. Ran, C. Wang, G. Hu, X. Wang, X. Zhang, J. Li, and J. Li. Photovoltaic effects in InGaN structures with p–n junctions. *Phys. Stat. Sol.* (a), 204(12): 4288–4291, 2007

[76] O. Jani, I. Ferguson, C. Honsberg, and S. Kurtz. Design and characterization of GaN/ InGaN solar cells. *Appl. Phys. Lett*., 91(13): 132117-1–132117-3, 2007.

[77] X. Chen, K.D. Matthews, D. Hao, W.J. Schaff, and L.F. Eastman. Growth, fabrication, and characterization of InGaN solar cells. *Phys. Stat. Sol. (a).*, 205(5): 1103–1105, 2008.

[78] P. Misra, C. Boney, N. Medelci, D. Starikov, A. Freundlich, and A. Bensaoula, Fabrication and characterization of 2.3eV InGaN photovoltaic devices. 33rd IEEE Photovoltaic Specialists Conf., 2008.

[79] R. Dahal, B. Pantha, J. Li, J.Y. Lin, and H.X. Jiang. InGaN/GaN multiple quantum well solar cells with long operating wavelengths. *Appl. Phys. Lett.*, 94(6): 063 505-1–063 505-3, 2009.

[80] J.P. Shim, S.R. Jeon, Y.K. Jeong, and D.-S. Lee. Improved efficiency by using transparent contact layers in InGaN-based p-i-n solar cells. *IEEE Electron Device Lett.*, 31(10):1140–1142, 2010.

[81] J.-P. Shim, M. Choe, S.-R. Jeon, D. Seo, T. Lee, and D.-S. Lee. InGaN based p–i–n solar cells with graphene electrodes. *Appl. Phys. Express.*, 4(5): 052302-1–052302-3, 2011.

[82] Y. Kuwahara, T. Fujii, T. Sugiyama, D. Iida, Y. Isobe, Y. Fujiyama, Y. Morita . GaInN-based solar cells using strained-layer GaInN/GaInN superlattice active layer on a freestanding GaN substrate. *Appl. Phys. Express*, 4(2): 021001-1–021001-3, 2011.

[83] N. G. Young, E. E. Perl, R. M. Farrell, M. Iza, S. Keller, J. E. Bowers, S. Nakamura, S. P. DenBaars, and J. S. Speck. High-performance broadband optical coatings on InGaN/GaN for multijunction device integration, *Appl. Phys. Lett.*, 104:163902-1-163902-4, 2014.

[84] A.G. Bhuiyan, K. Sugita, A. Hashimoto, and A. Yamamoto. InGaN solar cells: Present state of the art and important challenges. *IEEE J. Photovoltaics*, 2(3):276-293, 2012.

[85] Yamamoto, Md. R. Islam, T.T. Kang, and A. Hashimoto. Recent advances in InN based solar cells: Status and challenges in InGaN and InAlN solar cells. *Phys. Stat. Sol.(c)*, 7(5): 1309–1316, 2010.

[86] C. Boney, I. Hernandez, R. Pillai, D. Starikov, A. Bensaoula, M. Henini, M. Syperek, J. Misiewicz, and R. Kudrawiec. Growth and characterization of InGaN for photovoltaic devices. *Phys. Stat. Sol*. (c), 8(7–8): 2466–2668, 2011.

[87] B.R. Jampana, A.G. Melton, M. Jamil, N.N. Faleev, R.L. Opila, I.T. Ferguson, and C.B. Honsberg. Design and realization of wideband-gap (~2.67 eV) InGaN p-n junction solar cell. *IEEE Electron Device Lett*., 31(1): 32–34, 2010.

[88] X. Cai, Y. Wang, B. Chen, M.-M. Liang, W.-J. Liu, J.-Y. Zhang, X.-Q. Lv, L.-Y. Ying, and B.-P. Zhang. Investigation of InGaN p-i-n Homojunction and Heterojunction Solar Cells. *IEEE Photonics Technology Letters*, 25(1):59-62, 2013.

[89] X.-M. Cai, S.-W. Zeng, and B.-P. Zhang. Fabrication and characterization of InGaN p-i-n homojunction solar cell. *Appl. Phys. Lett.*, 95(17): 173 504-1–173 504-3, 2009.

[90] O. Jani, M. Mehta, H. Yu, I. Ferguson, R. Opila, and C. Honsberg, Optimization of GaN window layer for InGaN solar cells using polarization effect. 33rd IEEE Photovoltaic Specialists Conf., 2008.

[91] O. Jani, H. Yu, E. Trybus, B. Jampana, I. Ferguson, A. Doolittle, and C. Honsberg, Effect of phase separation on performance of III-V nitride solar cells, 22nd European Photovoltaic Solar Energy Conference.pp. 64–67, 2007.

[92] X. Zheng, R.-H. Horng, D.-S. Wuu, M.-T. Chu, W.-Y. Liao, M.-H. Wu, R.-M. Lin, and Y.-C. Lu. High-quality InGaN/GaN heterojunctions and their photovoltaic effects. *Appl. Phys. Lett*., 93(26): 261108-3, 2008.

[93] E. Matioli, C. Neufeld, M. Iza, S. C. Cruz, A. a. Al-Heji, X. Chen, R. M. Farrell, S. Keller, S. DenBaars, U. Mishra, S. Nakamura, J. Speck, and C. Weisbuch, High internal and external quantum efficiency InGaN/GaN solar cells. *Appl. Phys. Lett.*, 98(2):021102, 2011.

[94] J-H. Horng, S.-T. Lin, Y.-L. Tsai, M.-T. Chu,W.-Y. Liao,M.-H.Wu, R.- M. Lin, and Y.-C. Lu. Improved conversion efficiency of GaN/InGaN thin-film solar cells. *IEEE Electron Device Lett* .30(7):724–726, 2009.

[95] C.-L. Tsai, G.-S. Liua, G.-C. Fana, and Y.-S. Leea. Substrate-free large gap InGaN solar cells with bottom reflector. *Solid-State Electron*. 54(5):541–544, 2010.

[96] R. Dahal, J. Li, K. Aryal, J.Y. Lin, and H.X. Jiang. InGaN/GaN multiple quantum well concentrator solar cells. *Appl. Phys. Lett*., 97(7): 073115-1–073115-3, 2010.

[97] R.M. Farrell, C. J. Neufeld, S. C. Cruz, J. R. Lang, M. Iza, S. Keller, S. Nakamura, S. P. DenBaars, U. K. Mishra, and J. S. Speck. High Quantum Efficiency InGaN/GaN Multiple Quantum Well Solar Cells with Spectral Response Extending out to 520 Nm. *Applied Physics Letters* 98(20): 201107, 2011.

[98] T. Nakao, T. Fujii, T. Sugiyama, S. Yamamoto, D. Iida, M. Iwaya, T. Takeuchi, S. Kamiyama, I. Akasaki, and H. Amano. Fabrication of Nonpolar a-Plane Nitride-Based Solar Cell on r-Plane Sapphire Substrate, *Appl. Phys. Express*, 4(10):101001-1-101001-3, 2011.

[99] B. Jampana, T. Xu, A. Melton, M. Jamil, R. Opila, C. Honsberg, and I. Ferguson. Realization of InGaN solar cells on (111) silicon substrate. 35th IEEE Photovoltaic Specialists Conf (PVTC), 457, 2010.

[100] C. Y. Liu, C. C. Lai, J. H. Liao, L. C. Cheng, H. H. Liu, C. C. Chang, G. Y. Lee, J.-I. Chyi, L. K. Yeh, J. H. He, T. Y. Chung, L. C. Huang, K. Y. Lai. Nitride-based concentrator solar cells grown on Si substrates. *Solar Energy Materials and Solar Cells* 117:54-58, 2013.

[101] Y. Kuwahara, T. Fujii, Y. Fujiyama, T. Sugiyama, M. Iwaya, T. Takeuchi, S. Kamiyama, I. Akasaki, and H. Amano. Realization of Nitride based solar cell on freestanding GaN substrate*. Appl. Phys. Express*., 3(11): 111001-1–111001-3, 2010.

[102] L. Hsu and W. Walukiewicz. Modeling of InGaN/Si tandem solar cells*. J. Appl. Phys.*10(2): 024507-1–024507-7, 2008.

[103] J.W. Ager III, L.A. Reichertz, Y. Cui, Y.E. Romanyuk, D. Kreier, S.R. Leone, K.M. Yu, W.J. Schaff, and W. Walukiewicz. Electrical properties of InGaN-Si heterojunction. *Phys. Stat. Sol*. (c), 6(S2): S413–S416, 2009.

[104] B.-T. Tran, E.-Y. Chang, H.-D. Trinh, C.-T. Lee, K.C. Sahoo, K.-L. Lin, M.-C. Huang. Fabrication and characterization of n-In0.4Ga0.6N/p-Si solar cell. *Energy Mater. Sol. Cells,* 102: 208–211, 2012.

[105] J. Sheu, C. Yang, S. Tu, K. Chang, M. Lee, W. Lai, and L. Peng. Demonstration of GaN-Based Solar Cells with GaN/InGaN Superlattice Absoprtion layers. *IEEE Electron Device Letters* 30(3) 225-227, 2009.

[106] M.-J. Jeng, Y.-L. Lee, and L.-B. Chang. Temperature dependences of In x Ga 1− x N multiple quantum well solar cells. *J. Phys. D. Appl. Phys.* 42(10):105101, 2009.

[107] H. C. Lee, Y. K. Su, W. H. Lan, J. C. Lin, K. C. Huang, W. J. Lin, Y. C. Cheng, and Y. H. Yeh. Study of Electrical Characteristics of GaN Based Photovoltaics with Graded In Ga Absorption Layer. *IEEE Photonics Technology Letters* 23(6):347–349, 2011.

[108] J. R. Lang, N. G. Young, R. M. Farrell, Y.-R. Wu, and J. S. Speck. Carrier escape mechanism dependence on barrier thickness and temperature in InGaN quantum well solar cells. *Appl. Phys. Lett.*, 101(18):181105, 2012.

[109] J. J. Wierer, D. D. Koleske, and S. R. Lee. Influence of barrier thickness on the performance of InGaN/GaN multiple quantum well solar cells. *Appl. Phys. Lett.* 100(11):111119, 2012.

[110] N. G. Young, R. M. Farrell, Y. L. Hu, Y. Terao, M. Iza, S. Keller, S. P. DenBaars, S. Nakamura, and J. S. Speck. High performance thin quantum barrier InGaN/GaN solar cells on sapphire and bulk (0001) GaN substrates. *Appl. Phys. Lett* 103(17):173903, 2013.

[111] S. Valdueza-Felip, A. Mukhtarova, L. Grenet, C. Bougerol, C. Durand, J. Eymery, and E. Monroy, Improved conversion efficiency of asgrown InGaN/GaN quantum-well solar cells for hybrid integration. *Appl. Phys. Express* 7 :032301, 2014.

[112] Soitec. Soitec CPV addresses a fast growing market. (http://www.soitec.com/en/markets/solar-energy/cpv-market-prospects/)

[113] Fraunhofer ISE, NREL. Current status of concentrator photovoltaic (CPV) technology. Last updated on January, 2015, (http://www.ise.fraunhofer.de/en/publications/veroeffentlichungen-pdf-dateien en/studien-und-konzeptpapiere/current-status-of-concentrator-photovoltaic-cpv-technology.pdf)

[114] K. Nishioka, T. Takamoto, T. Agui, M. Kaneiwa, Y. Uraoka, T. Fuyuki. Annual output estimation of concentrator photovoltaic systems using high-efficiency InGaP/InGaAs/Ge triple-junction solar cells based on experimental solar cell's characteristics and field-test meteorological data. *Solar Energy Materials & Solar Cells* 90:57-67, 2006.

[115] Y.P. Varshni. Temperature dependence of the energy gap in semiconductors. *Physica* 34:149-154, 1964.

[116] P.Singh, N.M. Ravindra Temprature dependence of solar cell performance. *Solar energy materials & Solar Cells* 101:36-45, 2012.

[117] J. W. Ager III and W. Walukiewicz. High efficiency, radiation hard solar cells. Lawrence Berkeley National Laboratory, Paper LBNL 56326, 2004.

[118] M. Kuball, F. Demangeot, J. Frandon, M. A. Renucci, J. Massies, N. Grandjean, R. L. Aulombard, and O. Briot. Thermal stability of GaN investigated by Raman scattering. *Applied Physics Letters*. 73(7):960-962, 1998.

[119] F. Medjdoub, J.-F. Carlin, M. Gonschorek, E. Feltin, M. A. Py, D. Ducatteau, C. Gaquiere, N. Grandjean, and E. Kohn. Can InAlN/GaN be an alternative to high power / high temperature AlGaN/GaN devices. Electron Devices Meeting, IEDM '06. 2006.

[120] S. Yamamoto, M. Mori, Y. Kuwahara, T. Fujii, T. Nakao, S. Kondo, M. Iwaya, T. Takeuchi, S. Kamiyama, I. Akasaki, and H. Amano. Properties of nitride-based photovoltaic cells under concentrated light illumination. *Phys. Status Solidi RRL*. 6(4):145-147, 2012.

[121] L. Zhao, T. Detchprohm, and C. Wetzel. High 400 °C operation temperature blue spectrum concentration solar junction in GaInN/GaN. *Applied Physics Letters.* 105(24):243903-243903(4), 2014.

[122] D.-H. Lien, Y.-H. Hsiao, S.-G. Yang, M.-L. Tsai, T.-C. Wei, S.-C. Lee and J.-H. He. Harsh photovoltaics using InGaN/GaN multiple quantum well schemes. *Nano Energy*. 11:104-109, 2015.

[123] M. Yamaguchi. Radiation-resistant solar cells for space use*. Sol. Energ. Mater. Sol. Cell.,* 68 :31–53, 2001.

[124] J. Wu, W. Walukiewicz , K. M. Yu , W. Shan , J. W. Ager III, E. E. Haller , H. Lu , W. J. Schaff , W. K. Metzger, and S. Kurtz. Superior radiation resistance of alloys: Full-solar-spectrum photovoltaic material system. *J. Appl. Phys*. 94(10):6477-6782, 2003.

[125] M A Moram and M E Vickers. X-ray diffraction of III-nitrides. *Reports on Progress in Physics* 72(3):036502-1-036502-40, 2009.

[126] T. Riedl, University of Paderborn. Transmission and scanning transmission electron microscopy (TEM/STEM), (http://physik.uni-paderborn.de/en/lindner/research/temstem/)

[127] P. Lavenus, A. Messanvi, L. Rigutti, A. D. L. Bugallo, H. Zhang, F. Bayle, F. H. Julien, J. Eymery, C. Durand, M. Tchernycheva. Experimental and theoretical analysis of transport properties of core-shell wire light emitting diodes probed by electron beam induced current microscopy*. Nanotechnology*, 25(25):255201, 2014.

[128] L. Görgens, O. Ambacher, M. Stutzmann, C. Miskys, F. Scholz, and J. Off. Characterization of InGaN thin films using high-resolution x-ray diffraction. *Applied Physics Letters*. 76(5):577-579, 2000.

[129] K. Pantzas, G. Patriarche, G. Orsal, S. Gautier, T. Moudakir, M. Abid, V. Gorge, Z. Djebbour, P. L. Voss, and A. Ougazzaden. Investigation of a relaxation mechanism to InGaN for

improved MOVPE growth of nitride solar cell materials. *Phys. Status Solidi* A209 (1):25–28, 2012.

[130] G.Orsal, Y.El Gmili, N. Fressengeas,J.Streque, R. Djerboub, T.Moudakir, S.Sundaram, A. Ougazzaden, and J.P. Salvestrini. Bandgap energy bowing parameter of strained and relaxed InGaN layer. *Optical Materials Express*, 4(5):1030-1041, 2014.

[131] W-C Tsai, C-H. Hsu, S-F. Fu, F-W.Lee, C-Y. Chen, W-C. Chou, W-K Chen, W-H. Chang. Optical Properties associated with strain relaxations in thick InGaN epitaxial films. *Optics Express*, 22(S2): A417-A424, 2014.

[132] S.O. Mariager, X-Ray Diffraction from semiconductor nanowires, Master Thesis, 2006.

[133] X. H. Wu, C. R. Elsass, A. Abare, M. Mack, S. Keller, P. M. Petroff, S. P. DenBaars, J. S. Speck, and S. J. Rosner. Structural origin of V-defects and correlation with localized excitonic centers in InGaN/GaN multiple quantum wells*. Appl. Phys. Lett.*72:692, 1998.

[134] D. M. Graham, A. Soltani-Vala, P. Dawson, M. J. Godfrey, T. M. Smeeton, J. S. Barnard, M. J. Kappers, C. J. Humphreys, and E. J. Thrush. Optical and microstructural studies of InGaN/GaN single quantum well structures. *Journal of Applied Physics* 97(10):103508, 2005.

[135] J.R. Jinschek, R. Erni, N.F. Gardner, A. Y. Kim, and C. Kisielowski. Local indium segregation and band gap variations in high efficiency green light emitting InGaN/GaN diodes. *Solid State Communications* 137(4):230-234, 2006.

[136] T. M. Smeeton, M. J. Kappers, J. S. Barnard, M. E. Vickers, and C. J. Humphreys, Electron beam induced strain within InGaN quantum wells: False Indium "cluster" detection in the transmission electron microscope, *Appl. Phys. Lett*. 83 (26):5419-5421, 2003.

[137] J.P. O'Neill, I. M. Ross, A.G. Cullis, T. Wang, and P. J. Parbrook, Electron beam induced segregation in InGaN/GaN multiple quantum wells. *Appl. Phys. Lett.* 83:1965, 2003.

[138] T. Li, E. Hahn, D. Gerthsen, R. Rosenauer, A. Strittmatter, L. Reissmann, and D. Bimberg, Indium redistribution in an InGaN quantum well induced by electron beam irradiation in a transmission electron microscope. *Appl. Phys. Lett*. 86:241911, 2005.

[139] K. H. Baloch, A. C. Jonhston-Peck, K. Kisslinger, E. A. Stach, and S. Gradecak. Revisiting the "In-clustering" question in InGaN through the use of aberration corrected electron microscopy below the knock-on threshold. *Applied Physics Letters* 102:191910-1-191910-4, 2013.

[140] L. Redaelli, A. Mukhtrarova, S.V. Felip, A. Ajay, C. Bougerol, C. Himwas, J. Faure-Vincent, C. Durand, J. Eymery, and E. Monroy. Effect of quantum well thickness on the performance of InGaN photovoltaic cells. App. Phy. Lett. 105(13):131105-1-131105-4, 2015.

[141] S.B. Kim, H. Seo, Y. Kim, H. Jeon, J. Song, H. Soh, Y.C. Kim. Remote RF oxygen plasma cleaning of the photoresist residue and RIE-related fluorocarbon films. *Journal of Korean Physical Society* 41(2):247-250, 2002.

[142] W.-Y. Uen, Z.-Y. Li, S.-M. Lan, T.-N. Yang, S.-M. Lio, Fabrication of low resistivity and gold colored TiN films by halide chemical vapor deposition with a low [NH3]/[TiCl4] flow ratio. *Thin Solid Films* 516(1):99, 2007.

[143] Z. X. Qin, Z. Z. Chen, Y. Z. Tong, X. M. Ding, X. D. Hu, T. J. Yu, and G. Y. Zhang, Study of Ti/Au, Ti/Al/Au, and Ti/Al/Ni/Au ohmic contacts to n-GaN, *Appl. Phys. A Mater. Sci. Process*., 78(5):729–731, 2004.

[144] Y. Koide, T. Maeda, T. Kawakami, S. Fujita, T. Uemura, N. Shibata, and M. Murakami, Effects of annealing in an oxygen ambient on electrical properties of ohmic contacts to p-type GaN, *J. Electron. Mater.,* 28(3):341–346, 1999.

[145] J. Smalc-Koziorowska, S. Grzanka, E. Litwin-Staszewska, R. Piotrzkowski, G. Nowak, M. Leszczynski, P. Perlin, E. Talik, J. Kozubowski, and S. Krukowski, Ni–Au contacts to p-type GaN Structure and properties, *Solid. State. Electron.*, 54(7):701–709, 2010.

[146] J.-K. Ho, C.-S. Jong, C. C. Chiu, C.-N. Huang, K.-K. Shih, L.-C. Chen, F.-R. Chen, and J.-J. Kai, Low resistance ohmic contacts to p-GaN achieved by the oxidation of Ni/Au films, *J. Appl. Phys.,* 86(8):4491–4493, 1999.

[147] P.A. Nikolaychuk and A.G. Tyurin, Thermodynamics of chemical and electrochemical stability of Copper-Nickel alloys, *Protection of Metals and Physical Chemistry of Surfaces,* 48 (4):432-476, 2012.

[148] P. Horak, V. Bejsovec, V. Lavrentiev, J. Vacik, M. Vrnatan, and J. Khun, Preparation of NiOx films by post-deposition thermal annealing of Ni: Electrophysical and structural properties, Nanocon 2013, 2013.

[149] R. Pode and B. Diouf. Solar lightning. Springer Verlag, London, 2011.

[150] K. Y. Lai, G. J. Lin, C.-Y. Chen, Y.-L. Lai, and J. H. He. Origin of Hot Carriers in InGaN-Based Quantum-Well Solar Cells. *IEEE Electron Device Lett*. 32:179–181, 2011.

[151] J. R. Lang, C. J. Neufeld, C. A. Hurni, S. C. Cruz, E. Matioli, U. K. Mishra, and J. S. Speck. High external quantum efficiency and fill-factor InGaN/GaN heterojunction solar cells grown by NH3-based molecular beam epitaxy. *Appl. Phys. Lett.* 98: 131115, 2011.

[152] XA Cao, EB Stokes, PM Sandvik, SF LeBoeuf, J Kretchmer, D Walker. Diffusion and tunneling currents in GaN/InGaN multiple quantum well light-emitting diodes, *Electron Device Letters, IEEE* 23 (9):535-537, 2002.

[153] D. Zhu, J. Xu, A. N. Noemaun, J. K. Kim, E. F. Schubert, M. H. Crawford, and D. D. Koleske, *Appl. Phys. Lett.* 94:081113, 2009.

[154] C.-L. Tsai, and W.-C. Wu, Effects of Asymmetric Quantum Wells on the Structural and Optical Properties of InGaN-Based Light-Emitting Diodes. *Materials* 7:3758-3771, 2014.

[155] M. Tchernycheva, V. Neplokh, H. Zhang, P. Lavenus, L. Rigutti, F. Bayle, F. H. Julien, A. Babichev, G. Jacopin, L. Largeau, R. Ciechonski, G. Vescovi, et O. Kryliouk, *Nanoscale* pp.1-9 2015.

[156] S.A. Bel'nik, P.S. Vergeles, N.M. Shmidt, and E.B. Yakimov. Defects with bright contrast in the induced-current mode in GaN-based light-emitting structures. *J. Surf. Investig. X-ray, Synchrotr.Neutron Techniq*. 1:394, 2007.

[157] P S Vergeles and E B Yakimov. EBIC investigation of InGaN/GaN multiple quantum well structures irradiated with low energy electrons. *Journal of Physics: Conference Series* 281:012013-1-012013-6, 2011.

[158] Amano H, Kito M, Hiramatsu K and Akasaki P-type conduction in Mg-doped GaN treated with low-energy electron beam irradiation (LEEBI). *Jpn. J. Appl. Phys*. 28: L2112-L2114, 1989.

[159] M. Sumiya, T. Honda, L. Sang, Y. Nakano, K. Watanabe, et F. Hasegawa. Improvement of strained InGaN solar cell performance with a heavily doped n+-GaN substrate. *Phys. Status Solidi* A 212:1033-1038, 2015.

[160] R. M. Farrell, D.J. Friedman, N. Young, E. Perl, N. Singh, J. Lang, C. Neufeld, M. Iza, S. Cruz, S. Keller, W. E. McMahon, S. Nakamura, S. P. DenBaars, U. K. Mishra, J. E. Bowers, and J. S. Speck. InGaN-based solar cells and high-performance broadband optical coatings for ultrahigh efficiency hybrid multijunction device designs. *Applications and Technology-Optical Society of America,* ATh4N-4, 2013.

[161] A. Mukhtarova. InGaN/GaN Multiple Quantum Wells for Photovoltaics, PhD thesis 2015.

[162] L. Redaelli, A. Mukhtrarova, A. Ajay, A. N. Cascajero, S.V. Felip J. Bleuse, C. Durand, J. Eymery, and E. Monroy. Effect of the barrier thickness on the performance of mutipl-quantum-well InGaN photovoltaic cells. Japanese Journal of Applied Physics 54(7):072302, 2015.

[163] D. Yan, G. Weiling, Z. Yanxu, L. Jianpeng, and Y. Weiwei, Rapid thermal annealing effects on vacuum evaporated ITO for InGaN/GaN blue LEDs. *Journal of Semiconductors* 33:066004, 2012.

[164] S.D. Hersee, D. Zubia, X. Sun, R. Bommena, M. Fairchild, S. Zhang, D. Burckel, A. Frauenglass, and S.R.J. Brueck, Nanoheteroepitaxy for the integration of highly mismatched semiconductor materials. *Quantum Electron., IEEE J.* 38:017–1028, 2002.

[165] A. Alizadeh, P. Sharma, S. Ganti, S.F. LeBoeuf, and L. Tsakalakos, Templated wide band-gap nanostructures. *J. Appl. Phys.* 95:8199–8206, 2004.

[166] S. Sundaram, Y. El Gmili, R. Puybaret, X. Li, P. L. Bonanno, K. Pantzas, G. Patriarche, P. L. Voss, J. P. Salvestrini, and A. Ougazzaden. Nanoselective area growth and characterization of dislocation-free InGaN nanopyramids on AlN buffered Si (111) templates. *Applied Physics Letters* 107:113105-1-113105-5, 2015.

[167] McMahon, W.E.Lin, C.-T. J.S. Ward, J.F. Geisz, M.W. Wanlass, J.J. Carapella, W. Olavarria, M. Young, M.A. Steiner, R..M. France, A.E. Kibbler, A. Duda, J.M. Olson, E.E. Perl, D.J. Friedman, and J.E. Bowers. Metal pillar interconnection topology for bonded two terminal multijunction III-V solar cells, *IEEE Journal of Photovoltaics*, 3(2):868-872, 2012.

[168] S. Krishnamoorthy, D.N. Nath, F. Akyol, P.S. Park, M. Esposto, and S. Rajan. Polarization-engineered GaN/InGaN/GaN Tunnel Diodes. *Appl. Phys. Lett.* 97:293502, 2010.

[169] S. Krishnamoorthy, P.S. Park, and S. Rajan, Demonstration of Forward Inter-band Tunneling in GaN by Polarization Engineering. *Appl. Phys. Lett.* 99:233504, 2011.

[170] Z. Zhang, S.T. Tiam, Z. Kyaw, Y. Ji, W. Liu, Z. Hu, N. Hasanov, X.W. Sun, and H.V. Demir. InGaN/GaN light-emitting diode with a polarization tunnel junction. *Applied Physics Letters* 102:193508, 2013.

[171] J.T. Leonard, E.C. Young, B.P. Yonkee, D.A. Cohen, T. Margalith, S.P. DenBaars, J.S. Speck, and S. Nakamura. Demonstration of a III-nitride vertical-cavity surface-emitting laser with a III-nitride tunnel junction intercavity contact. *Applied Physics Letters* 107(9):091105, 2015.

[172] S. Krishnamoorthy, F. Akyol, P.S. Park, S. Rajan. Low Resistance GaN/InGaN/GaN Tunnel Junctions. *Appl. Phys. Lett* 102 :113503, 2013

Publications in peer-reviewed international journals

E. Dogmus, M. Zegaoui, L. Largeau, M. Tchernycheva, V. Neplokh, S. Weiszer, F. Schuster, M. Stutzmann, M. Foldyna, and F. Medjdoub. High structural quality InGaN/GaN multiple quantum well solar cells. *Physica status solidi* (c) 1-4, 2015.

Publications in conference proceedings

E. Dogmus, L. Largeau, N. Rolland, and F. Medjdoub. Characterization of $In_xGa_{1-x}N$ heterostructures for solar cell applications. 29th European Photovoltaic Solar Energy Conference Proceedings 2014, Amsterdam, Netherlands, pp. 221-224, 2014.

E. Dogmus, L. Largeau, N. Rolland, and F. Medjdoub. $In_xGa_{1-x}N$ heterostructures for solar cell applications. 38th Workshop on Compound Semiconductor Devices and Integrated Circuits in Europe, WOCSDICE 2014, Delphi, Greece. p.1-4, 2014

E. Dogmus, L. Largeau, and F. Medjdoub. Characterization of $In_xGa_{1-x}N$/GaN MQWs heterostructures for solar cells applications 17èmes Journées Nationales du Réseau Doctoral en Micro-Nanoélectronique, JNRDM 2014, Villeneuve d'Ascq, France. 3 p, 2014.

E. Dogmus, A. Addad, C. Lethien, P. Roussel, E. Dogheche, N. Rolland, and F. Medjdoub. Characterization of InxGa1-xN/GaN heterostructures for x~0.30 and x~0.55 by XRD and TEM methods. 3èmes Journées Nationales sur la Récupération et le Stockage d'Energie pour l'Alimentation des Microsystèmes Autonomes, JNRSE 2013, 2013, Toulouse, France. 2 p, 2013.

Abstract

This PhD thesis reports on the structural and optical characterization of solar cell structures with various active region designs and different substrates as well as the subsequent fabrication and electrical characterization of InGaN solar cells. The epitaxial growth of solar cell designs with p-GaN/i-InGaN/n-GaN structures were performed by metal-organic vapor phase epitaxy (MOCVD) by the company NovaGaN. The structural and optical characterization is assessed by X-Ray diffraction, scanning transmission electron microscopy, atomic force microscopy and photoluminescence spectroscopy. A structural comparison of solar cell designs including bulk 200 nm thick InGaN layer and InGaN/GaN multiple quantum wells (MQWs) with similar indium compositions (~30%) is presented. Furthermore, structural quality of designs with InGaN/GaN MQWs were analyzed with variation of the indium content, thickness of InGaN quantum wells and type of the substrate, i.e. (0001) sapphire or bulk GaN substrate. An optimized and reproducible processing has been developed for fabrication of InGaN based solar cells. The challenges in device processing such as mesa etching of GaN and contamination on the device sidewalls, which caused high reverse leakage currents were studied and solutions of using SiO_2 mask and protection of sidewalls by SiO_2 layers were proposed. An optimization study of thermal treatment of Ni/Au current spreading layer is also presented. The electrical activity in the active region and the spectral response of the solar cells are investigated by electron beam induced current (EBIC) analysis and external quantum efficiency measurements. EBIC analysis is used to clarify the origin of the S-shape behavior in illuminated current-voltage characteristics of the solar cell with $25\times In_{0.15}Ga_{0.85}N$/GaN MQWs, which has performed the best performance in this study with a conversion efficiency of 0.59% under 1sun illumination (AM1.5G).

Résumé

Ce projet a pour ambition de concevoir et de réaliser une nouvelle filière de cellule photovoltaïque utilisant la conversion directe de l'énergie solaire en électricité à base de la filière InGaN permettant d'atteindre un rendement de 50% de conversion directe de l'énergie solaire en électricité. Cette nouvelle approche constitue un défi technologique majeur pour la recherche académique et les applications industrielles dans les années avenir. Les cellules solaires actuelles à base de Silicium approchent leur limite théorique de rendement de conversion d'énergie (environ 25%). Les cellules solaires multi-jonctions permettent de repousser ces limites en empilant plusieurs matériaux possédant différentes énergies de bande interdite, chacun absorbant une petite portion du spectre solaire de manière plus efficace. Alors que les LEDs violettes et bleu à base du matériau InGaN sont déjà commercialisées, il apparaît essentiel de relever le défi qui consiste à fabriquer et utiliser ce matériau InGaN avec de fort taux d'Indium (i.e. des énergies de bandes interdites plus faibles) afin de couvrir l'ensemble du spectre solaire et ainsi réaliser des cellules photovoltaïques à très haut rendement, bien au-delà de l'état de l'art international. Au vu des limitations des cellules au silicium, des travaux théoriques ont montrés que des cellules à jonctions multiples à base de couches absorbantes d'InGaN permettraient d'atteindre un rendement de 50%. L'amélioration du rendement des cellules solaires aura un impact majeur sur de nombreuses applications. L'objectif de ce travail concerne la conception et de réalisation d'une nouvelle génération de cellule solaire à base d'InGaN. Ce travail concerne dans une première phase : la caractérisation du matériau InGaN à fort taux d'Indium (> 20%) élaboré à l'EPFL en collaboration avec l'IEMN ayant pour but de démontrer une énergie de bande interdite en dessous de 2 eV. Dans une seconde phase, après la validation électrique et structurelle de ce nouveau matériau, il s'agit de concevoir et de réaliser une nouvelle génération de cellule solaire mono-jonction sur saphir et sur substrat GaN. Cette nouvelle cellule solaire pourra être intégrée au sein d'une microsource d'énergie pour réseau de capteur autonome.